Open Research Online

The Open University's repository of research publications
and other research outputs

Water from Lunar Regolith: Reduction by Hydrogen for a Small-scale Demonstration of in situ Resource Utilisation for the Moon

Thesis

How to cite:

Sargeant, Hannah Marie (2020). Water from Lunar Regolith: Reduction by Hydrogen for a Small-scale Demonstration of in situ Resource Utilisation for the Moon. PhD thesis The Open University.

For guidance on citations see FAQs.

© 2020 Hannah Marie Sargeant

https://creativecommons.org/licenses/by-nc-nd/4.0/

Version: Version of Record

Link(s) to article on publisher's website:
http://dx.doi.org/doi:10.21954/ou.ro.00011fb6

Copyright and Moral Rights for the articles on this site are retained by the individual authors and/or other copyright owners. For more information on Open Research Online's data policy on reuse of materials please consult the policies page.

oro.open.ac.uk

Water from Lunar Regolith

Reduction by hydrogen for a small-scale demonstration of in situ resource utilisation for the Moon

Hannah M. Sargeant

B.Sc. Hons (Sheffield, 2013), M.Sc. (Leicester, 2016)

A thesis submitted for the degree of

Doctor of Philosophy

School of Physical Sciences

The Open University

November 2020

Abstract

Water is a critical resource required for long-duration space exploration missions, and in situ water production will be key to enabling a sustained human presence on and around the Moon. There are two potential sources of lunar water: from frozen ice deposits in polar craters; and from the extraction of oxygen from regolith. The Package for Resource Observation and in Situ Prospecting for Exploration, Commercial exploitation and Transportation (PROSPECT) will be used to investigate both sources of water when it is flown on the Luna-27 mission to a high-latitude region of the Moon. The aim of this work was to determine whether a static system, such as that found on the onboard Sample Processing and Analysis suite (ProSPA), could be used to perform hydrogen reduction of lunar regolith to produce water. If successful, it would be one of the first in situ resource utilisation (ISRU) demonstrations to be performed on the Moon. To achieve this aim, the movement of gases in a static system was modelled and then trialled experimentally on a breadboard, where ilmenite, a common lunar mineral, was successfully reduced. A second breadboard with improved thermal control was developed and evaluated, and then used to perform ilmenite reduction experiments where the reaction temperature and hydrogen pressure were optimised to produce the highest yields of water. Finally, the optimised procedure was applied to the reduction of lunar-like and lunar materials, including a lunar highland simulant, crushed lunar meteorite, and two Apollo soil samples. Water was successfully produced from all samples in a four hour reaction. The highest yields were produced from the high-ilmenite-bearing 10084 Apollo soil, resulting in an average yield of 0.94 wt % O_2. The results of this study suggest that hydrogen reduction of regolith in a static system like ProSPA should be feasible.

Acknowledgements

Thank you to my supervisors Andrew, Simeon, Mahesh, Simon, Ian, and Feargus for your support, guidance, and expertise throughout my PhD. I would also like to thank STFC, the Space SRA, and the ProSPA team for their financial support which enabled me to procure the supplies needed to undertake this project, and supported my attendance at numerous invaluable conferences.

Thank you to my fellow lab workers, in particular Feargus and James, for all of the help and advice they provided in both building machines and getting through the ups and downs of PhD life. I am indebted to Tom, Pete, Simona, and Lis, for their never-ending lab support.

I would not have made it through my PhD without my fellow students. Hannah and Shannon, thank you for looking out for me and showing me that all things can be fixed with a slice of home-made cake. My PhD officemates Narissa, David, Tara, Meghan, and Ross, thank you for letting me draw on your different expertise, for talking through my research problems with me, and for being my sounding board. To the members past and present of RocSoc and the planetary surfaces group, you have been a great source of support, fun, and understanding, particularly when faced with the challenges of a nationwide lockdown.

My time at the Broughton house was wonderful, and I can't thank Stacy, Pegg, Carrie, and Melissa enough for welcoming me in to their home and always being there to pick me up after long and exhausting days. I would also like to thank my housemate Claire for her support and encouragement, and for being the best company when my loved ones were so far away. A special mention to my teammates at HP ultimate for the joy they bring to my life, and to my coach and teammates at MMKAC for reminding me why I love to run.

I would like to thank my family and the Andrews clan for their unwavering support and love. A special thank you goes to my mum and Brian. Your belief in me and my passions is what has led me to achieve more than I could have dreamed.

Last but by no means least, I would like to thank Michael for being my biggest supporter and my rock. Thank you for always encouraging me to chase my goals, even if it means you can't be there by my side. It means the world to me.

List of Acronyms

1D	One Dimensional
2D	Two Dimensional
BDL	Below Detectable Limits
BDM	Bench Development Model
BSE	Backscatter Electron
BSLSS	Buddy Secondary Life Support System
CAPTEM	Curation and Analysis Planning Team for Extraterrestrial Materials
COTS	Commercial Off-The-Shelf
EAC	European Astronaut Centre
EATG	EthanolAmine ThioGlycollate
ECLSS	Environmental Control and Life Support Systems
EDS	Energy Dispersive Spectroscopy
ESA	European Space Agency
FIB-SEM	Focus Ion Beam - Scanning Electron Microscope
GAP	Gas Analysis Package
ICP-MS	Inductively Coupled Plasma - Mass Spectrometry
ID	Internal Diameter
IPA	IsoPropyl Alcohol
ISRU	In Situ Resource Utilisation
ISRU-BDM	In Situ Resource Utilisation - Bench Development Model
ISS	International Space Station
KREEP	Potassium (K), Rare Earth Elements, and Phosphorus (P)
LEND	Lunar Exploration Neutron Detector
LRO	Lunar Reconnaissance Orbiter
LCROSS	Lunar CRater Observation and Sensing Satellite
LMO	Lunar Magma Ocean

Continued on next page

Table 1 – *Continued from previous page*

MID	Multiple Ion Detection
np-Fe	Nanophase Iron
NASA	National Aeronautics and Space Administration
NIR	Near Infrared
NWA	North West Africa
OD	Outer Diameter
PCTFE	Polychlorotrifluoroethylene
PILOT	Precursor ISRU Lunar Oxygen Testbed
ProSEED	PROSPECT Sample Excavation and Extraction Drill
ProSPA	PROSPECT Sample Processing and Analysis
PROSPECT	Package for Resource Observation and in Situ Prospecting for Exploration, Commercial exploitation and Transportation
PSR	Permanently Shadowed Region
QIC	Quartz Inert Capillary
RESOLVE	Regolith and Environmental Science, Oxygen and Lunar Volatiles Extraction
RPM	Revolutions Per Minute
RSF	Relative Sensitivity Factor
SD	Standard Deviation
SEM	Scanning Electron Microscope
SOI	Silicon On Insulator
SPA	South Pole-Aitken
SPIN	Space Placements in INdustry
STA	Simultaneous Thermo-Analyzer
STP	Standard Temperature and Pressure
TGA	ThermoGravimetric Analyser
TG-MS	ThermoGravimetric - Mass Spectrometry
TRL	Technology Readiness Level
UVVIS	Ultraviolet/Visible
XRD	X-Ray Diffraction

Contents

List of Figures

List of Tables

Chapter 1

Introduction

1.1 Lunar exploration: a brief overview

Driven by the space race, the 1960s saw a flood of the first missions to the Moon including orbiters, impactors, and landers. Although success rates were limited at first, the lessons learned from each mission fed back into the design of more advanced spacecraft and the mission success rate increased, as did the knowledge of the lunar surface. Images obtained in 1966 from Luna-9, the first successful lunar lander mission, provided reassurance that spacecraft would not sink into the lunar dust (Fielder et al., 1966): welcome news for future crewed surface missions. By 1968 the first life forms had orbited the Moon and successfully returned to Earth aboard Zond 5, including two tortoises amongst others (Norris, 2019). The first and only crewed missions to the Moon were a part of the Apollo program, with astronauts Frank Borman, Jim Lovell, and William Anders making 10 orbits of our natural satellite in 1968 (NASA, 1969*b*). Finally, in July 1969, humans first set foot on another celestial body as Neil Armstrong and Buzz Aldrin landed in the Sea of Tranquility on the lunar nearside while Michael Collins orbited the Moon in the command module (NASA, 1969*a*). Over the next three and a half years Apollo astronauts spent collectively just over 80 hours on the lunar surface before the Apollo program was brought to an end in 1972 and Gene Cernan left the final footprint on the Moon to date (NASA, 1969*a*,*b*, 1970, 1971*a*,*b*, 1972, 1973).

A return to the Moon has increasingly become a focus in the last few decades, starting with a number of lunar orbiter missions operating in the 1990s (Hiesinger and Head III, 2006), and the addition of the Moon to the critical exploration path for the National Aeronautics and Space Administration (NASA) in 2004 (Aldridge, 2004). An increasing number of lunar orbiters, landers, and rovers have since been deployed (Ip et al., 2014; Keller et al., 2016) which have resulted in a significant advancement in the knowledge of the lunar composition,

internal structure, and impact flux of the inner Solar System amongst many other things (Hiesinger and Head III, 2006).

Since the Apollo era, however, human spaceflight has been limited to Earth orbit as the focus was shifted to a more sustainable approach to space exploration. With the ultimate goal of becoming an interplanetary species and landing humans on the surface of Mars, developments are required in the technologies needed to keep crews alive in the harsh space environment for long-duration missions. The Earth-orbiting facility known as the International Space Station (ISS) has been continuously crewed since 2000 and has led to advances in Environmental Control and Life Support Systems (ECLSS) which can support crews for long periods of time with limited resupplies from Earth (Bagdigian et al., 2015; Shaw, 2019). Investigations into the long-term effects of microgravity and radiation on the human body have also been carried out on the ISS (Garrett-Bakelman et al., 2019), and therefore technologies to counteract such effects have been developed (e.g. Thornton and Bonato, 2017; Vuolo et al., 2017). The outputs of the ISS studies are being fed into the design and operation of an orbiting station around the Moon; that is, a human-tended facility enabling human and robotic exploration of the lunar surface (International Space Exploration Coordination Group, 2018). To support the orbiting station, resources on the Moon are being investigated as a source of supplies, with the aim (at least in concept) of reducing the dependence of the facility on Earth. Known as in situ resource utilisation (ISRU), accessing and making use of resources from the local environment can ultimately reduce the cost of large scale exploration missions, and potentially enable missions that would otherwise be economically unfeasible (Lewis et al., 1993). By understanding the lunar surface and the resources available (otherwise known as prospecting), ISRU technologies can be developed to support future exploration missions leading to a sustained human presence on the Moon, and ultimately Mars.

1.2 Resources on the Moon

There are many different types of resources available on the Moon (Schrunk et al., 2007). Temperature extremes can enable the operation of heat engines (Climent et al., 2014) while the minimal lunar atmosphere can be favourable for some manufacturing processes (Landis, 1990). Solar irradiance can be used as an energy resource (Hickman et al., 1990) and regolith can be utilised as a building material (Cesaretti et al., 2014). This thesis focuses on chemical resources that are found in lunar rocks and regolith. To understand the occurrence of these resources we need to briefly consider the nature of the lunar crust.

1.2.1 Formation of the lunar crust

The Moon is thought to have formed through solidification of a widespread lunar magma ocean (LMO) in the aftermath of a giant impact $\sim$ 4.5 Ga ago (Genda, 2018). As the LMO cooled, the Moon experienced differentiation where the light-coloured anorthositic rocks formed the top surface, commonly known as highlands (Vaniman et al., 1991). The highlands are dominantly composed of anorthitic plagioclase feldspar and, therefore, contain abundant calcium, aluminium, silicon, and oxygen. Other rock types such as troctolites and norites are minor but important constituents (from a resource perspective) of the highlands as they contain more mafic minerals such as olivine and pyroxene (Papike et al., 1991). The deeper layers within the Moon are dominated by more mafic minerals such as olivine and pyroxene that are major constituents of mantle rocks. Partial melting of the lunar mantle between 4.5 and 3 Ga led to the generation of basaltic melts, some of which erupted and were emplaced in the lowland areas and impact basins, creating the mare regions. The mare regions contain basaltic materials that are categorised into high-, low- and very low-titanium basalts, all of which have relatively high iron and magnesium contents compared to the highlands (Taylor et al., 1991). The titanium- and iron-bearing mineral ilmenite ($FeTiO_3$) is commonly found in mare basalts, and is often considered a potential source of lunar oxygen (Taylor and Carrier, 1993). Another chemical resource available on the lunar surface is sulfur in the form of troilite (FeS), which is often found in association with ilmenite as thin stringers or as sub-mm inclusions (Evans, 1970).

At a similar time to the formation of the mare lavas, fire fountaining volcanic eruptions were also occurring at the lunar surface (Heiken et al., 1974). The fire fountains released magma from the lunar mantle which quickly quenched in the cold vacuum at the lunar surface forming pyroclastic deposits (Gaddis et al., 1985). These pyroclastic deposits capture some of the volatile inventory of the lunar interior, and large deposits could be a source of water (Milliken and Li, 2017). Also, titanium-rich pyroclastic glasses contain relatively high concentrations of chemically equivalent ilmenite which has not crystallised (Hawke et al., 1990).

Melts rich in incompatible elements such as potassium, rare earth elements and phosphorus (collectively known as KREEP), solidified during the final stages of the cooling of the LMO (Warren and Wasson, 1979). KREEP-rich rocks are localised mostly to the Oceanus Procellarum and Mare Imbrium regions as identified by the Lunar Prospector Gamma Ray Spectrometer, but they are also found dispersed across the lunar surface as they are exhumed

through impacts. The KREEP-rich regions also contain significantly higher concentrations of uranium and thorium compared to the rest of the lunar surface (Lawrence et al., 1998).

1.2.2 Current status of the lunar crust

A schematic cross-section of the modern-day lunar crust is shown in Figure 1.1. The top-most layer, termed regolith, is underlain by the upper and lower megaregolith, and the fractured crust which lies above the remainder of the lunar crust (Richardson and Abramov, 2020). The surficial regolith is composed of unconsolidated material as a result of comminution from billions of years of constant bombardment from large and small micrometeoroids and from the solar and galactic wind, otherwise known as space weathering (Pieters and Noble, 2016). The regolith has an average thickness of between 4 and 5 m in mare regions, while in the highland regions the average thickness of the regolith varies between 10 and 20 m (McKay et al., 1991a). The majority of the regolith is defined as lunar soil which is the < 1 cm fraction that coats the surface of the Moon. Lunar soil contains mechanically disintegrated basaltic and anorthositic rocks, and volcanic glasses. It also contains material that is the product of micrometeorite bombardment, namely agglutinates and impact glasses, as well as a small fraction of meteoritic content. Agglutinates are formed through micrometeorite bombardment of the upper 1 mm of lunar regolith resulting in mineral, lithic and glassy grains that are bonded together by an inhomogenous glassy matrix (Basu, 1977; McKay et al., 1972), while impact glasses are formed by the impact melting of regolith (Zellner, 2019). Beneath the regolith lies what is known as the megaregolith (Hartmann, 1973). The upper megaregolith is thought to contain large scale ejecta (> 1 m blocks) that has been balistically transported from large impacts and is estimated to reach depths of ~ 2 km (Aggarwal and Oberbeck, 1979; Hartmann, 1980). The lower megaregolith is thought to contain fragmented crustal material that has formed in situ as a result of impacts, estimated to reach depths of ~ 20 km (Wiggins et al., 2019). Beneath the megaregolith is assumed to be a fractured crust which overlies the intact lunar crust (Dainty et al., 1974).

Fine-grained surficial regolith will likely be of most interest to future ISRU technologies. There are no mineral concentration mechanisms in the lunar crust, such as the hydrothermal systems on Earth (Prokof'ev, 1998), sufficient to justify mining much deeper. Also, if bulk processing of regolith is required for resource extraction, the fine-grained regolith material is more desirable as it reduces the need for an energy consuming crushing/grinding step that would otherwise be required before the separation of minerals could be performed (Ballantyne et al., 2012).

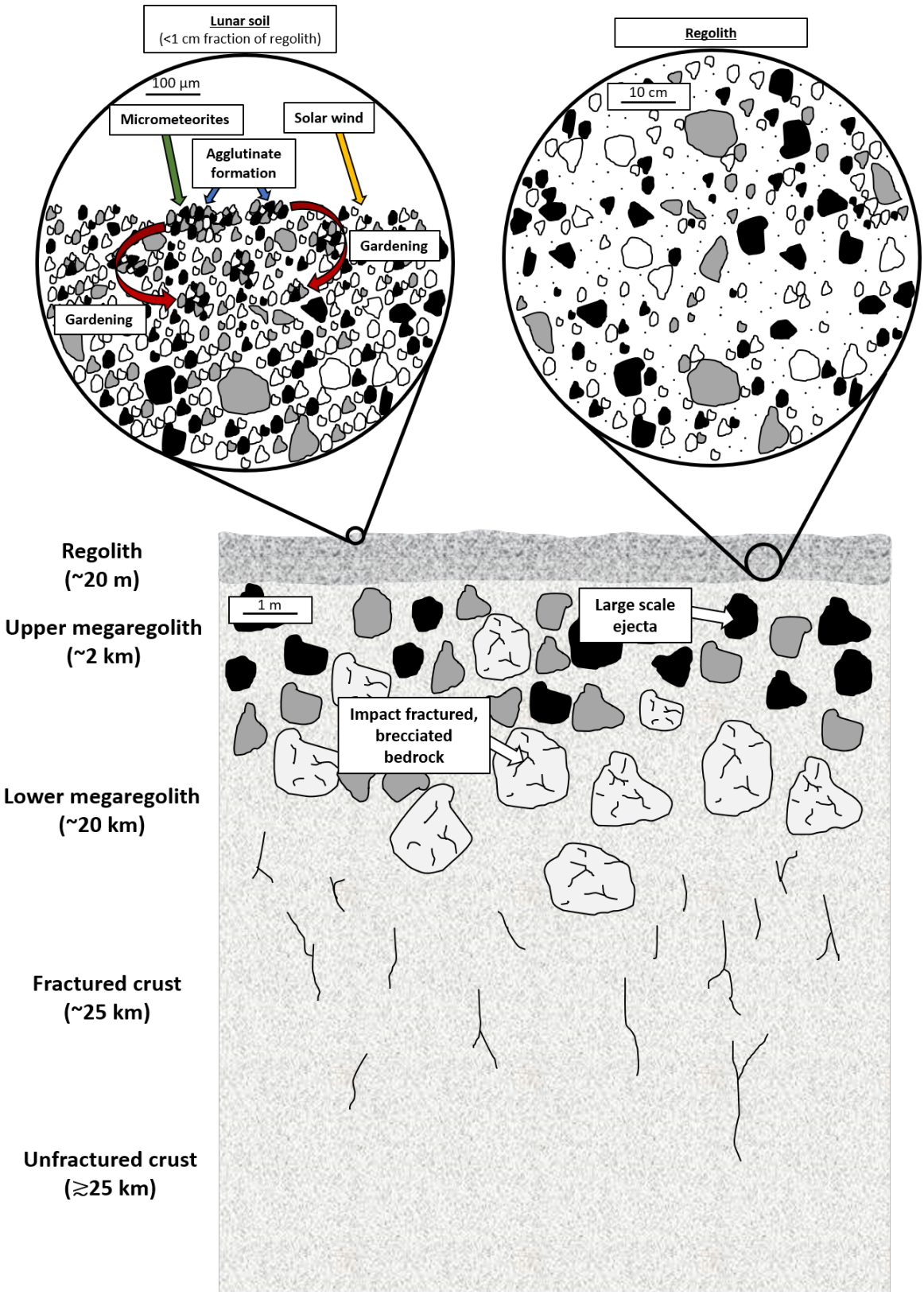

Figure 1.1: Schematic of the lunar surface crust, adapted from Hörz et al. (1991) and Taylor (n.d.).

1.2.3 External contributions to lunar surface material

Resources can be found on the lunar surface from a variety of external sources such as solar wind implanted volatiles, and cometary and meteorite deposits. The solar wind implanted volatiles are mostly composed of hydrogen and helium nuclei, but also include nitrogen, carbon, and noble gases (Fegley and Swindle, 1993). Volatiles deposited in the lunar regolith can be distributed through the soil after impacts, where volatile abundances are often correlated with soil maturity and solar wind fluence. Native water may be produced from interactions between the solar wind and the regolith (Ichimura et al., 2012), while cometary or hydrated meteorite impacts may also deposit water (Greenwood et al., 2011). Metallic meteorites may deposit metal ores providing localised resources, meanwhile, secondary troilite can be formed when native iron sulfurises during meteorite impacts (Taylor et al., 1991).

1.2.4 The lunar poles

There is an interest in exploring the lunar poles specifically because of the presence of permanently shadowed and illuminated regions. Evidence of frozen water was detected in the shadowed regions by Clementine's ultraviolet/visible (UVVIS) camera (Meng et al., 2011), the near infrared (NIR) and UVVIS instruments in the shepherding spacecraft of the Lunar CRater Observation and Sensing Satellite (LCROSS) impactor (Colaprete et al., 2010), the Lunar Reconnaissance Orbiter's (LRO's) Lunar Exploration Neutron Detector (LEND) (Mitrofanov et al., 2010), and Chandrayaan-1's Moon Mineralogy Mapper (Li et al., 2018). Paige et al. (2010) note that as a result of the Moon's 1.5° spin axis inclination angle with respect to the ecliptic, the lunar poles have permanently shadowed 'cold traps' which can maintain temperatures of < 30 K. Water molecules produced by cometary or hydrated meteorite impacts, or volcanic outgassing, or from interactions between the solar wind and the regolith, could potentially migrate to the lunar poles where they are retained for hundreds of millions of years (Siegler et al., 2018; Watson et al., 1961). Recent evidence has also shown conclusively that molecular water is present on the sunlit lunar surface with increasing concentrations (100 to 400 $\mu g \cdot g^{-1}$) towards the higher latitudes (Honniball et al., 2020). This suggests that water is contained within glassy grains or trapped between grains.

With respect to the solar wind implanted volatiles, higher latitudes may retain volatiles more easily as a result of the lower temperatures, where light volatiles diffuse more slowly from mineral lattices (Anand et al., 2012). However, the flux of volatiles at the polar regions of the Moon is significantly less than that experienced at the equatorial regions (Fegley and

Swindle, 1993). The extent to which the high retention of solar wind implanted volatiles compensates for the low flux in the polar regions is not well understood and therefore the concentrations of such volatiles may vary significantly from those of the highlands, which is where the estimations for polar regions are taken in this work.

The geology of the lunar polar regions is relatively poorly understood with only remote sensing data currently available. It is assumed that the regions are mostly composed of highlands-type material (Spudis et al., 2008) and will therefore be depleted in iron- and titanium-bearing minerals as well as KREEP-bearing minerals. An exception to this is the South Pole-Aitken (SPA) basin, which is an ancient impact basin that represents the largest crater on the Moon. The basin contains increased levels of iron, titanium and thorium (Lucey et al., 1998), although recent in situ evidence obtained from the Chang'e 4 Yutu 2 rover suggest ilmenite concentrations are lower than expected in the Von Karman crater within the SPA basin (Lai et al., 2019). There is evidence for metallic iron being present at the SPA basin because of magnetic anomalies, potentially from an impact of a differentiated metallic asteroid (Wieczorek et al., 2012).

The lunar south pole in particular has been a focus for future missions as there are more permanently shadowed regions (PSRs) in the south polar regions as compared to the north polar regions. Consequently, there is increased evidence for frozen water ice in south polar regions (Li et al., 2018). Also, the high priority science target of the SPA basin overlaps with the lunar south pole (National Research Council, 2007, 2011) making the south pole an attractive goal for prospecting and sample return missions (Flahaut et al., 2020).

1.2.5 Classifying resources

There are a number of factors to consider when determining which resources could usefully be extracted from the lunar surface including extraction energy; complexity of the extraction process; usefulness of the products; and by-products of extraction. The usefulness of a product will initially drive the focus of ISRU technologies as the most urgently required resources will be extracted first. The usefulness of each resource is determined here by its potential applications for lunar activities. A summary of the applications of lunar resources is presented in Table 1.1; it should be noted that this table is by no means exhaustive.

Nitrogen is the inert gas in breathable air. It is necessary to have such a gas in a habitable environment although it is not consumed and so it does not need constant replenishing. Nitrogen could play another key role in lunar agriculture, and so its usefulness increases in the longer term. Aluminium has multiple uses including its use in solid rocket fuel. However,

Resource	Potential applications
Aluminium	Rocket propellant, construction, electrical conductor [1]
Carbon dioxide	Lunar agriculture[2]
Helium-3	Fused with deuterium to produce energy[3]
Hydrogen	Rocket propellant, reducing agent for oxygen extraction[4]
Iron	Construction[4]
Nitrogen	Lunar agriculture, breathable air[2,5]
Oxygen	Rocket propellant, life support[4]
Silicon	Computer chips, photo-voltaics (solar cells), fibre-optic cables, mirrors, lenses[4]
Sulfur	Hydrogen sulfide reduction of metal oxides[6]
Thorium	To enable the production of fissile ^{233}U[3]
Titanium	Construction[4]
Uranium	To develop space based nuclear power[3]
Water	Source of oxygen and hydrogen for rocket propellant, life support, use as a solvent, lunar agriculture, radiation protection[4,7]
[1]- Prado (2013), [2]- Yazawa et al. (2012), [3]- Crawford (2015), [4]- Schrunk et al. (2007), [5]- Quattrone (1985), [6]- Christiansen et al. (1988), [7]- Lewis et al. (1993)	

Table 1.1: Potential applications of lunar resources.

producing the associated oxidiser, ammonium perchlorate, in situ will be more challenging. Sulfur can be used to produce oxygen and metals through a reduction process (Vaniman et al., 1992). However, further purification of the oxygen would be required and more research and development is needed. Silicon has numerous applications, with arguably the most important being the development of solar cells to produce power. Power sources will be in high demand and solar power is one of the largest sources of energy available on the Moon. There is potential for the development of nuclear power with the use of thorium/uranium and potentially ^{3}He. However, the infrastructure required is significantly greater than that required for solar power. Therefore, silicon will be one of the resources initially exploited for power generation (Crawford, 2015). Other resources will become essential as a lunar base is matured, and the need for local resources increases with the increase of infrastructure.

Arguably the most useful resources are those that are used for rocket propellant or for life support systems. Producing rocket propellant in situ on the Moon for return or onward journeys will significantly reduce the initial launch mass from Earth. Hydrogen and oxygen are some of the most commonly used rocket propellants (Dawson and Bowles, 2004) and could be harvested from the lunar surface either separately or in the form of water. Water and oxygen are also critical for the life support needs of humans and ultimately they are the most imminently required resources required for space exploration missions. It would be

reasonable to expect that hydrogen would initially be supplied from Earth when used as a reducing agent for oxygen extraction from regolith. Hydrogen has relatively low mass and is not consumed in the reduction reaction, therefore it would be more economical to launch the required supplies from Earth rather than extracting hydrogen from the lunar polar water ice or small quantities as solar wind implanted hydrogen.

1.2.6 Extracting lunar water/oxygen

There are three key methods for accessing water on the Moon: from frozen water ice deposits at the lunar poles; extraction from glasses; or production from the constituent oxygen and hydrogen within lunar regolith.

Lunar polar water is thought to be located inside PSRs. PSRs are extremely challenging to access in terms of the low temperatures, lack of solar energy, and relatively unknown regolith properties (Burke, 2012) compared to the relatively flat and illuminated regions on the nearside equator where the majority of previous missions have landed. Before frozen water deposits can be utilised, their abundance and distribution needs to be better understood. A number of rover/lander instrument concepts are in development to more fully understand the lunar polar ice deposits (e.g. Biswas et al., 2020; Lasue et al., 2012; Roush et al., 2015), however, to date there has not been any in situ water ice measurements at the lunar poles.

Trace amounts of water have been found in lunar volcanic glasses (e.g. Füri et al., 2014; Saal et al., 2008), although with estimated concentrations of up to 54 ppm of H_2O in samples returned from the lunar surface, they would not be suitable for harvesting. Higher estimates have been made, of up to 150 ppm, of H_2O in large pyroclastic deposits through remote sensing techniques (Milliken and Li, 2017), with pyroclastic vents hosting up to 400 ppm. Pyroclastic deposits may be economically viable for harvesting water, however further ground truth is required and one particular challenge will be their limited geographical distribution on the lunar surface (Gaddis et al., 2003). There is limited research into the extraction of water from pyroclastic glasses, there is however significant research into the extraction of oxygen from these materials through reduction reactions (e.g. Allen et al., 1992, 1994, 1996; McKay et al., 1991b). The recent discovery of molecular water in higher latitude material (thought to be inside glassy grains) may also be considered as a source of water (Honniball et al., 2020). However, broader mapping is still required to understand the distributions across the entire lunar surface and in situ measurements will be required to understand the distribution with depth.

There are numerous methods which have been proposed for extracting chemically-bound

oxygen from lunar minerals, most of which fall into the following categories; solid/gas interaction; molten separation; and pyrolysis (Schlüter and Cowley, 2020; Taylor and Carrier, 1993). Solid gas interaction refers to the use of a reactive gas to extract the oxygen from the solid regolith. Molten separation techniques heat regolith to a molten state before performing electrolysis to separate the oxygen and metal ions, or the solid regolith can be immersed in a molten salt to lower the temperatures required for electrolysis. Reduction reactions can also be performed in the molten phase to extract oxygen. Finally, pyrolysis refers to the heating of regolith to the vapour phase in order to dissociate the metal and oxygen. Each process has advantages and disadvantages with respect to the feedstock used, the resupply mass, the complexity of the process, and the energy required.

1.3 Water/oxygen production with ProSPA

1.3.1 ESA ISRU strategy

The European Space Agency (ESA) ISRU roadmap comprises four steps as follows: "1) prospecting to characterise resource deposits; 2) technology verification and demonstration; 3) an ISRU pilot plant integrated with human missions; 4) full implementation" (Carpenter et al., 2016, 2018). The Package for Resource Observation and in Situ Prospecting for Exploration, Commercial exploitation and Transportation (PROSPECT) addresses the first two steps of the roadmap and is currently in development. The PROSPECT package will feature on the Luna-27 lander (Figure 1.2) in $\sim$ 2025 and it consists of the PROSPECT Sample Excavation and Extraction Drill (ProSEED), and the PROSPECT Sample Processing and Analysis (ProSPA) suite (Sefton-Nash et al., 2018, 2020). ProSPA will be used to characterise volatiles in a lunar south polar region and also perform an ISRU demonstration to produce water/oxygen (Barber et al., 2018).

1.3.2 The ProSPA instrument

The ProSPA system derives its heritage from the Ptolemy instrument onboard the Philae Lander (Wright et al., 2007) and the Gas Analysis Package (GAP) onboard the Beagle 2 Mars lander (Talboys et al., 2009). ProSPA has been adapted and designed primarily for the extraction and characterisation of volatiles, and isotope analysis (Carpenter et al., 2014). The analytical laboratory contains a range of onboard gases (H_2, CO, CO_2, CH_4, N_2, and noble gases), a gas control system, pressure sensors, two cold fingers, two mass spectrometers, and furnaces capable of heating samples to 1000 °C (Figure 1.3). Further details of some of

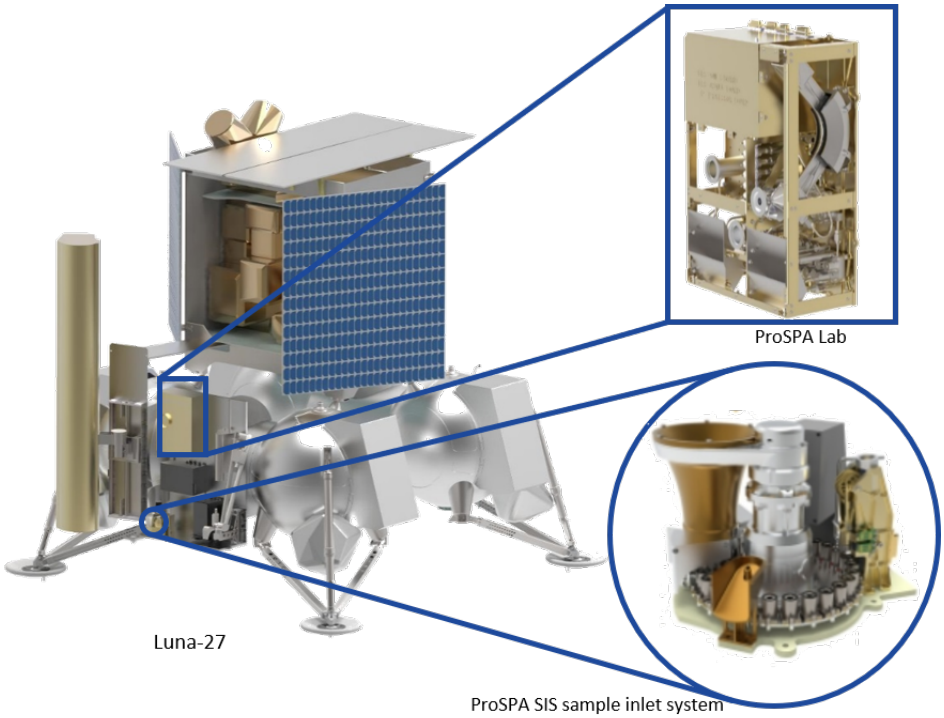

Figure 1.2: Luna-27 and the PROSPECT payload.

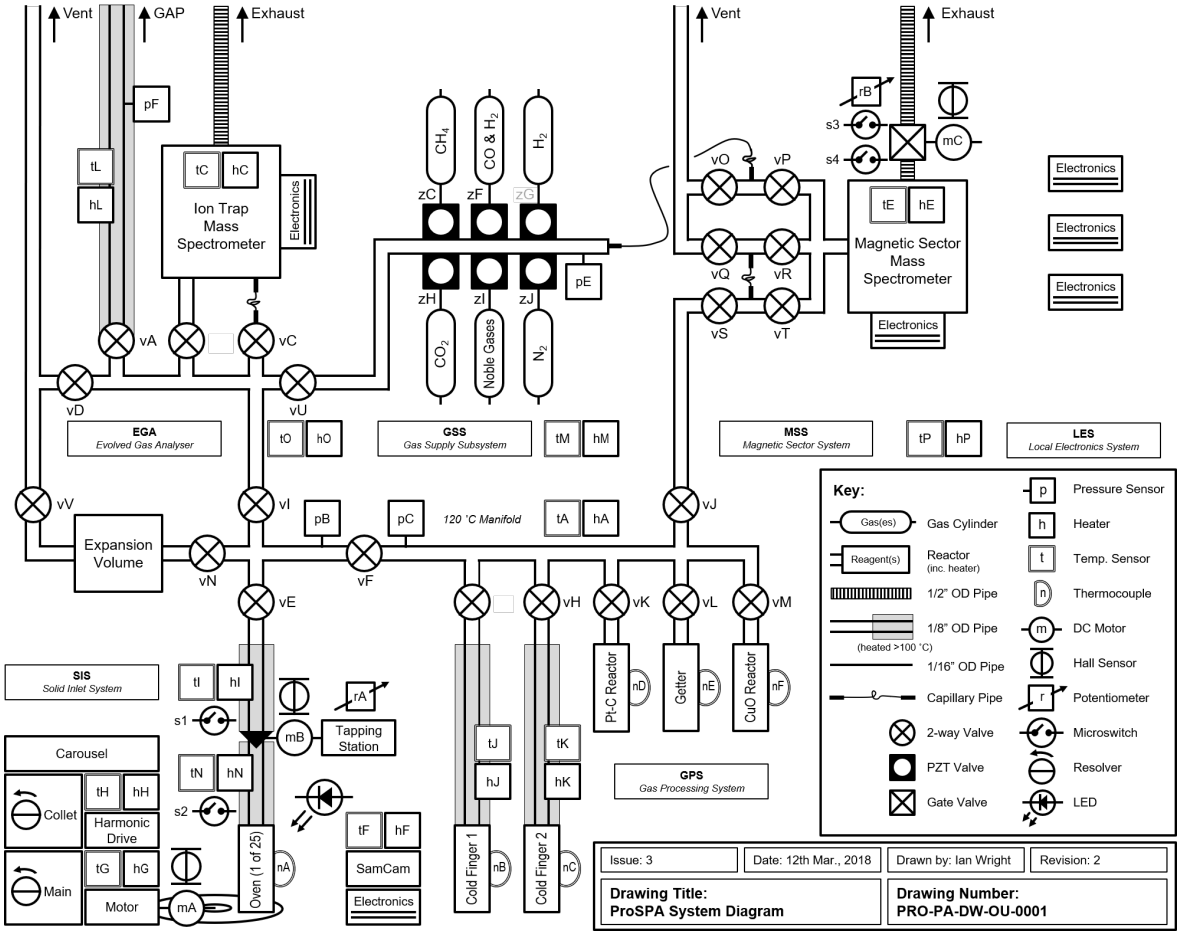

Figure 1.3: ProSPA schematic at the time of writing.

the relevant ProSPA capabilities are shown in Table 1.2. These capabilities will be used to inform theoretical models and the development of experimental systems and procedures.

Component	Capabilities
Furnace	Can hold a 30 mm^3 sample of regolith Can operate at temperatures of up to 1000 °C Can monitor the furnace temperature with a resolution of ± 1 °C
Cold finger	Can operate at temperatures as low as -90 °C Can monitor the cold finger temperature with a resolution of ± 5 °C
Manifold	Can operate at temperatures of up to 120 °C Can monitor the manifold temperature with a resolution of ± 5 °C Can record pressures of up to 1 bar with a safe overload pressure of 1.5 bar Can record pressures with a resolution of 0.25 mbar Has pipe dimensions of 2-4 mm internal diameter and a length of up to 1 m from furnace to cold finger
Gas supply	Has a purity of at least 99.999 %

Table 1.2: Capabilities of the ISRU relevant components of ProSPA.

As it stands, the ProSPA design is optimised for extraction of volatiles through heating and pyrolysis. However, other volatile extraction techniques have been proposed for use with the instrument including oxidation with fluorine, and reduction using hydrogen and methane (Carpenter et al., 2014). Here, different ISRU experiments are evaluated for their feasibility with the current ProSPA design before further theoretical and experimental investigations were carried out.

1.3.3 Selecting an ISRU experiment for ProSPA

Considering the temperature limitations of ProSPA ovens of up to 1000 °C (Barber et al., 2018), most molten separation and pyrolysis reactions will not be feasible. The molten salt electrolysis process has been shown to be successful at temperatures as low as 950 °C (Lomax et al., 2020), however the technique is complex and ProSPA is not designed to carry the molten salt, anode, or cathode required for such a process. Therefore, only solid/gas interactions are to be considered for use on ProSPA.

Solid/gas interaction techniques utilise redox (reduction and oxidation) reactions. In reduction reactions, the reducing agent, X (in this case the gas), loses electrons to the metal in the metal oxide, MO, within the regolith, and gains an oxygen as follows:

$$MO + X \rightarrow M + XO \tag{1.1}$$

Iron oxides are the most easily reducible of the abundant oxides found on the Moon (Schlüter and Cowley, 2020), with ilmenite having the lowest activation energy as compared to other abundant iron oxide-bearing minerals such as pyroxene and olivine (Massieon et al., 1992). The most common reducing agents considered for ilmenite reduction are hydrogen and meth-

ane (Li et al., 2012; Zhang, 2000; Zhao and Shadman, 1993). Large scale ilmenite reduction reactors were the first to be considered for the production of oxygen on a scale of tens to thousands of tonnes of oxygen per year on the Moon (Christiansen et al., 1988; Gibson and Knudsen, 1985). Other iron oxide-bearing minerals such as pyroxene and olivine, which are found in abundance in lunar soils, can also be reduced under the same conditions albeit at significantly lower efficiencies, making the reaction feasible at all lunar locations (Massieon et al., 1992). Reduction of solid regolith with hydrogen or methane results in the lowest potential yield as compared to other extraction processes because only iron oxides are reduced and the process is strongly influenced by ilmenite composition of the regolith. However, the process can be performed at relatively low temperatures of $\sim$ 900 °C (Zhao and Shadman, 1993), it has the highest Technology Readiness Level (TRL) of 5 (indicating breadboard validation in a relevant environment) (NASA, 2017; Sanders and Larson, 2012), and the relatively simple process could be demonstrated with the ProSPA instrument hardware.

Another potential solid/gas interaction technique is the fluorination process, which uses highly reactive fluorine (more oxidising than oxygen) by displacing oxygen in metal oxides. The fluorination process can be performed at relatively low temperatures of $\leq$ 750 °C (Turan et al., 2020) and can be used to extract oxygen from all oxides making it suitable for all locations on the Moon (Landis, 2007). However, fluorine is highly corrosive and the process requires multiple reactors (Seboldt et al., 1993). Therefore, the fluorination process is not suitable for ProSPA.

Reduction of regolith is considered further in this work to determine its feasibility for use with ProSPA and any future ProSPA-type instrument.

1.3.4 Reduction with hydrogen

Ilmenite is a common lunar mineral (Papike et al., 1991) that can be reduced in the solid phase to produce water as in Eqn. 1.2. The state of each reactant and product is denoted as (s) solid or (g) gas:

$$FeTiO_{3(s)} + H_{2(g)} \rightleftharpoons Fe_{(s)} + TiO_{2(s)} + H_2O_{(g)} \tag{1.2}$$

In order to sustain the reduction process, the water vapour produced by the reaction must be constantly removed from the gas phase, e.g. via a flowing gas to a condenser. Taylor et al. (1993) suggested that the partial pressure of H_2O vapour at the reaction site must remain below 10 % for the reaction to continue, while work by Altenberg et al. (1993) suggested that

in systems operating at 900 °C with pressures of 1-100 mbar, the reaction would continue with up to 30 % partial pressure of H_2O. To be conservative, a 10 % partial pressure limit of H_2O as identified by Taylor et al. (1993) is assumed in this work.

The process of ilmenite reduction can be described by a shrinking core model as shown by Dang et al. (2015) (Figure 1.4). The reduction of ilmenite proceeds from the surface to the interior of the grain as hydrogen diffuses inwards, reduces the ilmenite, and water diffuses out of the grain. Metallic iron forms on the outer edges of the grains where the reaction has occurred, acting as nuclei for further metallic iron formation towards the centre of the grains. By recording the amount of iron formation within grains through techniques such as backscatter electron (BSE) imaging and energy dispersive spectroscopy (EDS), the reduction extent within grains can be determined (e.g. Dang et al., 2015; Zhao and Shadman, 1993). The same techniques can also be used to identify which other iron-bearing minerals in lunar simulants or samples can reduce (Massieon et al., 1993, 1992). X-ray diffraction (XRD) is another technique that is used to measure the changes in metallic iron content between reacted and unreacted grains as another confirmation of reduction (e.g. Bardi et al., 1987; Zhao and Shadman, 1993).

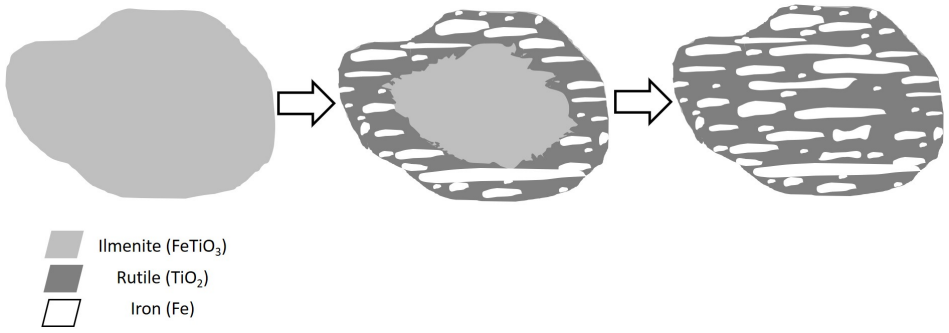

Figure 1.4: Ilmenite grain reduction by hydrogen via the shrinking core model, adapted from (Dang et al., 2015).

The shrinking core model suggests that reduction occurs quickly at first, as a larger surface area of grains is exposed to hydrogen. As the reaction progresses, the reduction process slows as the surface area decreases; in addition, hydrogen gas must diffuse through the reacted layer to access the unreacted core and water must diffuse through the reacted layer to be removed. Zhao and Shadman (1993) discuss three stages of the reduction process; namely induction, acceleration and deceleration. The induction stage (where there is initially slow transport of iron from the mineral pores because of insufficient iron nuclei sites at the start of the reaction), is followed by an accelerated reaction rate until the iron oxide supply decreases to a point where the reaction is decelerated.

1.3.5 Carbothermal reduction

Carbothermal reduction of regolith is an alternative to hydrogen reduction as the reducing agent methane is easier to store than hydrogen, and when performed in the molten phase can extract oxygen from silicon and titanium oxides in addition to iron oxides (Schlüter and Cowley, 2020). In the solid-state reaction (< 1100 °C) only iron oxides are reduced, as with hydrogen reduction of regolith. In a carbothermal reduction reaction, methane decomposes into carbon and hydrogen when it comes into contact with hot regolith (Eqn. 1.3). The carbon is deposited onto the regolith where it reacts with iron oxides to produce carbon monoxide and iron (Eqn. 1.4). The hydrogen produced from Eqn. 1.3 can also reduce iron oxides as demonstrated in Eqn. 1.2. The carbon monoxide can reduce the iron oxides to produce carbon dioxide (Eqn. 1.5). The produced carbon dioxide will react with the deposited carbon to produce carbon monoxide that reduces more iron oxide (Eqn. 1.6).

$$CH_4 \rightarrow C + 2H_2 \tag{1.3}$$

$$C + FeO \rightarrow CO + Fe \tag{1.4}$$

$$CO + FeO \rightarrow CO_2 + Fe \tag{1.5}$$

$$C + CO_2 \leftrightarrow 2CO \tag{1.6}$$

The carbothermal reaction may be beneficial for use on static systems that have onboard methane supplies but no hydrogen. However, the reaction products may not be condensible in a static system and could inhibit the diffusion of methane into the grains to react. Also, the reaction results in carbon deposits and yields no additional oxygen to the hydrogen reduction reaction when performed at temperatures that can be reached with ProSPA ovens, only hydrogen reduction is considered further in this work.

1.3.6 Regolith reduction concepts for use on the Moon

Small scale (gram to kilogram scale batches) reduction reaction demonstrator concepts such as the Regolith and Environment Science, Oxygen and Lunar Volatiles Extraction (RESOLVE) payload, the Precursor ISRU Lunar Oxygen Testbed (PILOT) project, and the ROxygen

project successfully demonstrated reduction of iron oxide-bearing minerals in terrestrial field tests in Mauna Kea, Hawaii (Sanders and Larson, 2012). The demonstrators were optimised for the reduction process, each utilising a flow of hydrogen gas in dynamic reactor systems (Keller et al., 2009; Kleinhenz et al., 2009; Lee et al., 2013). Other concepts, such as those theorised for large scale production of oxygen on the Moon are optimised to include a beneficiation stage to increase the ilmenite concentration of the feedstock before it enters the reactor, resulting even higher yields of oxygen (Christiansen et al., 1988; Gibson and Knudsen, 1985).

ProSPA is an analytical instrument with a mass budget limited to 10 kg, and it does not have the resources for a complete ilmenite reduction system, including fluidised/rotating ovens or recirculating hydrogen plumbing. ProSPA also does not have beneficiation capabilities. Instead, a different approach is proposed, adapting to the available hardware to evaluate the regolith at the Luna-27 landing site as a feedstock for oxygen production by reduction with hydrogen. A static process is considered where the iron oxide-bearing regolith is exposed to hydrogen (in a closed system), while a cold finger condenses any produced water as trialled by Williams (1985), thus removing water from the reaction site and enabling the reaction to continue.

The reaction process being considered for use with ProSPA goes as follows: 1) A sample of granular material such as ilmenite or lunar regolith is placed inside a furnace and heated to temperatures of $\sim$ 1000 °C, 2) Hydrogen is introduced into the manifold where it reduces iron oxides within the sample, 3) Water is produced which then diffuses through the remaining hydrogen in the manifold towards a cold finger that is operating at $<$ -90 °C, 4) Water condenses at the cold finger reducing the partial pressure of water:hydrogen, enabling the reaction to continue, 5) The pressure in the manifold is monitored to quantify the conversion of hydrogen to water, 6) After a defined period of time the furnace is cooled and any remaining gases are evacuated from the manifold, 7) The manifold is closed again and the cold finger is heated to convert condensed water into a vapour, 8) The pressure of water vapour is recorded and compared to the pressure change during the reaction. The proposed experiment is considered theoretically and experimentally in this work.

1.4 Research aims

In this work I plan to address the following overarching science question:

"Can ProSPA be used to perform hydrogen reduction of lunar regolith to produce water?"

To answer this question I have devised three research aims which will be addressed with a

series of theoretical and experimental studies that are outlined below.

1.4.1 Aim 1:

- Demonstrate that the hydrogen reduction of ilmenite reaction can proceed in a static system.

In the first phase of this work I investigate the behaviour of gases in a static system to determine whether the reaction will proceed without a continuous hydrogen flow. In a static system, hydrogen is converted to water at the reduction reaction site and the partial pressure of water increases. If the partial pressure rises above 10 % then it is assumed that the reaction will not proceed (Taylor et al., 1993). In a static system like ProSPA, the water should condense at the cold finger causing the partial pressure of water to decrease and therefore the reaction can continue. For ProSPA to perform effective reduction experiments on lunar samples, it must first be determined whether water can diffuse sufficiently quickly away from the reaction site to the cold finger. If the diffusion rate is too slow, it may become the rate controlling step and ultimately inhibit the reaction. The reduction of ilmenite is first considered in this work as it is the most easily reduced iron oxide in the regolith and the reduction process is well characterised.

The rate controlling step in ilmenite reduction reactions is generally found to be the chemical reaction, and/or the diffusion of gases through the product layer of the ilmenite grains (e.g. Dang et al., 2013, 2015; Wang et al., 2009; Zhang et al., 2012). However, the aforementioned ilmenite reduction studies were performed in dynamic systems which utilise a flow of hydrogen gas to draw water away from the reaction site. The diffusion rate of water through hydrogen in a static manifold of ProSPA-like dimensions (Table 1.2) is first determined using a simple one dimensional (1D) model. Considering the ProSPA ISRU experiments are planned to be performed in under four hours, it was deemed reasonable to target a diffusion time of at least one hour so that the reaction can continue to reduce within the four-hour time frame.

Next, the 1D model is adapted to consider the production rate of water as well as the diffusion time through a manifold, and how the two react to the partial pressures of hydrogen and water present. The production rate of water from hydrogen reduction of lunar regolith is simplified to consider pure ilmenite. Water production rate calculations are integrated into a two dimensional (2D) model along with diffusion calculations utilised in the 1D model to predict the extent of a reduction reaction in an ilmenite sample under ProSPA-like conditions. The sample mass considered in this work is calculated to be 45 mg assuming a sample size of

30 mm^3 (Table 1.2), and a density of lunar regolith of 1.5 g cm^{-3} as noted by Carrier et al. (1991). Considering an optimised sample containing pure ilmenite, there will be 0.3 mmol of ilmenite available for reduction.

Feasibility studies are also performed in an experimental setup using a pre-existing bench development model (BDM). The BDM consists of a furnace, cold finger, and stainless steel manifold which can be supplied with hydrogen. The manifold is designed to have pipes with diameter and length on the same scale as that which would be expected with the current ProSPA design to maintain equivalent pressures of gases within the manifold as would be expected with ProSPA. Using the BDM a range of ilmenite sample masses (up to 45 mg) are reduced in the presence of hydrogen for one hour. The pressure change during the reaction and during the release of water from the cold finger is recorded and compared to a blank measurement. If the pressure changes are higher than the blank measurements by at least the resolution of the ProSPA pressure sensors (Table 1.2) then the reaction is deemed to produce measurable yields. Measurable yields within one hour suggest that hydrogen reduction of ilmenite can proceed in a static system such as ProSPA.

1.4.2 Aim 2:

- Determine the optimum reaction conditions for performing hydrogen reduction of ilmenite with a ProSPA-like static system

To optimise the reaction conditions in a ProSPA-like system, an experimental setup is required that has the same capabilities of the ISRU relevant components of ProSPA (Table 1.2). The ISRU bench development model (ISRU-BDM) is developed to meet these capabilities and a comprehensive analysis of each component is carried out. The furnace, cold finger, and manifold are each evaluated for their ability to reach the required temperatures needed to perform ilmenite reduction reactions. The system is then used to quantify water vapour using pressure measurements to the required resolution of the ProSPA instrument, and the necessary calibrations determined.

Optimal reaction conditions will result in the highest yields of water from the reduction reaction. The variables that can be controlled with the ProSPA instrument are the furnace temperature and initial hydrogen pressure. Numerous studies have been performed which look at the effect of temperature and hydrogen pressures on reduction reactions in flowing gas systems. It has been shown experimentally that ilmenite reduction reactions at higher temperatures produce higher yields (Briggs and Sacco, 1991; Li et al., 2012; Zhao and Shadman, 1993). Altenberg et al. (1993) also modelled how higher temperatures increase the

equilibrium constant and ultimately the yield. The influence of sample temperature upon reaction rate is less well understood in a static system, where the rate of diffusion of gases is influenced more significantly by the furnace temperature as there is no circulating gas pump. Meanwhile, investigations into hydrogen pressures in a flowing system have considered the system pressures and the flow rate of the gas (Hegde et al., 2011; Zhang et al., 2012; Zhao and Shadman, 1993). In a static ilmenite reduction system hydrogen pressure was investigated theoretically by Altenberg et al. (1993), who showed that optimal reaction rates occur at pressures of < 1 bar. When hydrogen pressure is reduced, Altenberg (1992) showed that the equilibrium point of the reaction is shifted so that higher yields of water are produced, however no experimental studies were performed. In this work ilmenite reduction is performed at temperatures from 700 °C to 1100 °C and the yields are compared. Temperatures are trialled above that of the ProSPA capabilities so that recommendations for increased capabilities could be made if necessary. Initial hydrogen pressures of up to 584 mbar (0.4 mmol) are trialled for ilmenite reduction reactions as this would be more than sufficient to reduce a pure ilmenite sample and higher pressures are not necessary as the literature suggests that lower pressures are more suitable. The temperature and pressure conditions that result in the highest yields of water from the reduction of an ilmenite sample in a four hour reaction in the ISRU-BDM will be used for all proceeding experiments.

1.4.3 Aim 3:

- Demonstrate successful hydrogen reduction of lunar material in a ProSPA-like static system

Ilmenite comprises just a fraction of lunar soils which contain many other minerals of mostly basaltic and anorthositic origin (McKay et al., 1991a). The high-latitude regions of the Moon where the Luna-27 mission is likely to land (King et al., 2020) are known to have relatively low iron abundances (Lawrence et al., 2002; Spudis et al., 2013) indicating they comprise highland-type regolith and are expected to contain low ilmenite concentrations. Ilmenite concentrations in lunar highland soils have been recorded as low as < 1 wt % (Simon et al., 1982). Therefore, ilmenite alone may not be in sufficient abundance to produce measurable yields of water from highland soils without beneficiation (production of higher grade ilmenite-rich regolith) in a ProSPA-like static system. It is therefore of interest to consider whether a ProSPA-like system is able to demonstrate measurable reduction of lunar-like material which includes the reduction of other minerals as well as ilmenite. Iron oxides are the most easily reducible oxides (Sabat et al., 2014) and aside from ilmenite, evidence of reduction of

iron oxide-bearing pyroxenes and olivines has also been demonstrated previously in fluidised systems (Britt, 1993; Massieon et al., 1993, 1992), including the reduction of Apollo soils (Allen et al., 1994, 1996; Gibson et al., 1994). A static system has not yet been used to reduce lunar simulants or samples.

The optimised reaction procedure is carried out on lunar simulant, lunar meteorite, and Apollo lunar soils in the ISRU-BDM. The lunar simulant used in this work is the lunar highland simulant NU-LHT-2M. A highland simulant was selected because it provides a 'worst-case-scenario' for reduction with hydrogen. If the reduction reaction is feasible in highland-like materials, which are thought to have the lowest ilmenite concentrations, it should be feasible at all lunar locations. The highland simulant is also doped with increasing quantities of ilmenite to determine the effect on the yield of water, thus simulating the beneficiation of feedstock (Williams et al., 1979). The lunar meteorite selected for analysis is North West Africa (NWA) 12592, which has been classified as a fragmental regolith breccia (Meteoritical Bulletin Database, 2019). NWA 12592 was chosen because sufficient mass ($\sim$ 2 g) was available and the meteorite was deemed a suitable representative of a bulk lunar regolith. However, as there was no identifiable ilmenite (Personal Communication, T. Hayden, September 11th 2019), it would also work as a 'worst-case-scenario' for yields. Two Apollo soils were selected for use for reduction by hydrogen. First an Apollo 11 mare soil, 10084, was selected as it is relatively rich in iron oxide-bearing minerals (Meyer, 2009). As a comparison, Apollo 16 highland soil, 60500, was selected for its relatively low iron oxide-bearing mineral content (Meyer, 2010). Together, the mare and highlands soils provide a range for the possible mineral composition expected on the lunar surface. The soils were approved for destructive analysis by NASA's Curation and Analysis Planning Team for Extraterrestrial Materials (CAPTEM) providing promising results were obtained from the experiments with lunar simulant and the lunar meteorite, i.e. measurable quantities of water were produced.

Each sample is reacted for four hours as per the restrictions on ProSPA ISRU experiments. If the amount of water produced (recorded via pressure measurements) is measurably above the blank value by at least the resolution of the ProSPA pressure sensors then the experiments are deemed a success.

1.4.4 Thesis structure

Each research aim is addressed upon completion of the previous research aim, therefore this thesis is structured chronologically.

Chapters 2 and 3 address Aim 1 where the feasibility of the ilmenite reduction reaction is

evaluated for a static system. A theoretical analysis was performed to determine whether the diffusion of gases in a static system is sufficient to enable the equilibrium reaction to proceed. An experimental analysis was then performed on the BDM where terrestrial ilmenite was reacted with hydrogen.

Chapters 4 and 5 address Aim 2 where the development of a second breadboard, the ISRU-BDM, is described and evaluated. The ISRU-BDM was designed to address the thermal control issues highlighted in Chapter 3, enabling improved quantification of yields of water from the reaction. The ilmenite reduction reaction was then optimised by trialling a range of temperature and hydrogen pressure conditions.

Chapter 6 addresses Aim 3 where the optimised procedure was then applied to a lunar simulant, a lunar meteorite, and lunar soils to determine the suitability of the reaction for use on ProSPA at the lunar surface. Finally, in Chapter 7 the results and the overarching conclusions of the work are summarised, and plans for future work are discussed.

1.4.5 Attribution of published work

Chapter 2 includes preliminary gas flow modelling work described in the peer-reviewed published journal article in *Planetary and Space Science: PROSPECT* Special Issue (Sargeant et al., 2020a). The remainder of the article is used to form the majority of Chapter 3 where ilmenite reduction is trialled in the BDM.

The design and build of the ISRU-BDM and the assessment of water quantification with the ISRU-BDM, as described in Chapter 4, is derived from the peer-reviewed published journal article in *Planetary and Space Science: Space Resources* Special Issue (Sargeant et al., 2020b). The article also describes the reaction optimisation tests and analysis that forms the majority of Chapter 5.

The introduction sections of each of the described first author publications, along with the introduction section of the peer-reviewed published journal article in the *Journal of Geophysical Research: Planets* (Sargeant et al., 2020c) are integrated throughout Chapter 1.

1.4.6 Unpublished contributions of others

The details of the ilmenite reduction 2D static model that is described in Appendix A is adapted from the model and user-manual that was produced by J. Martin as part of a Space Placements in Industry (SPIN) internship at the Open University in 2018. The ethanolmine thioglycollate (EATG) treatment protocol described in Appendix D was described and implemented by J. Gibson at The Open University. Meanwhile, the bulk analysis of the

NU-LHT-2M and NWA 12592 samples was performed at the Natural History Museum, UK, by E. Humphreys-Williams and B. Schmidt and recorded in Table 6.1 in Chapter 6.

Chapter 2

A theoretical evaluation of ilmenite reduction in a static system

This chapter is formed from sections of the published paper Sargeant et al. (2020a) and the associated supplementary material. The calculations used to estimate the diffusion rate in Sargeant et al. (2020a) have been updated here. The modelling from Sargeant et al. (2020a) is expanded upon in this chapter by applying a model formulated by J. Martin, and their contributions are included in Appendix A.

In this chapter the gas flow type is determined for water diffusing through hydrogen in a 1D model of the ProSPA pipework. The rate of diffusion was calculated to determine, to a first order, the time scales involved for the produced water to diffuse through the system. The results were evaluated and the feasibility of an ilmenite reduction reaction in a ProSPA-like static instrument is discussed. Next, a more detailed 2D model was developed (by J. Martin) which considers the production rate of water as well as its diffusion rate through the system. Results from the 2D model were extrapolated to ProSPA and other potential spacecraft instruments implementing a static reduction technique.

2.1 1D model

A 1D static model of a pipe was used to approximate, to a first order, the ProSPA manifold that connects the furnace (where water production occurs) to the cold finger (where water is condensed). In the model, it is assumed that at the start of the reaction the system contains enough hydrogen (0.3 mmol) to reduce a full ProSPA oven of ilmenite (0.3 mmol) which is sufficient for the 1:1 reaction in which one mole of hydrogen will reduce one mole of ilmenite (see Eqn. 1.2 in Chapter 1). As the reaction proceeds, hydrogen converts to water, which

then diffuses through the pipework to the opposing end where it is removed from the vapour phase (Figure 2.1).

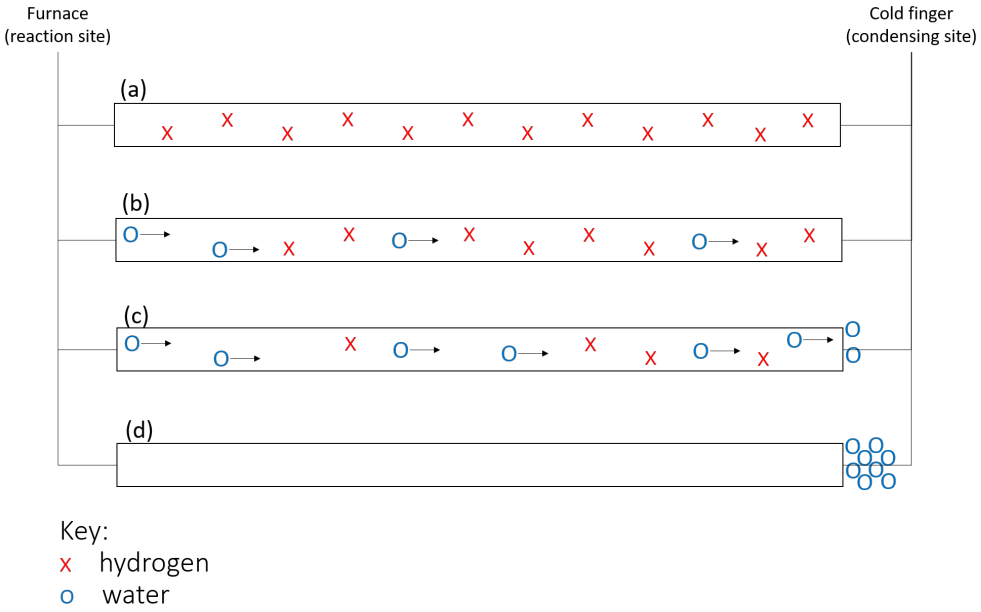

Figure 2.1: A 1D model used to determine the gas flow regime for hydrogen reduction of ilmenite in a static system. (a) indicates the start of the reaction where only hydrogen is in the system. (b) shows hydrogen converting into water at the reaction site and the water diffuses through the system. (c) shows how the hydrogen levels deplete as more water is produced which is then removed from the vapour phase at the condenser. (d) indicates the end of the reaction where all the hydrogen has been converted to water, and all the water has been condensed.

The diffusion mechanism is determined by the gas flow regime. The movement of gases through pipes falls into three regimes termed viscous, transitional, and molecular flow. Viscous flow occurs in low vacuum environments where gas molecules collide frequently, and therefore the mean free path is significantly shorter than the dimensions of the pipework. Meanwhile, molecular flow occurs in high-vacuum systems where the mean free path is significantly larger than the dimensions of the pipework. Transitional flow occurs when the conditions fall between viscous and molecular flow (Pfeiffer Vacuum, 2013). Knudsen diffusion, which is influenced by the pipe diameter, occurs in the viscous (otherwise known as Knudsen) flow regime. Meanwhile molecular diffusion, which is influenced by the mean free path of the gaseous particles, occurs in the viscous flow regime.

2.1.1 Determining the gas flow regime

The gas flow regime is defined by the Knudsen number, K_n. Viscous flow occurs when $K_n < 0.01$, transitional flow occurs when $0.01 \leq K_n \leq 1$, and molecular flow occurs when $K_n > 1$ (Delchar, 1993). In the 1D model, the Knudsen number was calculated as increasing

quantities of water were released into the pipe. The Knudsen number for the flow of water from the furnace to the cold finger was calculated using Eqn. 2.1 where λ is the mean free path of a gas particle and a is the radius of the pipe.

$$K_n = \frac{\lambda}{a} \tag{2.1}$$

The mean free path of gas molecules can be determined with Eqn. 2.2 which uses the Boltzmann constant, k_B, the temperature of the system, T, the average diameter of the molecules, d_{avg}, and the pressure of the molecules, P.

$$\lambda = \frac{k_B T}{\sqrt{2}\pi {d_{avg}}^2 P} \tag{2.2}$$

The diameter of the molecules in the system is taken as an average at defined intervals (in this case defined as 10 % increments in the amount of water produced) as the amount of water and hydrogen changes. The average diameter of gaseous molecules is calculated using the molar quantity of water molecules, n_A, and hydrogen molecules, n_B, in the system and their respective diameters d_A and d_B (Eqn. 2.3). The initial molar quantity of hydrogen, n_B, is defined as the maximum molar quantity of ilmenite, $n_{Max_{ilm}}$, to be trialled. This means that there will be an excess of hydrogen in the system when there are low concentrations of ilmenite to be reacted. As the reaction proceeds, n_B is derived from the molar quantity of ilmenite that has reacted, n_{ilm}, with respect to the reduction extent, ξ, a proportion of reacted ilmenite with a value from 0 to 1 (Eqn. 2.4). Meanwhile, n_A is derived from the amount of initial hydrogen in the system with respect to the reduction extent and the water trapping efficiency of the system, ϵ (Eqn. 2.5). Water trapping efficiency defines how much of the water vapour present is condensed at the cold finger.

$$d_{avg} = \frac{n_A d_A + n_B d_B}{n_A + n_B} \tag{2.3}$$

$$n_B = n_{Max_{ilm}} - \xi n_{ilm} \tag{2.4}$$

$$n_A = n_{ilm}\xi(1 - \epsilon) \tag{2.5}$$

The molar amount of gas in the system, n_{avg}, at each stage of the reaction is calculated by summing n_A and n_B. The ideal gas law (Eqn. 2.6) is then used to calculate the pressure,

P, of gases within the system, using the universal gas constant, R, and system temperature, T.

$$P = \frac{n_{avg}RT}{V} \tag{2.6}$$

The gas flow regime of water in the 1D model was determined for a pipe of length 1 m and internal diameter (ID) of 4 mm. The pipe temperature was assumed to be 115 °C which is more than sufficient to keep water in the vapour phase at pressures of > 1.7 bar (experiments performed with ProSPA will not exceed the safe overload pressure of the instrument of 1.5 bar). Using data from Table 2.1, the Knudsen number was determined for different ilmenite concentrations (25 %, 50 %, 75 % and 100 %) of the 45 mg standard mass that will be sampled by the ProSPA ovens. Various ilmenite concentrations were trialled to determine whether the gas flow regime would be significantly influenced by lower yields of water. It was not known how much of the water produced would condense at the cold finger, i.e. the trapping efficiency ϵ. Therefore, two tests were performed which consider the gas flow regime when all the water is condensed ($\epsilon = 1$), compared to when only half the water is condensed ($\epsilon = 0.5$). Calculations were performed using MATLAB® where the variables d_{avg} and P, and the associated variables used to calculate them, were updated with each iteration of the program.

Data type	Symbol	Value	Unit
Diameter of H_2O molecule	d_A	2.75×10^{-10}	m
Diameter of H_2 molecule	d_B	7.4×10^{-11}	m
Mass of H_2O molecule	m_A	2.989×10^{-26}	kg
Mass of H_2 molecule	m_B	3.211×10^{-27}	kg
Initial molar quantity of H_2	n_B	0.3	mmol
Boltzmann constant	k_B	1.381×10^{-23}	$m^2 \cdot kg \cdot s^{-2} \cdot K^{-1}$
Ideal gas constant	R	8.314	$J \cdot mol^{-1} \cdot K^{-1}$

Table 2.1: Data table for 1D and 2D model calculations.

The Knudsen numbers as calculated for different ilmenite concentrations are shown in Figure 2.2. When it is assumed that all the water produced is immediately condensed ($\epsilon = 1$), the Knudsen number increases as a result of the progressively lower pressure in the system. As the total gas pressure in the system reduces, the gas flow regime moves to transitional flow. When only 50 % of the water produced is condensed ($\epsilon = 0.5$), the relative proportions of water molecules to hydrogen molecules increases, which leads to an increase in the average diameter of molecules in the system as the reaction progresses and the gas flow becomes more viscous. It was assumed that the gas flow would be mostly viscous in the planned ilmenite reduction reactions, with transitional flow only occurring when the reaction of a

100 % ilmenite sample is near completion, and the trapping efficiency is high. Under a viscous flow regime the mechanism of water diffusion towards the cold finger is molecular diffusion through the hydrogen gas.

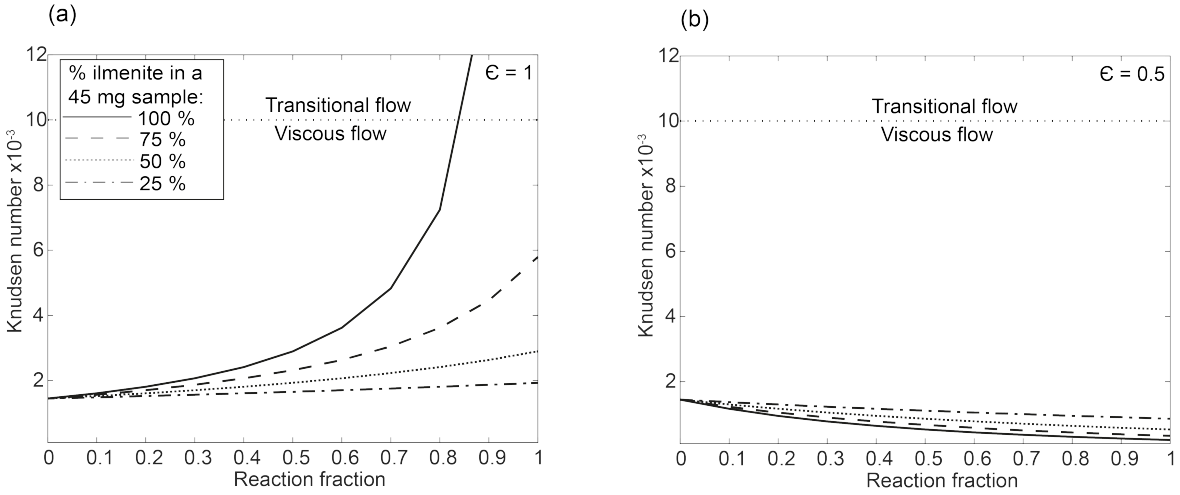

Figure 2.2: Knudsen number for a range of ilmenite concentrations throughout the reduction reaction considering a trapping efficiency of (a) ϵ=1, and (b) ϵ=0.5.

2.1.2 Rate of diffusion

The molecular diffusion rate can be derived from the molar flux of water (gas A) into hydrogen (gas B) in the z direction, in this case, the flux of water through the hydrogen gas towards the cold finger. The molar flux of water, J_{AZ}, can be calculated using Fick's Law which describes the influence of concentration gradient, surface area, and distance of diffusion on the rate of diffusion. Fick was able to develop his model of diffusion processes with a molecular physics approach, and showed how the interactions of microscopic particles result in macroscopic properties of matter (Tyrrell, 1964). The molar flux is calculated using Eqn. 2.7 which can be solved to form Eqn. 2.8 where the diffusion coefficient, D_{AB}, defines the molecular diffusivity of gas A in gas B (water in hydrogen), C_A is the concentration of gas A, and $z_2 - z_1$ is the distance of diffusion (Geankoplis, 1993) (subscript 1 and 2 refer to the location of the furnace and cold finger respectively).

$$J_{AZ} = -D_{AB}\frac{dC_A}{d_z} \tag{2.7}$$

$$J_{AZ} = D_{AB}\frac{(C_{A1} - C_{A2})}{(z_2 - z_1)} \tag{2.8}$$

The concentration of gas A can be substituted using Eqn. 2.9, to form Eqn. 2.10, where P_A is the partial pressure of water and therefore $P_{A2} - P_{A1}$ is the difference in partial pressure

between the furnace and cold finger.

$$\frac{P_A}{RT} = \frac{n_A}{V} = C_A \tag{2.9}$$

$$J_{AZ} = D_{AB}\frac{(P_{A1} - P_{A2})}{RT(z_2 - z_1)} \tag{2.10}$$

The diffusion coefficient is found using Eqn. 2.11, adapted from Delchar (1993), where $\bar{C}_{A|B}$ is the average speed of the molecules A or B, $\lambda_{A|B}$ is the mean free path of the molecules, $n_{A|B}$ is the molar quantity of the molecules, and $n = n_A + n_B$. In the following analysis it is assumed that the molar quantity of hydrogen used is equal to 0.3 mmol, which is the amount of ilmenite that is planned to be reacted, and the hydrogen levels will decrease as the reaction proceeds ($n_B = n_{ilm}(1 - \xi)$). Meanwhile the molar quantity of water at the reaction site is defined as 10 % of the hydrogen in the system ($n_A = 0.1n_B$), as this is the limit as defined by Taylor et al. (1993).

$$D_{AB} = \frac{1}{3}\left(\bar{C}_A\lambda_A\frac{n_B}{n} + \bar{C}_B\lambda_B\frac{n_A}{n}\right) \tag{2.11}$$

The average speed of a molecule can be found using Eqn. 2.12 where k_B is the Boltzmann constant, T is the temperature of the pipe, and m is the mass of the molecule.

$$\bar{C} = \left(\frac{8k_BT}{\pi m}\right)^{\frac{1}{2}} \tag{2.12}$$

The mean free path of the molecule can be found using Eqn. 2.13 where $d_{A|B}$ is the diameter of the molecules A or B.

$$\lambda_{A|B} = \frac{1}{\sqrt{2}\,\pi C_{A|B}{d_{A|B}}^2} \tag{2.13}$$

The partial pressure of water at the furnace, P_{A1}, is assumed to be equivalent to Eqn. 2.14, where all the water molecules in the system are at the furnace temperature, T_f (here 900 °C is used), but dispersed across the entire system volume, V_{sys}. The partial pressure of water at the cold finger, P_{A2}, is assumed to be 0.

$$P_{A1} = \frac{n_ART_f}{V_{sys}} \tag{2.14}$$

Using data from Table 2.1, the molar flux of water into hydrogen is used to determine the time of diffusion, t, across the length of the pipe, l, using the concentration of water molecules

in the pipe, C_A, as in Eqn. 2.15.

$$t = \frac{lC_A}{J_{AZ}} \tag{2.15}$$

2.1.3 1D model - Results

The time taken for water to diffuse through the 1D model was determined for various pipe dimensions. The ilmenite concentration applied in the model was 0.3 mmol (45 mg i.e. 100 % ilmenite concentration) as this would result in the maximum amount of potential water in a ProSPA-like system.

The ProSPA pipe design at the time of writing is yet to be finalised, however the latest design indicates a pipe with ID of $\sim$ 2 mm will be used, with potential to expand the diameter to up to 4 mm, therefore both 2 mm and 4 mm pipe IDs were considered. The pipe length between the ProSPA oven and the cold finger is also yet to be determined however early drawings suggest it will likely be up to 1 m. Both 0.5 m and 1.0 m pipes were considered to show how reducing the pipe length affects the diffusion time. The gas flow regime determined in Section 2.1.1 was calculated for a pipe of length 1 m and ID of 4 mm. All other pipe designs trialled here would therefore result in smaller volumes and higher system pressures, resulting in a viscous flow regime for each pipe design trialled here, and therefore the molecular diffusion model still applies. The results of the analysis of the 1D model are shown in Table 2.2.

Pipe diameter (mm)	Pipe length (m)	t Towards the start of reaction ($\xi = 0.1$) (min)	t Towards the end of reaction ($\xi = 0.9$) (min)
2	0.5	16.6	1.8
2	1	33.1	3.7
4	0.5	4.1	0.5
4	1	8.3	0.9

Table 2.2: Calculated diffusion times for various pipe designs.

The fastest diffusion rate was calculated for shorter pipes with wider pipe diameters, with water taking 4.1 mins to diffuse at the start of a reaction through a pipe with a 4 mm ID and length of 0.5 m. Meanwhile at the end of a reaction water will take just 0.5 mins to reach the cold finger under the same conditions.

2.1.4 1D model - Discussion

The diffusion rate calculated in this work with the 1D model is an improvement on the model used in Sargeant et al. (2020a). In the updated model used in this work the amount of initial hydrogen is always 0.3 mmol. In the previous iteration of the model the initial hydrogen

concentration was defined as the amount of ilmenite present in the sample. However, as the ilmenite concentration would not be known on the lunar surface, it was deemed appropriate to always have sufficient hydrogen to react any amount of ilmenite present, i.e. 0.3 mmol. Another modification to the model is how the furnace temperature (900 °C) is utilised in the pressure calculations at the furnace. Previously the pressure was always calculated using the significantly cooler system temperature (115 °C). Fick's law assumes a homogeneous system temperature and no convective terms (known as drifts) which also cause movement of particles. However, even though the temperatures will vary between the furnace and cold finger on ProSPA it is common practice to use Fick's law as a first order approximation for calculating molar flux even when the underlying assumptions are not met (van Milligen et al., 2005). It should be noted that the 1D model in its current form does not account for circumstances when < 10 % of potential water from hydrogen is produced, which would occur if the diffusion rate was not the rate controlling step.

In the 1D model, the diffusion rate is significantly quicker at the end of the reaction as there are fewer molecules in the system for the water to move past. It is for this reason that wider ID pipes result in lower pressures and therefore faster diffusion. The pipe diameter has the largest influence on the diffusion rate with a four-fold increase when the diameter is doubled. Meanwhile, a reduction in the pipe length will shorten the distance the molecules need to travel and will result in the diffusion rate doubling when the pipe length is halved.

The 1D model results suggests that when 10 % of the hydrogen in the system is converted to water, the water molecules will diffuse on a scale of tens of minutes from the furnace to the cold finger. It should be noted that the reported timescales represent the time for all of the water present in the system at that time to completely diffuse to the cold finger. However, the reaction will continue in this time as fractions of the water are condensed and the partial pressure of water is lowered. It is therefore assumed that the reduction reaction should be able to proceed in the ProSPA timescales of up to four hours. However, the model is limited by the assumptions that are made. For example, pressure gradients that induce the diffusion are calculated between the furnace and cold finger, which are the two pressure extremes. Realistically, there will be gradual pressure gradients across the pipe and so dividing the pipe into multiple cells would provide a more accurate representation of the system. The cold finger temperature may also be significant as it would influence the partial pressure of the water molecules as they neared the cold finger. Also, the 1D model does not account for the production rate of water, which is influenced by the amount of ilmenite present, grain size, reaction temperature, partial pressures, and activation energy. Another drawback of the 1D

model is that a singular straight pipe does not accurately represent the ProSPA design, and that of any experimental work, that will require the diffusion of gases through pipes that split in multiple directions that may influence the diffusion rate (Figure 1.3 in Chapter 1). A 2D model was therefore developed to address these concerns.

2.2 2D model

The 2D model was developed by J. Martin and is detailed in Appendix A. The model breaks down the manifold design into cells that can be assigned the relevant temperature and volume dependent on the system design. The 2D model also considers the production rate of water from ilmenite reduction as described by Dang et al. (2015), enabling a theoretical analysis of the rate controlling step of the reaction in a static system. A flow chart detailing the steps involved in the 2D model is shown in Figure 2.3 where the loop is applied to each time interval.

2.2.1 2D model - Setup

Four designs (Figure 2.4) were tested using the 2D model where different pipe lengths were applied between the furnace and cold finger, and of any extra pipework which is attached. The internal pipe diameters were defined as 4 mm as in the 1D model. The 2D model was executed for each pipe design assuming 45 mg samples of ilmenite (0.3 mmol), which have an average grain size of 85 μm, were reacted with the equivalent required hydrogen (0.3 mmol). The furnace, manifold, and cold finger temperature were defined as 900 °C, 120 °C, and -180 °C respectively. Each run operated with 0.1 second time intervals over a one hour period where each cell has a length of 0.01 m. The ProSPA cold finger is expected to reach < -90 °C so end member cold finger temperatures of -180 °C and -80 °C are also considered for designs 3 and 4 to show the effects on rate of diffusion.

2.2.2 2D model - Results

The reaction fraction, pressure change, and condensation rate were all calculated using the 2D model and are shown in Figure 2.5. The reaction fraction represents how much the ilmenite grains have reduced, where the gradient indicates the reaction rate. The condensation rate represents how quickly the water is diffusing through the pipes and condensing at the cold finger. The gradient of the pressure change plot is indicative of the reaction fraction, and is what will be recorded in the subsequent reduction experiments. Key inputs and outputs from

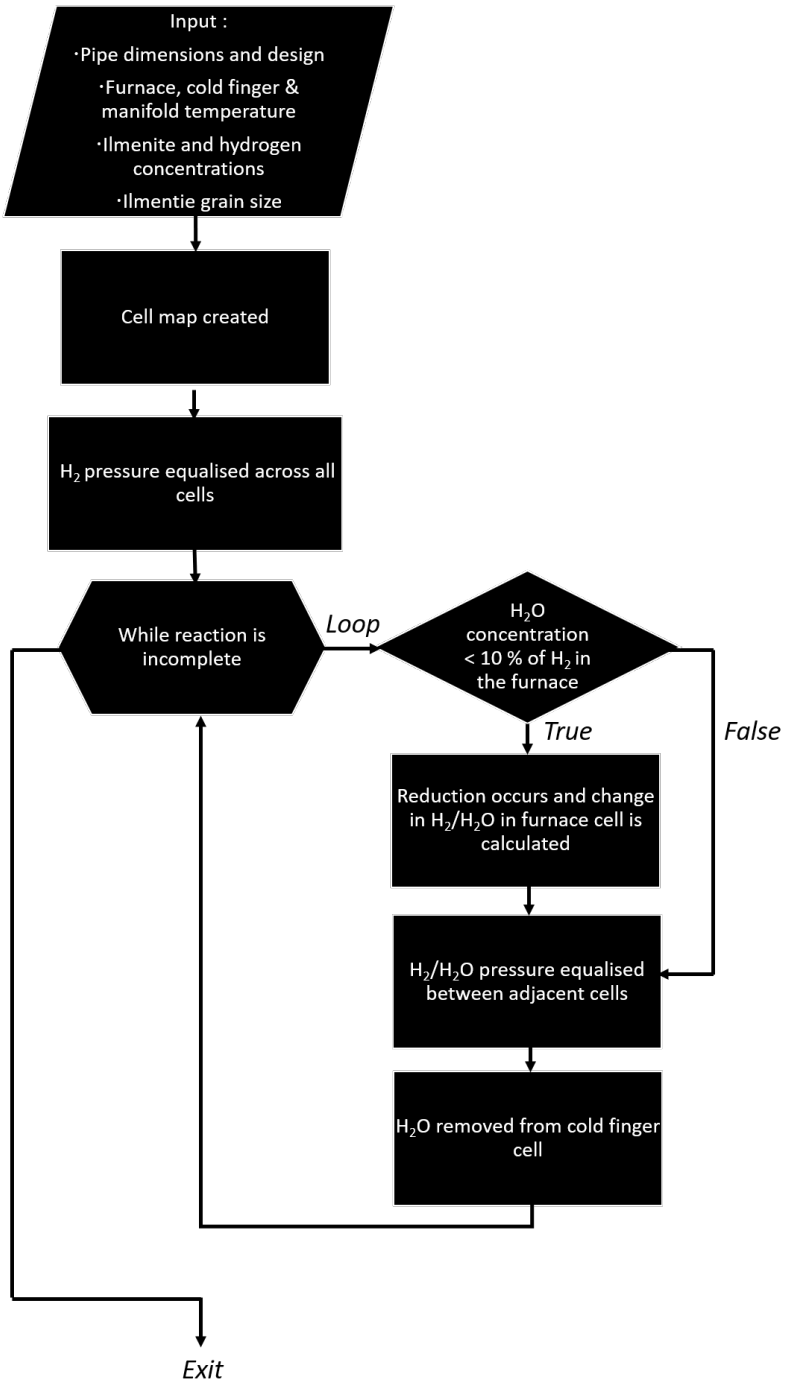

Figure 2.3: Flow chart for the 2D ilmenite reduction model.

the models are shown in Table 2.3 including the volumes of the designs, the final reaction extent ξ, the initial and final pressures (P_i and P_f respectively), and the total amount of water condensed.

The reaction fraction increases steadily at a similar rate for designs 1, 2, and 4, where the length of the pipe between the furnace and cold finger are all the same. The shorter pipe, design 3, results in a significantly greater reaction fraction in the one hour time frame, demonstrating more than 5 % further reduction than any other design. The condensation rate is also similar for designs 1, 2, and 4, however, by halving the length of pipe between

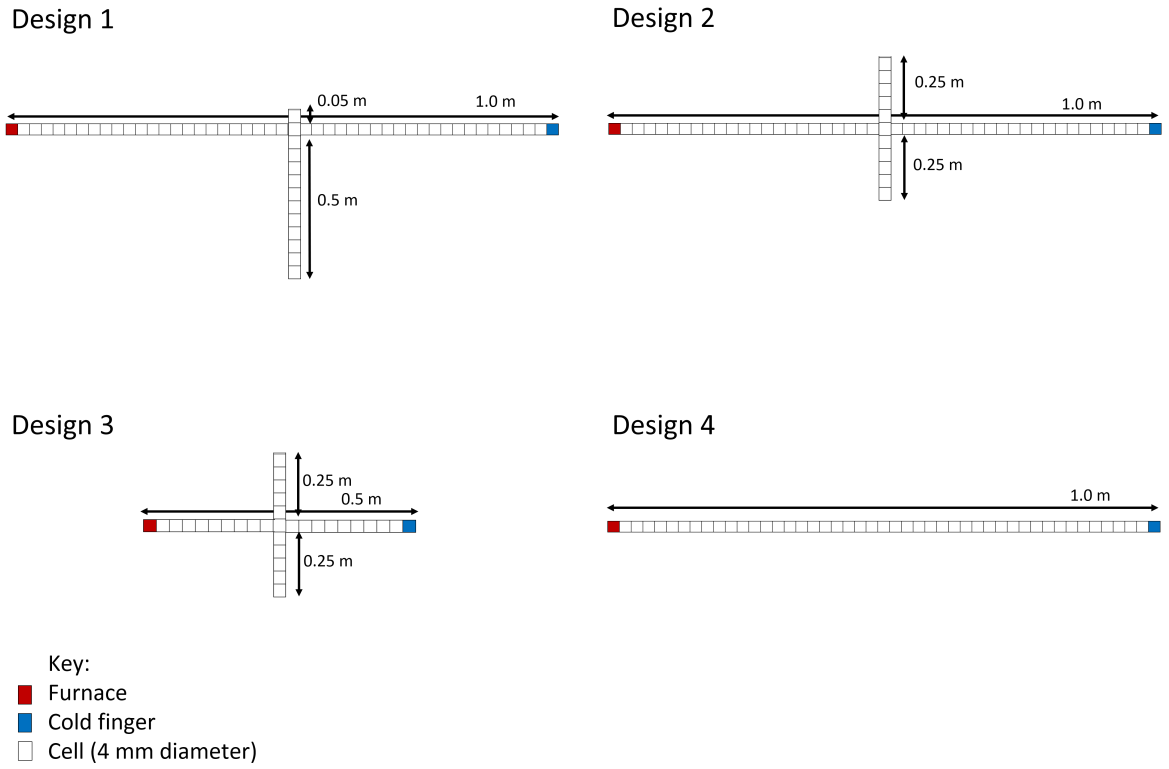

Figure 2.4: Four pipe designs trialled in the 2D model. Designs are not to scale.

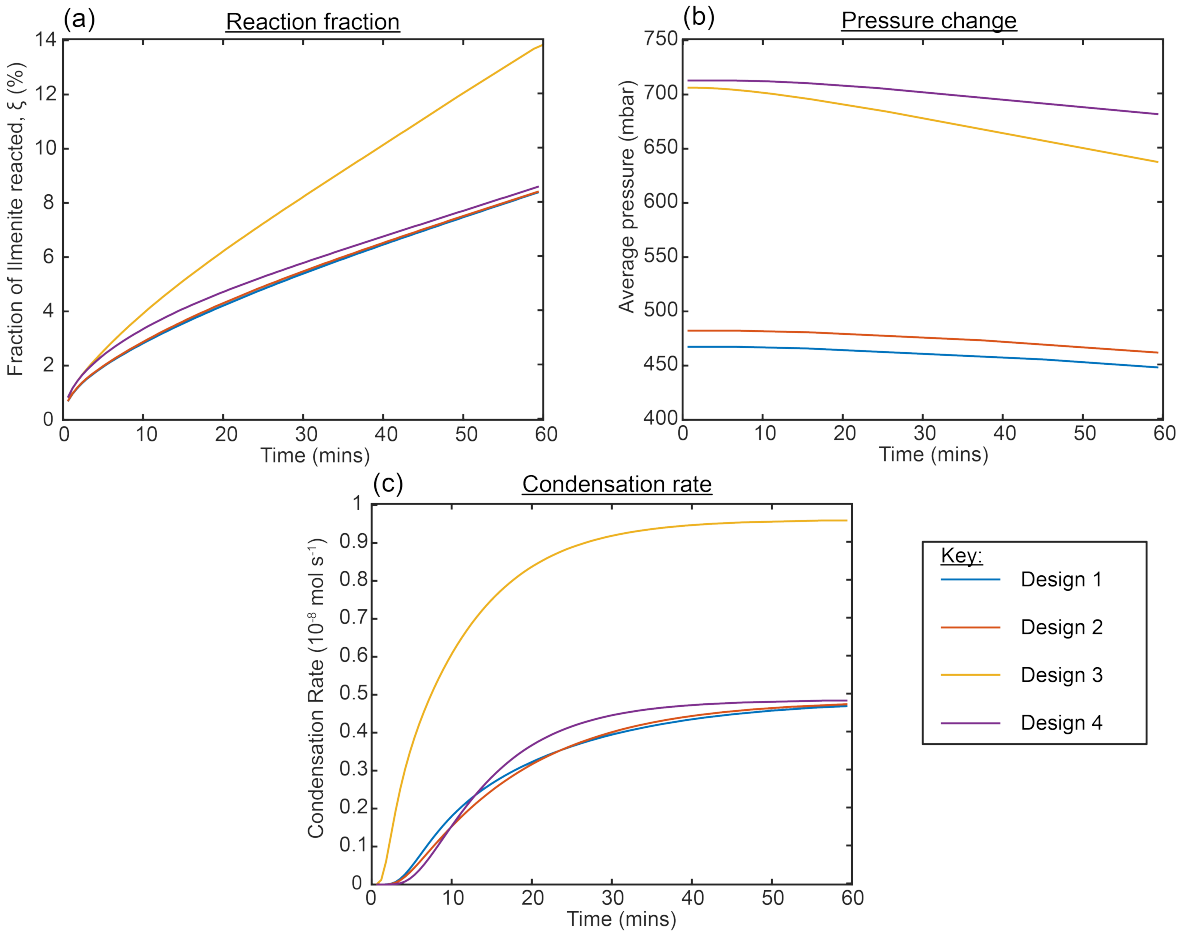

Figure 2.5: Reaction fraction, pressure change, and condensation rate for the four considered pipe designs using the 2D model.

Pipe design	Volume (m^3)	ξ (%)	P_i (mbar)	P_f (mbar)	Condensed water (μl)
Design 1	1.985×10^{-5}	8.4	467	448	0.217
Design 2	1.923×10^{-5}	8.5	482	463	0.216
Design 3	1.294×10^{-5}	13.8	706	638	0.517
Design 4	1.282×10^{-5}	8.7	718	687	0.232

Table 2.3: Results of the 2D model for different pipe designs.

the furnace and cold finger the condensation rate doubles as can be seen with design 3. The addition of secondary pipes added to the design have minimal effect on the condensation rate or reaction fraction, regardless of how long the additional pipes are, or whether there are multiple additional pipes. A system with a smaller volume (such as design 4 which has $\sim$ 65 % of the volume of design 1), and therefore higher pressures (the initial pressure in design 4 is 153 % of that of design 1), has only a small effect on the reaction extent/condensation rate (the amount of water condensed in one hour in design 4 is 107 % of that of design 1), providing the length of pipe between the furnace and cold finger was kept the same. In the first $\sim$ 15 minutes, the reaction fraction is higher when pressures are higher, where there is more hydrogen available for conversion to water. However, with higher pressures in the system the water will diffuse more slowly to the cold finger. Consequently, the two factors appear to cancel each other out resulting in minimal changes in the reaction fraction and condensation rate at 60 minutes for systems of differing pressures.

Two cold finger temperatures (-80 °C and -180 °C) were input into designs 3 and 4 and the difference in yield was minimal. For both designs, when the cold finger temperature was set to -80 °C, the resultant yield of water was equivalent to 99.6 % of the yield when the cold finger was set to operate at -180 °C.

2.2.3 2D model - Discussion

The 1D model suggests that lower system pressures will increase the rate that water will diffuse to the cold finger; the 2D model shows that this is counteracted by the reduced rate at which water is produced from ilmenite. The reaction fraction in the 2D model is calculated using the model detailed in Dang et al. (2015) where the chemical reaction is assumed to be the rate controlling step in ilmenite reduction (See Eqn. A.2 in Appendix A). The 2D model prevents the reaction from proceeding by stalling the reaction fraction when the partial pressure of water exceeds 10 % (Taylor et al., 1993). Consequently, the reaction can be limited by the diffusion of water away from the reaction site. If the diffusion of water is quick enough so that the partial pressure never exceeds 10 %, the reaction fraction is unaffected by

the pipe length. However, as pipe length has such a significant effect on the reaction fraction, it suggests that in a static system the diffusion of water away from the reaction site is the rate controlling step, unlike dynamic gas flowing systems. It should be noted that the 10 % partial pressure of water limit was derived from the results obtained through the reduction of ilmenite at 1000 °C in a flowing hydrogen system. The actual partial pressure limit to the reaction in a static system with a furnace operating at other temperatures would likely vary, however, the 10 % limit provided by Taylor et al. (1993) is a suitable starting point for preliminary modelling purposes.

When using the 2D model, the cold finger temperature has minimal effect on the diffusion rate, and therefore the yield. The expected temperature of the ProSPA cold finger ($<$ -90 °C) should be sufficient to maintain the diffusion of water and therefore the reaction, and further cooling is not recommended.

The results of the 2D model show that the addition of extra pipework will not significantly influence the diffusion rate of water to the cold finger. It should therefore be sufficient to build a breadboard model utilising only the relevant components of ProSPA for this work as completely replicating the design with additional pipework will likely have minimal effect on the reaction rates measured. The pipework between the furnace and cold finger on a breadboard should be kept to $<$ 1 m as per the ProSPA design, as this distance does strongly influence reaction rate.

With the four pipework designs, the reduction reaction is predicted to progress no more than 10 % in one hour. The model broke down over longer time periods (as a result of difficulties that arise when balancing the number of data points and the time intervals so that there is always movement of gases between adjacent cells) and so an estimation of completion time was made based on a linear extrapolation of the reaction fraction up to 100 %. It is estimated that it will take $>$ 500 minutes for the reaction to complete in design 2, with up to nearly 900 minutes for design 4, and 1000 minutes for designs 1 and 3. The estimated time frame for complete reduction is well in excess of four hours for the trialled designs, however it is estimated that the reaction will be at least 24 % complete in the desired time frame for ProSPA and would still be worth performing on the lunar surface.

Early tests using the 2D model are useful in determining the implications of system design on the reaction rate for ilmenite reduction in a static system, and the feasibility of such reactions in a ProSPA-like system. The model could be used in future work to optimise the system design and operational conditions. However, the model is limited in that it is only relevant to ilmenite reduction, this does mean it could be suitable for modelling reduction of

beneficiated feedstock. The reaction rate varies significantly for different iron oxide-bearing minerals, with different grain sizes and shapes, therefore this model is not able to replicate reaction conditions for complex mineralogies like those found in lunar simulants and samples. Experimental tests will be required to better understand the effects of other factors such as water adsorption onto pipes, and to also determine the feasibility of the reduction of more lunar-like materials

2.3 Implications for experimental work

The ProSPA capabilities outlined in Table 1.2 in Chapter 1 were used to determine the operating temperatures and manifold design applied in the 1D and 2D models. The results from the simple models indicate that in one hour there would be a pressure change of at least 19 mbar in a ProSPA-like static system as a result of hydrogen reduction of ilmenite, which is significantly above the 0.25 mbar resolution of ProSPA pressure sensors. It is expected that a reaction over four hours would yield even higher pressure changes.

Theoretical models do not account for factors such as water adsorption onto pipework that would lower any pressure changes recorded. Also, it is important that any pressure changes can be distinguished from blank readings to conclusively state that a reaction has occurred. An experimental study is required to better understand whether a reaction could be measured with ProSPA. As the ProSPA pressure sensors can measure to a resolution of 0.25 mbar, it was deemed reasonable to require a pressure change of at least 1 mbar above blank readings (including uncertainties) to confirm a reaction has taken place. Pressures within the manifold are dependant on the the pipe ID and length, therefore an experimental setup should be on the same scale as those defined in the ProSPA capabilities.

Reaction yields are generally presented in terms of volume of water and ultimately weight percentage of oxygen extracted from the iron-oxides. Yields are calculated using the pressure changes measured, the system volumes in use, and the temperature of the components. Therefore, the system volumes and temperatures must be characterised. Experimental hardware should be at least as capable as the ProSPA instrument in terms of resolution of temperature and pressure sensors, and the operational temperatures it can reach, so that the resolution of the calculated yields is on the same scale as what would be possible with ProSPA.

2.4 Conclusions

Preliminary tests were performed using a 1D model to determine the diffusion rate of water through a static system, the results of which suggest that water should diffuse to a condenser in a 1 m $\times$ 4 mm pipe sufficiently quickly to enable the reaction to proceed in a four hour time frame. Next, a 2D model was implemented which considers more complex pipework designs, and diffusion rates were calculated across multiple divisions within the pipework. The 2D model responds to the water production rate from the reduction of ilmenite. The results suggest that significant changes to the current ProSPA design are not needed to support its use as an instrument to perform ilmenite reduction experiments. As the diffusion of water away from the reaction site is identified as the rate controlling step in the static system, shorter and wider pipes would be recommended where possible to reduce the diffusion distance and ultimately increase the yields.

ProSPA requires experiments to be completed on a scale of four hours, and the results of the 2D model suggest that the system should be capable of reducing ilmenite and condensing measurable quantities of the product water in that time frame and should therefore be considered for experimental studies. It was therefore decided to trial the ilmenite reduction reaction in a breadboard model of the ISRU-relevant ProSPA components so that an analysis of other factors such as water adsorption onto pipework could be analysed. Reduction of more lunar-like materials is recommended for experimental analysis, as such reactions cannot be evaluated with the 2D model.

Chapter 3

Reduction of ilmenite using the ProSPA breadboard

This chapter is adapted and expanded upon from the published paper Sargeant et al. (2020a). The BDM system was built by F. Abernethy and I made minor modifications. The thermogravimetric analyser (TGA) work was performed by P. Landsberg, and the discussion of the TGA results is a combined effort of me and P. Landsberg. G. Degli-Alessandrini and P. Anand assisted with operating the SEM and Nikon microscope respectively.

3.1 Introduction

The ProSPA development program includes the construction of a ProSPA breadboard called the BDM at The Open University, UK (Sefton-Nash et al., 2020). The BDM was built from off-the-shelf parts replicating key components of the ProSPA design with the purpose of testing and optimising experiments that will ultimately be performed by ProSPA on the lunar surface. Hydrogen reduction of ilmenite was selected as an ISRU experiment to be performed by ProSPA in order to produce water (Chapter 1).

Modelling has shown that hydrogen reduction of ilmenite should be feasible in a static system such as ProSPA (Chapter 2), however there are factors such as water adsorption onto pipework and vapour diffusion through granular material that were not considered in the models. The BDM was therefore used to perform precursor experimental tests to determine the viability of ilmenite reduction in a static system.

In this chapter the BDM design is outlined, along with details of how the system was tested to determine how accurately volumes of water can be collected and quantified within it. Next, the ilmenite reduction procedure is defined and the suitability of a static system to

produce water from ilmenite is investigated. The operating parameters of the reaction are also analysed, providing inputs to the design and operation of ProSPA, and considerations for the optimisation of the hydrogen reduction of ilmenite experiment.

3.2 Equipment and materials

3.2.1 BDM design

In terms of space instrument design, a so-called breadboard model is one that replicates the intended functionality without recourse to using highly specialised space-qualified components, and is largely free of the overall mass/volume/power consumption constraints imposed on flight hardware. One of the breadboard models of the ProSPA gas processing system, the BDM, is shown in Figure 3.1, with a system diagram shown in Figure 3.2. The BDM contains mainly commercial-off-the-shelf (COTS) parts connected together in a similar configuration to that of the intended flight design. This early version of the BDM utilises select components of the ProSPA system design (Figure 1.3 in Chapter 1) which are required for the chosen ISRU experiments; namely a furnace, cold finger and pressure sensor, connected via the manifold.

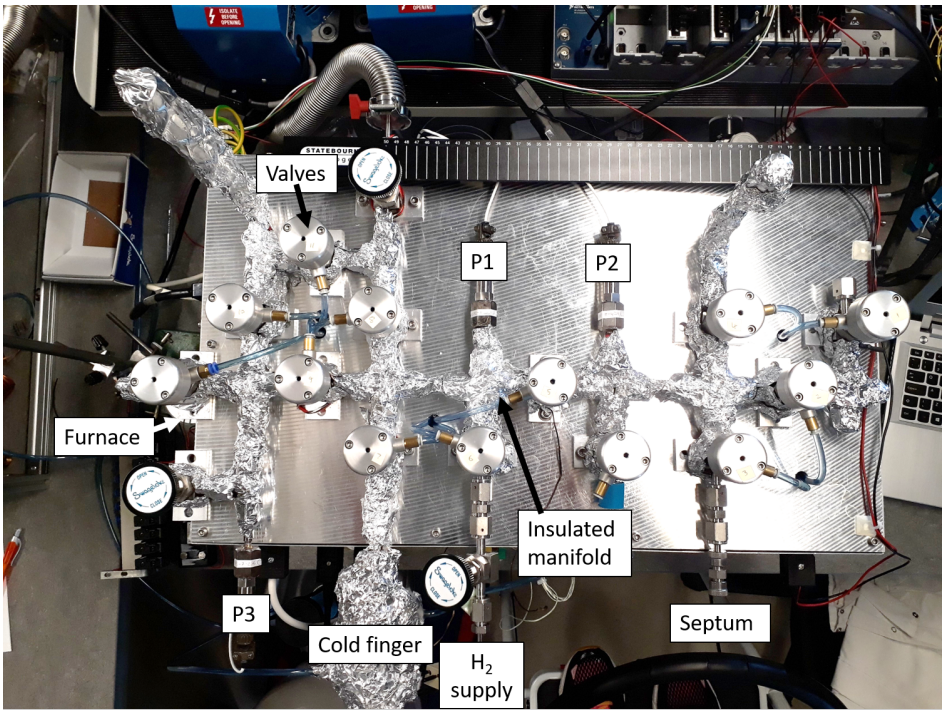

Figure 3.1: Top view of the BDM.

The breadboard model is built with stainless steel Swagelok® actuator valves (SS-4BK-V51-1C) with polychlorotrifluoroethylene (PCTFE) stem tips. The pipework that comprises the manifold is made from 1/4 inch OD (4.2 mm ID) Swagelok® fittings (4 VCR face sealed

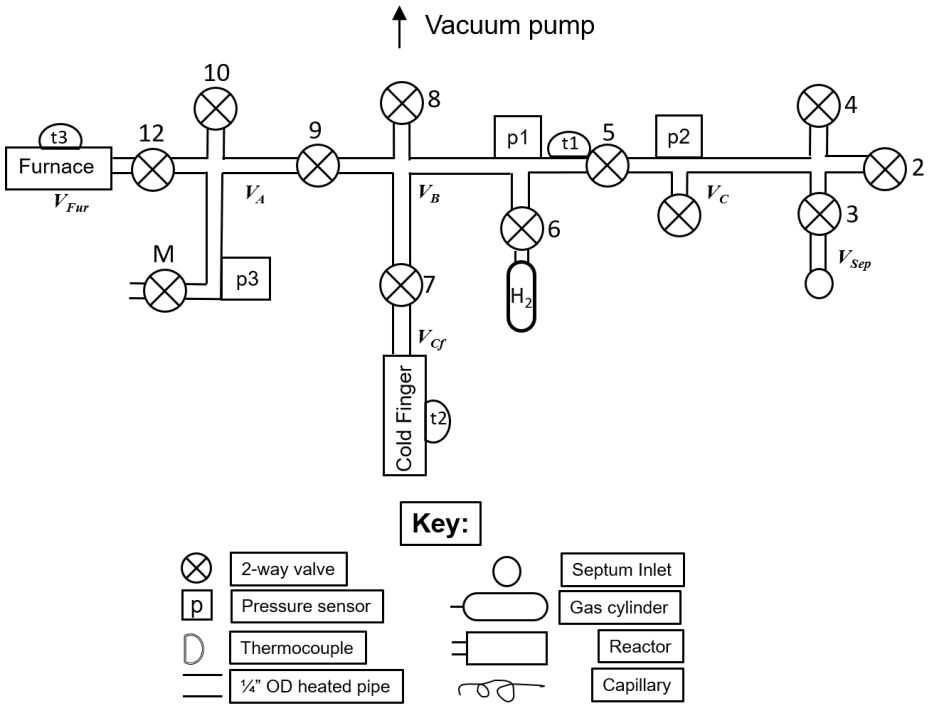

Figure 3.2: BDM system diagram with labelled volumes.

with copper gaskets), and the septum inlet is an 11 mm Thermogreen® LB-2 septum. A 60 μm gasket filter was added to valve 12 (Figure 3.2) to limit the movement of grains from the furnace to the rest of the system. A hydrogen supply is also included in the BDM design (Laborgase, 99.999 % purity which meets the ProSPA capabilities) from a 12 L lecture bottle. The temperature of each element of the breadboard model is controlled by Eurotherm® devices which activate the relevant heating or cooling elements. Automated valves and heating components are controlled with LabVIEW™ software using a programme designed by F. Abernethy.

The furnace consists of a 200 mm long ceramic tube (LEWVAC, 99.7 % Al_2O_3) of 4.0 mm ID and 6.0 mm outer diameter (OD), placed inside a resistance element furnace capable of reaching temperatures of 1200 °C (Figure 3.3a). At the time of writing, the ProSPA flight ovens (Figure 3.3b) have internal dimensions of 4.0 mm ID and 13.6 mm depth. As such, the BDM oven arrangement replicates the flight oven's 4 mm internal diameter, ensuring the sample is contained in the same geometry as would be in the ProSPA oven. The ProSPA oven is capable of holding up to $\sim$ 45-50 mg of regolith samples (dependent on sample density). Although the hot zone is significantly longer in the BDM design, both the BDM and ProSPA furnace hot zones are sufficient to uniformly heat a 45 mg sample. The base of the ceramic sample holder is approximately at the midpoint of the furnace and within the 'hot zone'. The thermocouple that measures the temperature of the furnace is placed inside

of the furnace, adjacent to the base of the sample holder. When the temperature measured by the thermocouple is below that which is required, the furnace is activated. When the temperature is above that which is required, the furnace is deactivated.

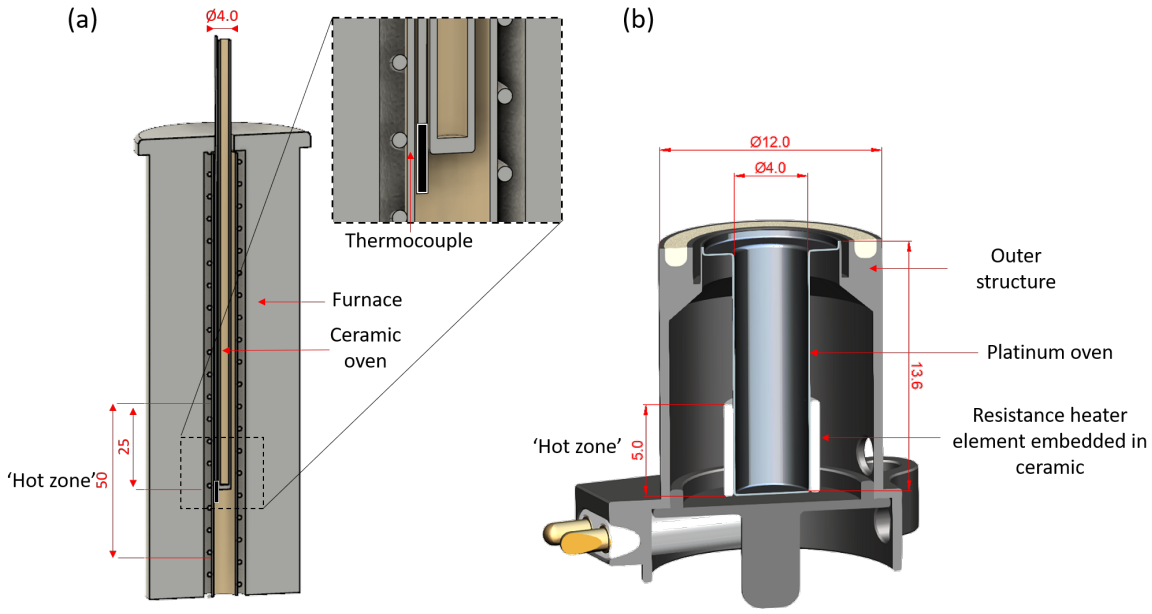

Figure 3.3: (a) BDM furnace heater design, cross section. (b) ProSPA oven design CAD drawing. The samples are deposited by the drill into the 4 mm ID oven and heated by an electrical resistance element. All measurements are in mm.

The BDM cold finger temperature is controlled by automated cooling and heating measures (Figure 3.4). When cooling, a supply of nitrogen gas is cooled as it passes through a liquid nitrogen dewar, which is then passed through the cold finger cooling jacket. When heating, an electric heating wire that is integrated into the cold finger is activated. A thermocouple is placed on the outside of the cold finger which is then completely encased in fibreglass wool and finally aluminium foil. When the temperature measured by the thermocouple is below that which is required, the heater wire is activated. When the temperature measured is above that which is required, the nitrogen gas supply is activated. The ProSPA flight cold fingers are designed to be cooled by the space environment and will be nominally operating at $<$ -90 °C, and can be heated by a surrounding heater element. Although the cooling techniques are different for the BDM and ProSPA cold fingers, they are functionally similar.

The manifold is heated with Omega™ resistance heater tape which is wound around any exposed pipework and covered with aluminium foil. Heater tape and foil was not wrapped around the valves and pressure sensors as they are not rated to the target manifold temperature of 115 °C.

The temperature of the furnace, cold finger, and manifold are recorded using K-type

thermocouples (in accordance with tolerance class IEC 584-2) which are capable of recording temperatures of up to 1200 ± 2.5 °C. The temperature resolution is sufficient to exceed that of the ProSPA cold finger and manifold, however the ProSPA furnace has a higher resolution of ± 1 °C. The furnace temperature does not influence calculations of yields and therefore the resolution of ± 2.5 °C was deemed sufficient for the BDM.

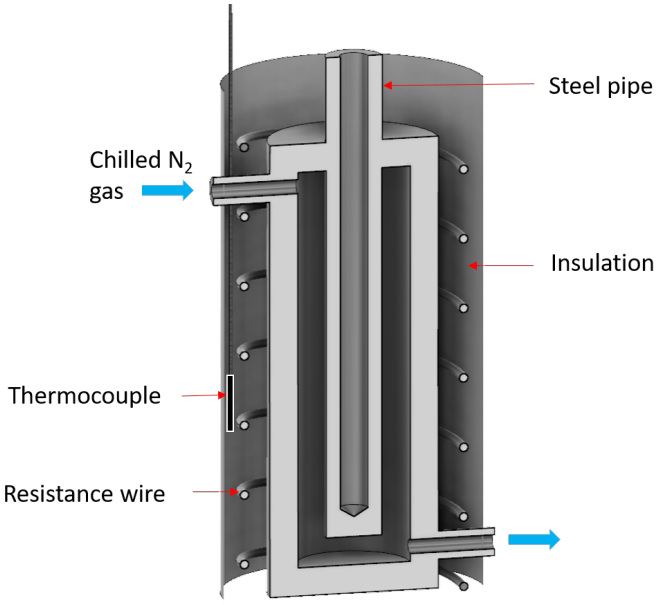

Figure 3.4: Cold finger design cross section.

The pressure of gas in the system is measured by silicon on insulator (SOI) diaphragm pressure sensors (Kulite®, ETL-375CO-1.1BARA), and the manifold is heated by heater tape to 115 °C in order to prevent water vapour condensing when measuring total gas pressure. The pressure sensors used on the BDM have a compensated temperature range of -18 to 100 °C and therefore they are not directly heated to ensure they operate within the compensated temperature range. The bit-accuracy of the 16-bit pressure sensor, S_p, is calculated as follows:

$$S_p = \frac{S_{V/b}}{S_{V/p}} \tag{3.1}$$

$$S_{V/b} = \frac{V_{max}}{n_{bits}} \tag{3.2}$$

where $S_{V/b}$ is the voltage per bit sensitivity and $S_{V/p}$ is the voltage per mbar sensitivity (4.553 mV·mbar^{-1}). $S_{V/b}$ is determined by the voltage range, V_{max}=10 V, with respect to the number of divisions (bits) available, $n_{bits} = 2^{16}$. The bit-accuracy was therefore calculated to be 0.03 mbar, meaning the sensor cannot detect pressure differences of less than this value. The resolution of the pressure sensors on the BDM are well within the capabilities of the

ProSPA pressure sensors which have a resolution of 0.25 mbar. The valves and pressure sensors are not directly heated in order to avoid exceeding their permissible temperature range; they therefore operate at $\sim$ 65 °C and $\sim$ 35 °C, respectively. It should be noted that the Kulite® sensors were calibrated with nitrogen or air (Personal Communication, S. Bancroft - Kulite Sensors Ltd., November 3rd 2020) and there may be an offset of a few mbar when operating with hydrogen however the discrepancy is not fully quantified.

Internal volumes of the BDM pipework were calibrated by expanding dry nitrogen gas from a 2 L volume incrementally into various sections of the extraction system. The system was operated at room temperature for the volume calibration work. Assuming that the temperature is constant across the manifold, it is possible to estimate the volumes of each section of the vacuum system using Boyle's Law where $P_1V_1 = P_2V_2$. The experiment was repeated five times (n = 5) using a 2 L volume of nitrogen attached temporarily in lieu of where the furnace is, and a further five times (n = 5) with air from a 50 ml expansion volume attached to valve 10. The results of the analysis showed that the volumes calculated from both experiments are within 1 standard deviation (SD) of each other. The calculated volumes with the smallest uncertainty were selected and are shown in Table 3.1 which correspond to the labelled volumes in Figure 3.2.

Volumes	Final volume ($\times 10^{-6}$ m^3)	Standard deviation ($\times 10^{-6}$ m^3)
V_{Fur}	5.74	0.02
V_A	10.16	0.02
V_B	10.12	0.01
V_C	12.32	0.02
V_{Cf}	7.85	0.01
V_{Sep}	3.52	0.01

Table 3.1: Volumes of BDM segments (n = 5).

3.2.2 Ilmenite feedstock

The ilmenite feedstock used in this work was supplied by A. Cowley from the European Astronaut Centre (EAC), who sourced the material from the Mineral Trade Company (GmD Mineral Trade Company, 2020). The ilmenite powder is dominated by modal ilmenite (95 %) with some minor modal impurities comprising silica (1 – 2 %), quartz (1 – 2 %), and other phases (1 – 2 %) (as stated by the supplier and verified at the EAC). The chemical composition of the ilmenite can be seen in Table 3.2, and includes iron in the form of both Fe^{2+} and Fe^{3+}. This terrestrially sourced ilmenite is therefore different to lunar ilmenite which only contains Fe^{2+} as a result of the reducing conditions within the Moon (Papike et al., 1991). A

representative aliquot of ilmenite feedstock was used for grain size distribution analyses as in Ness Jr et al. (1992) using a Nikon SMZ1500 microscope; images were taken with INFINITY CAPTURE software at a magnification of 10× before being analysed in ImageJ open source software. Assuming that the grains are spherical, the grain diameters were determined to be between 80 and 260 μm with an average diameter of 170 μm across the randomly selected grains analysed (n = 167). The ilmenite feedstock is relatively coarse compared to lunar soil (Zeng et al., 2010). However, the ilmenite was determined to be a suitable proxy for ilmenite that is found in lunar soils as for example in an Apollo 17 soil, ilmenite was found to have grain sizes of 45 – 500 μm (McKay et al., 1991a). To remain representative of ProSPA capabilities, ilmenite samples of 45 mg (0.3 mmol) were used in the ilmenite reduction studies.

Chemical	Min (%)	Max (%)
TiO_2	49	51.5
FeO	30	35
Fe_2O_3	10	13
Total Fe	30	40
SiO_2	0.5	2
Al_2O_3	0.5	1.5
P	0.02	0.04
ZrO_2	0.02	2
Cr_2O3	0.04	0.07
U + Th	< 50	

Table 3.2: Chemical composition of ilmenite powder as obtained from GmD Mineral Trade Company (2020)

3.3 Preliminary tests

Prior to performing ilmenite reduction reactions in the BDM, the ilmenite samples were first baked-out to remove any surficial or adsorbed volatiles. The bake-out conditions required for the ilmenite samples were determined using thermogravimetric - mass spectrometry (TG-MS). Next, an investigation was performed into how accurately water can be quantified in the BDM system using pressure measurements. The results of the investigation were then used to more accurately interpret yields of the subsequent reduction reaction experiments.

3.3.1 Bake-out conditions

TG-MS analysis provides information on the types of volatiles contained within a sample, and the temperatures at which they are released. Here, TG-MS analyses were used to determine

the bake-out parameters to ensure that ilmenite samples are thoroughly dried before reduction reactions are carried out. TG-MS analyses were performed on the ilmenite feedstock using a Netzsch Jupiter STA (Simultaneous Thermo-Analyzer) 449C, coupled to a Hiden HPR-20 quadrupole mass spectrometer via a quartz inert capillary (QIC) inlet. The consumption rate of gas from the STA was approximated to 16 $cm^3 \cdot min^{-1}$ helium. The system will be referred to as the TGA from here.

The temperature of bake-out was determined by heating a 122.99 mg ilmenite sample to 600 °C (temperature limit of the TGA) at a rate of 8 $°C \cdot min^{-1}$. The mass loss of the sample was recorded and compared to a blank reading where an empty crucible was heated under the same conditions. Mass loss indicates that volatiles are released from the ilmenite sample and the temperature at which these releases occur were used to determine a suitable bake-out temperature (Figure 3.5). There are two key phases of mass loss: the first is the release of surficial and loosely bound volatiles, and the second is the higher temperature release of adsorbed volatiles. The blank reading resulted in an equivalent mass change of just 0.015 % indicating that the mass change features from the ilmenite sample are real. The adsorbed volatiles appear to release from $\sim$ 340 °C and so a bake-out temperature of 500 °C was deemed more than sufficient to release all volatiles from the ilmenite. Ideally this experiment would have been repeated with a slower ramp to more accurately determine the temperature of release and optimise the bake-out procedure for future experiments. However, the experiments could not be repeated/optimised as a result of faulty equipment.

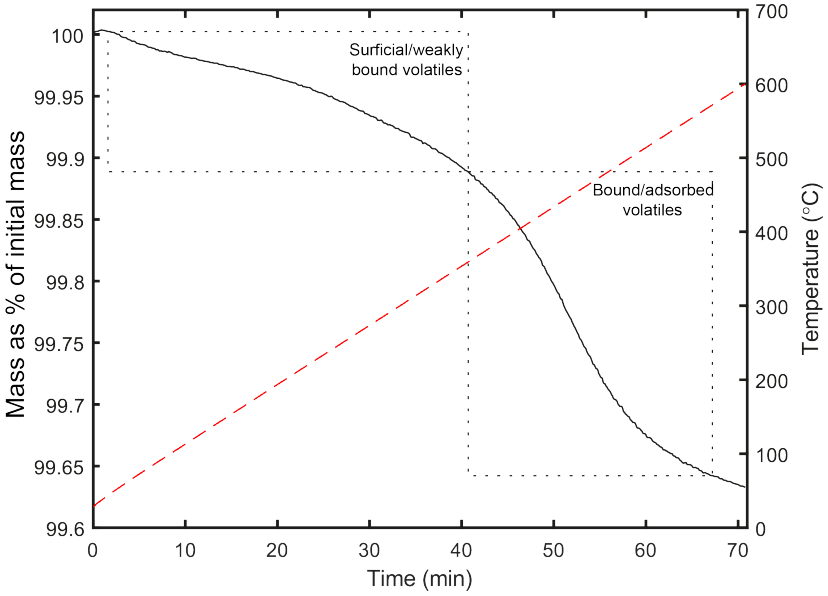

Figure 3.5: Mass change caused by volatile release when ilmenite was heated to 600 °C. The solid black line is the mass as a % of initial mass, and the dashed red line is the temperature.

The bake-out time required to completely remove volatiles was determined by heating a 110.0 mg sample of ilmenite to 500 °C at 40 °C·min^{-1}, followed by a 90 minute isotherm. The results from the blank and ilmenite sample are shown in Figure 3.6. Initially, there was a rapid release of volatiles (significantly more so from the ilmenite than the blank). A sharp m/z 18 (H_2O) peak was observed, with the release appearing complete before the isothermal stage. The signal then stabilised as the gases sampled from the thermo-analyser reached equilibrium at the higher temperature. A small peak of $< 10^{-8}$ mbar at m/z 44 (CO_2), and corresponding m/z 28 peak (N_2 and/or CO from fragmentation of CO_2) were observed in line with the m/z 18 peak as adsorbed moisture from the air was released from the sample. As the purpose of this analysis was primarily to identify water release, no specific cleaning or drying methods which could potentially affect moisture content were applied to the sample before analysis. These analyses do not, therefore, attempt to distinguish if these releases are part of the sample or are from foreign matter. Background levels within the system appear to fully equilibrate by 65 minutes, representing approximately 50 minutes into the isothermal stage. Total mass loss was approximately 0.35 % of the starting sample mass (385 μg). From this analysis a bake-out time of one hour was selected for the much smaller ilmenite samples (45 mg) that are used in the ilmenite reduction experiments. It is suggested that a repeat blank reading is obtained as the spectra had not equilibrated by the start of data acquisition, meaning a direct blank-correction cannot be applied to the ilmenite spectra.

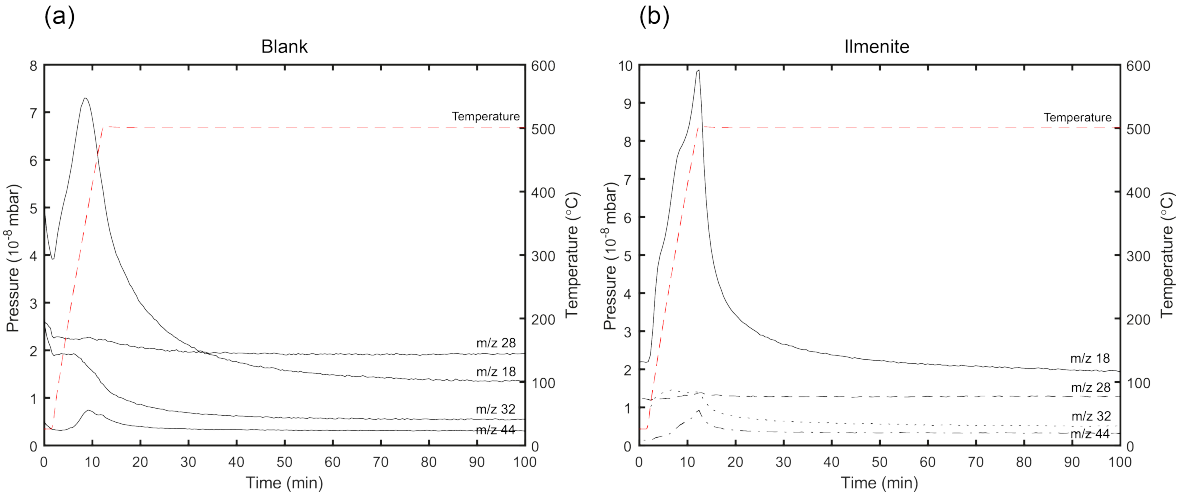

Figure 3.6: The gas release profile from (a) the blank experiment and (b) when ilmenite was heated at a rate of 40 °C·min^{-1} up to 500 °C followed by a 90 minute isotherm.

To confirm that the bake-out procedure is effective, a test was performed on an ilmenite sample in the BDM furnace to determine whether all volatiles were removed. Ilmenite samples of various masses were rapidly heated in the BDM furnace to 500 °C and maintained at that temperature for one hour in a closed system before the released gases were evacu-

ated. It should be noted that in the subsequent ilmenite reduction experiments discussed in Chapters 5 and 6 the bake-out was performed in an open system with released volatiles being instantaneously removed, likely increasing the volatile removal rate. The pressure release profiles corrected for the blank reading are shown in Figure 3.7. The uncertainty in pressure readings is taken as the variability in pressure as determined when air was held in the manifold for one hour (± 0.5 mbar), which is significantly higher than the resolution of the pressure sensor (± 0.03 mbar). As the blank reading was subtracted from the raw data, the uncertainty in the pressure measurements are propagated and an uncertainty of ± 0.71 mbar is given.

Generally, the larger samples release greater volumes of volatiles during the bake-out, however, the 33.7 mg sample has a relatively small pressure release profile (0.5 ± 0.7 mbar) as compared to the 45 mg sample (2.2 ± 0.7 mbar). One potential cause of a lower than expected bake-out pressure profile could be the presence of fewer impurities in the 33.7 mg sample as the feedstock may contain some heterogeneities. All samples appear to have reached a plateau within the one hour time frame, indicating no more outgassing will occur and the bake-out conditions appear sufficient. However, it is recommended that a bake-out test be performed for more than one hour to confirm that no additional volatiles would be released.

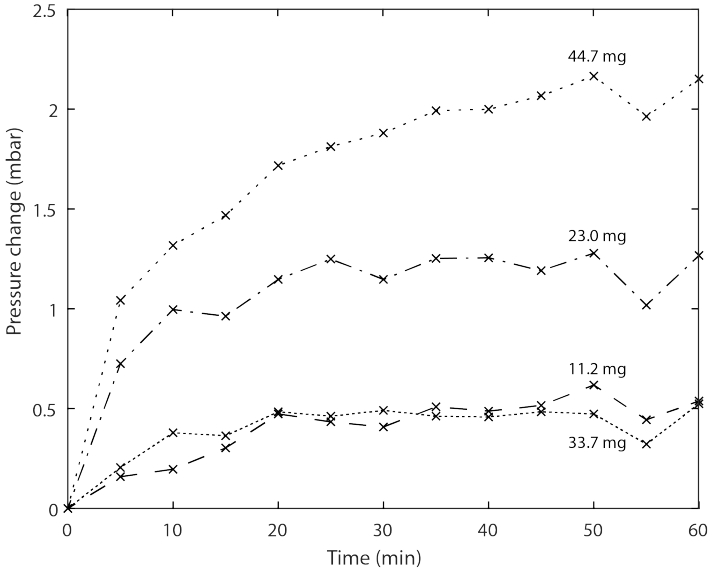

Figure 3.7: Pressure change with time as a result of the 500 °C bake-out process with various masses of ilmenite. The blank reading has been subtracted from the data. The uncertainty in pressure values is ± 0.71 mbar.

3.3.2 Quantifying water in the BDM

In the BDM, and ultimately ProSPA, the quantity of water produced from the reduction of ilmenite is estimated by measuring the pressure of water in a sealed system. However, the

strong polarity of water molecules leads to significant adsorption of water onto surfaces (Pfeiffer Vacuum, 2013). Typically, vacuum systems that process water samples are maintained at temperatures of $\sim$ 100 °C but to account for the relatively high volumes of water anticipated in the system, the BDM manifold is heated to 115 °C to keep water in the vapour phase (Section 2.1.1 in Chapter 2). However, with the need for specific components to operate at cooler temperatures (e.g. valves and pressure sensors) it is necessary to characterise the behaviour of water vapour in the BDM to determine whether secondary condensation occurs and to what extent. Secondary condensation here refers to condensation of volatiles on cold surfaces other than the cold finger.

To determine whether the BDM can be used to quantify the amount of water in the system, known quantities of water were injected into the BDM and condensed at the cold finger. The cold finger was then heated and the water vapour quantified with pressure measurements.

The system pipework was heated to 115 °C and was evacuated to pressures of $< 10^{-6}$ mbar overnight before each water quantification experiment. Quantities of deionised water (0.5, 1, 2, 3, and 5 μl of 18.2 MΩ·cm^{-1} water) were injected into the BDM using a 10 μl syringe through a septum at valve 3 and were condensed at the -180 °C cold finger (see Figure 3.2). The volumes of water were selected to represent the approximate yield of water expected from the subsequent ilmenite reduction studies. The resultant pressure readings were then compared to theoretical values, where a 45 mg (0.3 mmol) ilmenite sample has a theoretical yield of 0.3 mmol water (5.33 μl). The uncertainty in injected volumes of water ($\pm$ 0.1 μl) is derived from the 2 SD error produced from the mass measurements of 10 injections of 1 μl of water into a vial, and repeated four times. The 10 injections of water per vial resulted in a large enough mass for the uncertainty to be accurately recorded before being scaled down proportionally.

After allowing 60 minutes for the water to condense at the cold finger, the BDM was evacuated to remove non-condensibles. The cold finger was then heated to release the water into a 17.97 $\pm$ 0.03$\times10^{-6}$ m^3 volume and the pressure was measured at P1. A blank data set was also obtained for comparison where an empty syringe was used to pierce the septum and any associated pressure changes were recorded. Predicted pressures were calculated using the ideal gas law, $P = nRT/V$, assuming a temperature, T, for the pipework of the BDM of 115 °C, a volume, V, of 17.97 $\pm$ 0.03$\times10^{-6}$ m^3, where n is the molar amount of water injected, and R is the ideal gas constant.

The plot of measured pressure against quantity of water injected is shown in Figure 3.8a, along with the predicted pressure if water behaved as an ideal gas. At low pressures

($\leq$ 40 mbar) water follows the predicted ideal gas line but progressively begins to deviate significantly, eventually approaching a saturation pressure of $\sim$ 130 mbar for quantities of 0.015 mmol and above. Considering intermolecular forces alone (using the van der Waals equation), the resulting difference in predicted pressure would be negligible ($\pm$ 1 mbar). Therefore, other factors must be considered for the discrepancy between predicted and measured pressures in the system, and it is believed that the dominant process occurring is the adsorption of water onto cold spots as the saturation vapour limit is reached. The Clausius-Clapeyron equation (Eqn. 3.3) can be used to determine the boiling point, T_0, of gases under different pressures (otherwise known as the saturation vapour limit).

$$T_{\mathrm{B}} = \left(\frac{1}{T_0} - \frac{R ln \frac{P}{P_0}}{\Delta H_{\mathrm{vap}}} \right)^{-1} \tag{3.3}$$

Where R, is the ideal gas constant, P is the vapour pressure of the liquid at the pressure of interest, $\mathrm{P_0}$ is a pressure (in this case atmospheric pressure, 1013.25 mbar) corresponding to a known boiling temperature, T_0 (for water is 373.17 K), and ΔH_{vap} is the heat of vaporisation. The ΔH_{vap} value is taken from Dean (1999) as 40.66 kJ·mol^{-1}. The saturation temperature is found to be $\sim$ 50 °C at the maximum pressure of water recorded, 129 mbar. The pressure sensors are identified as being the coldest part of the system with a temperature of $\sim$ 34 °C and could therefore result in secondary condensation of water at this location. To calibrate the actual amount of water in the BDM, a calibration factor was determined by plotting the predicted pressure, P_i, divided by the measured pressure, P_m, against measured pressure as shown in Figure 3.8b. From these results a calibration factor, F (Eqn. 3.4), was obtained which can be used to convert the measured pressure of produced water (up to 120 mbar) to the pressure that would have been obtained for an ideal gas, where $P_i = F P_m$. In other words, the total yield of water produced in the BDM can be corrected for secondary condensation up to pressures of 120 mbar.

$$F = 3.76 \times 10^{-5} {P_m}^2 + 8.79 \times 10^{-4} P_m + 1.00 \tag{3.4}$$

For measured pressures below 120 mbar, the calibrated results are accurate to within $\pm$ 2 %. At low pressures F approaches 1, where $F = 1.03$ at 20 mbar. At measured pressures above 120 mbar, close to the saturation pressure, the uncertainty in F means that a correction cannot be meaningfully applied and that the predicted pressure of water is at least $\sim$ 120 mbar. The calibration factor can be applied to measured pressures to determine the pressure that would be observed if water produced from ilmenite reduction experiments behaved as an ideal

gas and does not condense at cold spots. The corrected pressure reading can then be used to calculate the yield of water produced from ilmenite reduction reactions in the BDM.

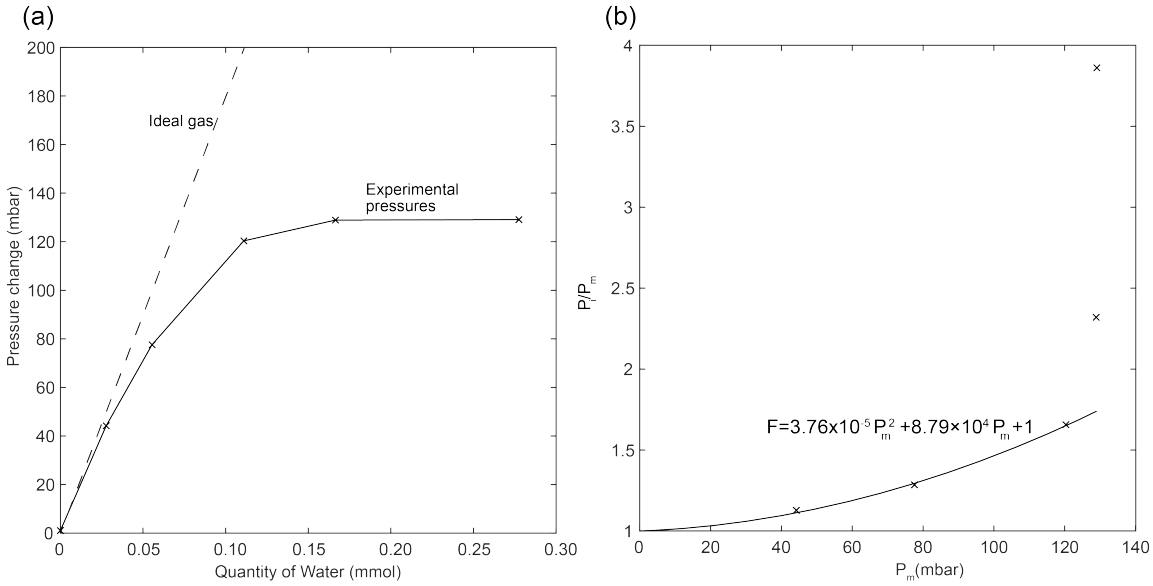

Figure 3.8: (a) Pressure change associated with different quantities of injected water into the BDM system for use as a calibration scale. The dashed line represents the predicted pressures in the system, while the solid line is the trend in experimental results. (b) The ratio between the predicted pressure and measured pressure is plotted against measured pressure to create a calibration curve. The uncertainty in pressure readings is ± 0.5 mbar. There may be a contribution of uncertainty from the use of the pressure sensor to measure water vapour pressures as opposed to nitrogen and air which is how the sensor was calibrated, however such an uncertainty is not quantified and not included here.

3.4 Methodology

Here the experimental procedure is outlined for ilmenite reduction experiments that were performed with the BDM system. Details of the data analysis techniques used to calculate yields from the reaction are defined, and the sample analysis techniques used to investigate the reaction extent within the ilmenite grains are described.

3.4.1 General experimental procedure

To determine whether hydrogen reduction of ilmenite can produce water in a static system, different quantities of ilmenite (11.2 mg, 23.0 mg, 33.7 mg, and 44.7 mg) were heated in the presence of hydrogen. A cold finger was used to remove the produced water from the vapour phase, before the cold finger was heated, releasing the water vapour for quantification. A summary of the operational conditions for each stage of the reaction is shown in Table 3.3, while a visual representation of the experimental procedure is shown in Figure 3.9.

Each ilmenite sample was loaded into the ceramic sample holder and placed inside the

Experimental stage	System conditions			
	Operational volume ($\times 10^{-6}$ m^3)	Cold finger temperature (°C)	Furnace temperature (°C)	Manifold temperature (°C)
Bake-out	48.77 ± 0.14	115.0 ± 2.5	500.0 ± 2.5	115.0 ± 2.5
H_2 addition	35.18 ± 0.10	-180.0 ± 2.5	900.0 ± 2.5	115.0 ± 2.5
Reduction reaction	48.77 ± 0.14	-180.0 ± 2.5	90.0 ± 2.50	115.0 ± 2.5
Water release	32.86 ± 0.10	115.0 ± 2.5	115.0 ± 2.5	115.0 ± 2.5

Table 3.3: Operational conditions of the BDM during each experimental stage. The uncertainty in volume is derived from the volume calibration in Table 3.1, while the uncertainty in temperature is taken as the uncertainty in the temperature sensor.

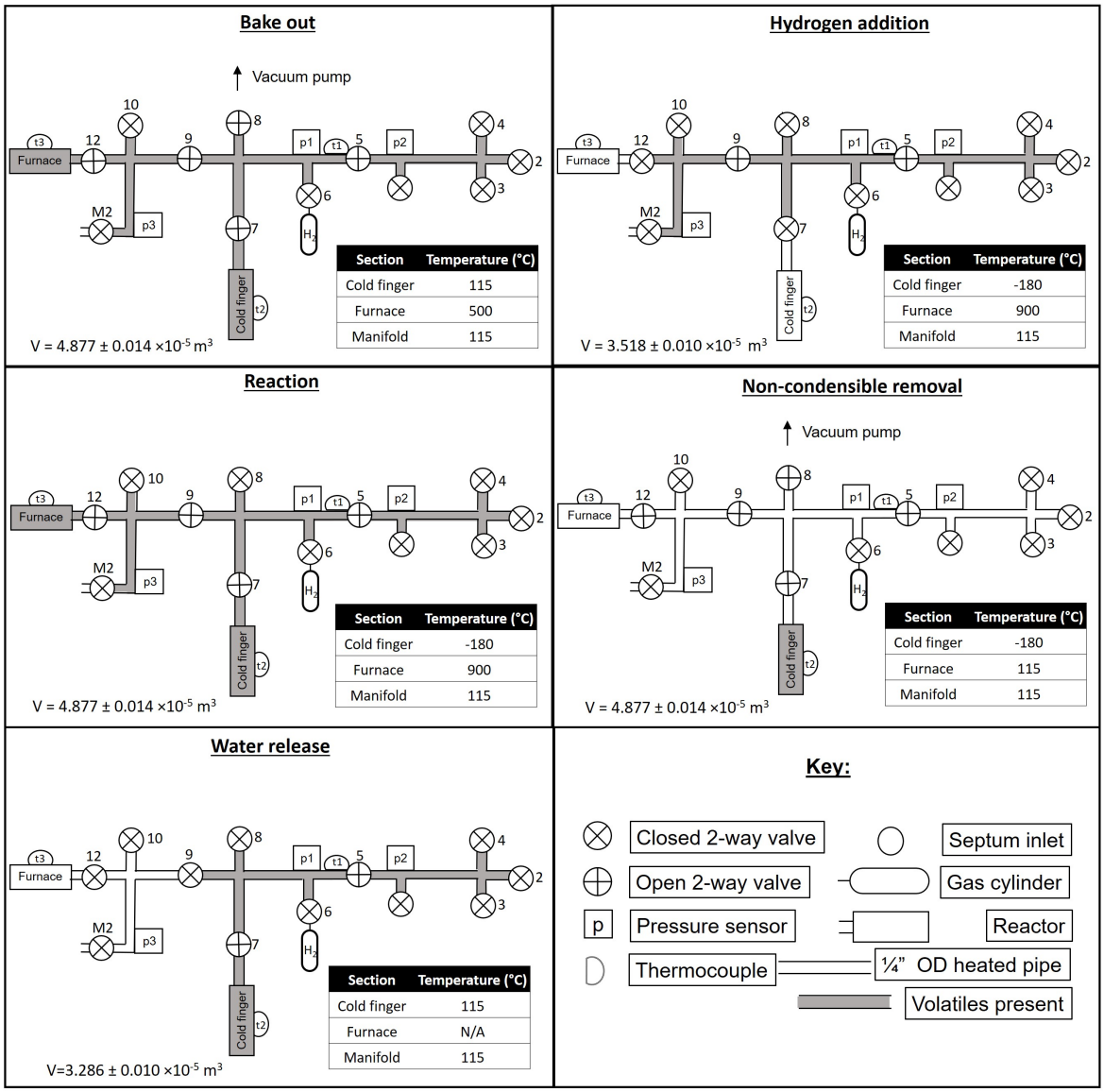

Figure 3.9: Phases of the operational procedure for ilmenite reduction studies in the BDM, with associated operational volume and temperature conditions.

furnace and attached to the BDM where it was evacuated to a pressure $< 10^{-6}$ mbar as measured at the vacuum pump (Figure 3.2). Next, the furnace was heated to a bake-out temperature of 500 °C for one hour to remove any volatiles. After the bake-out, the volatiles

were evacuated through vacuum pumps via valve 8. For each experiment, the same amount of hydrogen gas (0.3 ± 0.01 mmol), as was selected in Section 2.1 in Chapter 2, was then introduced into the BDM. A reaction temperature of 900 °C was chosen as a suitable starting point for ilmenite reduction studies as it is the minimum temperature required to obtain reasonable reaction rates (Christiansen et al., 1988) and is within the operating range of ProSPA. A cold finger temperature of -180 °C was selected as it is the coldest possible temperature the BDM cold finger can reach. The effect of cold finger temperature on the diffusion rate had not been modelled at the time of the experiment, therefore the coldest temperature was selected. It was later determined that cold finger temperature had minimal effect on the diffusion rate (providing the temperature was below the saturation vapour limit), therefore a cold finger temperature of -80 °C would be appropriate and should give rise to similar results (Section 2.1 in Chapter 2). After a one hour reduction reaction phase, any remaining hydrogen was removed from the system to halt the reaction by pumping to vacuum ($< 10^{-6}$ mbar as measured at the vacuum pump) and the valve to the furnace was closed. A reaction time of one hour was selected as this is comfortably within the ProSPA operational power and time budgets. The cold finger was then heated to 115 °C at a rate of ~ 125 °C·min^{-1} to release the condensed water which was measured via a pressure sensor at P1. A manifold temperature of $\sim$ 115 °C was maintained throughout the experiments, chosen to keep water in the vapour phase when in the connecting pipework. It should be noted that the assumed average system temperature used for analysis was taken to be 115 °C. Although valves and pressure sensors operate at lower temperatures, they represent relatively small volumes of the entire system, and overestimating the temperature will only lead to an underestimate of the yield as per the ideal gas equation.

3.4.2 Data analysis

The pressure drop recorded in the reduction reaction phase of each experiment corresponds to the conversion of H_2 to H_2O and the subsequent removal of gaseous H_2O by the cold finger. The pressure change is corrected by subtracting the associated blank reading from the reaction phase of the experiment (0.7 mbar) to give ΔP_{cr}. The pressure change recorded from the water release phase, however, is first multiplied by the F factor (Eqn. 3.4) before being corrected for the associated blank reading (0.8 mbar) to give ΔP_{cw}. The uncertainty in the pressure reading is taken as ± 0.5 mbar, determined from the variability of pressure readings when air was held in the manifold for one hour. An estimated molar quantity of H_2, n_h, that reacted in the reaction phase is calculated from the ideal gas equation (Eqn. 3.5).

The same formula can be used to calculate the molar amount of water released, n_h, from the cold finger during the water release phase:

$$n_{h|w} = \frac{\Delta P_{cr|cw} V}{RT} \tag{3.5}$$

where the volume of the system, V, is taken from Table 3.3, R is the ideal gas constant, and the average temperature of the gas is assumed to be 115.0 ± 2.5 °C (388.2 ± 2.5 K). However, the actual average temperature of gases in the manifold was lower as a result of the unheated components.

Although water is the product of the reduction reaction, its constituent oxygen is the resource most commonly referenced when discussing yields for ISRU studies. There are many ways in which yield can be calculated. For instance, yield could be the mass of oxygen extracted compared to the sample mass, or the mass of oxygen extracted compared to the total oxygen in the sample, or the mass of oxygen extracted compared to the maximum amount of oxygen that can be extracted from particular oxides (Eqn. 1.2 in Chapter 1). In addition, the yield can be calculated as the mass of water extracted. Here yield is defined as the wt % of oxygen extracted compared to the total sample mass (Hadler et al., 2019), from here described as calculated oxygen yield (Eqn. 3.6). This term is more useful for ISRU and a mining perspective as the desired product is commonly oxygen. The calculated oxygen yield is the ratio between the mass of oxygen produced, m_o, with respect to the initial mass of ilmenite, m_{ilm}, the mass of oxygen produced is calculated here from the mass of water produced, m_w, by multiplying it by the ratio between the molar mass of oxygen, M_o, and the molar mass of water, M_w. The amount of water produced, n_w, can be substituted for m_w/M_w and can be calculated from Eqn. 3.5 using the pressure rise from the water release phase. In theory, the maximum yield of oxygen from water for the ilmenite reduction process as given in Eqn. 1.2 is 10.5 wt % oxygen (where M_o/M_{ilm}=16 g·mol^{-1}/152 g·mol^{-1}).

$$wt.\%O_2 = \frac{m_o}{m_{ilm}} = \frac{m_w M_o}{m_{ilm} M_w} = \frac{n_w M_o}{m_{ilm}} \tag{3.6}$$

When comparing the efficiency of a particular reaction it is more useful to measure the extent of the reduction reaction, ξ, derived from the ratio of the mass of oxygen produced, m_o, with respect to the maximum available oxygen from the reaction, $m_{o,max}$. The reduction extent is therefore equivalent to the amount of water produced as a percentage of the total

water that could be produced by the reaction (Eqn. 3.7).

$$\xi = \frac{m_o}{m_{o,max}} = \frac{m_o M_{ilm}}{M_o m_{ilm}} \tag{3.7}$$

The uncertainty in the total water produced and oxygen yield is calculated from the propagation of uncertainties in the measured sample mass, pressure, operational volume, and manifold temperature values (± 0.5 mg, ± 0.5 mbar, ± 0.10×10^{-6} m^3, and ± 0.1 K respectively).

3.4.3 Sample analysis

After each experiment, ilmenite grains were analysed for evidence of the reduction reaction. ∼ 15 mg aliquots of each unreacted and reacted sample were set in epoxy resin in 10 mm brass rings and then polished and carbon coated for analysis using a FEI Quanta 200 3D FIB-SEM, or more simply, the focused ion beam scanning electron microscope (FIB-SEM, or SEM), at The Open University. To remove the grains from the ceramic sample tube they must be poured out, therefore, the grains selected for SEM analysis are assumed to be a random cross section from multiple locations within the sample tube.

Spectral analysis was performed on the grains to identify the minerals that show evidence of reaction. Meanwhile, BSE images were taken to determine how far the reaction proceeded into the grains by highlighting the product iron that forms as a result of the reduction of iron oxides. The contrast in grey-scale highlights differences in the average atomic numbers of constituent elements (Goldstein et al., 2018). Heavy elements such as iron are known to appear brighter as a result of a stronger backscatter of electrons. Element maps were also produced for grains selected from both unreacted and reacted samples.

3.5 Results

3.5.1 Reduction phase

The pressure profiles recorded during the reduction of each sample are shown in Figure 3.10. The initial pressure (P_{H2i}) and blank corrected pressure change (ΔP_{cr}) in the system are recorded in Table 3.4 for each sample, along with the calculated amount of hydrogen that has reacted. The results show that, generally, increasing the ilmenite mass results in an increase in the pressure change as more hydrogen was converted to water. The continuous downward trend in the pressure change data after one hour indicates the reaction had not

completed in this time.

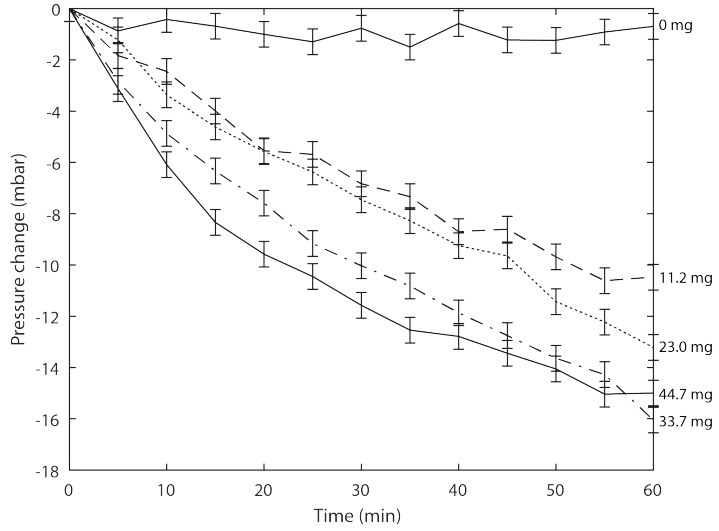

Figure 3.10: Pressure change during the reaction phase with various masses of ilmenite. An uncertainty of ± 0.5 mbar in the pressure readings is applied.

Ilmenite mass (mg)	P_{H2i} (mbar)	ΔP_{cr} (mbar)	n_h (μmol)
11.2 ± 0.5	170.9 ± 0.5	-9.8 ± 0.5	14.8 ± 1.0
23.0 ± 0.5	163.7 ± 0.5	-12.5 ± 0.5	18.9 ± 1.0
33.7 ± 0.5	168.8 ± 0.5	-15.6 ± 0.5	23.2 ± 1.0
44.7 ± 0.5	167.2 ± 0.5	-14.3 ± 0.5	21.6 ± 1.0

Table 3.4: Results from the reduction reaction phase. Pressure changes during the reaction were used to calculate the amount of H_2 reacted.

3.5.2 Water release phase

The water release phase pressure data are shown in Figure 3.11, where the cold finger was heated from -180 °C to 115 °C at a rate of $\sim$ 125 °C·min^{-1} at $t = 0$. There is a small peak (up to $\sim$ 0.3 mbar) at $\sim$ 5 minutes where it is assumed that water was released and recondensed as a result of non-uniform heating of the cold finger. It took a further $\sim$ 10 minutes for the pressure in the system to start to rapidly increase as condensed volatiles were re-released as gases into the system. The large pressure rise was then followed by a gradual downward drift in pressure of as much as 2.3 mbar. With increasing ilmenite mass, the peak pressure increases because larger volumes of volatiles were released from the cold finger. It is assumed that the pressure rise during the water release stage was wholly as a result of water vapour produced from the ilmenite reduction reaction (mass spectrometry was recommended for the next series of experiments to validate this assumption).

The amount of hydrogen reacted in the reaction phase is compared to the amount of water measured in the water release phase in Figure 3.12. In an ideal setup, the amount

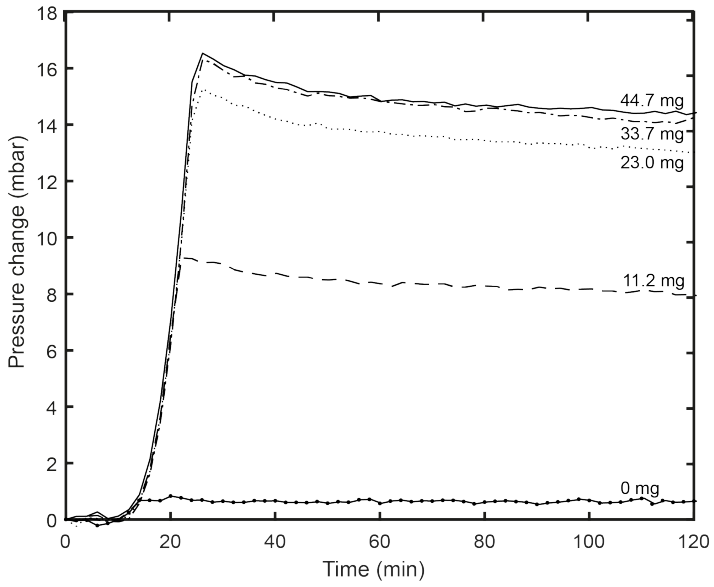

Figure 3.11: Pressure change during the water release phase with various masses of ilmenite. An uncertainty of ± 0.5 mbar is not included in this plot.

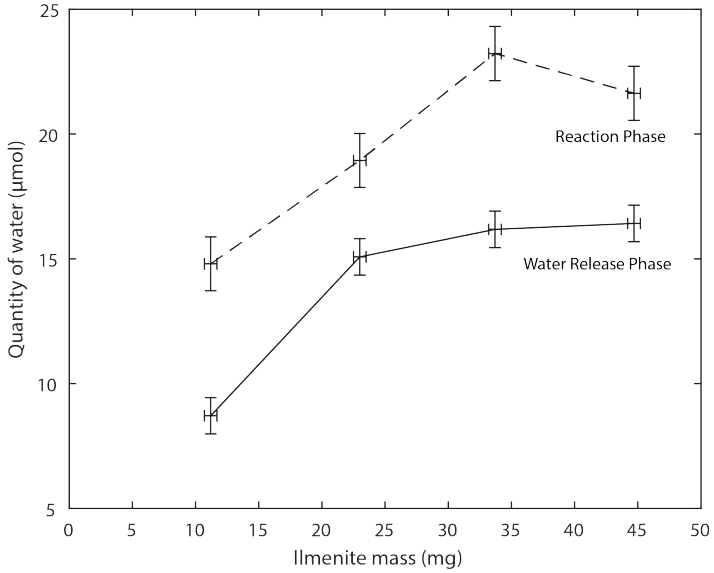

Figure 3.12: Estimated amount of hydrogen reacted and water produced from various ilmenite masses as calculated from pressure data from the reaction and water release phases respectively with a 1 SD uncertainty.

Ilmenite mass (mg)	ΔP_{cw} (mbar)	Calculated H_2O released (μmol)	O_2 yield (wt % O_2)	ξ (%)
11.2 ± 0.5	8.5 ± 0.5	8.7 ± 0.7	1.24 ± 0.12	11.8 ± 1.1
23.0 ± 0.5	14.8 ± 0.5	15.1 ± 0.7	1.05 ± 0.06	10.0 ± 0.5
33.7 ± 0.5	15.9 ± 0.5	16.2 ± 0.7	0.77 ± 0.04	7.3 ± 0.4
44.7 ± 0.5	16.1 ± 0.5	16.4 ± 0.7	0.59 ± 0.03	5.6 ± 0.3

Table 3.5: Results from the water release phase. The baseline and F corrected pressure rise from the release of water from the cold finger was used to calculate the amount of H_2O produced, and therefore the yield and reduction extent.

of hydrogen reacted should equal the amount of water produced and condensed at the cold finger. The experimental data suggests that more hydrogen ($\sim$ 4 - 7 μmol) was consumed in the reaction as compared to the amount of water that was condensed at the cold finger.

The yield outputs are summarised in Table 3.5, and it can be seen that the maximum yield and reduction extent occurred in smaller masses of ilmenite. For an 11.2 mg ilmenite sample, a peak oxygen yield of 1.24 $\pm$ 0.12 wt % was calculated, equating to a reduction extent of 11.8 $\pm$ 1.1 %.

3.5.3 2D model

During the reaction phase, the gases are always in the viscous flow regime (Pfeiffer Vacuum, 2013), therefore, the 2D model implemented in Chapter 2 is applicable. The 2D model was run for the four different sample masses, and assuming a straight pipe of 0.8 m long (the approximate length between the sample and cold finger in the BDM) and pipe ID of 6.35 mm with the associated system temperatures as defined in Table 3.3. With increasing ilmenite mass, the corresponding reaction fraction values are predicted to be 48.5 %, 23.9 %, 16.4 %, and 12.3 % respectively, significantly higher than the experimentally calculated reaction fraction, indicating the 2D model overestimates reaction rate.

3.5.4 Sample analysis

Unreacted ilmenite grains were studied with BSE imaging using a SEM (Figure 3.13a-d). Some grains appear to have non-uniform chemical composition, they display lamellar features (identified as rutile) corresponding to darker BSE regions. An X-ray multi-element map of an unreacted grain (Figure 3.13e) shows relatively homogeneous distribution of Fe and Ti contents with some Ti hotspots.

The reacted ilmenite samples were also analysed using BSE (Figure 3.14a - d). The edges of reacted grains show darkening where iron has been removed to leave rutile, while bright spots show the formation of pure iron. In some grains, the reaction proceeded further into the grain, preferentially along the lamellar features. This suggests that lamellae provide a pathway for hydrogen into the ilmenite structure as they are a physically separate mineral structure within the main mineral structure. A reaction front can be seen moving inwards from the grain surface and producing metallic iron. This suggests that the reduction reaction occurs preferentially from the outside in supporting the Dang et al. (2015) shrinking core model (Figure 1.4 in Chapter 1). An element map of a reacted grain (Figure 3.14e) shows separate areas of concentrated Ti and Fe, indicating that Fe has been separated from the

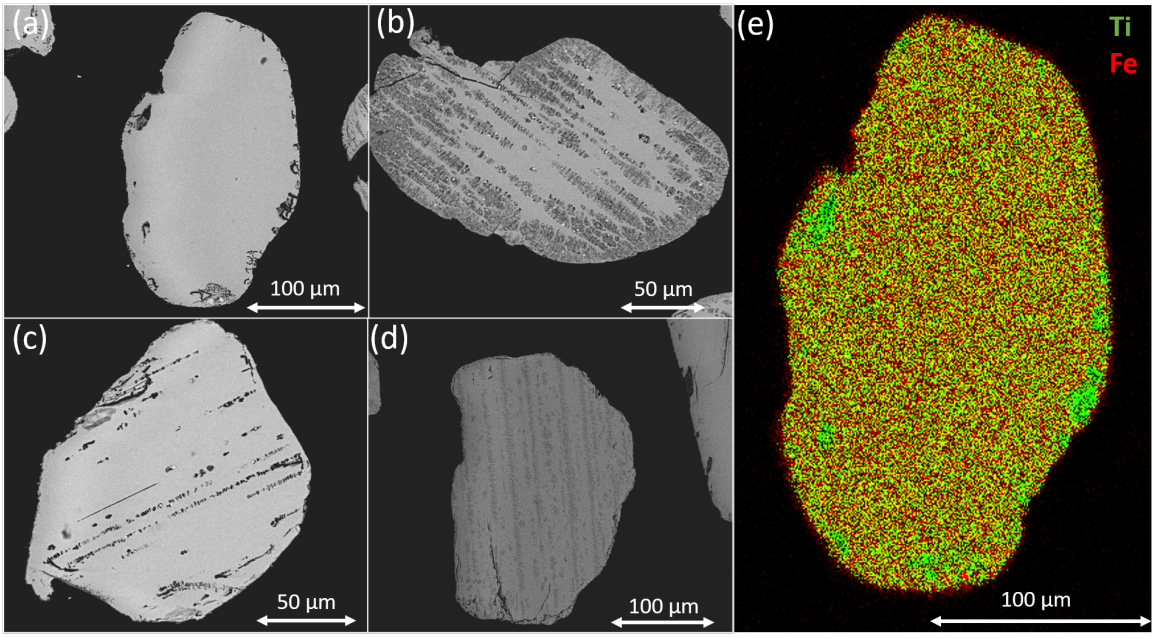

Figure 3.13: (a - d) Example BSE images of unreacted ilmenite grains. (e) Ti and Fe element map of grain (a).

ilmenite mineral structure leaving a TiO_2 residue. This trend follows the grain from the outside in, representing the extent to which the reaction has penetrated into the grain.

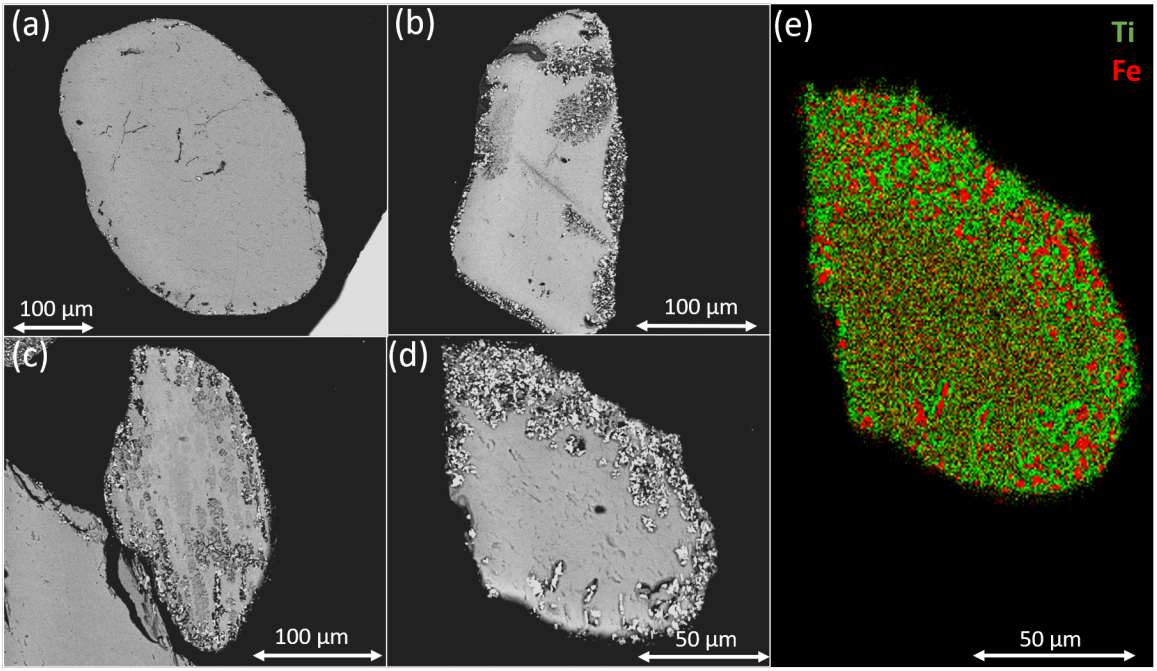

Figure 3.14: (a - d) Example BSE images of reacted ilmenite grains taken from the 23.0 mg ilmenite sample. (e) Ti and Fe element map of grain (d).

The reduction extent for each sample was determined by categorising imaged grains on a scale of no reduction to complete penetration of the reaction front into the grain. The reduction extent was quantified using a scale from 0 to 4 where 0 shows no reaction, 1 shows partial reaction of the outer rim of a grain, 2 shows full reaction on the outer rim of a grain,

3 shows significant penetration of reaction into a grain, and 4 shows complete penetration of the reaction front into a grain. The results of the analysis are shown in Figure 3.15. The fraction of grains for each sample represent 7 %, 3 %, 3 %, and 2 % of the 11.2 mg, 23.0 mg, 33.7 mg, and 44.7 mg sample respectively.

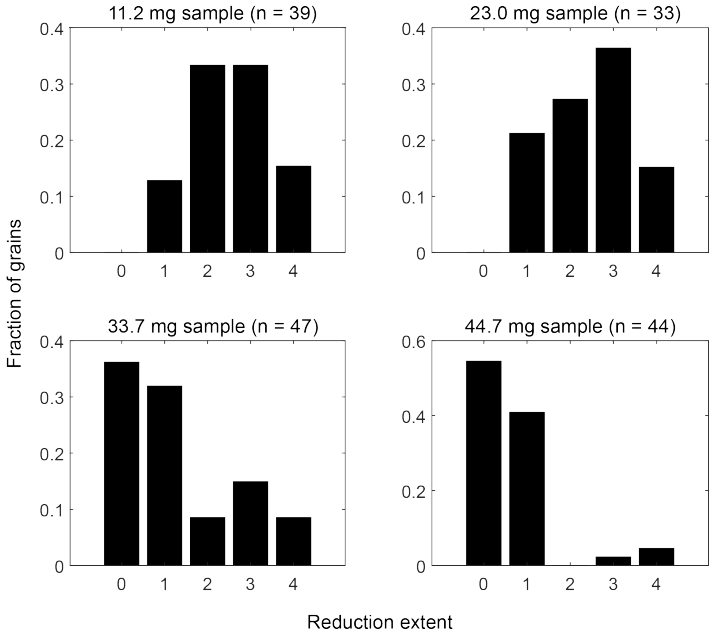

Figure 3.15: Histograms displaying the distribution of reduction extent, as defined by the extent of the reduction reaction around and into the grain, as a fraction of the number of grains for each sample size.

3.6 Discussion

3.6.1 Bake-out process

The bake-out process was demonstrated to successfully remove volatiles from ilmenite samples, although a longer bake-out test would be recommended to confirm that the one hour time frame is sufficient. If a bake-out is performed at the start of each experiment, any volatiles measured during the reaction and water release phases may be assumed to be associated only with the ilmenite reduction process. The evolved gas analysis and stepped analysis planned to be performed with the ProSPA experiment would act as a substitute to the bake-out process, and so the ISRU experiment could follow such analyses (Barber et al., 2018).

3.6.2 Quantifying water in the BDM

The yields produced in the one hour reaction resulted in water releases of < 16 mbar, which is much less than the saturation pressure of 120 mbar in the BDM (Figure 3.8 in Section 3.3.2) and hence the calibration factor, F, applied to the pressure readings was close to 1

(maximum 1.02). The maximum water pressure, therefore, was not limited by secondary water condensation within the system. However, the current BDM design would not be suitable for quantifying higher yields, for example when reacting larger samples and/or for longer periods of time, should they result in water vapour pressures beyond 120 mbar. Modifications are required in order to achieve improved thermal control with all the manifold components safely operating at temperatures of at least 115 °C so that the saturation vapour limit would remain significantly above 1.5 bar (the safe overload pressure of ProSPA pressure sensors).

3.6.3 Reaction rate

If the reaction rate is sufficient enough that the reaction measurably progresses in four hours (the time constraints imposed on ProSPA experiments), then the reaction would be deemed suitable for use on ProSPA. The larger samples generally resulted in higher reaction rates as more ilmenite grains reduced simultaneously, but the percentage yields were lower i.e. the smaller samples produced greater yields per unit mass of ilmenite compared to the larger samples (Figure 3.16). Sample mass has been shown to be a limiting factor in the reaction rate for ilmenite reduction, albeit with larger samples and in a flowing hydrogen system (Li et al., 2012). However, Li et al. (2012)'s observed sample mass limit of 20 g will likely vary dependant on sample geometry, hydrogen flow rate, and temperature.

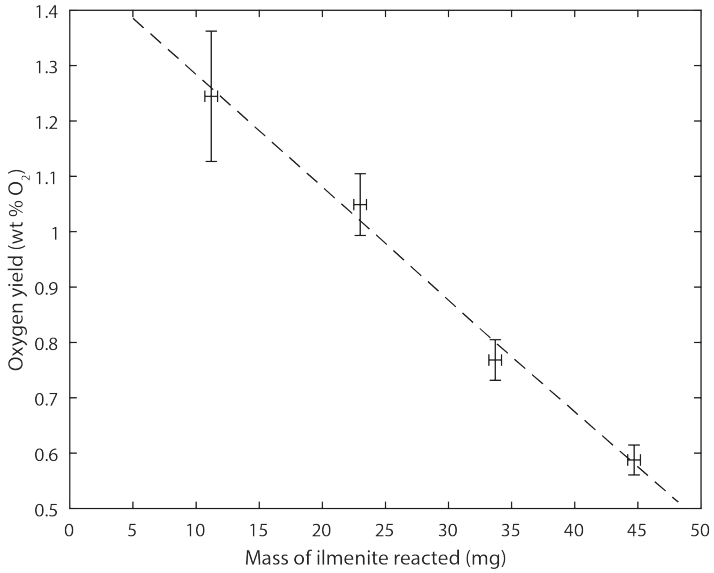

Figure 3.16: Yield (wt % O_2) as a function of ilmenite sample mass for a one hour experimental run.

Two reduction processes are considered in the present static setup to understand how sample geometry may influence the diffusion of gases between grains, and therefore the reaction rate. The two proposed processes are defined as: simple static reduction and progressive static reduction (Figure 3.17). In both models the starting conditions are the same, in which

the ilmenite grains are all exposed to a defined pressure of hydrogen. In the simple model, the ilmenite grains all begin to reduce at the same rate, and the water produced diffuses away from the grains at the same rate, no matter their location within the sample holder. In the progressive model as the grains begin to reduce, the rate at which the water diffuses away from the grains is variable and dependent on the depth within the sample. For example, at the top of the sample, the water can diffuse easily away from the grains resulting in faster reduction of the top-layer grains of ilmenite. However, at the bottom of the sample the water diffuses more slowly as it migrates through the pore spaces between grains. Consequently, the reaction rate will slow and the grains at the bottom of the sample holder will undergo less reduction overall. The reaction fraction in the larger samples will therefore be lower when applying the progressive model, which is what was observed experimentally (Table 3.5).

The distribution of reduction extent in Figure 3.15 shows how the smaller sample experiences less variation in reduction extent as compared to the larger sample which has a significant number of grains showing no or little reduction with only a small fraction (5 %) showing complete reduction. Such a large variation in reduction extent in the larger samples can be explained by the progressive reduction model. The 2D ilmenite reduction model discussed in Chapter 2 does not consider diffusion through porous media and therefore models simple static reduction. Consequently, the 2D model would output higher reduction extents and yields as compared to the experimental results in Section 3.5 (when all other reaction conditions were defined as the those outlined in Section 3.4).

If the average ilmenite grain size were smaller, which could be the case on the lunar surface (McKay et al., 1991a), the reaction rate would increase as the surface area of reducible minerals increases, and the distance of gas diffusion required through the interior of the grains is reduced. However, smaller grain sizes would also result in a longer diffusion pathway between grains, suppressing the diffusion of gases deeper into the sample. A wider sample holder, and/or smaller grain size could potentially enable greater penetration of hydrogen gas into the sample, and quicker removal of water from the reaction site, increasing the reaction rate.

3.6.4 Incomplete reaction

During the reaction phase the pressure continues to drop for the entire hour, and so it is assumed that the reaction has not reached completion, as confirmed by BSE imaging of reacted grains showing incomplete reduction. The amount of H_2 present at the start of each reaction (0.3 mmol) is stoichiometrically sufficient to reduce a 45 mg (0.3 mmol)

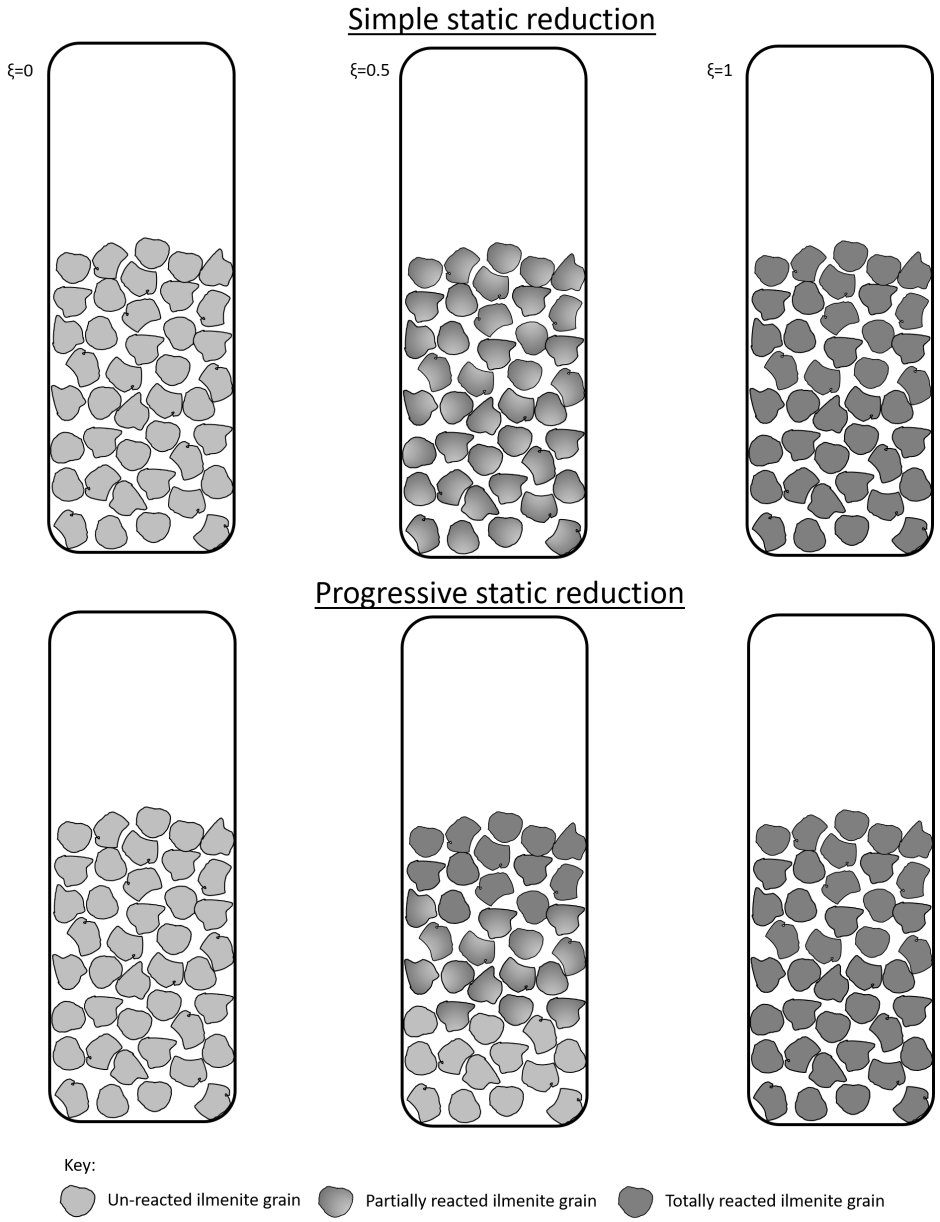

Figure 3.17: Schematic of the proposed simple static and progressive static reduction models as the reaction extent, ξ, proceeds from $\xi = 0$ to $\xi = 1$.

ilmenite sample, that is, the hydrogen is present in excess for ilmenite samples < 45 mg. The quantity of hydrogen was kept consistent so that the reaction pressures were consistent between experiments. With the current setup and assuming as a first order analysis that the reaction rate is linear from 30 minutes onwards (Figure 3.10), it would take more than five hours for the 11.2 mg ilmenite sample to completely reduce and more than 25 hours for a 44.7 mg sample. Such timescales are not suitable for the ProSPA instrument and adaptations to the experiment are recommended to increase reaction rates to ensure that measurable reduction (where pressure changes are significantly greater than a blank reading, i.e. greater than the uncertainty in pressure measurements of 0.5 mbar) of lunar soil is feasible within the four hour time frame imposed on ProSPA experiments.

3.6.5 Water losses

In an ideal system, one mole of hydrogen will reduce one mole of ilmenite to produce one mole of water. However, the molar amount of hydrogen that is used in the reaction phase is always less than (by 4 - 7 μmol) the molar amount of water that is condensed and subsequently released by the cold finger. Either, the amount of hydrogen/gas in the system is miscalculated, or not all the water that is produced is condensed at the cold finger, a result of inefficient condensing or inefficient transport. Both sources of discrepancy are considered here.

To calculate the molar amount of hydrogen/water vapour in the BDM the ideal gas equation is used (Eqn. 3.5). The gas temperature is assumed to be 115 °C (the heated manifold temperature), however, an average temperature during the reaction phase would need to be $\sim$ 230 °C to account for the discrepancy in calculated yields. The hot furnace is isolated to a small portion ($\sim$ 0.6 %) of the operational volume and would not account for such a large difference in average temperature required to miscalculate the yields. The operational system volumes were also considered as a possible source of error, as the volume used in the reaction phase is different compared to that used for the water release phase. To account for the discrepancy in calculated yields the volume used in the reaction phase would need to be smaller by 12×10^{-6} m^3, however the ceramic sample holder alone has a volume of 10×10^{-6} m^3 so volume measurements were not deemed to be the cause of the discrepancy. Therefore, it is assumed that yields were calculated correctly, and instead it was concluded that not all the produced water condenses at the cold finger.

When considering the progressive static reduction model, while there is still unreacted ilmenite there will always be some water in the pore spaces, more so at the base of the sample. The ilmenite reduction studies discussed in this chapter were not reacted to completion and so when the reaction was stopped (opened to vacuum and furnace switched off) any remaining gases were removed from the system including the portion of water that was in the pore spaces. To validate the theory that some water does not condense at the cold finger, an experiment is suggested for future work where an ilmenite sample is reacted to completion. Once all the ilmenite is reacted there should be no more water produced and the remaining water in the pore spaces should diffuse to the cold finger and the amount of hydrogen used in the reaction should equate to the amount of water trapped and released at the cold finger. Also, the amount of water that remains within the pore spaces should remain constant at any point in the reaction. Therefore, if experiments are performed for longer periods of time resulting in higher yields, the discrepancy between the hydrogen used in the reaction, and

the water that is condensed should always be the same.

3.6.6 Implications for ProSPA

Lunar soils have been found to contain > 12 % by volume ilmenite, however some highland soils have been found to contain ≤ 1 % ilmenite (Papike et al., 1991). Assuming a 45 mg lunar sample is collected into a ProSPA sized oven and contains 1 % ilmenite (∼ 0.45 mg), a first order estimate can be made for the amount of water produced using the BDM setup. Assuming that the relationship between the yield and the mass of ilmenite is always linear (Figure 3.16), and that the presence and composition of other lunar minerals in the sample has no impact on the production of water from the ilmenite present, then ∼ 0.4 μmol of water (0.01 wt % O_2 from a 45 mg sample of lunar soil) would be produced and condensed in one hour in the BDM system. A yield of this size equates to a pressure in the BDM system of ∼ 0.4 mbar which is likely too small to be identifiable above a blank reading. The presence of lunar minerals will also likely slow down the movement of gases between grains, particularly if the ilmenite grains present happen to be at the bottom of the sample or integrated into the matrix of other minerals. Higher temperatures and longer reaction times should result in an increase in yields (Li et al., 2012), and therefore further reaction optimisation studies are required. It should also be noted that other iron oxide-bearing lunar minerals can reduce including pyroxene and olivine, albeit at much lower efficiencies than ilmenite (Allen et al., 1994). As a result, low ilmenite concentrations may not be a barrier to the production and measurement of water from a lunar sample using a ProSPA-like system.

3.7 Conclusions

It has been demonstrated that ilmenite can be reduced by hydrogen in a ProSPA-like static system operated at 900 °C for one hour, producing yields of up to 1.24 ± 0.11 wt % O_2. Smaller samples (11.2 ± 0.5 mg) were shown to react more fully in the static system setup, up to 11.8 ± 1.1 % complete, as a result of the sample holder dimensions and reaction kinetics. It is proposed that a static system will result in water diffusing more slowly away from ilmenite grains that lie deeper in the sample tube, and therefore slowing the reaction rate for larger samples.

The BDM design is limited in that system pressure cannot be used to quantify water at pressures of > 120 mbar as a result of condensation onto pipework. A separate breadboard model is required in which the manifold can be heated more uniformly to higher temperatures

and therefore higher pressures of water vapour can be measured before condensation occurs. No other reaction conditions were trialled on the BDM, therefore the reaction procedure should be optimised by considering alternative furnace temperature and hydrogen pressures to ensure the highest yields within the operational constraints of the ProSPA system.

It is recommended that ProSPA pipework between the furnace and cold finger is heated uniformly to ensure accurate quantification of yields and limit unwanted condensation. The ProsPA system is not optimised for an ISRU reaction, however static reduction is feasible with the proposed design and could be used to perform a proof-of-principle reduction reaction of lunar ilmenite in situ.

Chapter 4

Breadboard development

This chapter includes sections derived from Sargeant et al. (2020b) and the associated supplementary material in which the design of the ISRU-BDM and its ability to quantify yields of water is discussed. The work of Sargeant et al. (2020b) has been expanded upon by evaluating and calibrating key components of the design.

4.1 Introduction

Following the outputs of the preliminary ilmenite reduction experiments carried out with the BDM (Chapter 3), it was clear that the BDM would need major modifications to improve the thermal control of the system. As the BDM was required for other uses it was decided that I would build a new, independent system, for specific ISRU experiments. An independent system ensured uninterrupted use of the setup, and the design could be tailored to the needs of this research.

The new system, called the ISRU-BDM, was designed to have significantly improved thermal control as compared to the BDM in three key areas; the furnace; the cold finger; and the manifold. The furnace was evaluated to more accurately determine the temperature experienced by samples when the furnace is activated. Meanwhile, the cold finger was required to heat and cool uniformly to eliminate cold spots where secondary condensation can occur. A target heating/cooling rate of 6 °C·min^{-1} was chosen as a suitable compromise between the rapid and non-uniform heating of the BDM cold finger (∼125 ° C·min^{-1}) yet quick enough to keep within reasonable time constraints for experiments (heating from -80 ° C to 120 ° C in one hour). Finally, the manifold was required to be heated uniformly to $>$ 112 °C (with a target variance of $\pm$ 2.5 °C) to ensure that water remains in the vapour phase within the manifold when operating at pressures of up to 1.5 bar.

The following sections describe the design, evaluation, and calibration of the ISRU-BDM system, addressing the three key areas identified for improved thermal control. The final section of this chapter considers the behaviour of water in the ISRU-BDM and how accurately water can be quantified within the system.

4.2 Technology developments

4.2.1 ISRU-BDM design

In the ISRU-BDM design the furnace, cold finger, and interconnecting manifold are contained within a heated box so that the pipework between the key components are all at a uniform temperature (within ±2.5 °C, the resolution of the thermocouples). The aim of this design is to prevent condensation of water on unwanted cold spots and therefore enable improved quantification of yields of water. The cold finger was also redesigned to incorporate an increased thermal mass which ensures that the cold finger heats and cools uniformly so that the condensing and releasing of volatiles is more controlled. A further improvement of the system design comes from the use of a mass spectrometer which can be used to determine the composition of volatiles in the system and confirm the production of water from hydrogen reduction of metal oxides. As the mass spectrometer cannot itself be heated it is located on an external platform and connected via heated capillaries from the heated manifold. A schematic of the ISRU-BDM breadboard is shown in Figure 4.1. The septum inlet and hydrogen gas cylinder attachment are separate, and only one is used at a time, dependent on the experimental requirements.

The ISRU-BDM system was built and wired by the author with support from M. Abbott in building the heated box. F. Abernethy programmed the system for automation using LabVIEW™ software. Details of the electronic control of the ISRU-BDM is described in Appendix B. The ISRU-BDM system (Figures 4.2 & 4.3) was built using COTS parts to enable rapid development and adaptation of the system.

The heated box is made from vermiculite sheets on a 100 × 65 × 75 cm aluminium frame built by M. Abbott, and is heated to ∼ 120 °C by two 2 kW oven heating elements. Swagelok® 4-VCR fittings compatible with 1/4 inch OD (4.2 mm ID) pipe are used throughout. High temperature (up to 315 °C) Swagelok® actuator valves (SS-4BG-V51-3C) with stainless steel spherical tips are used inside the oven to control the movement of gases. A high temperature (temperature rated up to 120 °C) Kulite® diaphragm pressure sensor (ETL-641-375M-1.6BARA) is used to monitor the gas pressure in the system, which means the sensor

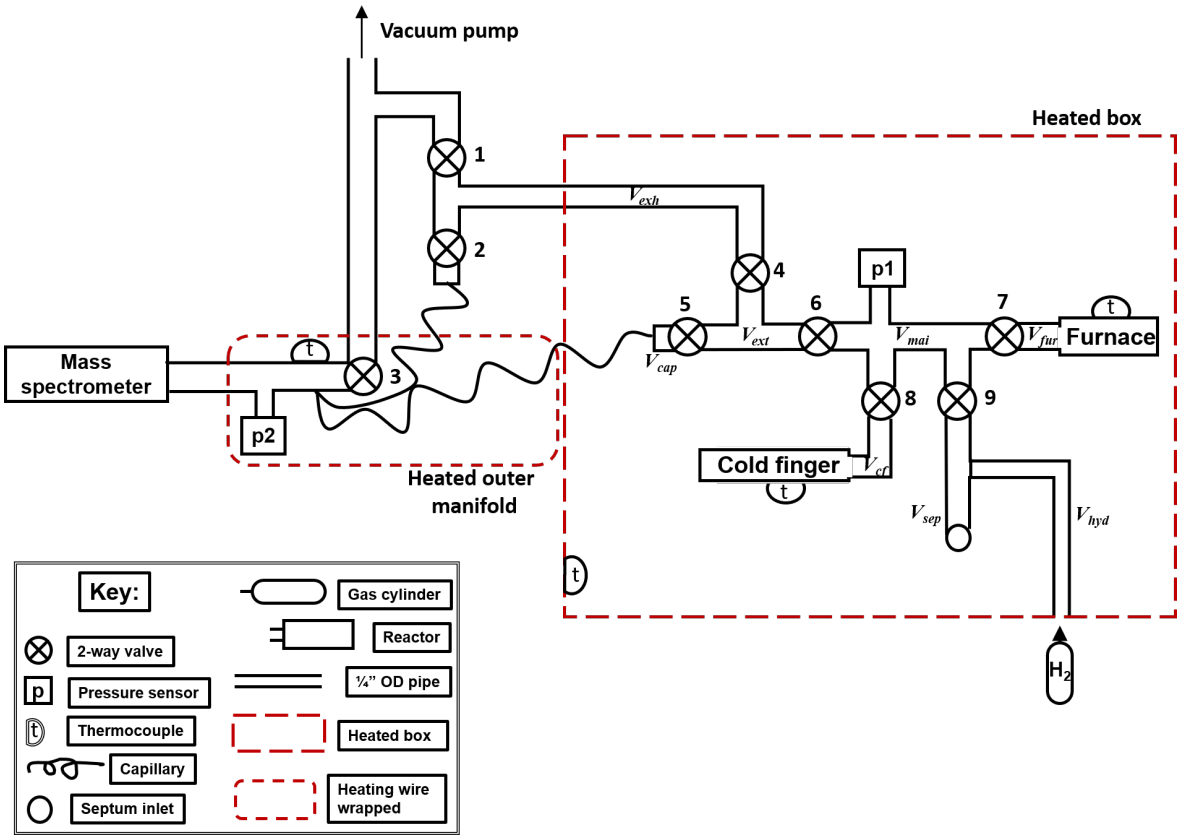

Figure 4.1: ISRU-BDM schematic.

and valves can be uniformly heated along with the rest of the manifold to the required temperature of 120 °C. The sensor has a sensitivity of 2.524 mV·mbar^{-1} which equates to a resolution of 0.06 mbar (see Eqn. 3.1 and 3.2 in Chapter 3) which is well within the ProSPA required resolution of 0.25 mbar (Table 1.2 in Chapter 1). A furnace, the same as that used in Chapter 3, utilises a ceramic chamber wrapped in resistance wires to heat samples up to 1100 °C. The 200 mm length, 4 mm ID, and 6 mm OD ceramic sample tube of 99.7 % Al_2O_3 purity and closed at one end is placed inside the furnace before each experiment. The system is connected to an outer manifold, where the mass spectrometer is located, via an exhaust pipe and capillary tubes. All outer components of the manifold except for the mass spectrometer are heated to 100 °C with Omega™ resistance heating wire. The outer manifold hosts the Hiden HPR-20 quadrupole mass spectrometer connected via stainless steel crimped capillaries, as used on the BDM in Chapter 3. The capillaries are also heated with resistance wire. K-type thermocouples like those used in the BDM (Chapter 3) are used to record temperatures in the furnace, cold finger, heated box, and outer manifold, therefore all temperature measurements have a resolution of ± 2.5 °C. The ISRU-BDM system was designed to be automated and respond to temperature controls using LabVIEW™ software. The 'real' temperature experienced by samples heated within the furnace was yet to be evaluated with the respect to the 'measured' temperature of the furnace. Also, work conducted in Chapter

3 highlighted the importance of defining the manifold and cold finger temperature during the volatile release stage to more accurately calculate the volumes of gases present. Therefore, a series of tests were performed to understand how accurately the desired temperatures are achieved.

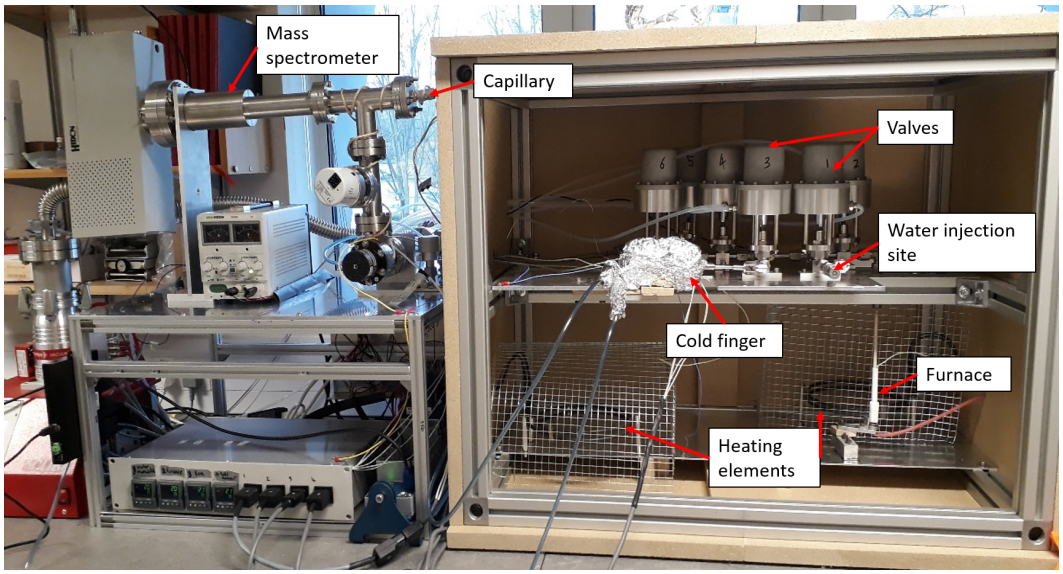

Figure 4.2: Front view of the ISRU-BDM with the oven door removed.

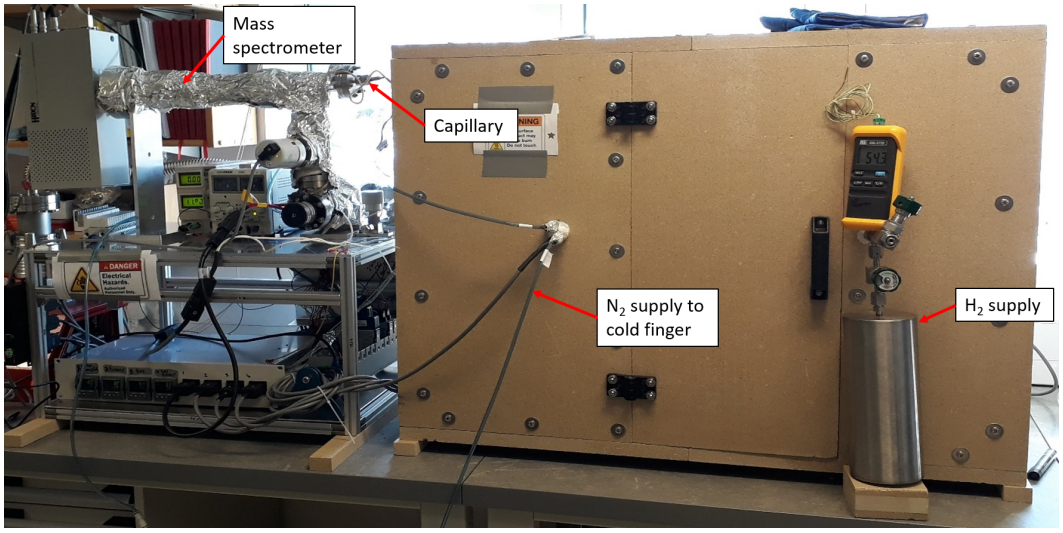

Figure 4.3: Front view of the ISRU-BDM with the oven door attached.

4.2.2 Furnace

The furnace is the same as that used on the BDM (Chapter 3). The temperature of the furnace was recorded by the thermocouple located outside the ceramic sample holder as seen in Figure 3.3a in Chapter 3. To understand the temperature of samples located within the sample holder during reactions, two studies were performed. In the first study the heating and cooling rate of the furnace and sample tube were analysed, while the next study analysed

the difference in temperature between the furnace and sample holder at each of the planned reaction temperatures. Each study was carried out in the heated box at 120 °C which is the starting temperature. To enable temperature measurements from inside the sample holder, it was detached from the vacuum system and a separate thermocouple was placed inside, ensuring it reached the bottom of the sample holder where the sample would be located. The sample holder was then held in place, inside the furnace, with a clamp stand where all components were inside the 120 °C heated box.

Furnace heating/cooling rate - Methodology

In the first study, the furnace was heated to 1100 °C and temperature recordings of the furnace and sample holder were taken every 30 seconds for one hour. Next, the furnace was set to 120 °C and the temperature of the furnace and sample holder were recorded every 30 seconds for two hours. The results are shown in Figure 4.4.

Furnace heating/cooling rate - Results

In the first instance, the furnace did not reach 1100 °C in one hour, instead reaching a peak of 1087 °C, while the sample holder reached 1043 °C. The furnace had a maximum heating rate of $\sim$ 58 °C·min^{-1} at the start of the heating process. The furnace cools quicker than the sample holder, reaching 120 °C from 1087 °C in $\sim$ 104 minutes. Meanwhile, the sample holder stabilised at 122 °C after $\sim$ 111 minutes. The maximum cooling rate of the furnace is $\sim$ 37 °C·min^{-1} at the start of the cooling process. The repeat heating and cooling step showed that the furnace was capable of reaching the required 1100 °C temperature from 120 °C in $\sim$ 54 minutes. As the furnace is drawing maximum current from the power supply, higher

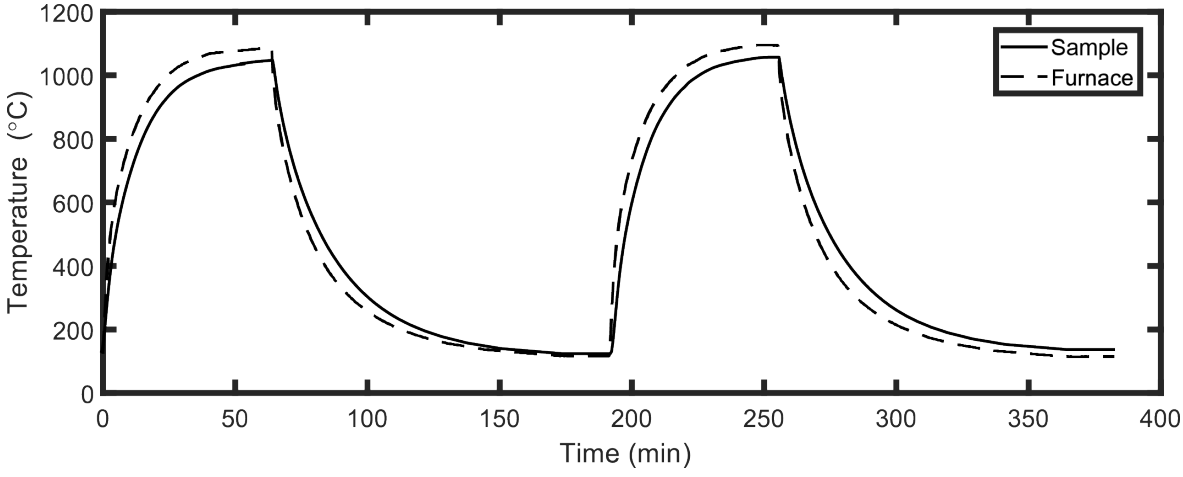

Figure 4.4: Heating and cooling rate of the furnace and sample from 120 °C to 1100 °C and back to 120 °C. An uncertainty of ± 2.5 °C from the resolution of the thermocouple is not included in this plot.

voltages cannot be used to increase the heating rate and ensuring the maximum temperature is reached. Ideally a different power supply would be used to enable increased current, however as this was not available a preheating of the furnace is performed before each high-temperature experiment to ensure that it is capable of reaching the required temperature.

Furnace temperature calibration - Methodology

In the second study, the furnace was set to 850 °C. Once the furnace recorded a temperature of 850 °C, the temperature of the furnace and sample were recorded for 30 minutes. Next, the procedure was repeated where the furnace was set to increasingly higher temperatures (900 °C, 950 °C, 1000 °C, 1050 °C, and 1100 °C) with temperatures being recorded for 30 minutes at each temperature step.

Furnace temperature calibration - Results

The difference in temperature recorded at the furnace and sample holder is shown in Figure 4.5. The temperature that would be experienced by the sample is significantly lower than that measured by the furnace, by as much as 53 °C at 1100 °C, with the difference increasing at higher temperatures. The furnace temperature should therefore be interpreted as an upper constraint on the reaction temperature for given yields in the subsequent reduction experiments. It should be noted that the sample temperature recorded in this study will likely be lower than that actually experienced by the sample during reaction experiments as the sample will be under lower pressures of hydrogen (< 1 bar). This temperature calibration study was performed under atmospheric conditions and so heat will be lost in the sample tube through convection of hot air. Also, this study does not include the presence of a sample such as ilmenite or lunar material which could provide conductive heat flow, reducing the thermal gradient across the inner diameter of the tube (Reiss et al., 2019).

To better understand the actual temperature experienced by samples during experiments, a more representative study could be performed. For example, the thermocouple could be placed inside the sample tube with a vacuum seal and different quantities of hydrogen could be added for each analysis. This study should be performed for each sample that is to be tested so that thermal properties of each sample could be considered. A thermal model could be produced to compare the relative contributions of convection, conduction, and radiation under these conditions. It is recommended that such calibration studies be performed in future work and on ProSPA.

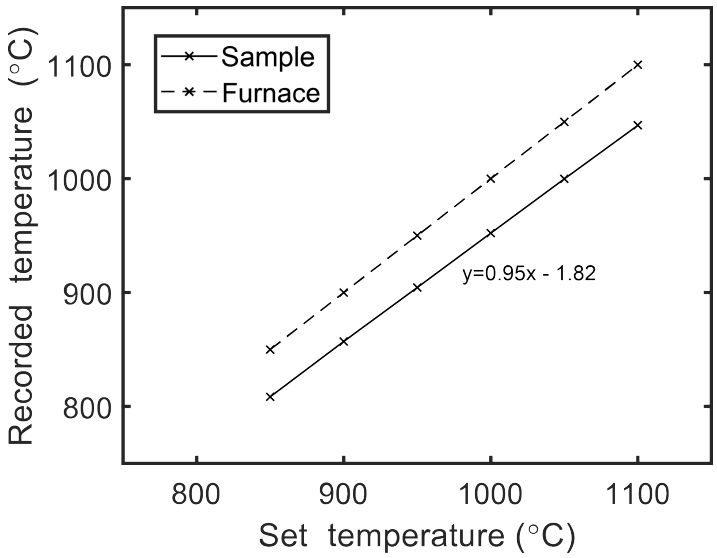

Figure 4.5: Calibration of the furnace with respect to the sample temperature. Difference in set temperature and recorded temperature experienced by the sample with respect to the furnace. An uncertainty of ± 2.5 °C from the resolution of the thermocouple is applied to the recorded temperatures but is negligible in this plot.

4.2.3 Cold finger

A cold finger (built by M. Abbott) was developed to provide increased thermal control when condensing and releasing gases, as compared to the cold finger utilised in Chapter 3. The cold finger is composed of a solid copper cylinder with a central hole for a steel insert to be screwed into which attaches to the manifold (see Figure 4.6 & 4.7). The use of a solid copper cylinder encasing the steel pipework ensures that the temperature of the internal steel is uniform. The copper acts as a thermal mass so that when the copper is heated or cooled, there is a lower thermal gradient along the internal steel. Consequently, when heated the cold finger should release water in one step, and not recondense at a colder location of the cold finger as was identified in Chapter 3. The copper cylinder has two holes for two 90 W cartridge heaters and a further hole for a K-type thermocouple. The copper cylinder is wrapped in 5 mm OD copper piping which enables a flow of cooled nitrogen gas to flow through at a user defined pressure of 2 bar. The whole cold finger is wrapped in fibreglass wool and aluminium foil to insulate it from the heated box.

To ensure accurate quantification of yields, the cold finger should be capable of condensing all available water within the bit-accuracy of the pressure sensor, i.e. as the sensitivity of the pressure sensor is ± 0.06 mbar, the saturation vapour limit of water at the cold finger should be ≤ 0.06 mbar. At -59 °C the saturation vapour limit is 0.06 mbar, calculated using the Clausius-Clayperon equation (Eqn. 3.3 in Chapter 3). Therefore, the temperature inside the steel insert of the cold finger must be ≤ -59 °C to ensure all the available water

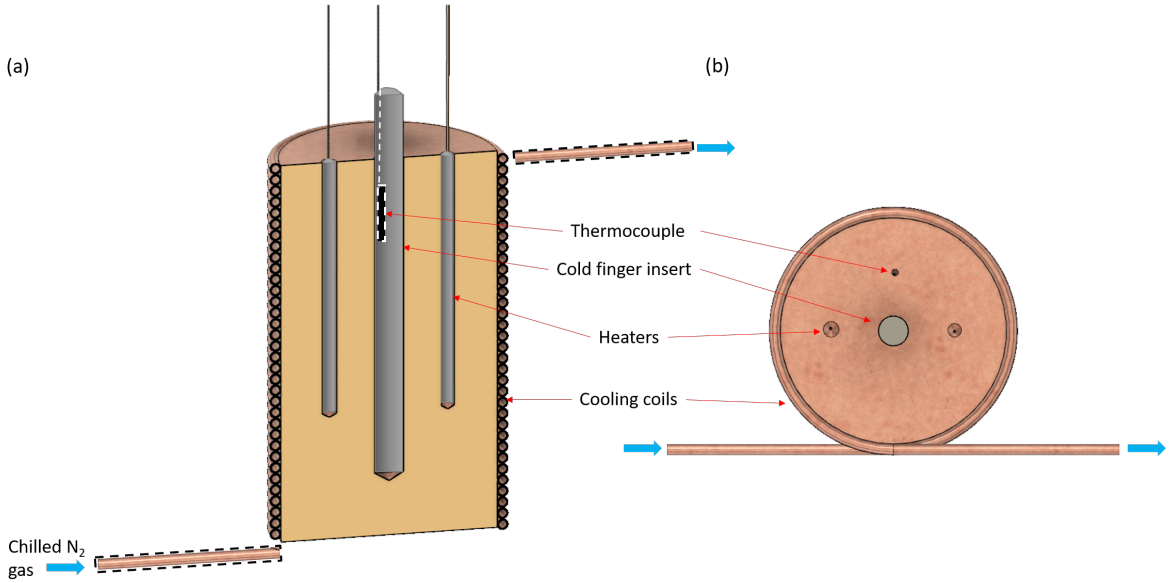

Figure 4.6: Cold finger schematic showing (a) a slice through drawing of the cold finger design, and (b) a top view of the cold finger design.

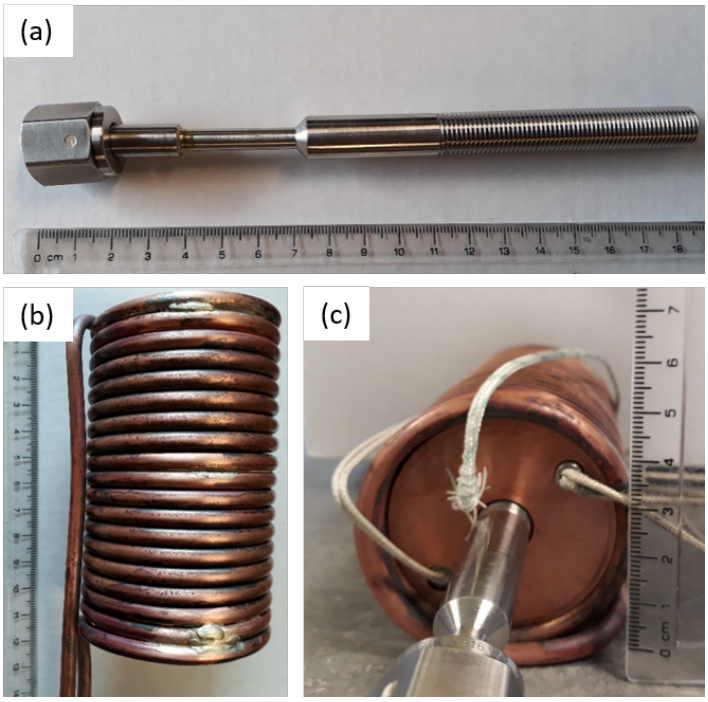

Figure 4.7: Images of the cold finger showing (a) the internal steel tube that connects to the manifold, (b) the copper piping surrounding cold finger, and (c) the copper cold finger with inserted steel tube, heaters and thermocouple.

is condensed. Assuming that under cooling conditions the steel insert will be warmer than the copper thermal mass (the latter being where the cold finger temperature will nominally be recorded), a target temperature of -80 °C was chosen for further testing. A cold finger temperature of -80 °C is significantly warmer than the -180 °C temperature applied in Chapter 3. By operating at a warmer temperature, the cold finger would not only require less energy and nitrogen supplies than it would if operating at -180 °C, but it would also reduce the time

taken for the cold finger to reach temperature. It was also shown in Section 2.2.2 in Chapter 2 that a significantly cooler cold finger did not significantly improve diffusion rates and therefore reaction rates. The maximum temperature required by the cold finger is 120 °C as this is the temperature that the heated box will operate. A heating rate constraint of $\geq 6°$ C·min^{-1} was determined to be reasonable, which would mean the cold finger could heat/cool from the minimum temperature setting of -80 °C to the maximum required temperature of 120 °C and back down again in one hour.

Cold finger temperature calibration - Methodology

The cold finger was tested to understand how the temperature reading of the thermocouple embedded in the copper cylinder compares to a thermocouple placed inside the steel cold finger insert. The following experiment was performed in a heated box operating at 120 °C. Once the temperature in the heated box was stable the experiment was performed. First, the cold finger was set to -80 °C, and once the copper reached this temperature the cold finger was then set to 120 °C and temperature readings at each thermocouple were recorded every 30 seconds for one hour. Then, the temperature was set to -80 °C where temperature readings were again recorded every 30 seconds for one hour. This cooling and heating process was repeated once more. The temperature controlled heating and cooling elements respond to the copper mass thermocouple readings.

Cold finger temperature calibration - Results

The temperature of the steel insert and the copper mass are shown in Figure 4.8. The cold finger took $\sim$ 27 minutes to heat so that the copper block measured 120 °C. There was a slight overshoot in temperature of the copper as it continued to reach a maximum of 121.6 °C before returning to 120 °C by 60 minutes. Meanwhile the steel insert reaches a maximum temperature of 119 °C within 29 minutes before returning to 118 °C by 60 minutes.

In the cooling stage, the copper cooled quicker than the steel insert as it is closer to the cooling coils. It took $\sim$ 28 minutes for the copper to reach -80 °C from 120 °C, with minimal overshooting. Meanwhile, the steel insert never reached –80 °C, as the cooling system stops once the copper reaches temperature. Instead, the steel insert reached a lowest temperature of -75 °C in $\sim$ 32 minutes before stabilising at -74 °C by 60 minutes. At this temperature only 0.002 % of the maximum possible water should remain in the vapour phase (0.089 mbar) which is still within the bit accuracy of the pressure sensor, and so these cold finger conditions should be suitable for condensing at least 99.998 % of the available water to enable accurate

quantification of yields.

The second heating and cooling phase showed good repeatability with the same characteristics as the first stage with the steel insert operating at $\sim$ 2 °C lower than the defined 120 °C, and $\sim$ 5 °C higher than the defined -80 °C. The cold finger has a maximum heating and cooling rate of $\sim$ 11 °C·min^{-1} which is significantly slower than that recorded in the cold finger used with the BDM in Chapter 3. As a result, there should be a smaller thermal gradient across the cold finger, and less likely to result in secondary condensation at a different area of the cold finger after water has been released. The heating and cooling rate meets the stated requirements of $\geq$ 6 °C·min^{-1} to ensure the experiments can be performed in a reasonable time frame. Manual thermocouple temperature readings were taken at the manifold join to the cold finger during these studies. These showed that the temperature of the manifold remained stable at 114 °C, which is equivalent to the manifold temperature measured in Section 4.2.4 and was therefore unaffected by the temperature of the cold finger.

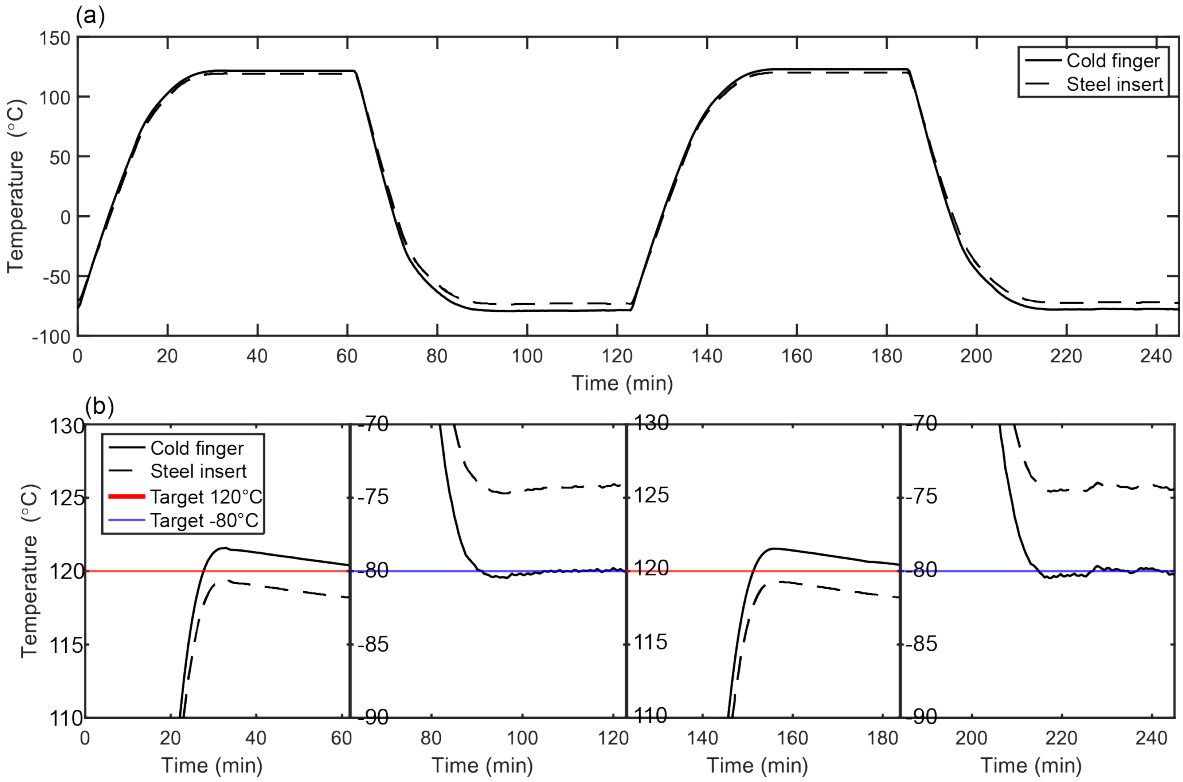

Figure 4.8: Results of the cold finger temperature calibration. (a) shows the heating and cooling cycles of the cold finger with temperatures measured inside the copper block, and inside the steel insert. (b) shows the heating and cooling cycles of the cold finger as separated by each change in target temperature. Results are shown for experiments conducted in the operational conditions of the 120 °C heated box. An uncertainty of $\pm$ 2.5 °C from the resolution of the thermocouple is not included in these plots.

4.2.4 Manifold

The heated box is designed to operate at temperatures of at least 120 °C (deemed to be sufficient to keep the manifold at the required temperature of at least 112 °C) to limit the amount of secondary condensation of water on the internal pipework. Therefore, each component within the heated box is required to safely operate at these temperatures. High temperature pressure sensors and pneumatic valves were utilised, which can operate at temperatures of up to 120 °C and 315 °C respectively. The external manifold and capillary are wrapped in heating wire that reaches 100 °C. This was deemed the highest reasonable temperature without causing damage to the connected mass spectrometer which is not recommended to be heated. The capillary is heated so that water can diffuse through it to the mass spectrometer for analysis. Some condensation of water in the capillary can be tolerated as the mass spectrometer will not be used for quantitative analysis.

Manifold heating/cooling test - Methodology

A heating and cooling test was performed on the heated box to determine how long it takes for the manifold to reach a stable temperature (within ± 0.1 °C). Temperature readings were recorded using K-type thermocouples next to a heating element of the heated box, and on the manifold. Starting at room temperature, the box was set to 120 °C. Eurotherm® PID controllers activate the power to the heating elements when the temperatures recorded at the heating elements are less than the set temperature. Manual temperature readings were recorded, using K-type thermocouples, of three different locations of the manifold which confirmed that the manifold temperature increases uniformly.

Manifold heating/cooling test - Results

The temperature readings from the heated box and the manifold are shown in Figure 4.9. The heating element reached 120 °C by 18 minutes followed by a small overshoot of $\sim$ 2 °C before steadily returning to 120 ± 2.5 °C by two hours. Meanwhile, the manifold reached a maximum stable temperature of 114 ± 2.5 °C by four hours. A manifold temperature of 114 °C will ensure that water in the system will remain in the vapour phase up to pressures of $>$ 1600 mbar, as determined by the saturation vapour pressure (Eqn. 3.3 in Chapter 3), although some level of water adsorption will still occur (Sefa et al., 2014; Weston, 1985). ProSPA is only expected to work with pressures of up to 1 bar (Table 1.2 in Chapter 1), therefore the ISRU-BDM manifold is suitable for handling pressures of water that may be

expected with ProSPA. The ProSPA manifold can operate at up to 120 °C, meaning the ISRU-BDM manifold falls slightly short of this requirement in its current setup. However, the difference in temperature between the manifold and the heater element (the latter being where the temperature is recorded during experiments) of 6 °C would result in a difference in yield calculation within uncertainty, therefore the current setup is deemed suitable for ISRU experiments. The manifold is attached to a stainless steel platform that is located above the heating elements (see Figure 4.2). Therefore, conductive heating of the metal platform and connecting joints to the manifold is required to heat the pipework, explaining the relatively slow heating of the manifold. In order to perform experiments that can take up to eight hours from start to finish, the heated box was set to 120 °C the night before experiments were performed to ensure the manifold was at the required temperature at the start of the day.

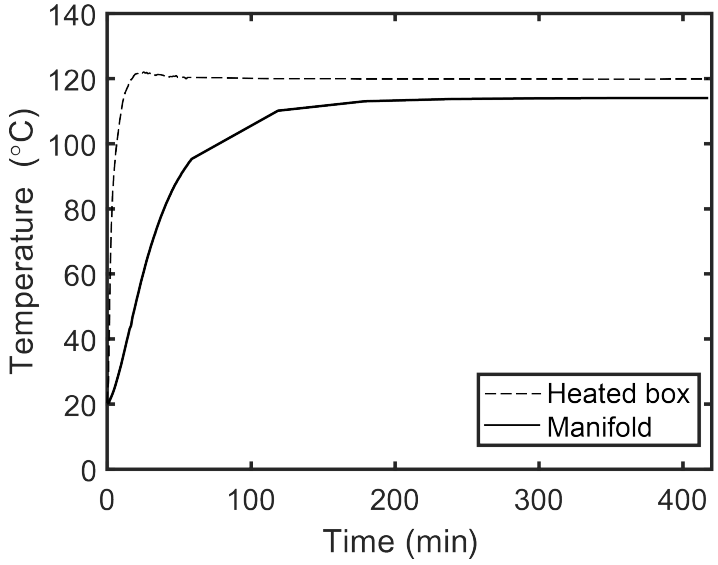

Figure 4.9: The temperature of the heated box and the manifold when set to 120 °C from room temperature. Readings were taken over a period of seven hours. An uncertainty of ± 2.5 °C from the resolution of the thermocouple is not included in these plots.

4.3 System Characteristics

Pressures recorded within the ISRU-BDM can be used in conjunction with system volume measurements to quantify the amount of hydrogen/water vapour in the system. Therefore a volume calibration study was performed to quantify each volume of the ISRU-BDM, and a series of temperature calibration factors were determined to account for the pressure changes that occur with each temperature setting of the ISRU-BDM.

4.3.1 Volume calibration

Volume calibration was performed on the system using gas expansion in which a known volume of gas was expanded into different volumes sequentially, where pressure changes directly relate to the change in volume. Assuming that the temperature is constant across the manifold, it is possible to estimate the volumes of each section of the vacuum system using Boyle's Law as in Section 3.2.1 in Chapter 3. Each configuration of the system was considered using both the hydrogen attachment and the septum inlet. Each gas expansion series was repeated five times.

First, a known volume was required, and so the internal dimensions of each component in V_{mai} was utilised. V_{mai} was then filled with air before progressively opening valves into the surrounding volumes (excluding V_{hyd} & V_{inj}) where the resulting pressures were recorded. A further gas expansion series was performed by filling the cold finger with air and evacuating the rest of the system so that the hydrogen attachment and injection port could be analysed. The resultant volumes and their associated standard deviation are shown in Table 4.1.

Volumes	Final volume ($\times 10^{-6}$ m^3)	Standard deviation ($\times 10^{-6}$ m^3)
V_{mai}	8.72	0.08
V_{cf}	3.45	0.01
V_{fur}	4.80	0.02
V_{inj}	2.31	0.03
V_{hyd}	7.71	0.01
V_{ext}	3.19	0.02
V_{cap}	1.72	0.03
V_{exh}	21.20	0.02

Table 4.1: Volumes of ISRU-BDM segments (n = 5).

4.3.2 Pressure characterisation

The temperature of the system is required for calculating the molar quantities of gas present. The components of the ISRU-BDM operate at different temperatures throughout different stages of experiments, resulting in a varying average system temperature. Instead of determining an average system temperature for each stage of an experiment, a temperature calibration factor, k_T, was determined. The k_T factor can be applied to pressure readings to account for the variation in pressure of a gas under different temperature conditions. For example, when all components are set to 120 °C, one can assume that the gas within the system is at 120 °C. When the furnace and cold finger operate at significantly different temperatures, the pressure of the gas will vary by a factor of k_T to that measured when all system

components are at 120 °C.

To determine the k_T factor, 416 mbar of hydrogen was placed into the standard operational volume (V_{mai}, V_{ext}, V_{cap}, V_{fur}, and V_{cf} as seen in Figure 4.1). All system components were set to 120 °C and the pressure recorded; this is the baseline temperature that all pressures are calibrated to. The cold finger and furnace temperatures were then varied and the pressure was monitored and recorded. The calibration factor was then calculated as $k_T = P_f/P_i$ where P_i is the pressure of the gas when the box, cold finger, and furnace are all at 120 °C, and P_f is the pressure of the gas when the cold finger and/or furnace temperature is varied. The k_T factors can be seen in Table 4.2. Pressure values recorded in the standard operating volume can be calibrated with the relevant k_T factor; it will be clearly stated in each chapter when the k_T factor is applied in any calculations.

Cold finger setting (°C) (± 2.5 °C)	Furnace setting (°C) (± 2.5 °C)	Air pressure (mbar) (± 0.5 mbar)	k_T factor (± 0.002)
120	120	415.7	1.000
120	850	434.0	1.044
120	900	434.5	1.045
120	950	435.1	1.047
120	100	435.6	1.048
120	1050	436.1	1.049
120	1100	436.5	1.050
-80	1100	421.4	1.014
-80	1050	421.2	1.013
-80	1000	421.2	1.013
-80	950	420.8	1.012
-80	900	420.4	1.011
-80	850	420.1	1.011

Table 4.2: k_T factors to be applied to pressure readings obtained at a range of ISRU-BDM system temperatures.

4.4 Quantifying yields of water in the ISRU-BDM

To evaluate how efficiently the ISRU-BDM system can condense and release water, and how accurately yields can be quantified, a series of experiments were performed. The chosen experiments are more in-depth than those performed on the BDM in Section 3.3.2 in Chapter 3, and are supported by an analysis on the uncertainty of the procedure.

The following experiments utilise a selection of system volumes and temperatures which are shown in Figure 4.10. During the water injection stage, all components within the heated box operated at 120 °C and then water was injected into the septum and allowed to expand into the operational volume. During the water trapping stage, the cold finger was set to

-80 °C where water can condense. Next, the cold finger was heated to 120 °C and the water released into the system in the gas phase. Finally, the cold finger was cooled again to -80 °C for further trapping.

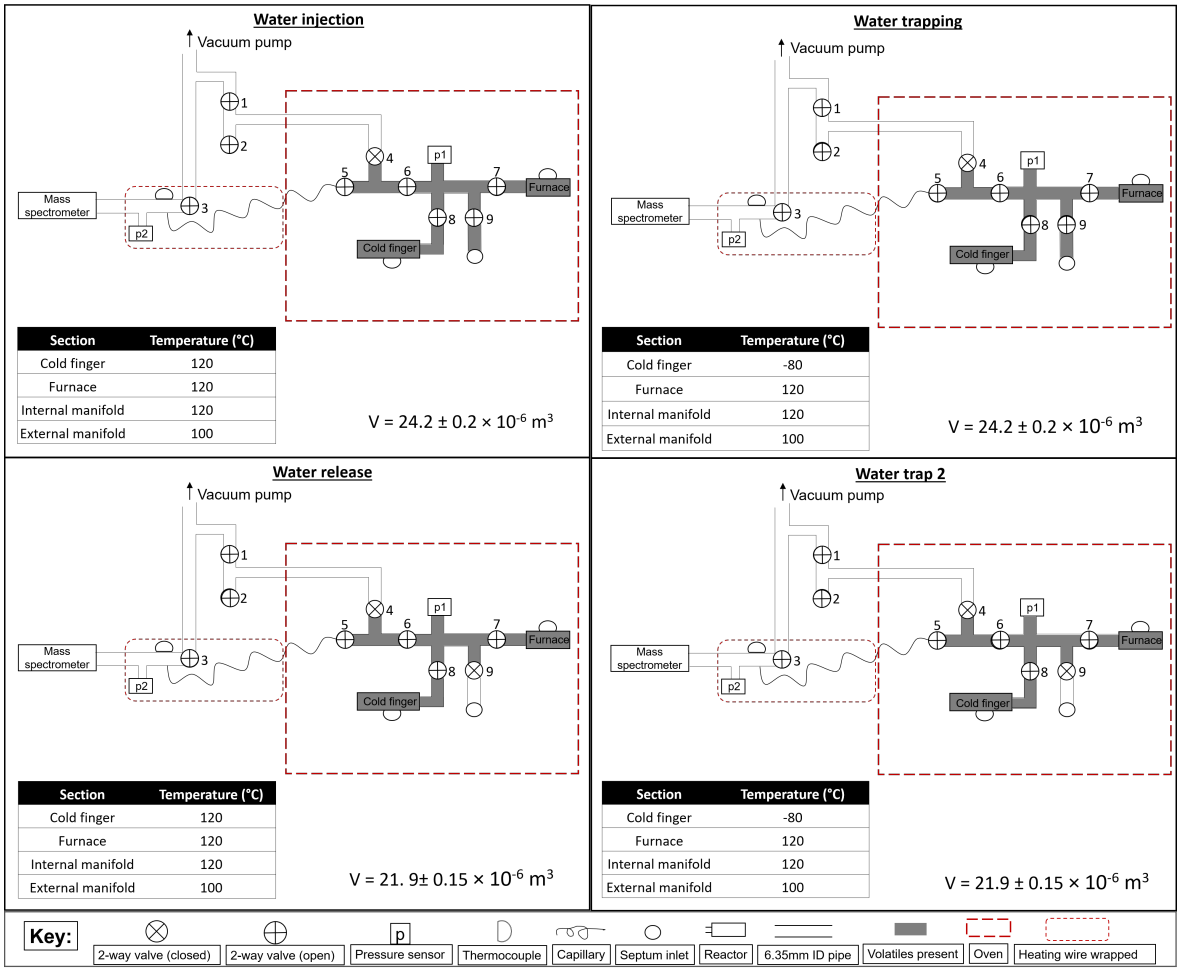

Figure 4.10: Phases of the operational procedure for water behaviour studies in the ISRU-BDM, with associated operational volume and temperature conditions.

The following studies in this section required the injection of water into a vacuum system. Water was drawn up through a 10 μl syringe and injected through a septum. There were two potential causes considered for additional water to be added to the system during this procedure. The first considers the dead volume in a syringe, which is where remaining fluid is stored after the injection, such as in the needle stem or base of the plunger. The second cause for additional fluid into a vacuum system considers the movement of air into the system when the septum is pierced. The dead volumes are accounted for in calibrated syringes, however, it is assumed that when injecting into a vacuum system the remaining dead volume fluid is drawn out as a result of a high pressure differential. To test this, a syringe was used to draw up water and then injected out at standard temperature and pressure (STP, 273 K and 101 kPa respectively). This 'empty' syringe was then used to pierce the septum of the vacuum system as in the water injection stage in Figure 4.10. The experiment was repeated three

times and the average increase in pressure of 25.6 mbar shows that the residual fluid in an 'empty' syringe can lead to a significant pressure change in the system. As a consequence, a blank reading was recorded in the following water condensibility and quantification studies to account for the contribution of dead volumes of water.

To determine whether additional fluid enters the system as a result of the piercing of the septum, a further test was conducted. The 10 μl syringe was completely emptied by exposing the needle stem to the vacuum system to draw out any remaining fluid in the dead volume. This syringe was then used to pierce the septum again as in the water injection phase and the pressure was recorded. There was no significant change in pressure when this test was repeated three times, therefore it is assumed that no significant addition of fluid enters the system as a result of piercing the septum.

4.4.1 Condensibility of water

Known volumes of water (1, 2, & 3 μl) were injected into the system and trapped down at the cold finger as in the water injection and water trapping stages respectively (Figure 4.10). The cold finger was then heated to release the water while pressure measurements were taken as in the water release stage. This trapping and heating was repeated once more as in the water trap 2 and water release stages respectively to understand how efficient this process is (Figure 4.10). The pressure profiles for each experiment are shown in Figure 4.11 along with the cold finger temperature profile.

The greater the volume of water injected into the system the greater the pressure, showing water can be quantified using this set up. The blank experiment also provides a measurable pressure reading demonstrating that the syringe does have a dead volume of water that is drawn into the vacuum system. There was a steady decline in pressure when the valve to the septum was open, likely a result of some water steadily adsorbing onto the interior manifold surface, which occurs more readily at higher pressures (Sefa et al., 2014; Weston, 1985). During the trapping stage, the cold finger was cooled to -80 °C and water vapour condensed at the cold finger causing a pressure drop to $\sim$ 2 mbar. This above-zero reading was likely a result of atmospheric gases injected into the system with the water. The temperature of release appears to begin at approximately -10 °C. The pressures recorded in the water release phase were higher than those measured in the water injection stage as a result of volume decrease caused by the closing off of the septum.

To determine whether the system efficiently trapped and released the volatiles, the molar quantity of water present, n_w, was calculated for the water injection stage and water release

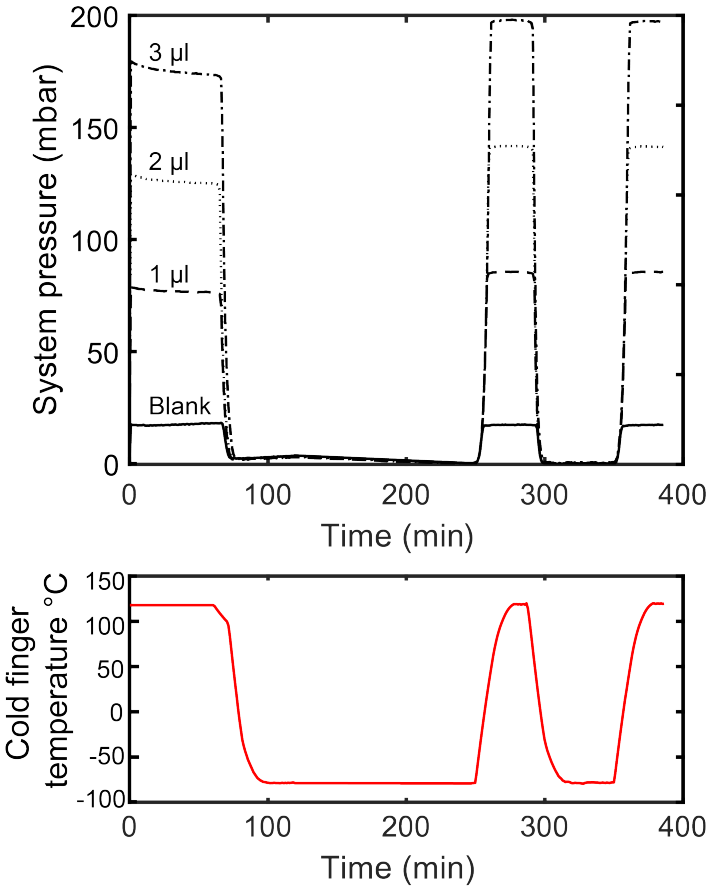

Figure 4.11: Pressure profiles from the release of 1, 2, and 3 μl of water, along with a blank reading, that has been trapped and released by the cold finger. Primary and secondary releases are shown. The cold finger temperature during the study is also shown. The uncertainty in pressure readings is ± 0.5 mbar.

stage using the ideal gas equation $n{=}PV/RT$, where P is the pressure of water in the system, R is the Boltzmann constant, and V and T are the volume and temperature of the system respectively. Applying the associated volume for each phase (Figure 4.10), assuming a temperature of 120.0 ± 2.5 °C (393.2 ± 2.5 K), and the uncertainty in the pressure readings is ± 0.5 mbar, n_w was calculated and is shown in Table 4.3. The uncertainty in pressure was determined through observations of pressure reading stability when pressure was held in the sealed operational volume for one hour. The difference in n_w between the water injection stage and the first water release stage was $\leq$ 1 %, which is within the uncertainty of the values calculated and thus demonstrates efficient trapping and release of water. Although a direct comparison of pressure can be applied between each water release phase, n_w was also calculated for the second water release phase and shown in Table 4.3 for comparison. Again, the second release shows highly efficient trapping and release of water using this technique.

Water release from the BDM cold finger in Chapter 3 showed an initial spike in pressure before the main release of water. A suggested cause for this was inhomogeneous heating of the cold finger, resulting in an initial release of water before condensing at another location on a

cooler part of the cold finger. There was no initial peak in pressure using the ISRU-BDM cold finger, suggesting the copper thermal mass worked as a way to produce homogeneous heating of the cold finger. Note that when volumes of water were expanded into two different system volumes in this experiment, and then calculated back to the number of moles from pressure readings (with volume and temperature variables), the quantities calculated are effectively the same (within uncertainty). This shows that the volume and temperature values (and their associated uncertainty) determined for the system, and the pressure readings recorded have been accurately determined, i.e. when the volume and therefore pressures are changed, they can consistently be used to calculate the same quantity of water present to within uncertainty ($\sim$ 4-8 % of the volume of water measured).

Volume of water injected (μl)	Derived water quantity after injection (μmol)	Derived water quantity in 1st release stage (μmol)	Derived water quantity in 2nd release stage (μmol)
1 μl	45.5 $\pm$ 0.6	46.0 $\pm$ 0.6	45.8 $\pm$ 0.6
2 μl	82.7 $\pm$ 0.9	83.4 $\pm$ 0.9	83.2 $\pm$ 0.9
3 μl	120.0 $\pm$ 1.2	120.6 $\pm$ 1.2	120.6 $\pm$ 1.2

Table 4.3: Quantity of water in the system during the injection of 1, 2, and 3 μl of water and subsequent trapping and release of water from the cold finger.

4.4.2 Quantification of water

An experiment was performed to understand how well the pressures of water in the system compare to those predicted theoretically as was done with the BDM in Section 3.3.2 in Chapter 3. Volumes of water ranging from 0.5 to 5 μl were injected into the system and condensed at the cold finger, before being released as a vapour. The pressure of water in the system, P_m, was recorded during the water release stage and compared to theoretical pressure values, P_i, which were calculated using the ideal gas equation where P_i=n_wRT/V. n_w is the molar amount of water injected calculated as n_w=$V_w/\rho_w \cdot M_w$, where V_w is the volume of water injected, ρ_w is the density of water, and M_w is the molar mass of water.

The experimental and theoretical values are shown in Figure 4.12. The data points are corrected for the blank, and therefore the blank reading lies on 0,0. An uncertainty of $\pm$ 0.1 μl was applied to the water volumes to account for limitations in the ability to faithfully reproduce the volumes of water injected into the system (See Section 3.3.2 in Chapter 3). The experimental pressures recorded were significantly lower than those predicted theoretically by as much as 30 % (the discrepancy increased with volume of water). Causes

such as inaccurate volume measurement, temperature, and/or pressure readings were ruled out. One potential mechanism for reduction in pressure is through water adsorption onto vacuum system walls, where an increase in pressure results in greater amounts of adsorption (Sefa et al., 2014; Weston, 1985). The amount of adsorption of gases onto a surface can be characterised using adsorption isotherms (Singh and Thomas III, 1998) which describe how system pressure affects the adsorption of gases on a solid surface. Such isotherms could be used to investigate the increased discrepancy between measured and theoretical pressures if resulting from increased adsorption, however there was insufficient time to produce these isotherms theoretically or experimentally. Another point of note is the trend in measured data which, from 0.5 μl upwards produces a linear trend with a smaller gradient than that predicted theoretically. However, below 0.5 μl (pressures of < 35 mbar) there appears to be less adsorption and so a greater increase in pressure is recorded per unit volume of water present. At these low pressures the quantification of yield should be more accurate than those at higher pressures. Measurements of pressures for smaller volumes of water, and the measurement of an adsorption isotherm for this system would confirm this theory and is suggested for future work.

System temperatures may need to be increased beyond 120 °C to as much as 300 °C to desorb the weakly bound water molecules (Joly et al., 2000). As a result, the yields calculated from pressure readings in the following reduction experiments represent the yields of water/oxygen that can be retrieved using this set-up, but the yield from the reaction itself will likely be higher. In other words, more water is produced than is actually collected at the cold finger and measured at pressures of > 35 mbar. After each experiment the system is open to vacuum for a number of hours removing adsorbed volatiles. Therefore, the water adsorption effect will likely be repeated for each experiment. It is possible to estimate the yield of the reaction by applying a calibration factor. The factor can be derived from the relationship between the theoretical and measured pressure readings (P_i/P_m) as compared to the measured pressure readings (P_m). Such a calibration would be required on the ProSPA instrument to correctly interpret the amount of water produced from lunar soil.

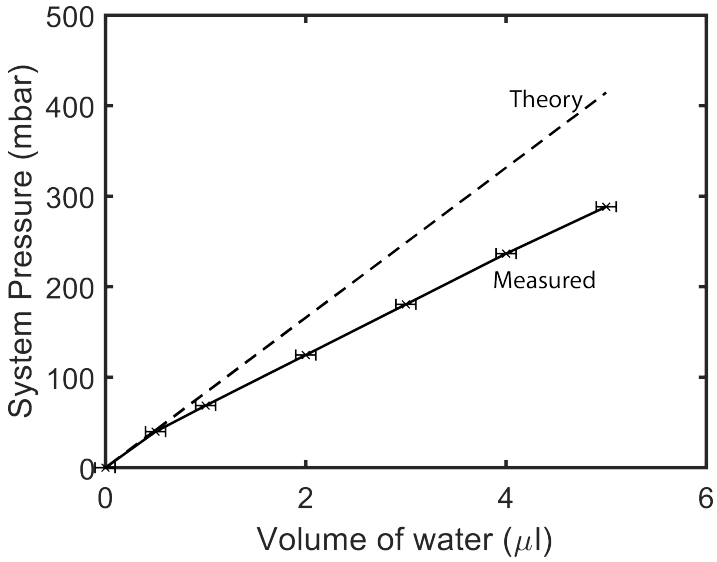

Figure 4.12: Theoretical and experimental pressures of known volumes of water as released from the cold finger. The uncertainty in pressure values (± 0.5 mbar) is negligible in this plot.

4.5 Conclusions

The ISRU-BDM has been designed to provide increased thermal control as compared to the BDM used in Chapter 3 and has been shown to meet the required design criteria. Thermal analysis of the furnace and the sample tube showed that samples may experience temperatures up to 53 °C cooler than the temperature recorded at the furnace when reacting samples up to 1100 °C, which should be considered in the interpretation of any reactions taking place in the sample tube. Meanwhile, an improved cold finger design ensures homogeneous heating so that water releases in a more controlled manner. The use of a heated box to contain the main manifold, where water production experiments will take place, ensures the pipework operates at a sufficiently high enough and uniform temperature so that secondary condensation is controlled to within acceptable limits.

In order to use the final ProSPA instrument for water production experiments on the lunar surface, system calibrations must be performed. The correct temperature and volume of all components would be required for correct quantification of yields. Water adsorption isotherms would also be required to quantify the amount of water that would be adsorbed onto the ProSPA manifold, allowing correction factors for yield quantification, but also for understanding the required bake-out of the system before being used for further experiments. Temperature calibration would also be required on the ProSPA ovens to better understand the thermal gradient experienced by samples during reactions.

Chapter 5

Optimising reaction conditions for ilmenite reduction in the ISRU-BDM

This chapter is adapted from the published paper (Sargeant et al., 2020b).

5.1 Introduction

Ilmenite reduction in a static system has been shown to be feasible with the BDM (Chapter 3). The present chapter describes the optimisation of the ilmenite reduction process, using the breadboard with improved thermal control (ISRU-BDM) described in Chapter 4. The optimisation is aimed at maximising the yield, and considers those factors that can be controlled within ProSPA i.e. reaction temperature and hydrogen pressure. Other factors such as sample size, grain size, and mineralogy can also influence yields, however they cannot be controlled by the ProSPA instrument.

The optimum reaction procedure in the ISRU-BDM in terms of reaction temperature and hydrogen pressure was investigated. The reaction temperatures considered were from 850 °C to 1100 °C, which are known to produce yields from ilmenite reduction and extends beyond the maximum ProSPA furnace temperature (1000 °C) to show how an increase in capability might affect yield. The hydrogen pressures trialled ranged from 118 mbar to 584 mbar (0.08 μmol to 0.39 μmol) to investigate the effects of relatively low pressures on the reaction. The lower and upper bounds were determined from estimations of how much hydrogen would be used in a four hour reaction, and how much hydrogen would be required to completely reduce an ilmenite sample with some remaining hydrogen respectively. The conditions that

resulted in the highest yields were then selected for the optimum reaction procedure.

5.2 Methodology

Here, the set-up of the ISRU-BDM is described and the general operational procedure is outlined in which the ilmenite reduction experiments were performed. The temperature and hydrogen concentration studies are discussed in further detail, along with the data and sample analysis techniques used to identify the mechanism of reduction.

5.2.1 General experimental procedure

The evening before each experiment the temperature of the internal manifold was set to 120 °C. The overnight heating guaranteed that the internal manifold was uniformly heated before the start of an experiment, minimising the condensation of water onto the pipework. The ilmenite used in this work was the same as that used in Chapter 3, i.e. $\sim$ 95 % pure with an average grain diameter of $\sim$ 170 μm. Each $\sim$ 45 mg ilmenite sample was placed into a ceramic tube and sealed onto the system at valve 7 using an O-ring tube fitting (Figure 4.1 in Chapter 4). The ilmenite mass was selected as it is the approximate sample size to be analysed with ProSPA. Each experiment was controlled using LabVIEW™ software which controlled pneumatic valves and temperature settings, which enabled a high level of automation and therefore consistency between each experiment.

A one hour bake-out procedure was performed at the start of each experiment wherein the furnace was heated to 500 °C and opened to the vacuum pump in order to remove any volatiles from the sample (the duration of one hour was based on the results of Section 3.3.1 in Chapter 3). Meanwhile, the cold finger was isolated from the pumping system and cooled to -80 °C (see Section 4.2.3 in Chapter 4). Next, the furnace was isolated and heated to the chosen reaction temperature. At this point the LabVIEW™ programme paused until the hydrogen supply valve was manually opened to admit hydrogen into the defined volume. When the required pressure was reached, valve 9 (Figure 4.1 in Chapter 4) automatically closed. Valves within the operational volume were then opened to allow the hydrogen gas to react with the sample and the water produced to condense at the cold finger. The pressure in the system was automatically monitored every minute during the reaction as the samples were left to react for four hours. A reaction time of four hours was selected as a reasonable time frame for such experiments to be performed on the Luna-27 mission. After the reaction, the system was evacuated of any remaining gases and the furnace was left to cool for two hours

to reach 120 °C, before the system was isolated from the vacuum pump. Finally, the cold finger was heated to 120 °C and the condensed water sublimated into the system where the pressure was recorded. A summary of the operational conditions of the ISRU-BDM during the experiments is shown in Table 5.1, while a graphical representation of the procedure is outlined in Figure 5.1. The internal and external manifold always were operated at 120 °C and 100 °C respectively during experiments.

Experimental stage	System conditions		
	Operational volume ($\times 10^{-6}$ m^3)	Cold finger temperature (°C)	Furnace temperature (°C)
Bake-out	47.3 ± 0.2	-80	500
H_2 addition	11.9 ± 0.1	-80	500
Reduction reaction	21.9 ± 0.1	-80	Reaction temperature
Water release	21.9 ± 0.1	120	500

Table 5.1: Operational conditions of the ISRU-BDM during each experimental stage.

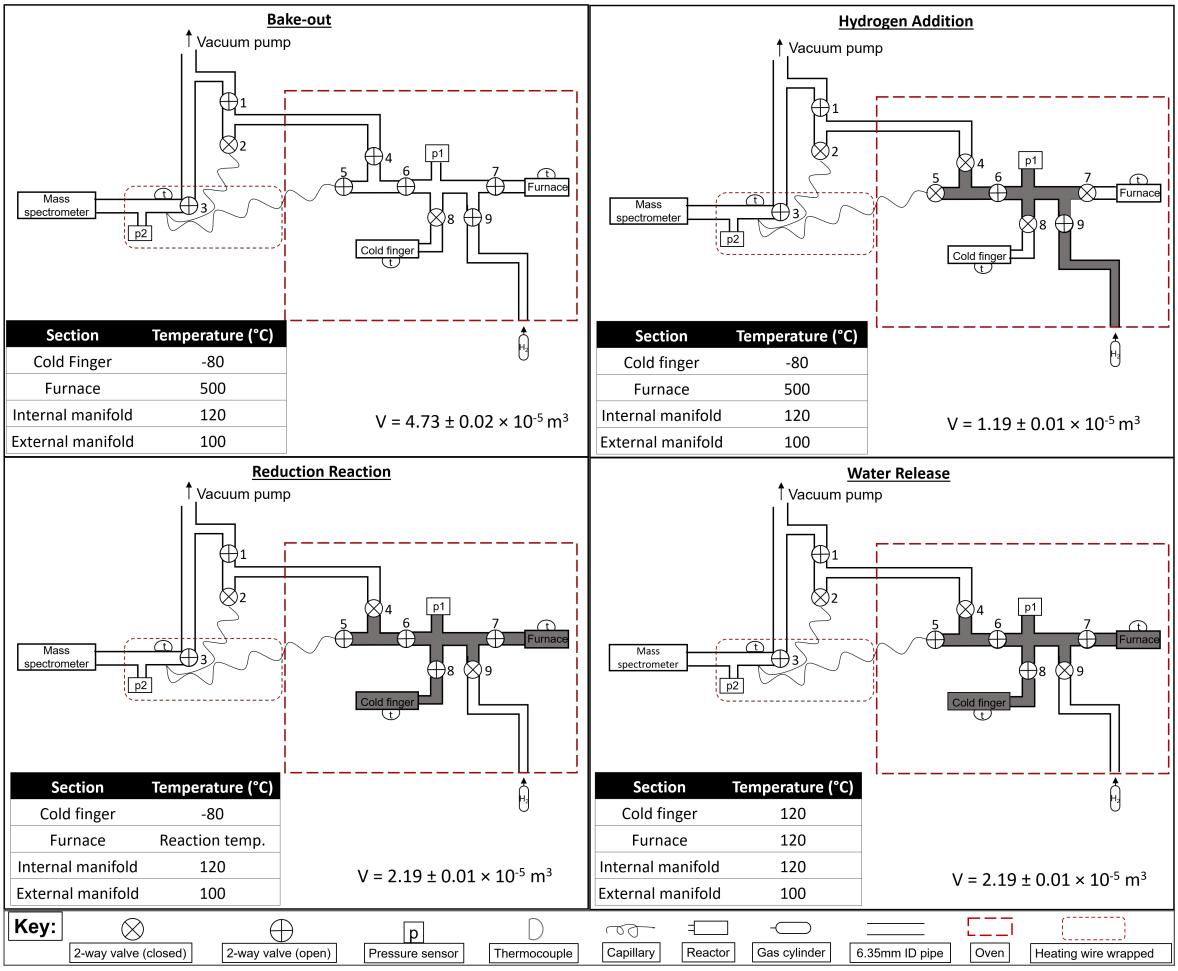

Figure 5.1: Phases of the operational procedure for ilmenite reduction studies in the ISRU-BDM, with associated operational volumes and temperature conditions.

The purpose of the quadrupole mass spectrometer was to analyse the volatiles released from the cold finger. It was found that the mass spectrometer required at least one hour for the baseline to stabilise after each change of the operational volume. Therefore, the mass spectrometer could not be used to monitor the reaction in real time because there are operational volume changes that occur just before the reaction phase that would affect the baseline spectra. Instead, a second condensing phase was added to the operational procedure. The mass spectrometer was then used to scan across m/z values of 1-50 and the operational volume was expanded to include the capillary at valve 2 (Figure 4.1 in Chapter 4). The cold finger was then heated to 120 °C to sublimate the volatiles which were then sampled by the mass spectrometer.

Temperature studies

The ilmenite reduction reaction was performed with a range of furnace temperatures from 850 to 1100 °C in increments of 50 °C. The temperature was defined as the nominal temperature as measured by the thermocouple located between the furnace and sample holder (see Figure 3.3 in Chapter 3), herein described as the furnace temperature. The thermocouple was placed at the same depth inside the furnace to within ± 2 mm, which resulted in a change in measured temperature, i.e. uncertainty of ± 5 °C which dominates over the uncertainty of the thermocouple reading. The amount of hydrogen used in each reaction was targeted to be 0.3 mmol, which was selected to achieve a hydrogen:ilmenite molar ratio of 1 (Equation 1.2 in Chapter 1). The amount of hydrogen at the start of the reaction should therefore have been 420 mbar, however, the operational procedure was susceptible to an 'overshoot' in the addition of hydrogen and therefore the hydrogen pressure was often higher than 420 mbar by as much as 50 mbar (an extra 0.036 mmol). The pressure was recorded during the reduction reaction and water release phases of each experiment. A blank reading was obtained for comparison where an empty sample tube was heated in a furnace operating at 1000 °C.

Hydrogen pressure studies

The ilmenite reduction experiments were performed with a range of hydrogen pressures with a furnace temperature of 1000 °C. The amount of hydrogen used in each experiment was defined as a ratio of hydrogen to ilmenite ($n_h : n_{ilm}$). Hydrogen to ilmenite concentrations of 0.28:1.00 up to 1.38:1.00 were trialled in this work, which equates to starting pressures of 118 mbar up to 584 mbar (when calculated for an internal manifold temperature of 120 °C).

5.2.2 Data analysis

The pressure changes measured for each experiment were corrected for furnace temperature by multiplying by the relevant k_T factor (see Section 4.3.2 in Chapter 4), and then corrected further by subtracting the corrected blank pressure change. The final corrected pressure values from the reaction phase are denoted as ΔP_{cr}. The pressure changes measured during the water release phase were corrected by subtracting the blank pressure change, and are denoted as ΔP_{cw}. Blank readings were obtained under nominal conditions at 1000 °C and an initial hydrogen supply with no sample present. Uncertainty in individual pressure readings was taken as the variability of pressure readings as determined when air was held in the manifold for one hour (± 0.5 mbar). The ΔP_{cr} and ΔP_{cw} values were converted into the quantity of hydrogen that had reacted, n_h, and the quantity of water produced, n_w, respectively using Equation 3.5 (Chapter 3) where V is the operational volume (Table 5.1), and T is the internal manifold temperature.

The rate of water production, R_w, was calculated as follows:

$$R_w = \frac{V_w}{t} = \frac{m_w}{\rho_w t} = \frac{n_w M_w}{\rho_w t} \tag{5.1}$$

where V_w is the volume of water produced, t is the time over which the rate of production was measured, m_w is the mass of water produced, ρ_w is the density of water under STP conditions, and M_w is the molar mass of water.

The yield of the reduction reaction is described by the wt % of oxygen extracted compared to the total sample mass as in Equation 3.6 in Chapter 3. The maximum theoretical yield of oxygen (in the form of water) from the ilmenite reduction process is 10.5 wt % O_2, rising to 31.6 wt % O_2 if the reaction additionally reduces the rutile product. Yields were calculated using the n_w value calculated from the water release phase results.

To understand how the yield varied during the reaction, the quantity of water that was being produced was equated to the amount of hydrogen removed from the system, as hydrogen converts to water in a 1:1 reaction. Therefore, n_h was used as a proxy for n_w. The extent of the reduction reaction, ξ, was calculated using Equation 3.7 in Chapter 3.

The uncertainty in water production rate, total water produced, oxygen yield, and reduction extent were calculated from the propagation of uncertainties in the measured sample mass, pressure, operational volume, and internal manifold temperature values (± 0.5 mg, ± 0.5 mbar, ± 1.49 $\times 10^{-7}$ m^3, and ± 2.5 °C respectively. See Chapter 4).

5.2.3 Sample analysis

Samples of $\sim$ 15 mg of unreacted and reacted ilmenite were analysed using the SEM as in Section 3.4.3 in Chapter 3 to identify how far the reaction had progressed through the ilmenite grains by identifying reactants and products. To better understand the mineral changes that occurred in the reacted ilmenite grains, XRD analyses were carried out at the Natural History Museum, UK, with the assistance of J. Najorka. The analyses were performed on $\sim$ 5 mg ($\sim$ 11 %) of each ilmenite sample to identify reaction products and confirm depletion in the reactant mineral. The XRD analysis was performed using an Enraf-Nonius Powder Diffraction System 120 utilising a CoKa1 radiation source.

5.3 Results

5.3.1 Reaction temperature

The pressure profiles recorded during the reaction phase are shown in Figure 5.2a. The change in pressure was greater for higher temperatures, indicating the reaction proceeded at a faster rate. A small drop in pressure (k_T corrected to 6.1 mbar) was recorded in the blank reading which was presumed to be the result of impurities in the hydrogen supply caused by inefficient seals. The initial pressure (P_{H2i}) and corrected pressure change (ΔP_{cr}) in the system are recorded in Table 5.2 for each experiment, along with the calculated amount of hydrogen used in the reaction (n_h). The water production rates during each hour of the reaction phase is shown in Table 5.3. The water production rate increased with temperature where the maximum rate was achieved at a furnace temperature of 1100 °C with a peak of 36.1 $\pm$ 0.5 μmol·hr^{-1}. The reaction rate does not appear to have significantly changed across the four hour reaction time at each temperature suggesting the reaction was not near completion.

The pressure rise from the water release phase is shown in Figure 5.2b. The results show that more water was released from the cold finger for reactions that occurred at higher temperatures. The corrected pressure change for the water release phase (ΔP_{cw}) and the calculated amount of water released (n_w) are shown in Table 5.4. The discrepancy between the amount of hydrogen used in the reaction and the amount of water released from the cold finger (n_h-n_w) is also shown, along with the calculated yield and reduction extent (ξ). The reaction proceeded further at higher temperatures resulting in higher yields. The sample reacted at a temperature of 1100 °C produced the highest yield at 4.42 $\pm$ 0.06 wt % oxygen

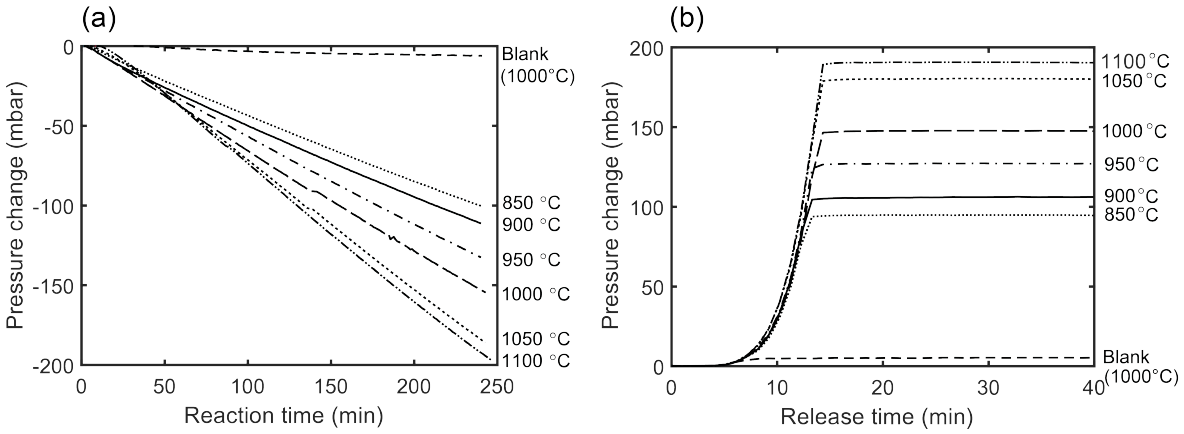

Figure 5.2: Pressure changes during (a) the ilmenite reduction reaction phase, and (b) the corresponding water release phase, for furnace temperatures of 850 °C to 1100 °C. The uncertainty in pressure readings is ± 0.5 mbar.

Furnace temperature (°C)	P_{H2i} (mbar)	ΔP_{cr} (mbar)	n_h (μmol)
850 ± 5	453.3 ± 0.5	-99.3 ± 0.5	66.5 ± 0.7
900 ± 5	417.1 ± 0.5	-110.6 ± 0.5	74.0 ± 0.8
950 ± 5	419.6 ± 0.5	-133.2 ± 0.5	89.2 ± 0.9
1000 ± 5	418.4 ± 0.5	-156.0 ± 0.5	104.5 ± 1.0
1050 ± 5	475.9 ± 0.5	-185.8 ± 0.5	126.0 ± 1.2
1100 ± 5	449.0 ± 0.5	-202.1 ± 0.5	135.4 ± 1.3

Table 5.2: Results from the reduction reaction phase of the temperature studies. Pressure changes during the reaction were used to calculate the amount of H_2 reacted.

Furnace temperature (°C)	Water production rate (μmol hr^{-1})			
	0-1 h	1-2 h	2-3 h	3-4 h
850 ± 5	17.3 ± 0.4	16.2 ± 0.4	16.4 ± 0.4	16.7 ± 0.4
900 ± 5	20.4 ± 0.4	17.7 ± 0.4	17.8 ± 0.4	18.1 ± 0.4
950 ± 5	22.3 ± 0.4	22.0 ± 0.4	22.2 ± 0.4	22.7 ± 0.4
1000 ± 5	25.4 ± 0.4	26.3 ± 0.4	26.2 ± 0.4	26.5 ± 0.4
1050 ± 5	25.2 ± 0.4	32.8 ± 0.5	34.4 ± 0.5	33.7 ± 0.5
1100 ± 5	29.5 ± 0.4	36.1 ± 0.5	34.6 ± 0.5	35.1 ± 0.5

Table 5.3: Water production rates as determined from the depletion of hydrogen for ∼ 45 mg samples of ilmenite reacted under different furnace temperature conditions. Values were calculated for each hour of reduction from the corrected pressure data obtained during the reaction phase.

with the maximum extent of the reduction reaction calculated as 42.0 ± 0.6 %. However, the amount of water that was unaccounted for from the yields was higher when the reaction rate was higher, as shown by the increase in n_h-n_w.

To confirm that water was being produced and condensed during the reaction, a mass spectrum of the produced volatiles was obtained and plotted alongside the temperature profile of the cold finger (Figure 5.3). A distinct increase in the intensity of certain m/z values was evident as the cold finger temperature rose. The gas released upon heating the cold finger appeared to be predominantly water, on account of the detection of m/z 16, 17, and 18. There was also some residual hydrogen (m/z 1 was measured as the m/z 2 reading was unstable), and some nitrogen detected (m/z 28). The nitrogen was assumed to be caused by residual atmospheric gas trapped within the capillary. The results were not corrected for relative sensitivity factors (RSF) and should therefore not be used for quantitative analysis.

BSE images of example grains from the samples reacted at a furnace temperature of 1000 °C, 1050 °C, and 1100 °C are shown in Figure 5.4. The grains shown were selected as they represent the majority of grains imaged in each sample. The greyscale contrast shows where the light grey ilmenite reduced to form the darker grey rutile and the bright white iron. For all reacted grains, the iron formed significantly larger deposits (iron blebs on average at least double in size) compared to the lower temperature and shorter reaction times applied in Chapter 3. For the 1000 °C sample it can be seen that voids were formed, a consequence of mass loss as oxygen was removed from the sample, as the reaction proceeded towards the middle of the grains. At 1050 °C, the reaction proceeded further into the grain and the rutile products appear to have formed vein-like features. Meanwhile, at 1100 °C a titanium enriched solid solution formed within the grain (later identified as ferrospeudobrookite through XRD analysis), often with a small unreacted core of ilmenite. Rutile was rare or absent, while the presence of metallic iron was clearly seen as bright features on the exterior grain surface as well as within the grain.

XRD was performed on samples reacted at 1000 °C, 1050 °C, and 1100 °C to identify the phase of the minerals of the reacted grains (Figure 5.5). For the 1000 °C sample all peaks can be explained by the presence of ilmenite, and the reduction products iron and rutile, indicating the sample was partially reduced. Meanwhile the 1100°C sample produced peaks that indicate the presence of ferropseudobrookite ($FeTi_2O_5$), along with iron, rutile, and ilmenite. The 1050 °C sample was mostly composed of ilmenite and its standard reduction products, rutile and iron, however there was also evidence to suggest that ferropseudobrookite was starting to form.

Furnace temperature (°C)	ΔP_{cw} (mbar)	Calculated H_2O released (μmol)	n_h-n_w (μmol)	O_2 yield (wt.% O_2)	ξ (%)
850 ± 5	89.7 ± 0.5	60.1 ± 0.7	6.4 ± 1.4	2.14 ± 0.03	20.3 ± 0.3
900 ± 5	101.0 ± 0.5	67.7 ± 0.7	6.4 ± 1.5	2.41 ± 0.04	22.9 ± 0.4
950 ± 5	122.1 ± 0.5	81.8 ± 0.8	7.4 ± 1.7	2.91 ± 0.04	27.6 ± 0.4
1000 ± 5	142.7 ± 0.5	95.6 ± 1.0	8.9 ± 2.0	3.40 ± 0.05	32.3 ± 0.5
1050 ± 5	175.3 ± 0.5	117.4 ± 1.1	8.6 ± 2.4	4.17 ± 0.06	39.7 ± 0.6
1100 ± 5	185.6 ± 0.5	124.3 ± 1.2	11.1 ± 2.5	4.42 ± 0.06	42.0 ± 0.6

Table 5.4: Results from the water release phase of the temperature experiments. The baseline corrected pressure rise from the release of water from the cold finger was used to calculate the amount of H_2O produced, and therefore the yield and reduction extent.

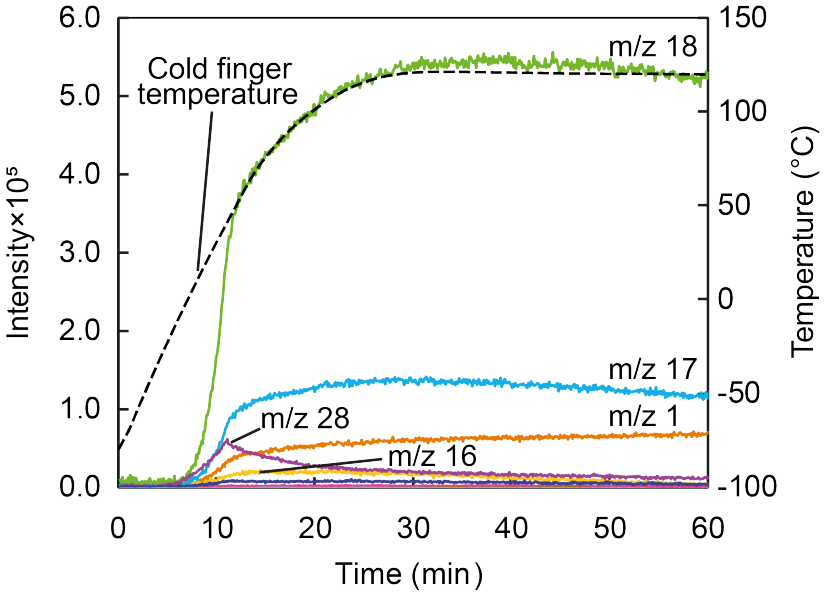

Figure 5.3: Baseline corrected mass spectrum data recorded during a second water release phase following the reduction of ilmenite. Spectra that showed a non-negligible change in intensity are labelled.

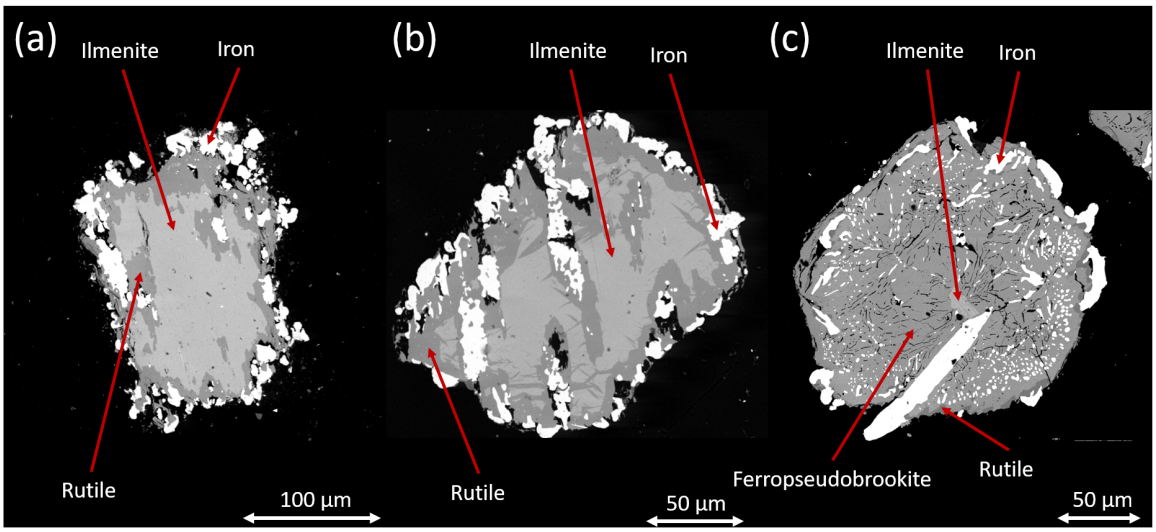

Figure 5.4: BSE images of ilmenite grains reduced in the presence of hydrogen for four hours at furnace temperatures of (a) 1000 °C,(b) 1050 °C,(c) 1100 °C. The reduction extent for each grain has been calculated as 32.3 ± 0.5 %, 39.7 ± 0.6 %, and 42.0 ± 0.6 % respectively.

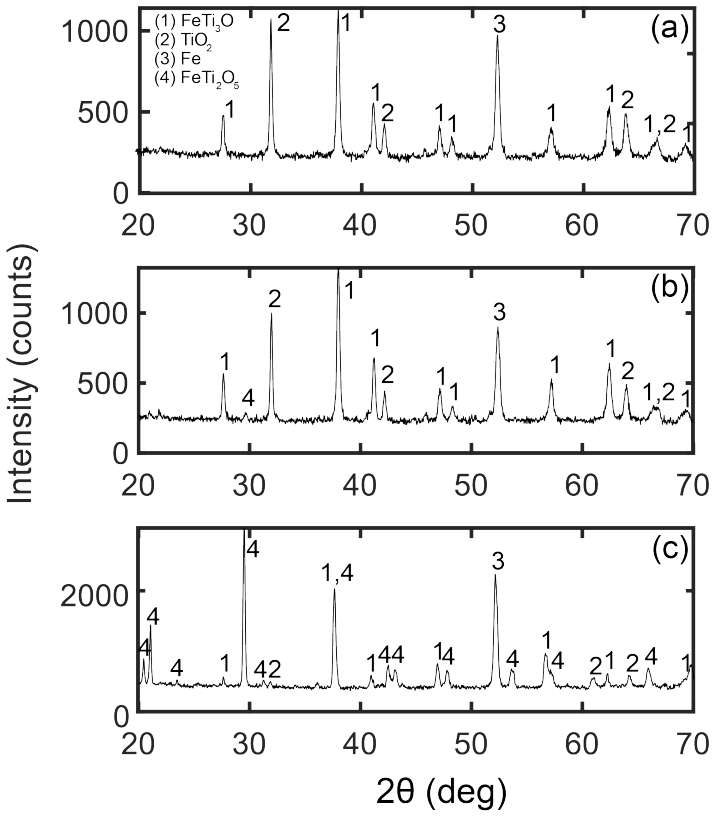

Figure 5.5: XRD analysis of ilmenite samples reacted in a furnace operating at (a) 1000 °C, (b) 1050 °C, and (c) 1100 °C in the temperature study. All peaks are labelled to their corresponding mineral.

5.3.2 Hydrogen pressure

The pressure change in the system during the reaction phase is shown in Figure 5.6a for each of the H_2:$FeTiO_3$ (n_h:n_{ilm}) concentrations considered (0.28:1.00, 0.50:1.00, 0.83:1.00, 0.99:1.00, and 1.38:1.00). The initial pressure and change in pressure is shown in Table 5.5, along with the calculated quantity of hydrogen reacted, n_h. In the first hour of the reaction the lower the initial hydrogen pressure, the more water produced and condensed. However, as the hydrogen supply was depleted the reaction rate slowed significantly, and relatively quickly, for the lower H_2 concentrations. For example, in the first hour the greatest pressure drop, and therefore the greatest production of water, resulted from a 0.28:1.00 ratio of n_h:n_{ilm} (P_{H2i} = 118 mbar). However, as the reaction proceeded past 80 minutes, higher pressures of hydrogen were required to sustain faster reaction rates. As the n_h:n_{ilm} concentration exceeded 0.99:1 to 1.38:1.00, the reaction rate was not improved within an experimental time of four hours (i.e. higher pressures did not result in higher reaction rates in four hours).

The water production rates during each hour of the reaction phase is shown in Table 5.6. The water production rate varied throughout the reaction. In the first hour, lower pressures of hydrogen were desirable resulting in water production rates of up to 30.2 ± 0.4 μmol·hr^{-1}

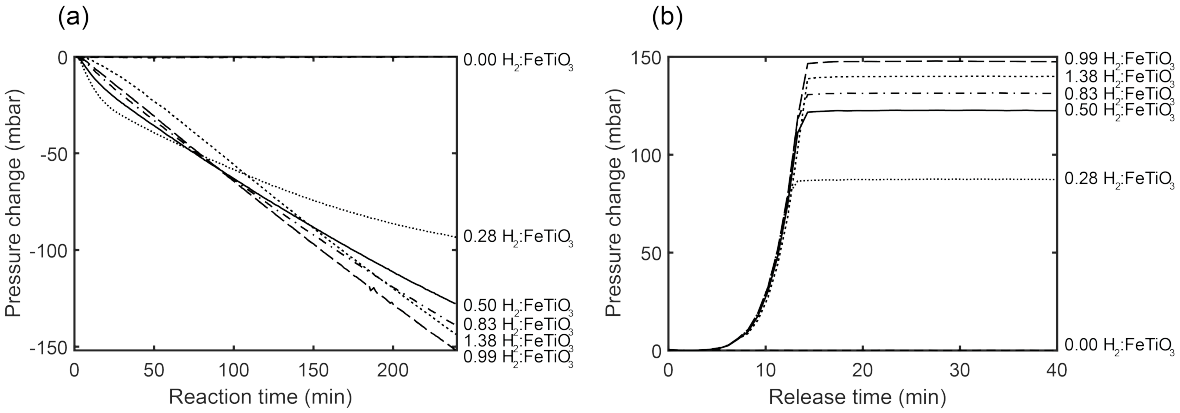

Figure 5.6: Pressure changes during (a) the ilmenite reduction reaction phase, and (b) the corresponding water release phase, for various initial H_2:$FeTiO_3$ concentrations. Results shown are not corrected for the blank reading. The uncertainty in pressure readings is ±0.5 mbar.

n_h:n_{ilm}	P_{H2i} (mbar)	ΔP_{cr} (mbar)	n_h (μmol)
0.28:1.00	117.8 ± 0.5	-98.1 ± 0.5	65.7 ± 0.7
0.50:1.00	209.7 ± 0.5	-135.8 ± 0.5	91.0 ± 0.9
0.83:1.00	345.2 ± 0.5	-147.9 ± 0.5	99.0 ± 1.0
0.99:1.00	418.4 ± 0.5	-162.2 ± 0.5	108.6 ± 1.1
1.38:1.00	584.1 ± 0.5	-153.1 ± 0.5	102.6 ± 1.0

Table 5.5: Results from the reduction reaction phase of the hydrogen concentration studies. Pressure changes during the reaction were used to calculate the amount of H_2 reacted.

n_h:n_{ilm}	Water production rate (μmol hr^{-1})			
	0-1 h	1-2 h	2-3 h	3-4 h
0.28:1.00	30.2 ± 0.4	15.5 ± 0.4	11.5 ± 0.3	8.4 ± 0.3
0.50:1.00	29.0 ± 0.4	22.4 ± 0.4	20.1 ± 0.4	19.4 ± 0.4
0.83:1.00	27.3 ± 0.4	25.3 ± 0.4	23.2 ± 0.4	23.2 ± 0.4
0.99:1.00	26.1 ± 0.4	28.0 ± 0.4	27.1 ± 0.4	27.4 ± 0.4
1.38:1.00	20.3 ± 0.4	27.7 ± 0.4	27.1 ± 0.4	27.4 ± 0.4

Table 5.6: Water production rates as determined from the depletion of hydrogen for ∼45 mg samples of ilmenite reacted under different hydrogen concentration conditions. Values were calculated for each hour of reduction from the corrected pressure data obtained during the reaction phase.

n_h:n_{ilm}	ΔP_{cw} (mbar)	Calculated H_2O released (μmol)	n_h-n_w (μmol)	O_2 yield (wt % O_2)	ξ (%)
0.28:1.00	87.4 ± 0.5	58.5 ± 0.6	7.2 ± 1.3	2.08 ± 0.03	19.8 ± 0.3
0.50:1.00	122.5 ± 0.5	82.1 ± 0.8	8.9 ± 1.7	2.92 ± 0.04	27.7 ± 0.4
0.83:1.00	131.2 ± 0.5	87.9 ± 0.9	11.2 ± 1.9	3.12 ± 0.05	29.7 ± 0.4
0.99:1.00	147.5 ± 0.5	98.8 ± 1.0	9.8 ± 2.0	3.51 ± 0.05	33.4 ± 0.5
1.38:1.00	139.8 ± 0.5	93.7 ± 0.9	8.9 ± 1.9	3.33 ± 0.05	31.6 ± 0.5

Table 5.7: Results from the water release phase of the hydrogen concentration experiments. The baseline corrected pressure rise from the release of water from the cold finger was used to calculate the amount of H_2O produced, and therefore the yield and reduction extent.

when the ilmenite was exposed to an initial pressure of 118 mbar of hydrogen (0.28:1 n_h:n_{ilm}). As the reaction proceeded into the fourth hour, the studies in which higher initial hydrogen pressures were used resulted in the highest water production rates of 27.4 ± 0.4 μmol·hr^{-1} for the studies using both 418 mbar and 584 mbar of hydrogen (0.99:1 and 1.39:1 n_h:n_{ilm} respectively).

The pressure changes recorded during the water release phase are shown in Figure 5.6b, which shows that after four hours the greatest production of water occurred as a result of a 0.99:1 concentration of n_h:n_{ilm} (418 mbar). The pressure data for the water release phase is shown in Table 5.7, along with the calculated yields and the difference between the hydrogen used in the reaction and the water collected at the cold finger (n_h-n_w). The final reduction extent of the reaction is also shown. The maximum final yield for this setup after a four hour reaction at a furnace temperature of 1000 °C and a hydrogen pressure of 418 mbar was 3.51 ± 0.05 wt % oxygen, where the reaction was 33.4 ± 0.5 % complete. The n_h-n_w values generally aligned with the calculated yields, i.e. the higher the reaction rate, the more water that was unaccounted for.

5.4 Discussion

5.4.1 Temperature effects

It is often stated that ilmenite reduction can be performed at temperatures of up to 1100 °C, particularly in work relating to ISRU applications (e.g. Gibson and Knudsen, 1985; Li et al., 2012; Taylor and Carrier, 1993; Zhao and Shadman, 1993). The temperature studies performed using a static setup in this work, and those in the wider literature which utilise gas flowing systems (Li et al., 2012; Zhao and Shadman, 1993), show that with increasing furnace temperature from 850 to 1100 °C the reaction rate increases and yields higher quantities of water. Ilmenite grains reacted in this work showed some evidence of melting within the grains at 1100 °C, although not sufficiently to decrease the yields (melting can close pore spaces for gas transport, causing the reaction rate to decrease). The temperatures experienced by the samples were lower than those measured at the furnace by as much as 50 °C (Section 4.2.2 in Chapter 4), therefore melting of the ilmenite grains (melting temperature of ilmenite is 1050 °C) would be expected to occur at a furnace temperature of ∼ 1100 °C. As a result of the lower sample temperatures, the furnace temperature should be interpreted as an upper constraint on the reaction temperature for given yields.

SEM and XRD analysis of the sample reacted at a furnace temperature of 1100 °C indic-

ated the formation of ferrospeudobrookite, $FeTi_2O_5$, suggesting a different reaction had taken place as compared to Eqn. 1.2 in Chapter 1. Ferropseudobrookite is isostructural with armalcolite, $(FeMg)Ti_2O_5$, and pseudobrookite, Fe_2TiO_5 and is known to form at low pressures and oxygen fugacities (Lindsley et al., 1974) which are also the conditions of the experiments in this study. Wang et al. (2009) reported an increase in pseudobrookite formation with increasing temperature when reducing ilmenite. The reaction process outlined in Eqn. 5.2 has been considered to explain the production of ferropseudobrookite as part of the reduction reaction.

$$3FeTiO_{3(s)} + 2H_{2(g)} \rightleftharpoons 2Fe_{(s)} + TiO_{2(s)} + 2H_2O_{(g)} + FeTi_2O_{5(s)} \tag{5.2}$$

This process is a subsolidus reaction occurring at grain temperatures of at least 1050 °C (Lindsley et al., 1974) and was demonstrated by Si et al. (2012) where the production of a M_3O_5-type solid solution was recorded, where M represents the elements Mg, Ti, and Fe. A different ratio of n_h:n_{ilm} is required for the reaction to proceed to the right as written as compared to Eqn. 1.2, meaning more ilmenite is required to produce the equivalent amount of water. There was no indication of a secondary reduction step where rutile reduced to a less oxidised state such as Ti_3O_5 (Bardi et al., 1987) supporting the literature which states that TiO_2 will only begin to reduce when all the ilmenite present has reduced (Zhao and Shadman, 1993).

5.4.2 Hydrogen pressure effects

Hydrogen pressures in the system appear to have a two-fold effect on the reaction. At the start of the reaction, lower pressures resulted in the highest rates of water production. The model of Altenberg et al. (1993) showed that lower hydrogen pressures equated to an increase in the equilibrium constant and therefore greater yields. However, after one hour, the highest rates of water production were measured at higher pressures. Hegde et al. (2011) noted similar results when reducing NU-LHT-2M, a lunar highland simulant, at pressures of 1 and 3 atm (1.01 & 3.04 bar respectively) in a gas flow system. A proposed model suggesting how hydrogen pressure affects the diffusion of gases within the grains, and therefore reaction rate, is shown in Figure 5.7. There are various pathways for gases to diffuse through minerals to enable the reduction reaction to continue to produce water. Such pathways include the movement of vacancies within the mineral structure or via movement through the interstitial structure (Watson and Baxter, 2007). However, when reduction of the outer ilmenite grain

occurs, the mineral structure loses mass and voids form which facilitate further movement of gases into and out of the grain (Figure 5.4a) as seen in Dang et al. (2015) and Li et al. (2012). As the reaction proceeds to the interior of the grain, the reaction rate slows, suggesting that the diffusion of gases through the grain is the rate controlling step. A batch mode process which implements low pressures at the start of the reaction and higher pressures as the reaction proceeds would be worth further investigation.

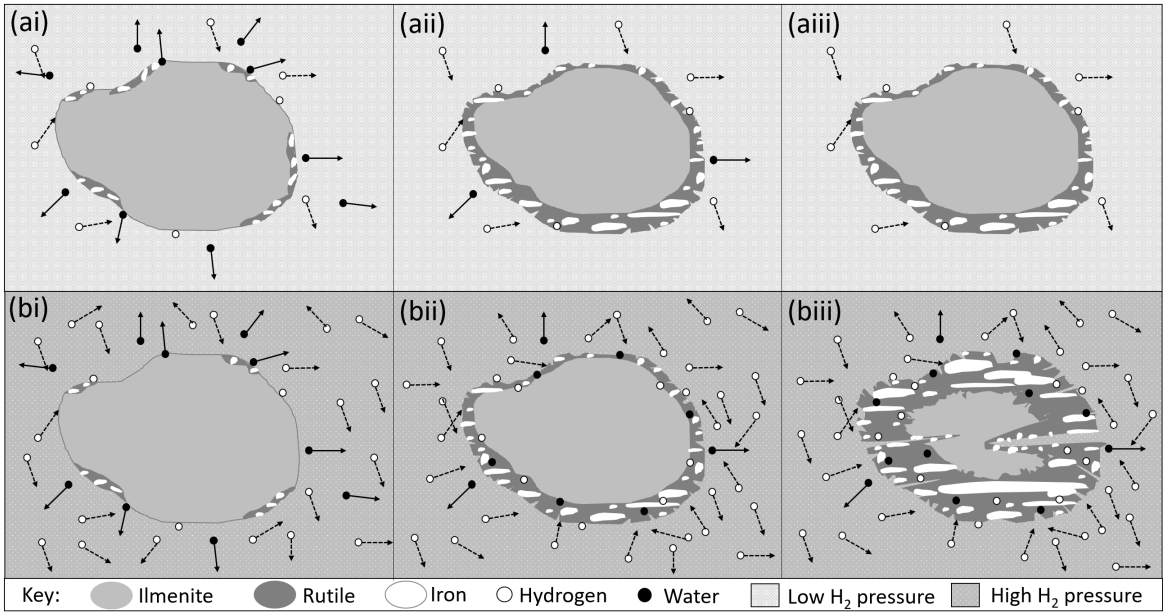

Figure 5.7: Diagram showing the effects of low (a) and high (b) hydrogen pressure on the reaction rate during the reduction of ilmenite. For low pressures, at the start of the reaction (ai) the hydrogen can react with the readily available ilmenite on the surface of unreacted grains. The produced water can easily diffuse away from the reaction site enabling fast reaction rates. As the reaction proceeds (aii), a reacted rim forms around the grain. At low pressures, hydrogen cannot easily penetrate the reaction rim into the unreacted core (aiii), and so the reaction rate slows. For high hydrogen pressures, at the start of the reaction (bi), the hydrogen readily reacts with the ilmenite at the surface of the grains. However, the produced water must diffuse away from the reaction site through high pressures of hydrogen and so the water takes longer to leave the reaction site as compared to low hydrogen pressures. As the reaction proceeds (bii), a reacted rim forms around the grain. At higher hydrogen pressures, the hydrogen can more easily penetrate through the reacted rim (biii), enabling further reduction of the interior ilmenite.

5.4.3 Water losses

In both the temperature studies and the hydrogen pressure studies, the amount of hydrogen that was reacted in each experiment was more than the amount of water collected at the cold finger. The amount of water that was unaccounted for (n_h-n_w) generally increased with reaction rate, and therefore, yield (Figure 5.8). A fraction of the produced water is assumed to have remained within the grains when the reaction was stopped after four hours (before complete reduction had occurred). When the reaction rate was higher, more water

was produced per unit time in each grain. Therefore, there would be higher concentrations of residual water 'trapped' within grains that experienced faster reaction rates (Figure 5.9).

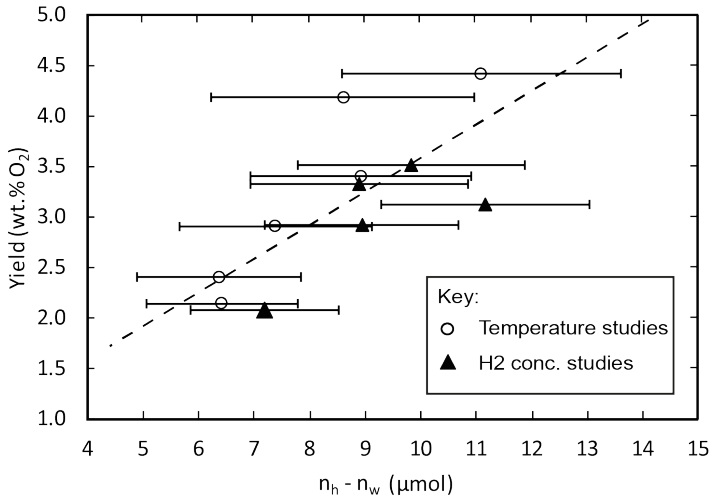

Figure 5.8: A plot showing the discrepancy between the amount of hydrogen used in the reaction and the amount of water released from the cold finger (n_h-n_w), against the calculated yields. Results are shown for all experiments from the temperature studies and the hydrogen pressure studies. Uncertainty in yield is < 0.1 wt %.

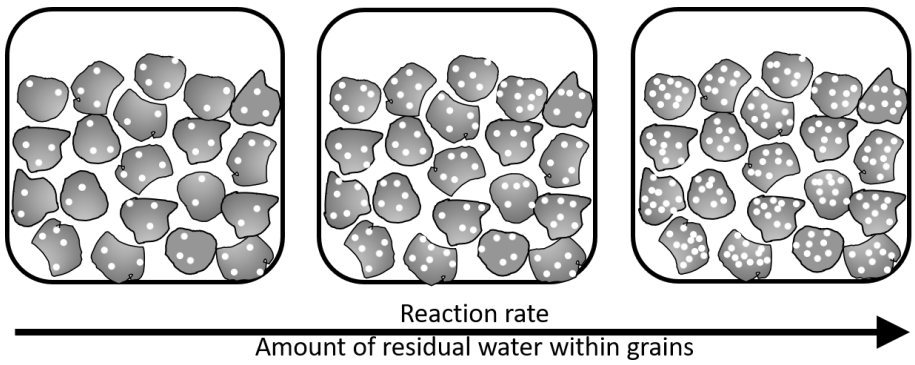

Figure 5.9: Diagram showing residual water molecules (white spots), that remain within reacting ilmenite grains when the reaction is halted before completion. When the reaction rate is higher, as a result of optimised temperature and hydrogen pressure conditions, more water molecules remain within the grains.

5.4.4 Considerations for lunar experiments

The ilmenite used in this work is of terrestrial origin. Terrestrial ilmenite has ~ 2 % magnesium in the mineral structure, compared to ~ 6 % for lunar ilmenite. Iron oxides reduce more readily than magnesium-oxides (Schlüter and Cowley, 2020), therefore terrestrial ilmenite would reduce to produce more water per unit weight compared to lunar ilmenite (Deer et al., 1992). Considering the small quantities of ilmenite expected in the bulk lunar material which can be as low as < 1 wt % in lunar highlands (Simon et al., 1982), and only a small discrepancy in iron oxide content in the mineral structure, it is assumed that terrestrial

ilmenite is a suitable proxy for lunar ilmenite in this study.

At the time of writing, the maximum temperature of the furnace ovens on ProSPA is 1000 °C, and so the optimised temperature for reduction reactions with ProSPA was selected to be 1000 °C. The optimum hydrogen pressure trialled was 418 mbar which equated to a 0.99:1.00 n_h:n_{ilm} ratio in the ISRU-BDM system. However, the optimal pressure in the ISRU-BDM will equate to a different n_h:n_{ilm} ratio in ProSPA as the operational volume will be different. If the molar quantity of H_2 in the operational volume of ProSPA is greater than the amount of reducible iron oxides present, then the procedure will be sufficient to reduce the sample. However, if the molar quantity of H_2 is not sufficient to reduce the sample then a batch mode would be recommended to ensure that enough hydrogen is added to the system without greatly exceeding the ideal pressure of $\sim$ 418 mbar. Once the ProSPA operational volume is finalised, the appropriate approach can be determined to optimise yields. However, if the purpose of the reduction experiments with ProSPA is to simply successfully produce water from lunar minerals then optimal yields may not be necessary and the batch mode approach may not be necessary.

5.5 Conclusions

In this study, ilmenite, a common lunar mineral, was reduced with hydrogen in the ISRU-BDM. Various furnace temperatures (850 to 1100 °C) and hydrogen pressures (118 to 584 mbar) were trialled in order to optimise the reaction procedure. Greater furnace temperatures resulted in greater yields, where a furnace temperature of 1100 °C resulted in an alternative reaction process with the formation of ferropseudobrookite. 1000 °C was identified as the optimal temperature for the reduction experiments as it is within the operational constraints of ProSPA. Hydrogen pressure has varying effects on the reduction reaction when reducing ilmenite at a furnace temperature of 1000 °C. Lower hydrogen pressures showed greater reaction rates in the first hour of the reaction, as the rate limiting step was determined to be the diffusion of water away from the ilmenite grains towards the cold finger. However, as the reactions proceeded, the rate limiting step was determined to be gas diffusion through the reacted rim of the grain. In a four hour period, the optimum hydrogen pressure that was trialled was identified to be 418 mbar, which equated to a 0.99:1.00 ratio of hydrogen to ilmenite in the ISRU-BDM system.

With the optimised procedure, a maximum yield of 3.51 $\pm$ 0.05 wt % O_2 can be produced from 95 % pure ilmenite. As lunar material contains only a fraction of ilmenite, the possible

yields that could be obtained with ProSPA on the lunar surface will be significantly smaller than that recorded with ilmenite alone. However, other lunar minerals may also reduce in the presence of hydrogen to produce water. To identify the potential yields of reduction experiments on the lunar surface, further studies are required using the optimised procedure to reduce lunar simulants and samples with the ISRU-BDM.

Chapter 6

Extraction of water from lunar simulant and samples

6.1 Introduction

The reduction by hydrogen technique trialled in the ISRU-BDM, as described in Chapter 5, successfully produced measurable quantities of water from ilmenite. The reaction conditions and procedure were optimised to produce the highest yields within the constraints of the ProSPA operating parameters. Next, experiments were performed with lunar-like and actual lunar samples. The samples follow a progression from lunar simulant to lunar meteorites, and ultimately to Apollo lunar soils which are increasingly representative of the lunar material expected to be analysed by ProSPA. Following successful experiments with a lunar simulant, lunar meteorite was used next to ensure that the technique is feasible on relatively less precious lunar material before analysis of Apollo samples was deemed appropriate. Each sample was evaluated for its suitability as a proxy for the expected material that will be sampled and studied with ProSPA on the lunar surface. The samples were then reduced with hydrogen, following the optimal reaction procedure from Chapter 5, in order to evaluate the scientific merits of performing such experiments on the Moon with a ProSPA-like instrument.

In the work described in this chapter the selected lunar simulant and samples were reacted in the ISRU-BDM to determine whether the reaction rates are sufficient to produce measurable yields of water within the four hour timescale of ProSPA experiments, and therefore are feasible for use with ProSPA on the lunar surface.

6.2 Material selection

6.2.1 Lunar simulant

The lunar simulant used in this work is the lunar highland simulant NU-LHT-2M. The simulant approximates the average bulk chemical composition of Apollo 16 regolith, and was created by Zybek Advanced Products Inc. using materials mostly sourced from Stillwater Mine in Nye, Montana (Manick et al., 2018). The simulant is designated 'M' (medium) as it has a grain size of < 1 mm. A particular benefit of the Stillwater Mine material is that it contains high-calcium plagioclase which is abundant on the Moon yet rarely found in bulk on Earth (Rickman et al., 2014). The NU-LHT-2M simulant generally approximates lunar highlands soils in terms of the bulk mineralogy, presence of agglutinates, and grain size (Rickman and Lowers, 2012; Zeng et al., 2010), and is arguably better suited for chemical reduction tests than other available highland simulants such as EAC-1 which do not replicate the aforementioned lunar regolith properties as well (Engelschiøn et al., 2020). The main differences between NU-LHT-2M and lunar regolith are the geotechnical properties which are related to weathering processes on the Moon that are difficult to replicate on Earth such as space weathering. As a result, NU-LHT-2M like most simulants cannot replicate the highly angular particle shapes found in lunar soils which affects cohesion and specific gravity (Zeng et al., 2010).

Generally, the grains are monomineralic (Rickman and Lowers, 2012), i.e. formed of one mineral. A small fraction of the grains include multi-phase minerals which can include combinations of plagioclase, pyroxene, and olivine. The simulant also contains synthetic agglutinates, made from partially and fully melted material (Zeng et al., 2010). The ilmenite grains in the simulant contain some pyrophanite ($MnTiO_3$), the manganiferous endmember of the solid solution series which is less susceptible to reduction. Although there is minimal ilmenite concentrations, NU-LHT-2M contains significant quantities of pyroxene and olivine totalling 15.7 vol. % (Rickman and Lowers, 2012) which are other FeO bearing minerals (Massieon et al., 1993, 1992). Similarly, the glass present in the simulant also contains some iron oxides (Stoeser et al., 2010). Therefore, there are multiple other components of the simulant that could be reduced in the presence of hydrogen to produce water, with ilmenite being the most easily reduced.

Chemical	Concentration (wt %)			
	NU-LHT-2M	NWA 12592	10084	60500
Al_2O_3	23.62 ± 0.34	26.18 ± 0.38	13.67 ± 0.27	26.43 ± 0.64
CaO	13.33 ± 0.42	16.13 ± 0.66	12.10 ± 0.45	15.59 ± 0.28
Fe_2O_3	4.03 ± 0.50	4.37 ± 0.13	*17.59 ± 0.52*	*6.24 ± 0.31*
FeO	*3.59 ± 0.44*	*3.89 ± 0.11*	15.66 ± 0.47	5.56 ± 0.27
K_2O	0.08 ± 0.01	-	0.14 ± 0.02	0.12 ± 0.01
MgO	8.18 ± 0.22	6.52 ± 0.20	7.87 ± 0.15	6.15 ± 0.35
MnO	0.07 ± 0.01	0.06 ± 0.01	0.21 ± 0.01	0.07 ± 0.01
Na_2O	1.44 ± 0.01	0.30 ± 0.05	0.44 ± 0.04	0.44 ± 0.04
P_2O_5	0.07 ± 0.01	0.05 ± 0.01	0.14 ± 0.08	0.11 ± 0.03
SiO_2	48.00 ± 0.64	44.60 ± 0.96	42.48 ± 0.20	45.20 ± 0.20
TiO_2	0.37 ± 0.02	0.17 ± 0.01	7.66 ± 0.65	0.60 ± 0.02
Total	99.2	98.4	100.4	100.3

Table 6.1: Chemical composition of NU-LHT-2M, NWA 12592, 10084, and 60500. The NU-LHT-2M and NWA 12592 data was determined from IC-PMS of three repeats, with uncertainty given as 1 SD. The 10084 and 60500 data are taken as the average of multiple analyses as compiled by Meyer (2009, 2010), with uncertainties given as 1 SD of all results. Values in italics are recalculations from the given iron oxide measurements.

6.2.2 Lunar meteorite

The lunar meteorite selected for analysis is NWA 12592. The meteorite comprises lithic clasts which are dominated by pyroxene and plagioclase with minor olivine components, with the mineral clasts mainly comprising olivine, plagioclase, chromite, troilite, and Fe-Ni phases (Meteoritical Bulletin Database, 2019). Bulk-rock analysis of the meteorite was performed by E. Humphreys-Williams and B. Schmidt using ICP-MS, and the results are shown in Table 6.1. The meteorite has an FeO content of 3.89 ± 0.11 wt % (recalculated from the measured Fe_2O_3 content). The TiO_2 content is very low at 0.17 ± 0.01 wt % (Table 6.1), supporting the conclusion of no ilmenite present (although stoichiometrically there is potential for 0.32 wt % ilmenite to be present). The iron oxide content is therefore attributed to the pyroxene and olivine present.

NWA 12592 is a 'find' and has experienced moderate weathering (Meteoritical Bulletin Database, 2019). Weathering causes the formation of terrestrial alteration products such as secondary carbonates and iron hydroxides on the surface of meteorites (Ali et al., 2016; Martins et al., 2007). If left untreated, these secondary iron oxides could also be reduced in the following reduction experiments giving higher yields. To limit the effects of weathering products on the final yield, some of the meteorite samples were pretreated to remove secondary oxides. The meteorite samples are herein denoted as untreated and treated.

6.2.3 Apollo soils

Two Apollo soils were selected for use in this work, 10084 and 60500. Soil 10084 is the $\leq$ 1 mm sieve fraction of a contingency sample collected during Apollo 11. It was formed through impacts of meteorites on fine-grained basalt and breccia (Carrier, 1973; Heiken, 1975), resulting in agglutinates, multi-phase grains, and glassy particles. The mature soil mostly comprises glass, plagioclase, pyroxene, olivine and ilmenite, and has a relatively high FeO content of 15.66 $\pm$ 0.47 wt % and TiO_2 content of 7.66 $\pm$ 0.65 wt % (Meyer, 2009) (Table 6.1). Based on the bulk TiO_2 content, the ilmenite present would be found in concentrations of up to 14.55 wt %. The Apollo 11 soil should therefore be highly suitable for reduction with hydrogen to produce water.

In comparison, 60500 is a $\leq$ 1 cm sieve fraction of a rake sample collected during Apollo 16. Like 10084, the soil samples obtained during the Apollo 16 mission mostly comprise glassy agglutinates and multi-phase grains with plagioclase, pyroxenes, and olivine (The Lunar Sample Preliminary Science Team, 1972). The FeO content of 60500 is 5.56 $\pm$ 0.27 wt %, which is relatively low compared to most Apollo soils (Meyer, 2010). The low TiO_2 content of 0.60 $\pm$ 0.02 wt % (Table 6.1) indicates particularly low levels of potential ilmenite (up to 1.14 wt %) in the soil and is expected to produce significantly lower yields than the 10084 soil.

6.3 Methodology

Each material (simulant, meteorite, and lunar soils) was analysed, prepared, and reacted in triplicate. The sample preparation process varied slightly between each material and is discussed in more detail in the relevant sections. Details of the bake-out test applied to each sample type, the experimental procedure applied to all samples, and the data and sample analysis performed after each series of experiments is outlined here.

6.3.1 Bake-out

A bake-out test was performed on one sample of each of the selected materials (simulant, untreated meteorite, treated meteorite, Apollo 11 soil, and Apollo 16 soil) prior to each series of experiments to ensure the bake-out procedure was suitable for each material. A successful bake-out should demonstrate that loosely bound and adsorbed volatiles are removed before the reduction reaction, so that pressure changes during the following experiments can be associated with the reduction process only. It has been shown that loosely adsorbed volatiles

can be removed from the NU-LHT-2M simulant at temperatures up to 300 °C, however, volatiles can be released at higher temperatures as a result of mineral decomposition. Reiss et al. (2019) showed that water is released from NU-LHT-2M at temperatures of ∼ 650 °C, on account of water-bearing minerals produced during hydrothermal alteration of the simulant source material being present (Rickman and Lowers, 2012; Street Jr et al., 2010). There is likely no significant quantities of lunar water to be released from the lunar meteorite or the Apollo samples as they originate from the relatively dry Moon. To account for any terrestrial hydration or mineral decomposition, a bake-out procedure at 800 °C in the ISRU-BDM was performed on each material type as follows:

1. Heated box set to 120 °C overnight for manifold to reach uniform temperature.
2. 45 mg of sample placed in a clean ceramic tube and placed inside the furnace, attached at valve 7 (see Figure 4.1 in Chapter 4).
3. Valves 1-7 opened to remove any volatiles from the system via the vacuum pump.
4. Mass spectrometer begins to record spectra in multiple ion detection (MID) mode analysing m/z 1-50.
5. Furnace is heated to 800 °C.
6. Mass spectrometer readings recorded for three hours.

The spectra of interest produced from the bake-out procedures can be seen in Figure 6.1. The volatiles H_2 (m/z 1 measured here as m/z 2 measurements were unstable), O_2 (m/z 16 & 32), H_2O (m/z 17 & 18), N_2 (m/z 28), and CO_2 (m/z 44), were released from each sample (with different intensities) rapidly in the first 20 minutes. SO_2 (m/z 64 with the fragmentation peak of m/z 48, SO, analysed here) and H_2S (m/z 34) were also released from NU-LHT-2M but not in other samples suggesting a higher sulfur content. The Apollo samples released the lowest quantities of m/z 32 indicating particularly low concentrations of the volatiles of O_2 and/or S as compared to the other samples (potentially a consequence of better curation of the Apollo samples which limited adsorption of ambient atmosphere). The m/z 18 peaks took approximately one hour to reach their maximum before showing a gradual decline. Water is difficult to remove from a vacuum system, hence the slow decline in the water (m/z 18) reading. The vacuum pump recorded a pressure reading of $\leq 10^{-6}$ mbar after two hours, which was deemed sufficient for beginning ilmenite reduction experiments as it is significantly below the sensitivity of the pressure sensor used in the experiments ($\pm$ 0.5 mbar).

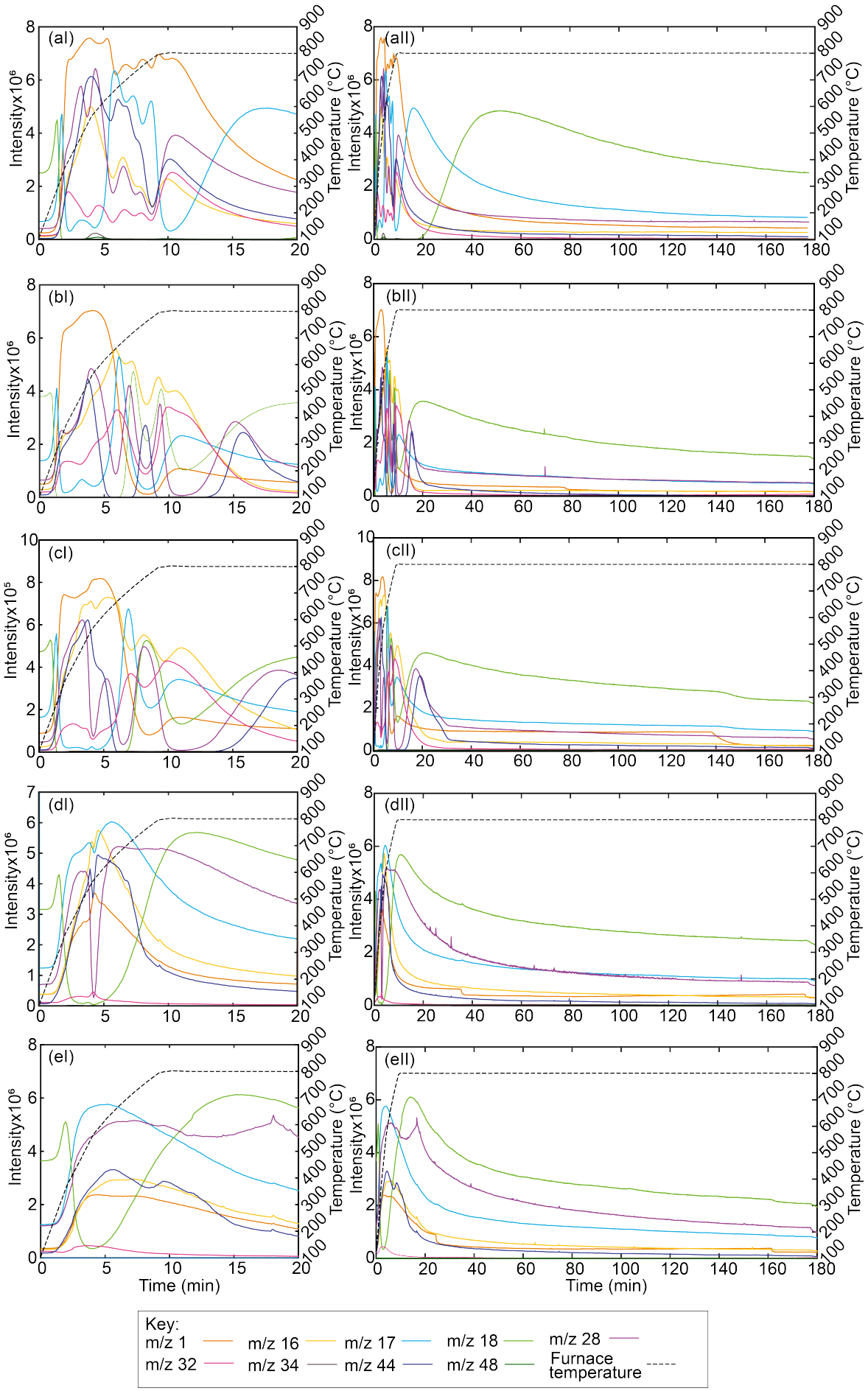

Figure 6.1: Mass spectra for m/z 1, 16, 17, 18, 28, 32, 34, 44, and 48 for samples during the first 20 minutes of a bake-out procedure and the three hour bake-out procedure for (a) NU-LHT-2M, (b) NWA 12592 (untreated), (c) NWA 12592 (treated), (d) 10084, and (e) 60500.

Therefore, a bake-out procedure requiring temperatures of 800 °C for two hours was used in the following studies. This procedure could potentially be optimised further for time/energy efficiency but is not considered in this work.

6.3.2 Experimental procedure

Each prepared sample, with a mass of 45 ± 0.5 mg, was placed into a ceramic sample holder which was attached to valve 7 of the ISRU-BDM manifold (Figure 4.1 in Chapter 4). After a two hour bake-out procedure at 800 °C, the same experimental procedure was followed as in Section 5.2.1 in Chapter 5 and applying the optimum reaction conditions. First, ∼ 0.3 mmol of H_2 (∼ 418 mbar) was inserted into the operational volume where it reacted with the sample at 1000 °C. Any water produced then condensed at the cold finger which was maintained at -80 °C. After four hours the remaining gases were evacuated from the system before the system was sealed under vacuum and the cold finger was heated to 120 °C. The released water was then recondensed at the cold finger before a final release with valves 2, 4 and 5 open so that the volatiles could move through the capillaries to be analysed by the mass spectrometer.

6.3.3 Data analysis

Each experiment was monitored through pressure readings that were obtained every minute during the reaction phase and the water release phase. As in Chapter 5, the pressure data from the reaction phase was corrected for the furnace temperature using the k_T factor from Table 4.2 (Chapter 4), and then the blank reading (obtained when an empty sample tube reacted under the same conditions) was subtracted. The resultant corrected pressure reading from the reaction phase is denoted as P_{cr}. The pressure data from the water release phase was also blank corrected, and denoted as P_{cw}. The total amount of water produced and collected was calculated using the ideal gas equation and P_{cw} (See Section 5.2.2 in Chapter 5). Reduction extent was not calculated for reactions performed with lunar simulant and samples as the total amount of reducible minerals in each sample was not known. Uncertainty in individual pressure readings is taken as the variability of pressure readings (± 0.5 mbar). The uncertainty in water production rate, total water produced, and oxygen yield, was calculated from the propagation of uncertainties in the measured pressure, operational volume, and box temperature values (± 0.5 mbar, $\pm 1.49 \times 10^{-7}$ m^3, and ± 2.5 °C respectively, see Chapter 4). The uncertainty in average values was calculated as a 1 SD uncertainty in the three repeats.

6.3.4 Sample analysis

SEM and XRD analyses were performed on unreacted and reacted samples of each material as in Section 5.2.3 in Chapter 5. SEM BSE imaging and EDS analysis of polished unreacted grains was used to perform petrographic analyses of each sample. Upon reaction of the samples, SEM imaging and EDS analysis were used to identify the presence of the reaction product, iron, and identify in which minerals the reaction had occurred. Meanwhile, XRD analysis was used to confirm a change in metallic iron content between the unreacted and reacted samples, and, where possible, other mineralogical changes.

6.4 Lunar Simulant

6.4.1 Sample preparation

The highlands simulant has a grain size distribution between 0.9 μm and 3 mm (Zeng et al., 2010). The 2 μm filter located next to the ceramic sample holder on the ISRU-BDM (see Figure 4.1 in Chapter 4) will therefore not be sufficient to prevent some fines from penetrating into the ISRU-BDM system and damaging the valves. As grain size affects the surface area available for reduction, and the pore space between grains for gases to move through, it is preferable to keep the grain size distribution as similar to the lunar material expected to be sampled with ProSPA, while also preventing damage to the ISRU-BDM system. To limit the number of fines penetrating into the ISRU-BDM, the NU-LHT-2M simulant was sieved

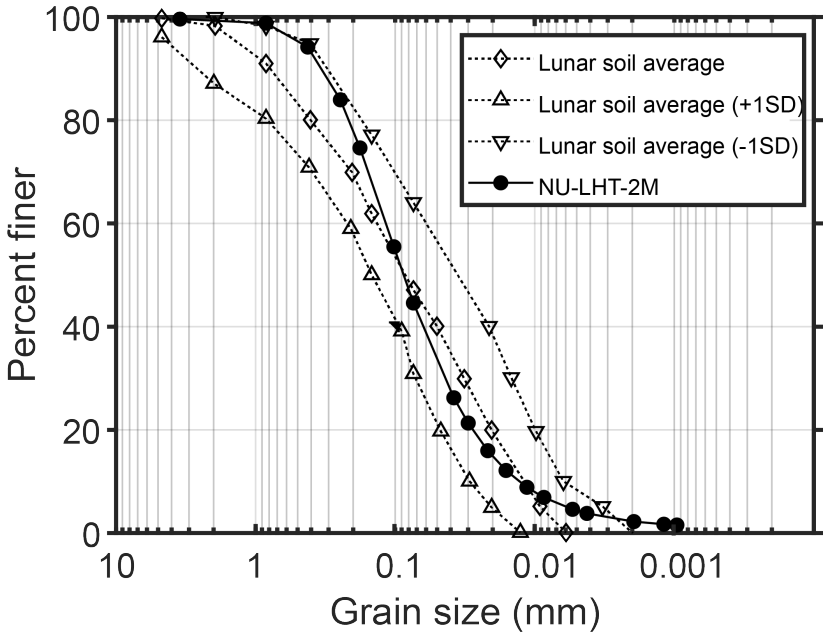

Figure 6.2: Grain size distribution of NU-LHT-2M as compared to the grain size distribution of the lunar soil average as adapted from (Zeng et al., 2010).

to remove all fines $\leq$ 38 μm. A smaller sieve mesh would be unsuitable for dry sieving (Retsch, 2004), while a larger sieve mesh would result in more than 25 % of the simulant to be removed. A wet sieving technique was deemed unsuitable for this work as it may result in further hydration of the sample. The grain size distribution of NU-LHT-2M is shown in Figure 6.2, plotted as the percentage of grains that are smaller in size (finer) than the plotted grain size. The grain size distribution lies within 1 SD of the average lunar soil grain size distribution. However, by removing the finer fraction of $\leq$ 38 μm, the range in the grain size distribution would be reduced, resulting in a less representative sample of lunar-like material.

A sample of 2.113 g of NU-LHT-2M was sieved into two separate size fractions, $\leq$ 38 μm and $>$ 38 μm. The complete details of the sieving procedure is described in Appendix C. From the original sample, 0.266 g of fines ($\leq$ 38 μm) and 1.771 g of larger grains ($>$ 38 μm) were separated, which equates to 12.6 % and 83.8 % respectively with a 3.6 % loss. Zeng et al. (2010) show that 25 % of NU-LHT-2M comprises the grain size fraction $\leq$ 38 μm, which suggests that our larger grain-size fraction contains some remaining fine grains. It was assumed that any remaining fines in the simulant would be prevented from contaminating the ISRU-BDM by the 2 μm filter. The sieved large grain-size fraction was used to prepare a series of samples for experimentation, each of mass 45 mg. SEM analysis of unreacted NU-LHT-2M grains was performed and example BSE images of the different minerals present are shown in Figure 6.3.

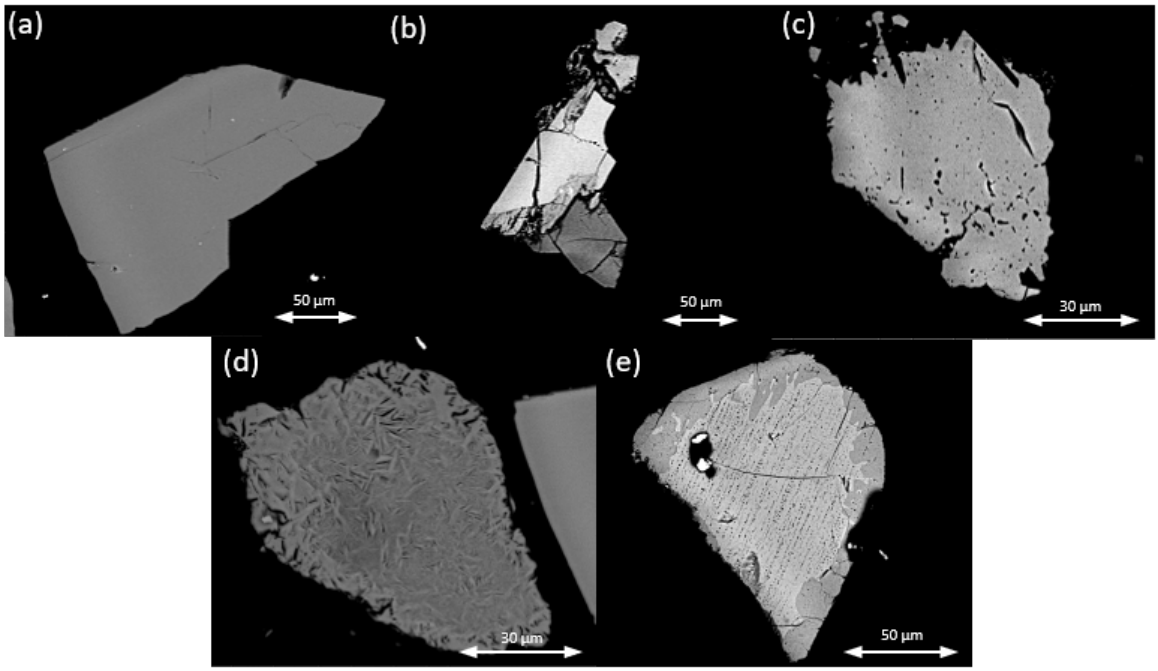

Figure 6.3: BSE images of unreacted NU-LHT-2M grains. Example grains include (a) plagioclase, (b) a multi-phase grain comprising pyroxene (light) and plagioclase (dark), (c) olivine, (d) glass that is chemically equivalent to pyroxene, and (e) ilmenite (light) with a pyrophanite rim (dark).

6.4.2 Results

NU-LHT-2M repeats

Three $\sim$ 45 mg samples of NU-LHT-2M were reacted in the presence of hydrogen, and compared to the blank data obtained in Chapter 5. During the reaction, as the hydrogen reacted with the sample and water was produced, a pressure drop was measured as the water condensed at the cold finger (Figure 6.4a). The initial pressure and total pressure change during the reaction are shown in Table 6.2, along with the calculated amount of hydrogen reacted. The amount of hydrogen used in each reaction is relatively consistent, suggesting the samples are homogeneous in their distribution of reducible minerals.

The water production rate was calculated for each hour of the reaction and shown in Table 6.3. The water production rate decreased with each hour of the reaction, indicating there were fewer reducible minerals in the NU-LHT-2M samples as compared to the highly reducible ilmenite samples in Chapter 5.

During the water release phase the cold finger was heated sublimating any trapped water, and the associated pressure rise was measured (Figure 6.4b). The pressure changes and calculated yields are shown in Table 6.4 along with the values for unaccounted water, described as the difference between the amount of hydrogen used in the reaction and the amount of water that is collected at the cold finger (n_h-n_w).

The results indicate that there was some reduction occurring in the NU-LHT-2M samples as there was a significant pressure change during the reaction phase (-14.5 $\pm$ 1.1 mbar) and water release phase (12.0 $\pm$ 1.5 mbar). As in Chapter 5, the n_h-n_w values indicate that more hydrogen was being used in the reaction compared to the amount of water that reached the cold finger, with on average 1.7 $\pm$ 0.3 μmol of water unaccounted for. As was proposed in Chapter 5, the unaccounted water was assumed to be 'trapped' within the reducing minerals when the experiment was terminated. The total estimated water produced and collected is 8.0 $\pm$ 0.1 μmol, which equates to a calculated yield of 0.28 $\pm$ 0.04 wt % oxygen in the form of water. Under the same conditions, ilmenite produced 3.51 $\pm$ 0.05 wt % oxygen, therefore NU-LHT-2M produced $\sim$ 8.2% of the oxygen produced from pure ilmenite under the same conditions.

To confirm the pressure changes were a result of water production, mass spectrum data were obtained as in Chapter 5. The mass spectra for the released gases are shown in Figure 6.5. Although the mass spectrometer was operating for $>$ 100 minutes before the release phase was started, this was not sufficient for the baseline readings to stabilise. However, a

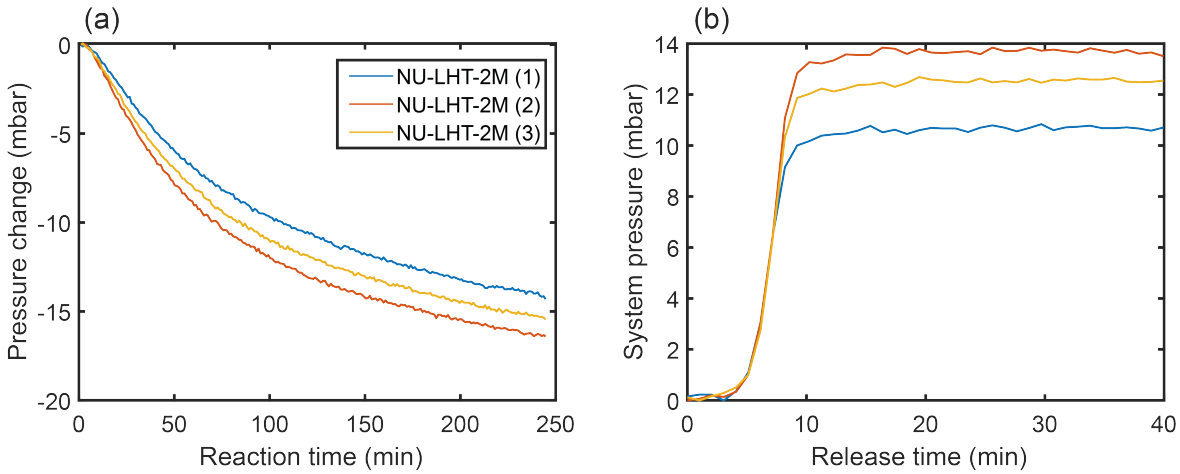

Figure 6.4: Pressure changes during (a) the NU-LHT-2M reduction reaction phase and (b) the corresponding water release phase. The uncertainty in pressure readings is ± 0.5 mbar.

Sample	P_{H2i} (mbar)	ΔP_{cr} (mbar)	n_h (μmol)
NU-LHT-2M (1)	436.1 ± 0.5	-13.4 ± 0.5	9.0 ± 0.3
NU-LHT-2M (2)	447.4 ± 0.5	-15.6 ± 0.5	10.4 ± 0.3
NU-LHT-2M (3)	425.8 ± 0.5	-14.6 ± 0.5	9.8 ± 0.3
Average	436 ± 11	-14.5 ± 1.1	9.7 ± 0.7

Table 6.2: Results from the reduction reaction phase of the NU-LHT-2M studies. Pressure changes during the reaction were used to calculate the amount of H_2 reacted.

Sample	Water production rate (μmol·hr^{-1})			
	0-1 h	1-2 h	2-3 h	3-4 h
NU-LHT-2M (1)	5.6 ± 0.3	1.8 ± 0.3	1.4 ± 0.3	0.3 ± 0.3
NU-LHT-2M (2)	7.0 ± 0.3	2.1 ± 0.3	1.3 ± 0.3	0.1 ± 0.3
NU-LHT-2M (3)	6.4 ± 0.3	1.9 ± 0.3	1.4 ± 0.3	0.1 ± 0.3
Average	6.3 ± 0.7	1.9 ± 0.2	1.3 ± 0.1	0.2 ± 0.1

Table 6.3: Water production rates as determined from the depletion of hydrogen when reacting ∼ 45 mg samples of NU-LHT-2M. Values are calculated for each hour of reduction from the corrected pressure data obtained during the reaction phase.

Sample	ΔP_{cw} (mbar)	Calculated H_2O released (μmol)	n_h-n_w (μmol)	O_2 yield (wt % O_2)
NU-LHT-2M (1)	10.35 ± 0.5	6.9 ± 0.3	2.1 ± 0.7	0.25 ± 0.01
NU-LHT-2M (2)	13.36 ± 0.5	8.9 ± 0.3	1.5 ± 0.7	0.32 ± 0.01
NU-LHT-2M (3)	12.20 ± 0.5	8.2 ± 0.3	1.6 ± 0.7	0.28 ± 0.01
Average	12.0 ± 1.5	8.0 ± 0.1	1.7 ± 0.3	0.28 ± 0.04

Table 6.4: Results from the water release phase following the reduction of NU-LHT-2M. The baseline corrected pressure rise from the release of water from the cold finger is used to calculate the amount of H_2O produced, and therefore the yield and reduction extent.

clear increase in intensity can be seen in the m/z 18 and associated m/z 17 and 16 spectra which confirms water as the main contributor. There is a small m/z 1 peak suggesting there was some residual hydrogen present in the vacuum system. There is also a small peak in m/z 28 and 44, indicating there is some CO_2/CO and perhaps N_2 in the system. It is assumed that there was a small peak in atmospheric gases as a result of a small leak into the closed system, and as the temperature of the cold finger rose, as did the pressure in atmospheric gases present. It should be noted that the mass spectra recorded was used for qualitative and not quantitative purposes. A more stable baseline reading would be required that could be subtracted from the spectra, and then the associated relative sensitivity factor applied before a quantitative analysis could be considered.

Example BSE images of reacted grains are shown in Figure 6.6. The plagioclase grains generally show no evidence for reduction with no bright spots (indicative of metallic iron) forming within the grain. However, there are some plagioclase grains that show iron blebs on the outer grain edge (see Figure 6.6a), suggesting the grains were adjacent to reducing minerals and the iron was transferred to the plagioclase grain, or, the small amount of iron oxide that can be present in some plagioclase minerals has been reduced. Pyroxene and olivine grains showed some reduction, with evidence for the formation of iron blebs in the form of bright spots within the grain. Where the bright spots are too small to be analysed with the SEM, the area containing the bright spots does indicate they are enriched in iron compared to any unreacted material elsewhere in the grain (see Figures 6.6b & c). As also shown by Massieon et al. (1993, 1992), reduced pyroxene contains small iron blebs (up to 2 μm) throughout the grain, while olivine generally shows larger agglomerations of iron (> 3 μm) as the product appears to be more mobile than in the pyroxene grains. Identified ilmenite grains within the sample show significant to complete reduction with iron formation found across the entire grain (see Figure 6.6d). The unreacted ilmenite core was identified as pyrophanite ($MnTiO_3$), which is less susceptible to reduction as compared to ilmenite.

The XRD spectra of unreacted and reacted NU-LHT-2M can be seen in Figure 6.7. The ilmenite content in the simulant was too low to detect, however, there was an obvious increase in elemental iron in the reacted sample, suggesting reduction of iron oxides had taken place. The exact modal mineralogy of NU-LHT-2M is complex and not well characterised. Therefore, although there are noticeable peak changes between the unreacted and reacted spectra it was not possible with this technique to identify specifically which mineral each peak represents and consequently determine which minerals have reduced.

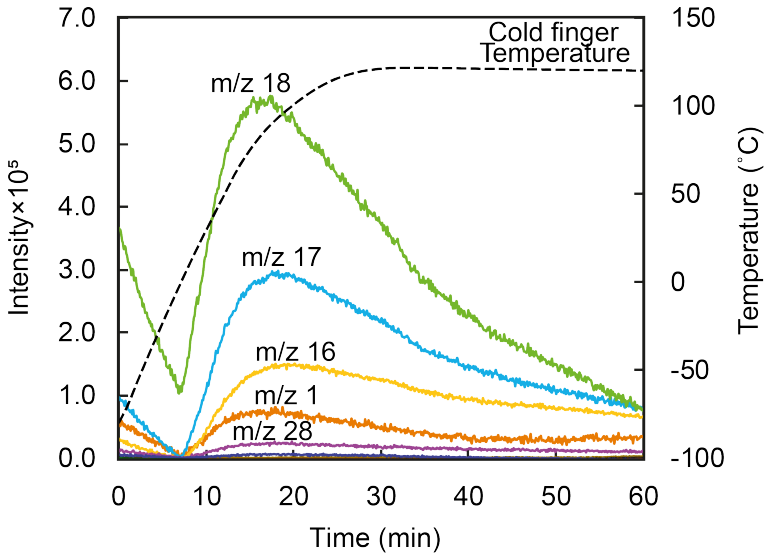

Figure 6.5: Baseline corrected mass spectrum data recorded during a second water release phase for NU-LHT-2M.

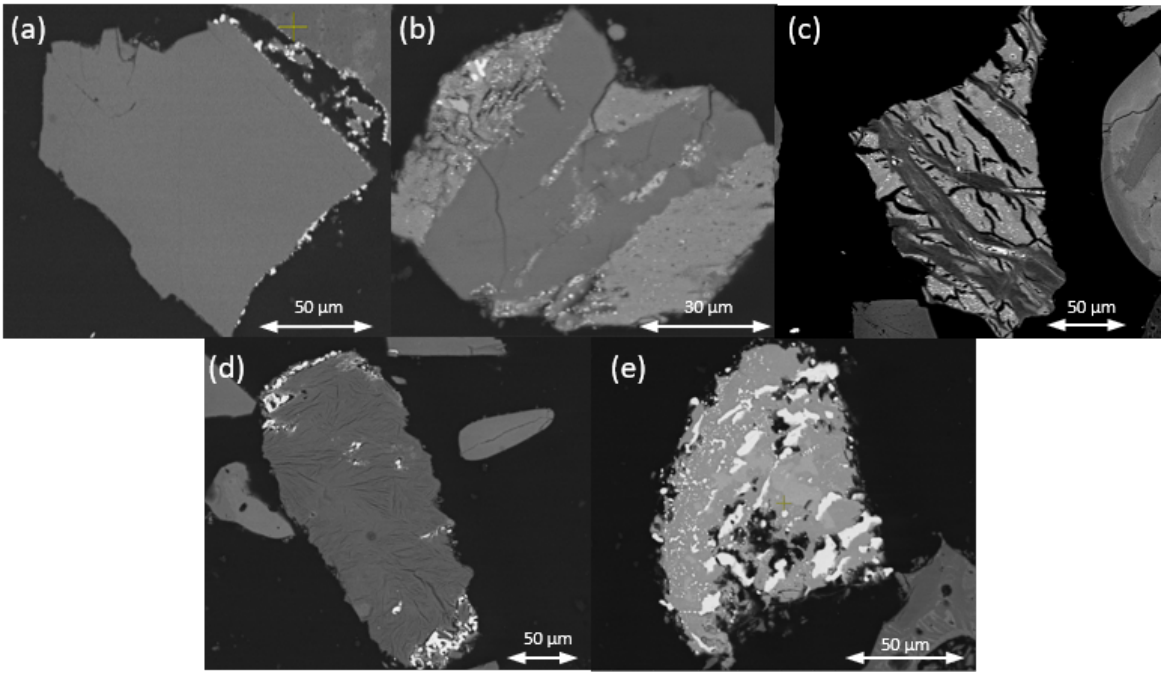

Figure 6.6: BSE images of partially reduced NU-LHT-2M grains. Example grains include (a) plagioclase, (b) pyroxene (light) with plagioclase inclusion (dark), (c) olivine (dark) and pyroxene (light), (d) glass, and (e) ilmenite.

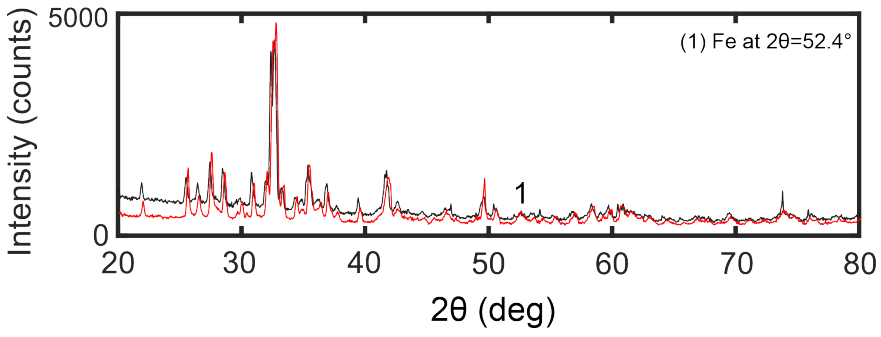

Figure 6.7: XRD analysis of NU-LHT-2M before (black) and after (red) reduction. Peaks of interest are labelled with their corresponding mineral.

NU-LHT-2M doped with ilmenite

Next, the lunar highlands simulant was combined with ilmenite, where the ilmenite used was the same as that used in Chapters 3 and 5. The samples were combined in different ratios of NU-LHT-2M to $FeTiO_3$ (100:0, 90:10, 75:25, 50:50, and 25:75), and reacted under the same standard conditions of 1000 °C with ∼ 0.3 mmol of hydrogen for four hours. Mixtures of up to 75 % ilmenite were analysed to represent a range of beneficiation grades (Williams et al., 1979). The resulting pressure changes during each reaction are shown in Figure 6.8a. The results for a sample comprising just ilmenite (0:100), as obtained from Chapter 5, are also included for comparison. The initial pressure and pressure change is shown in Table 6.5 along with the calculated amount of hydrogen used in the reaction. The results show that under the same reaction conditions, samples with more ilmenite reacted with larger quantities of hydrogen. The water production rate for each hour of the reaction is shown in Table 6.6. With increasing ilmenite concentrations, the water production rate was higher and decreased more slowly.

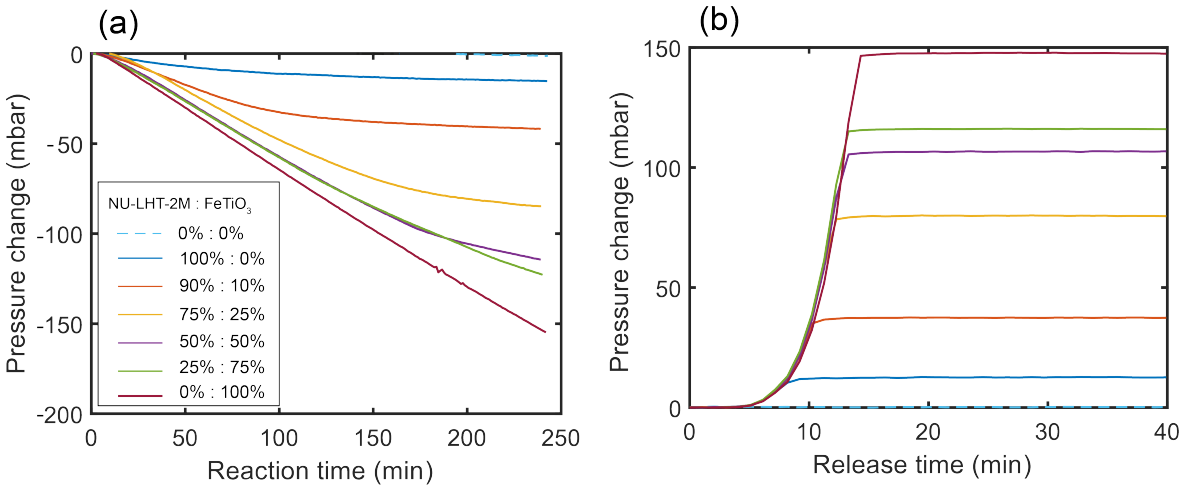

Figure 6.8: Pressure changes during (a) the doped simulant reduction reaction phase and (b) the corresponding water release phase. The results are compared to a blank measurement where a blank sample tube was reacted under the same conditions. Pressure readings have an uncertainty of ± 0.5 mbar.

As the cold finger was heated during the water release phase, there was an associated pressure rise which is shown in Figure 6.8b. The pressure changes are recorded in Table 6.7 along with the total amount of water produced and the reduction extent. The difference between the amount of hydrogen used in the reaction and the amount of water released from the cold finger is also recorded in Table 6.7. The n_h-n_w value increases with increasing ilmenite mass (from 1.6 ± 0.7 μmol for NU-LHT-2M to 5.5 ± 2.0 μmol for ilmenite). With

Sample composition NU-LHT-2M:$FeTiO_3$	P_{H2i} (mbar)	ΔP_{cr} (mbar)	n_h (μmol)
100 %: 0 %	425.8 ± 0.5	-14.6 ± 0.5	9.8 ± 0.3
90 %: 10 %	428.6 ± 0.5	-41.4 ± 0.5	27.7 ± 0.4
75 %: 25 %	460.4 ± 0.5	-84.4 ± 0.5	56.5 ± 0.6
50 %: 50 %	424.2 ± 0.5	-114.5 ± 0.5	76.7 ± 0.8
25 %: 75 %	431.0 ± 0.5	-123.8 ± 0.5	82.9 ± 0.8
0 %: 100 %	418.4 ± 0.5	-155.6 ± 0.5	104.3 ± 1.0

Table 6.5: Results from the reduction reaction phase of the ilmenite doped NU-LHT-2M studies. Pressure changes during the reaction were used to calculate the amount of H_2 reacted.

Sample composition NU-LHT-2M:$FeTiO_3$	Water production rate (μmol·hr^{-1})			
	0-1 h	1-2 h	2-3 h	3-4 h
100 %: 0 %	6.4 ± 0.3	1.9 ± 0.3	1.4 ± 0.3	0.1 ± 0.3
90 %: 10 %	15.0 ± 0.4	9.2 ± 0.3	2.7 ± 0.3	0.8 ± 0.3
75 %: 25 %	18.9 ± 0.4	20.2 ± 0.4	13.3 ± 0.4	4.2 ± 0.3
50 %: 50 %	22.2 ± 0.4	24.1 ± 0.4	20.5 ± 0.4	10.0 ± 0.3
25 %: 75 %	22.9 ± 0.4	23.8 ± 0.4	19.7 ± 0.4	16.4 ± 0.4
0 %: 100 %	26.4 ± 0.4	26.4 ± 0.4	26.0 ± 0.4	25.5 ± 0.4

Table 6.6: Water production rates as determined from the depletion of hydrogen when reacting $\sim$ 45 mg samples of NU-LHT-2M doped with ilmenite. Values were calculated for each hour of reduction from the corrected pressure data obtained during the reaction phase.

Sample composition NU-LHT-2M:$FeTiO_3$	ΔP_{cw} (mbar)	Calculated H_2O released (μmol)	n_h-n_w (μmol)	O_2 yield (wt % O_2)
100 %: 0 %	12.2 ± 0.5	8.2 ± 0.3	1.6 ± 0.7	0.28 ± 0.01
90 %: 10 %	37.2 ± 0.5	24.9 ± 0.4	2.8 ± 0.8	0.89 ± 0.02
75 %: 25 %	79.5 ± 0.5	53.2 ± 0.6	3.3 ± 1.2	1.89 ± 0.03
50 %: 50 %	106.2 ± 0.5	71.1 ± 0.7	5.6 ± 1.5	2.50 ± 0.04
25 %: 75 %	115.7 ± 0.5	77.5 ± 0.8	5.4 ± 1.6	2.75 ± 0.04
0 %: 100 %	147.4 ± 0.5	98.7 ± 1.0	5.5 ± 2.0	3.51 ± 0.05

Table 6.7: Results from the water release phase following the reduction of ilmenite doped NU-LHT-2M. The baseline corrected pressure rise from the release of water from the cold finger was used to calculate the amount of H_2O produced, and therefore the yield.

more reducible minerals present, more water molecules are likely to be 'trapped' within the minerals when the reaction is terminated, causing the discrepancy.

6.4.3 Discussion

NU-LHT-2M was sieved to remove the finer grains in order to limit damage to valves, therefore the simulant is less representative of the grain size distribution expected of the lunar soil that would be sampled by ProSPA. The change in grain size distribution has a two-fold (potentially

counteracting each other) effect on the reaction rate. As ilmenite in the simulant falls into the 75-150 μm grain size fraction only, the ilmenite concentration of the simulant is relatively high when the ≤ 38 μm fraction is removed. However, as the average grain size of the simulant is larger in the > 38 μm sieved fraction, and therefore the overall surface area of grains is smaller, the reaction rate would be slower as compared to an unsieved sample (Hegde et al., 2009; Yoshida et al., 2000). To limit the effects of a change in grain size (and therefore the bulk chemistry of the sample) on the reaction, ultrasonic sieving would be recommended, which would enable the removal of a smaller fraction of sample, down to 5 μm (Retsch, 2004).

NU-LHT-2M contains up to 0.7 wt % ilmenite. Therefore, if ilmenite alone were the only mineral that had reduced, then a yield of $\sim$ 0.02 wt % O_2 would be expected, as estimated from the yields produced under the same conditions from ilmenite alone (Chapter 5). However, the simulant produced significantly higher yields of 0.28 $\pm$ 0.01 wt % O_2 suggesting other minerals present were also reduced. As previously demonstrated by e.g. Allen et al. (1996); Britt (1993); Gibson et al. (1994), minerals such as olivine and pyroxene can reduce within the lunar simulant/sample. As well as ilmenite; glass, olivine, and pyroxene also show evidence of reduction in the NU-LHT-2M reacted samples as the blebs of metallic iron were identified in these grains with BSE imaging and EDS analysis. Although the ilmenite grains within the simulant generally show complete or near to complete reduction, the glass, pyroxene, and olivine grains show minor reduction, a consequence of their higher activation energies (Massieon et al., 1992). Reacted plagioclase grains also showed some evidence of reduction as iron blebs were found on the edge of some grains. The reducibility of plagioclase has been contested in literature with Gibson et al. (1994) showing no evidence of reduction, while Allen et al. (1993) showed some evidence of reduction and the formation of iron blebs on the edge of grains. It is unclear whether the longer reaction times of four hours applied in this work and by Allen et al. (1993) resulted in the plagioclase reducing, or whether the iron on the grain edges is simply transferred from an adjacent grain during the reaction. An isolated experiment reacting just plagioclase would be required to demonstrate whether the mineral is reducible under the stated reaction conditions.

The pressure change during the reaction phase shows an initial rapid pressure drop, followed by a slower drop in pressure. The samples with more ilmenite show an extended period of rapid pressure change as compared to those with less ilmenite. A suggested cause for this change in reaction rate is that there is an initial rapid reduction of ilmenite, followed by a slower reduction of the remaining iron oxide-bearing minerals. Complete reduction of olivine and pyroxene is not expected (Allen et al., 1994), thus, although the yields may be

increased if left to reduce for longer, only a fraction of the FeO present would reduce.

The yields obtained from the simulant that was doped with ilmenite can be used as estimates for yields from lunar regolith with varying ilmenite concentrations. For example, 10 % ilmenite concentrations provides a first order approximation for mare regolith (irrespective of other minerals present) (McKay and Williams, 1979) and produces a yield of 0.89 ± 0.02 wt % O_2. As the amount of ilmenite is increased, it provides a demonstration of how much beneficiation is required to produce desired yields. It should be noted that the ilmenite grain size used for doping is 80-260 μm, and therefore on average larger grains than those already found in the simulant or expected on the lunar surface. Applying the ilmenite reduction model developed by Dang et al. (2013, 2015), if the ilmenite grains were smaller, the expected yields would be higher.

The nature of the iron found in lunar simulants can vary significantly from the iron found in lunar material. Iron oxides of terrestrial origin contain Fe^{2+} and Fe^{3+}. The more oxidised Fe^{3+} is found in Fe_2O_3 and therefore has more available oxygen than FeO which contains Fe^{2+}. The low oxygen fugacity of the lunar environment means that iron oxides are all composed of Fe^{2+}. Therefore, there is less available oxygen in lunar iron oxides than terrestrial iron oxides (Taylor and Liu, 2010). The distribution of FeO and Fe_2O_3 in NU-LHT-2M is unknown, however, typical terrestrial rocks have a Fe^{2+}:Fe^{3+} ratio of 90:10 (Personal Communication, M. Anand, April 14th 2020). It is recommended that Mössbauer spectroscopy is performed on the simulant to identify the exact proportions of Fe^{2+} and Fe^{3+} in order to more fully understand the amount of available oxygen in the iron oxides.

NU-LHT-2M and lunar soil differ in their geotechnical properties in that the grain shape is more spherical, particularly with smaller grains, in the simulant as compared to lunar material which is significantly more angular (Lowers et al., 2008). Therefore, the surface area available for reduction is significantly smaller in the simulant which would ultimately slow down the reaction rate. The simulant is also mostly monomineralic, whereas lunar soil mostly comprises multiphase grains and agglutinates, where different minerals are fused together which may influence the reaction rate.

The successful production of water from the lunar simulant demonstrates the suitability of reduction experiments on lunar-like material with a ProSPA setup. Next, actual lunar material was reacted to identify the similarities and differences in how the reduction reaction proceeds in the differing materials.

6.5 Lunar meteorites

6.5.1 Sample preparation

The powdering technique outlined in Mortimer (2016) was applied to a 2.12 g chip of NWA 12592, with the aim of approximating a lunar regolith-type consistency. Care was taken not to crush the meteorite into too-fine a powder as the fine fractions were later sieved from the sample as in Section 6.4.1. The final mass of the crushed NWA 12592 sample was 1.96 g with 0.16 g lost (a loss of 7.55 %). The crushed meteorite contained a mixture of softer (anorthositic) and harder (basaltic) minerals, which made it difficult to produce a homogeneous grain size. As a consequence, the softer material would powder more quickly to a fine grain size and would remain in greater quantities as residue on the equipment during transfer, resulting in greater overall mass loss.

EATG is a frequently used acid treatment to remove weathering products as it reacts with soluble and insoluble iron compounds (Cornish and Doyle, 1984) to remove iron oxides, hydroxides, and metallic iron, but not silicate-bound iron (Martins et al., 2007). EATG has been successfully used to remove terrestrial weathering products from a range of meteorite types, while maintaining the primary oxygen isotope composition (Greenwood et al., 2012), suggesting that pretreatment with EATG will remove weathering products while having minimal effects on the lunar minerals present. The EATG treatment was performed on a 0.98 g sample of the crushed meteorite. The details of the EATG treatment procedure are outlined in Appendix D. This procedure was carried out by J. Gibson and J. Malley. As a result of the treatment, the meteorite experienced a 0.02 g mass loss. Untreated and treated samples were then sieved as outlined in Appendix C, where the sieving procedure was applied separately to each of the three untreated and treated samples. By sieving each sample, any heterogeneity within the samples could be constrained. The grain size of the sieved meteorite samples was measured using the technique outlined in Section 3.2.2 in Chapter 3. The small variance in grain size distribution of the sieved meteorite samples (Figure 6.9) indicate some minor heterogeneity in the distribution. The crushed meteorite samples have an average grain size of 96 μm, and contain more larger grains, and fewer smaller grains than the average lunar soil. As a result of the sieving process, up to 23 % mass loss was recorded from each sample (Table 6.8). Each sieved sample of $\geq$ 38 μm was used to prepare a 45 mg sample for reaction. SEM images show how most grains produced from the crushing of the meteorite resulted in mostly composite grains, with some monomineralic grains (See Figure 6.10). There was no

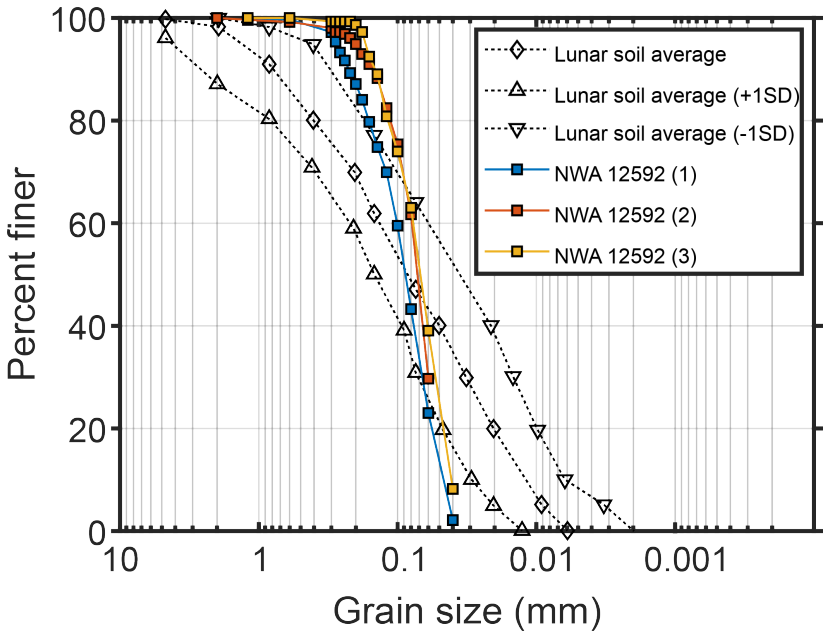

Figure 6.9: Grain size distribution of the three EATG treated samples of NWA 12592 (n = 326, 256, and 146 respectively), as compared to the grain size distribution of the lunar soil average as adapted from (Zeng et al., 2010).

Sample	Mass of sample (g)	Mass of sieved fraction (g)		Mass lost (g)
		$\geq$ 38 μm	$\leq$ 38 μm	
Untreated (1)	0.153	0.116	0.002	0.036
Untreated (2)	0.158	0.118	0.008	0.033
Untreated (3)	0.151	0.119	0.002	0.016
Treated (1)	0.155	0.139	0.002	0.014
Treated (2)	0.154	0.124	0.002	0.028
Treated (3)	0.158	0.143	0.002	0.033

Table 6.8: Mass of crushed NWA 12592 meteorite samples before and after the sieving process. Results are shown for meteorite samples that were untreated, and those that were pretreated with EATG.

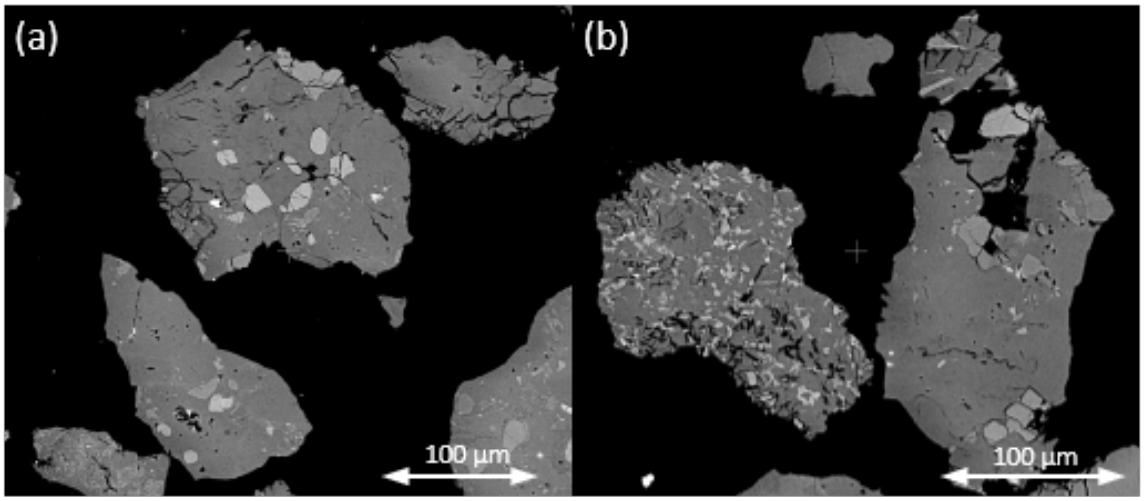

Figure 6.10: BSE images of crushed samples of NWA 12592 where (a) is untreated, and (b) is treated with EATG.

noticeable difference in the appearance of grains between the untreated and treated samples, suggesting there are minimal weathering products present in the crushed meteorite. EDS analysis with the SEM identified most composite grains as containing olivine and pyroxene inclusions set within a fine-grained regolith matrix.

6.5.2 Results

The pressure changes during the reaction phase of the experiments are shown in Figure 6.11a, with the initial pressure and pressure change recorded in Table 6.9 along with the calculated amount of hydrogen used in the reaction. The water production rate for each hour of the reaction is shown in Table 6.10. The pressure rise from the water release phase is shown in Figure 6.11b and the associated pressure rise shown in Table 6.11 along with the total calculated amount of water produced, oxygen yield, and n_h-n_w values.

The results indicate that some minor reduction had occurred with an average pressure change of 5.3 ± 0.2 mbar and 5.8 ± 0.5 mbar during the reaction phase for untreated and treated samples respectively. It appears that at this scale, there was negligible difference in the amount of reduction that occurred in the treated and untreated samples. The crushed meteorite samples produced significantly less water than the highland simulant with a calculated yield of 2.3 ± 0.3 μmol and 1.8 ± 0.3 μmol, which equates to a yield of 0.08 ± 0.01 wt % O_2 and 0.07 ± 0.02 wt % O_2 for untreated and treated respectively. On average, the NWA 12592 samples produced 70 % less water than NU-LHT-2M under the same conditions. One consequence of the small yields is that the water production rate in the final hour of the reaction is below detectable limits (BDL) as the equivalent blank reading measurements were larger than those recorded for the meteorite samples. The blank reading during the reaction phase resulted in a P_{cr} value of 6.1 mbar (see Section 5.3.1 in Chapter 5), and therefore when the blank reading is subtracted it results in a non-detectable pressure change at such small values. There was on average 1.3 ± 0.3 μmol and 2.0 ± 0.3 μmol of water unaccounted for from the unreacted and reacted samples respectively, as compared to the amount of hydrogen reacted. The n_h-n_w values are equivalent to those calculated from the reduction of NU-LHT-2M.

A mass spectrum of the produced water was obtained, however, as the yields (and therefore pressures) were so small the results were inconclusive and could not be used to identify the constituents of the product gases. Both the untreated and treated samples showed some minor evidence of iron formation in BSE imaging (see Figure 6.12), however, most grains did not show evidence of metallic iron formation. The iron blebs that were identified were mostly ≤ 1 μm indicating only minor reduction. XRD analysis was inconclusive in determ-

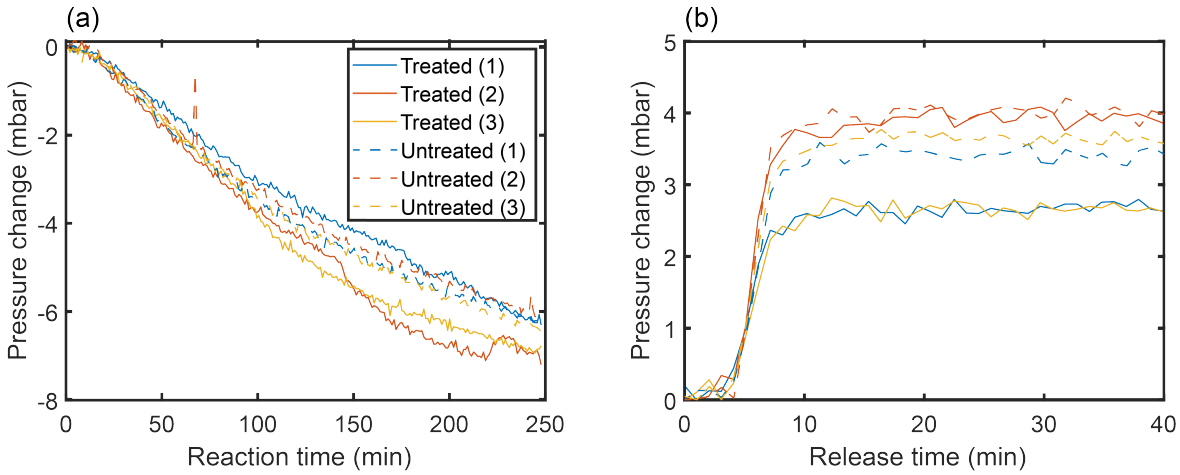

Figure 6.11: Pressure changes during (a) the NWA 12592 reduction reaction phase and (b) the corresponding water release phase. Results are shown for meteorite samples that were untreated, and those that were pretreated with EATG. The pressure readings have an uncertainty of ± 0.5 mbar.

Sample	P_{H2i} (mbar)	ΔP_{cr} (mbar)	n_h (μmol)
Untreated (1)	426.2 ± 0.5	-5.3 ± 0.5	3.6 ± 0.3
Untreated (2)	425.6 ± 0.5	-5.1 ± 0.5	3.4 ± 0.3
Untreated (3)	465.9 ± 0.5	-4.5 ± 0.5	3.7 ± 0.3
Untreated Average	439 ± 23	-5.3 ± 0.2	3.5 ± 0.1
Treated (1)	424.2 ± 0.5	-5.3 ± 0.5	3.5 ± 0.3
Treated (2)	423.0 ± 0.5	-6.2 ± 0.5	4.2 ± 0.3
Treated (3)	424.7 ± 0.5	-5.8 ± 0.5	3.9 ± 0.3
Treated Average	424.0 ± 0.9	-5.8 ± 0.5	3.9 ± 0.3

Table 6.9: Results from the reduction reaction phase of the NWA 12592 studies. Pressure changes during the reaction were used to calculate the amount of H_2 reacted. Results are shown for meteorite samples that were untreated, and those that were pretreated with EATG.

Sample	Water production rate (μmol·hr^{-1})			
	0-1 h	1-2 h	2-3 h	3-4 h
Untreated (1)	2.3 ± 0.3	0.7 ± 0.3	0.8 ± 0.3	BDL
Untreated (2)	2.2 ± 0.3	0.6 ± 0.3	0.9 ± 0.3	BDL
Untreated (3)	2.3 ± 0.3	0.7 ± 0.3	1.0 ± 0.3	BDL
Untreated Average	2.3 ± 0.7	0.6 ± 0.2	0.9 ± 0.1	BDL
Treated (1)	2.0 ± 0.3	0.6 ± 0.3	0.9 ± 0.3	BDL
Treated (2)	2.4 ± 0.3	0.7 ± 0.3	1.4 ± 0.3	BDL
Treated (3)	2.3 ± 0.3	1.1 ± 0.3	0.9 ± 0.3	BDL
Treated Average	2.2 ± 0.2	0.8 ± 0.3	1.1 ± 0.3	BDL

Table 6.10: Water production rates as determined from the depletion of hydrogen when reacting ∼ 45 mg samples of NWA 12592. Values were calculated for each hour of reduction from the corrected pressure data obtained during the reaction phase. Results are shown for meteorite samples that were untreated, and those that were pretreated with EATG.

Sample	ΔP_{cw} (mbar)	Calculated H_2O released (μmol)	n_h-n_w (μmol)	O_2 yield (wt % O_2)
Untreated (1)	3.1 ± 0.5	2.1 ± 0.3	1.5 ± 0.7	0.07 ± 0.01
Untreated (2)	3.7 ± 0.5	2.5 ± 0.3	0.9 ± 0.7	0.09 ± 0.01
Untreated (3)	3.3 ± 0.5	2.2 ± 0.3	1.5 ± 0.7	0.08 ± 0.01
Untreated Average	3.4 ± 0.3	2.3 ± 0.3	1.3 ± 0.3	0.08 ± 0.01
Treated (1)	2.3 ± 0.5	1.6 ± 0.3	2.0 ± 0.7	0.06 ± 0.01
Treated (2)	3.6 ± 0.5	2.4 ± 0.3	1.7 ± 0.7	0.09 ± 0.01
Treated (3)	2.3 ± 0.5	1.6 ± 0.3	2.3 ± 0.7	0.06 ± 0.01
Treated Average	2.8 ± 0.7	1.8 ± 0.3	2.0 ± 0.3	0.07 ± 0.02

Table 6.11: Results from the water release phase following the reduction of NWA 12592. The baseline corrected pressure rise from the release of water from the cold finger was used to calculate the amount of H_2O produced, and therefore the yield. Results are shown for meteorite samples that were untreated, and those that were pretreated with EATG.

ining whether a reaction had occurred as there were negligible changes in the peak structure and therefore unable to confirm a change in mineral composition (see Figure 6.13). There was a minor difference in the XRD spectra of the untreated and treated samples, suggesting that the EATG treatment caused some minor alteration to the mineral composition of the treated sample. It was not possible to identify the specific mineral change resulting from the treatment which caused the peak formation at $2\theta = 27.85°$. It is assumed that the untreated samples contained trace iron oxide-bearing weathering products. The number of counts (diffracted X-rays detected) was significantly reduced in each of the meteorite spectra as compared to the NU-LHT-2M spectra. Potential causes of low counts could be the highly amorphous nature of the meteorite which leads to poor diffraction, or simply because the grain packing on the slide was not sufficient. Improved sample preparation (such as increasing the sample density on the slide) and longer data acquisition times could highlight any other potential differences in the meteorite spectra leading to possible identification of the mineral changes with EATG treatment.

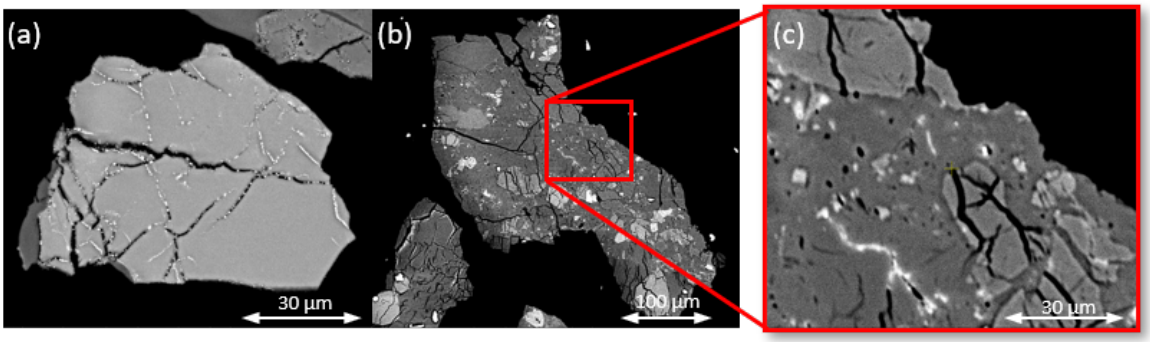

Figure 6.12: BSE images of partially reduced NWA 12592 grains. Example grains include (a) an olivine grain from an untreated sample, and (b) & (c) composite grains from the treated sample.

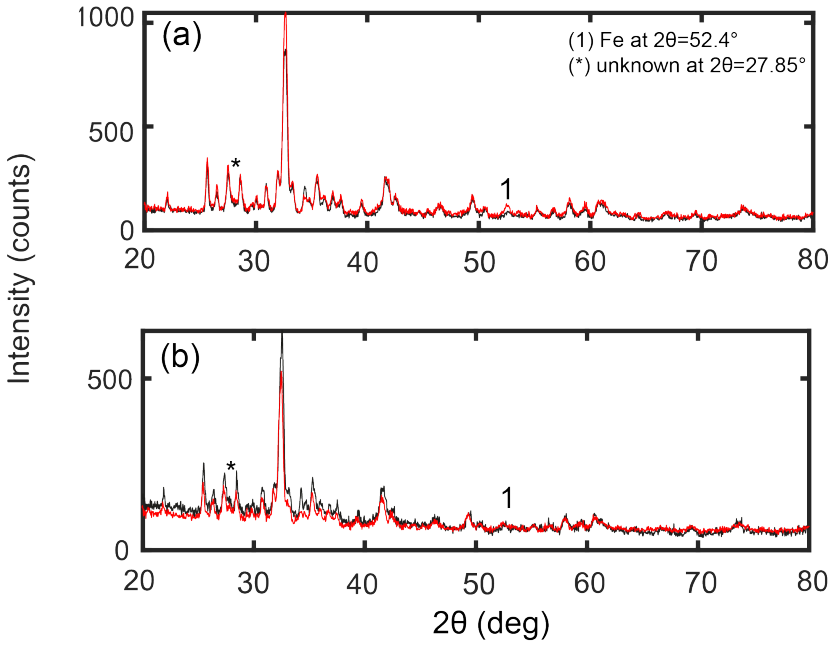

Figure 6.13: XRD analysis of (a) untreated and (b) treated NWA 12592 before (black) and after (red) reduction. Peaks of interest are labelled with their corresponding mineral.

6.5.3 Discussion

As a result of the limited mass of meteorite available, manually crushing the meteorite to imitate the grain size distribution of lunar soils was not possible. Consequently, the crushed NWA 12592 used in this work had a narrower range of grain sizes as compared to lunar soils. The grain size distribution of the meteorite was less representative of lunar soil than the highlands simulant. The crushed meteorite had more large grains and fewer small grains/fines. It is likely that the reaction rate could be improved upon if the average grain size was reduced. As the NWA 12592 meteorite is heterogeneous in its distribution of minerals and lithic clasts, aliquots of the crushed meteorite were sieved separately (as opposed to sieving all of the crushed meteorite in one batch) to maintain any heterogeneities. A grain size distribution of the three treated samples show that sieving the separate samples results in a similar distribution of grain size, showing no major inhomogeneities in the grain size. The yields produced from the reduction of the samples, although small, are relatively consistent, suggesting any heterogeneities in mineral composition did not influence the yield at this scale.

The EATG treatment had minimal effect on the mass of the crushed meteorite sample with just 2 % mass loss as opposed to $\sim$ 40-50 % as often found using this technique (Personal Communication, R. Greenwood, November 19th 2019). It was therefore assumed that there were minimal weathering products in the crushed sample used for this study; this is consistent with the XRD analyses. Generally, meteorites contain a larger proportion of weathering

products, and in such cases EATG treatment may be useful to ensure weathering products do not provide false-positive yields from the reduction of secondary oxides.

The iron oxide (FeO) content of NWA 12592 is not too dissimilar from the highlands simulant (3.89 ± 0.12 wt % and 3.59 ± 0.44 wt % respectively). However, the meteorite contains no identifiable ilmenite, therefore the FeO is most likely bound up in the less reactive pyroxenes and olivines. Consequently, the yields were significantly lower in the meteorite and there was minimal evidence of reduction products in the BSE imaging or XRD analyses.

The relatively large average grain size and low ilmenite content means that the crushed NWA 12592 samples produce low albeit still measurable yields, suggesting that ProSPA could be capable of producing water from such material, and quantifying it. It was therefore decided to proceed with the reduction experiments on the Apollo samples using the ISRU-BDM system, to understand if and how actual lunar soils reduce in such a system, in comparison to crushed lunar meteorite and lunar simulant.

6.6 Apollo Samples

6.6.1 Sample preparation

The Apollo soils each contain a high proportion of fines that must be removed before use in the ISRU-BDM (Figure 6.14). The sieving protocol outlined in Appendix C was applied to individual samples of each soil type. Apollo soils are known to be electrostatic (Carrier et al., 1991), and so an additional measure was applied to the protocol where a grounding cable

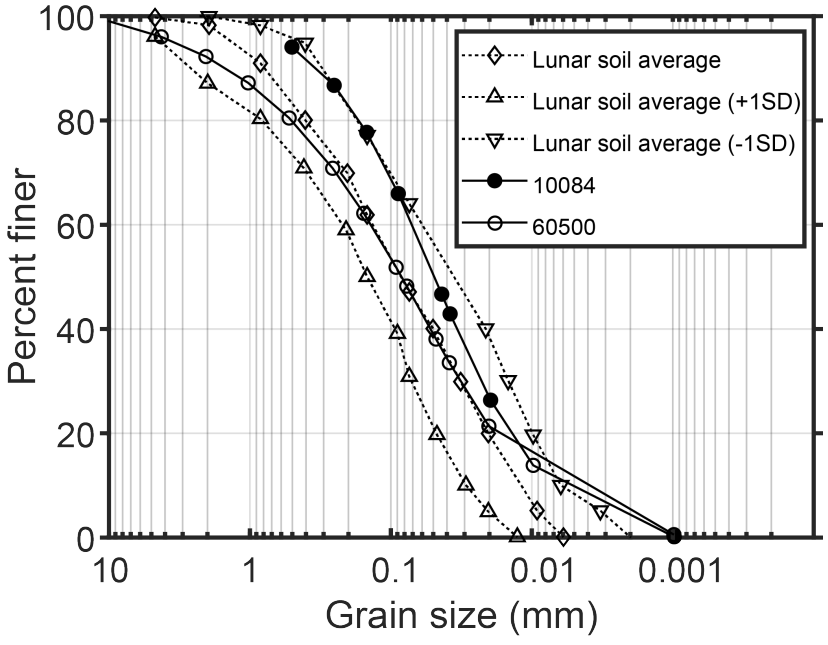

Figure 6.14: Grain size distribution of Apollo samples 10084 and 60500 as compared to the grain size distribution of the lunar soil average as adapted from (Zeng et al., 2010).

was attached to the sieve to minimise any build-up of charge and additional sticking of the soil to the sieve. Unfiltered water was mistakenly used (as opposed to deionised Milli-Q® water) to clean the sieve used to separate the fines from the 10084 soil and resulted in mass loss of up to 53 % (Table 6.12). It is assumed that salt crystals formed on the sieve causing the fines to stick to them and could not easily be emptied into the vials for storage. It can be seen that the sieving process was more efficient for soil sample 10084 (3), likely because there was a coating of fines on the sieve walls from the previous samples, and so fewer fines were sticking to the walls. Care was taken to use the highest grade of deionised water available, 18.2 MΩ·cm^{-1}, to clean the sieve before use on the 60500 soil. Consequently, only up to 7 % of the 60500 soil was lost (Table 6.12). The $\geq$ 38 μm fractions were then used to prepare the 45 mg samples which were to be used in the reduction experiments.

Sample	Mass of sample (g)	Mass of sieved fraction (g)		Mass lost (g)
		$\geq$ 38 μm	$\leq$ 38 μm	
10084 (1)	0.101	0.046	0.001	0.054
10084 (2)	0.122	0.063	0.005	0.054
10084 (3)	0.121	0.070	0.031	0.020
60500 (1)	0.127	0.100	0.018	0.009
60500 (2)	0.133	0.122	0.009	0.002
60500 (3)	0.129	0.111	0.013	0.006

Table 6.12: Mass of crushed Apollo soil samples before and after the sieving process.

Example grains from each soil sample were imaged with the SEM and are shown in Figures 6.15 and 6.16. The imaged grains are representative of the bulk sample which mostly contain multiphase grains and agglutinates. EDS analysis identified significant quantities of ilmenite and olivine with plagioclase and pyroxene in the multiphase grains in the 10084 soil. Meanwhile, olivine was scarce and ilmenite was not identified in the selection of imaged 60500 grains.

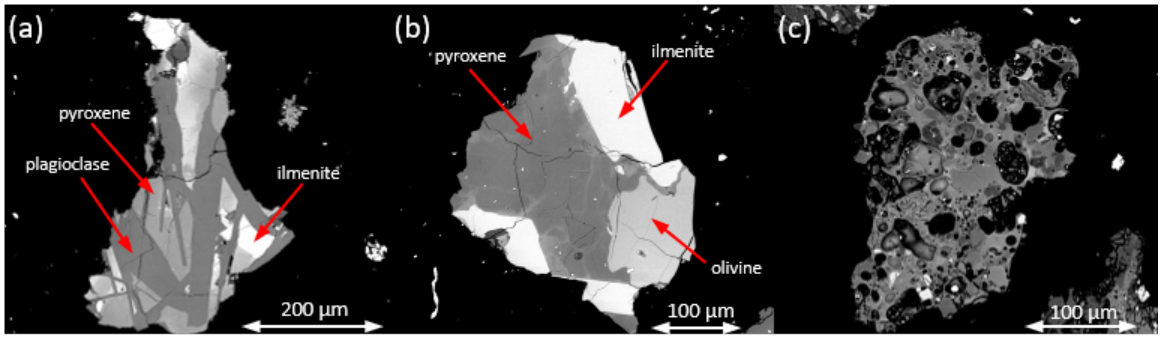

Figure 6.15: BSE images of the $\geq$ 38 μm size fraction of 10084 where (a) and (b) are multiphase grains, and (c) is an agglutinate.

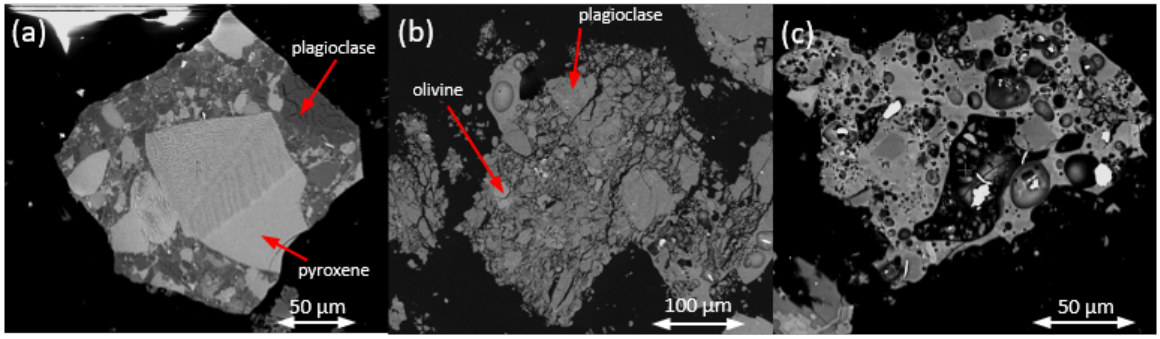

Figure 6.16: BSE images of the $\geq$ 38 μm size fraction of 60500 where (a) is a multiphase grain, (b) is a multiphase grain that has fractured through the polishing process, and (c) is an agglutinate.

6.6.2 Results

Both Apollo soils showed evidence of reduction as they each resulted in a pressure drop during the reaction, and a pressure rise when the cold finger was heated (See Figure 6.17 and 6.18). The initial pressures and pressure changes recorded in the reaction phase are outlined in Table 6.13, along with the calculated amount of hydrogen that had reacted. The water production rates calculated for each hour of the reaction are shown in Table 6.14. The pressure changes recorded during the water release phase are shown in Table 6.15 along with total calculated amount of water produced, the calculated yields, and the amount of water that is unaccounted for when compared to the amount of hydrogen reacted.

The results show that the mare soil (10084) reduced significantly more than the highland soil (60500). An average pressure change of 43.1 $\pm$ 0.5 mbar was recorded during the reaction phase, as compared to an average of 8.9 $\pm$ 0.4 mbar for the highlands soil. The pressure drop during the reduction of the mare soil showed an initial fast water production rate of 13.7 $\pm$ 0.1 μmol·hr^{-1} for the first 60 minutes, followed by a slower water production rate of 1.5 $\pm$ 0.1 μmol·hr^{-1} in the fourth hour which is only $\sim$ 11 % of the rate of the first hour. The highlands soil also showed an initial faster water production rate of 3.4 $\pm$ 0.1 μmol·hr^{-1} followed by significantly slower rates as compared to the mare soil. Similar to the meteorite results in Section 6.5, when such small yields are recorded, the blank corrected data results in yields below detectable limits towards the fourth hour of the reaction. The water release phase resulted in average yields of 0.94 $\pm$ 0.03 wt % O_2 and 0.18 $\pm$ 0.02 wt % O_2 for the 10084 and 60500 soils respectively. The amount of unaccounted water was higher in the 10084 soil as compared to the 60500 soil. This result correlates with the results from the doped simulant experiments where the samples containing more reducible minerals resulted in higher amounts of residual water within the grains.

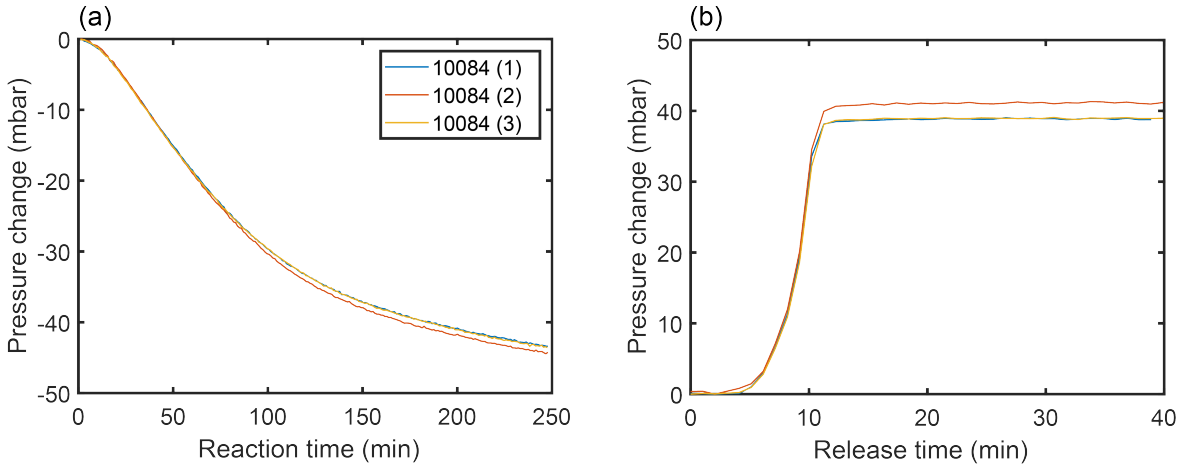

Figure 6.17: Pressure changes during (a) the 10084 reduction reaction phase and (b) the corresponding water release phase. The pressure readings have an uncertainty of ± 0.5 mbar.

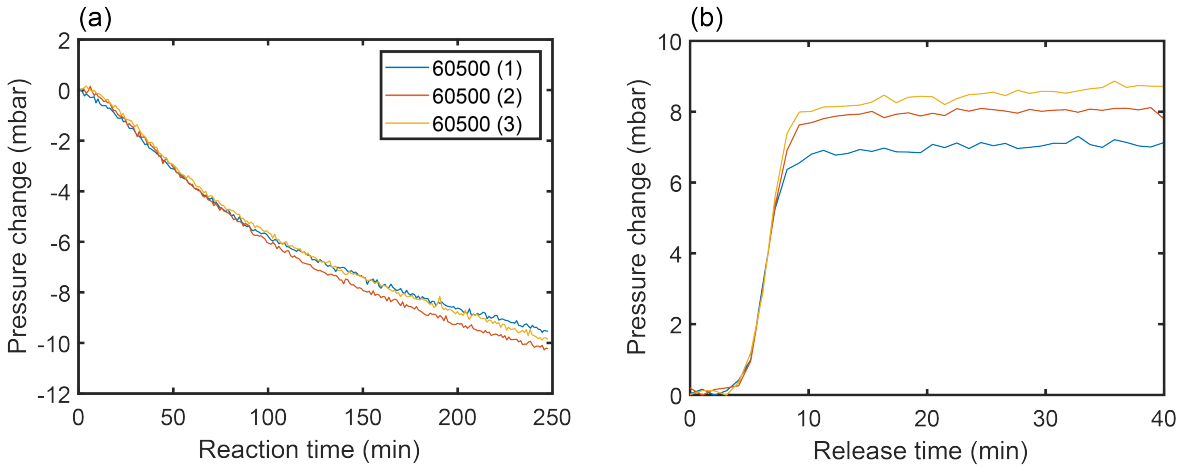

Figure 6.18: Pressure changes during (a) the 60500 reduction reaction phase and (b) the corresponding water release phase. The pressure readings have an uncertainty of ± 0.5 mbar.

Sample	P_{H2i} (mbar)	ΔP_{cr} (mbar)	n_h (μmol)
10084 (1)	433.5 ± 0.5	-42.8 ± 0.5	28.7 ± 0.4
10084 (2)	424.0 ± 0.5	-43.7 ± 0.5	29.2 ± 0.4
10084 (3)	423.2 ± 0.5	-42.9 ± 0.5	28.7 ± 0.4
10084 Average	426.9 ± 5.7	-43.1 ± 0.5	28.9 ± 0.3
60500 (1)	423.5 ± 0.5	-8.6 ± 0.5	5.7 ± 0.3
60500 (2)	424.3 ± 0.5	-9.3 ± 0.5	6.2 ± 0.3
60500 (3)	424.5 ± 0.5	-8.9 ± 0.5	6.0 ± 0.3
60500 Average	424.1 ± 0.5	-8.9 ± 0.4	6.0 ± 0.2

Table 6.13: Results from the reduction reaction phase of the 10084 and 60500 soil studies. Pressure changes during the reaction were used to calculate the amount of H_2 reacted.

Sample	Water production rate (μmol·hr^{-1})			
	0-1 h	1-2 h	2-3 h	3-4 h
10084 (1)	13.7 ± 0.4	9.2 ± 0.3	4.3 ± 0.3	1.4 ± 0.3
10084 (2)	13.9 ± 0.4	9.6 ± 0.3	4.2 ± 0.3	1.6 ± 0.3
10084 (3)	13.6 ± 0.4	9.2 ± 0.3	4.3 ± 0.3	1.5 ± 0.3
10084 Average	13.7 ± 0.1	9.3 ± 0.2	4.3 ± 0.1	1.5 ± 0.1
60500 (1)	3.5 ± 0.3	1.2 ± 0.3	1.2 ± 0.3	BDL
60500 (2)	3.5 ± 0.3	1.4 ± 0.3	1.3 ± 0.3	BDL
60500 (3)	3.3 ± 0.3	1.3 ± 0.3	1.3 ± 0.3	BDL
60500 Average	3.4 ± 0.1	1.3 ± 0.1	1.3 ± 0.1	BDL

Table 6.14: Water production rates as determined from the depletion of hydrogen when reacting $\sim$ 45 mg samples of 10084 and 60500 soils. Values were calculated for each hour of reduction from the corrected pressure data obtained during the reaction phase.

Sample	ΔP_{cw} (mbar)	Calculated H_2O released (μmol)	n_h-n_w (μmol)	O_2 yield (wt % O_2)
10084 (1)	38.5 ± 0.5	25.8 ± 0.4	2.9 ± 0.8	0.92 ± 0.02
10084 (2)	40.8 ± 0.5	27.3 ± 0.4	1.9 ± 0.9	0.97 ± 0.02
10084 (3)	38.6 ± 0.5	25.9 ± 0.4	2.8 ± 0.8	0.92 ± 0.02
10084 Average	39.3 ± 1.3	26.3 ± 0.9	2.5 ± 0.6	0.94 ± 0.03
60500 (1)	6.8 ± 0.5	4.6 ± 0.3	1.2 ± 0.7	0.16 ± 0.01
60500 (2)	7.7 ± 0.5	5.1 ± 0.3	1.1 ± 0.7	0.18 ± 0.01
60500 (3)	8.4 ± 0.5	5.6 ± 0.3	0.3 ± 0.7	0.20 ± 0.01
60500 Average	7.6 ± 0.8	5.1 ± 0.5	0.9 ± 0.5	0.18 ± 0.02

Table 6.15: Results from the water release phase following the reduction of 10084 and 60500 soils. The baseline corrected pressure rise from the release of water from the cold finger was used to calculate the amount of H_2O produced, and therefore the yield.

The yields from the reduction of the Apollo soils were sufficiently high that a mass spectrum of the produced water could be obtained. The resulting mass spectra of the m/z values of interest are shown in Figure 6.19. It can be seen that water was the dominant component of the released volatiles. The baseline readings were significantly more stable for the 10084 spectra as compared to the mass spectra obtained for the NU-LHT-2M reactions, probably because the ISRU-BDM was left in a closed state for significantly longer (936 minutes as a result of leaving the system overnight) before the re-release of the water. However, there was a signifiant nitrogen peak in the spectra, potentially caused by a small air leak into the system which resulted in a significant quantity of nitrogen entering the system over the extended stabilising time. The spectra from the re-release of water from 60500 was obtained after a more reduced period of time (145 minutes), which was not sufficient to stabilise the spectra, however, the dominant volatile was still identified as water. It is recommended that in future work the ISRU-BDM is checked for small leaks that may contribute significant quantities of

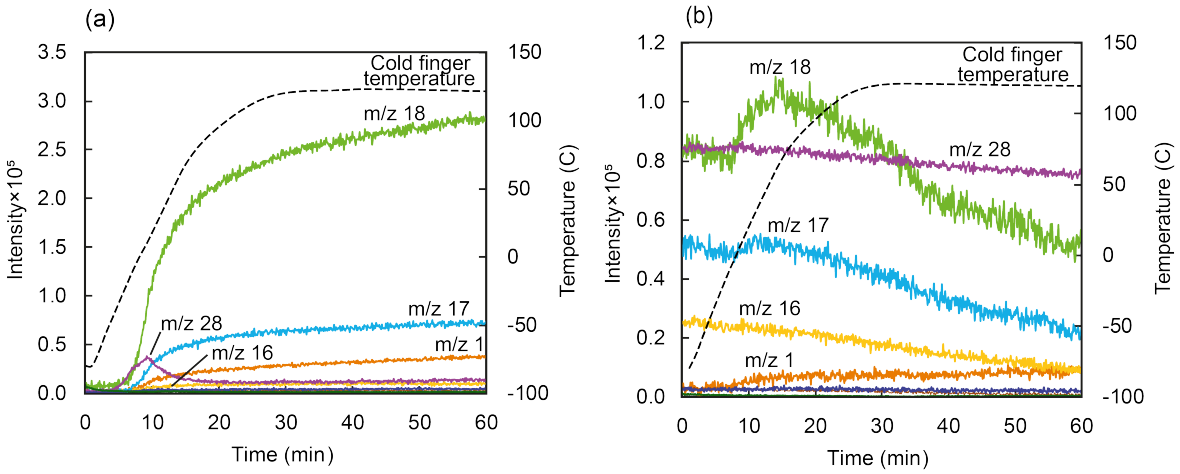

Figure 6.19: Baseline corrected mass spectrum data recorded during a second water release phase for (a) 10084 and (b) 60500.

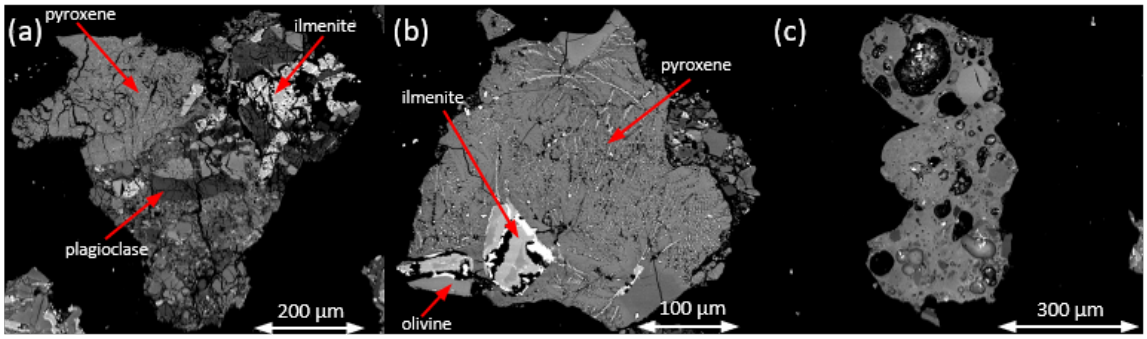

Figure 6.20: BSE images of partially reduced 10084 grains. Example grains include (a) a multiphase grain containing reduced ilmenite and pyroxene with unreacted plagioclase, (b) a multiphase grain with reduced pyroxene, ilmenite and olivine, and (c) an agglutinate with no evidence of reduction.

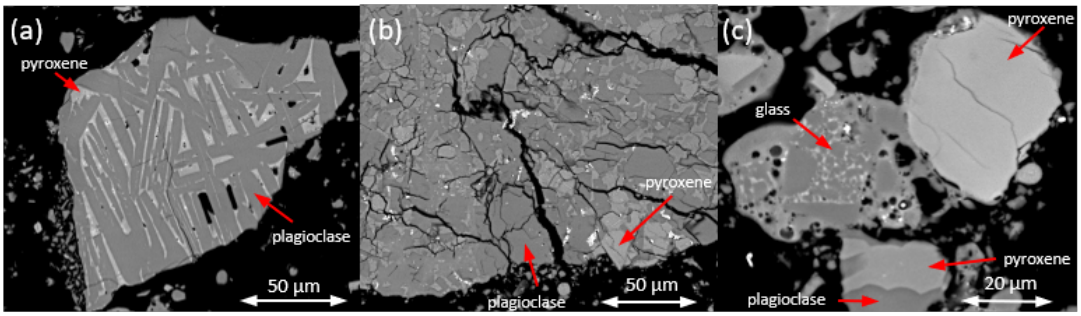

Figure 6.21: BSE images of partially reduced 60500 grains. Example grains include (a) & (b) plagioclase and pyroxene multiphase grains, and (c) an agglutinate grain with pyroxene, plagioclase and glass.

gas into the system while it is closed. Minimising such small leaks would enable longer stabilising times to be applied prior to the re-release of water without significant contributions of atmospheric gases.

Examples of the BSE images produced from the reacted Apollo soils are shown in Figures 6.20 and 6.21. Any identified ilmenite in the 10084 grains showed complete, or almost complete, reduction, with large iron veins (up to 14 μm wide and 29 μm long) being formed. The pyroxene and olivine showed obvious iron formation with veins of iron and multiple iron blebs scattered throughout the mineral. However, the pyroxene still contained significant quantities of FeO. The plagioclase showed no evidence of reduction. The agglutinates, which have a high glassy component, showed no evidence of iron formation, with bright spots seen through BSE often resulting from debris that had fallen into the vesicles from polishing and carbon coating, and not iron formation. As the 60500 soils contained no identifiable ilmenite and minimal olivine in the imaged grains, the only remaining mineral likely to have reduced was pyroxene. There is some evidence of iron formation in the pyroxene in the form of small iron blebs.

XRD analysis of the Apollo samples can be seen in Figures 6.22. The XRD spectra shows that there is iron formation in both the 10084 and 60500 soils, confirming the reduction of iron oxides. In 10084 there is also a loss of ilmenite and magnesian ilmenite detected in the reacted sample. However, as with the simulant and meteorite, the complex mineralogies of each of the samples means that XRD is not able to identify which other iron oxides had reduced.

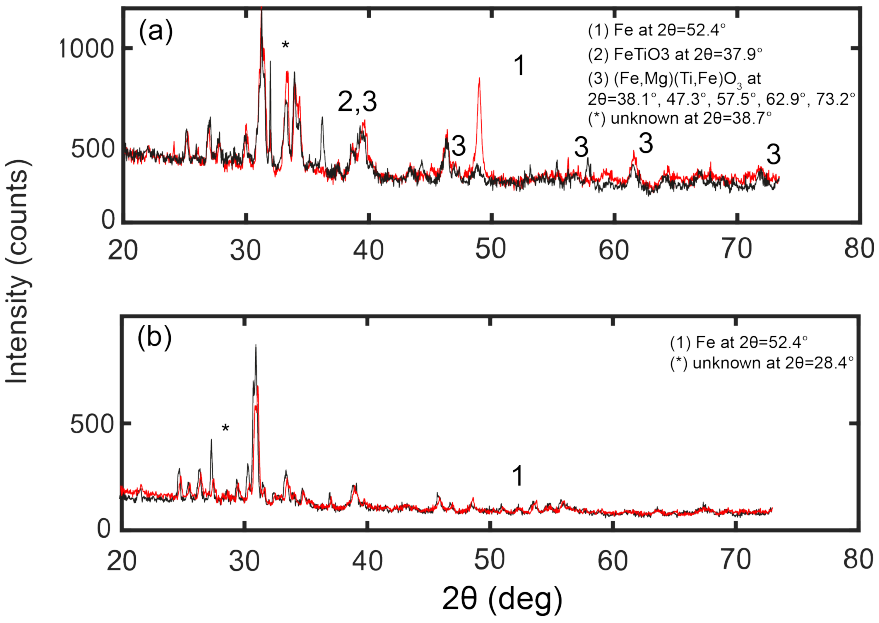

Figure 6.22: XRD analysis of (a) 10084, and (b) 60500 before (black) and after (red) reduction. Peaks of interest are labelled with their corresponding mineral.

6.6.3 Discussion

Both Apollo soils, 10084 and 60500, were successfully reduced in the ISRU-BDM system. The mare soil produced significantly higher yields as compared to the highlands soil. When considering the available FeO in 10084 and 60500 (15.81 ± 0.15 wt % and 5.53 ± 0.26 wt % O_2 respectively), the yields correspond to an oxygen extraction efficiency of 27 % and 15 % respectively from the FeO. Although FeO content strongly dictates how much oxygen can be extracted (Allen et al., 1996), the minerals in which the iron oxides are contained strongly influence the potential yields. Yoshida et al. (2000) showed that when the ilmenite present in multiphase grains reduced, it opened up channels into the grain. As highland soils have little-to-no ilmenite, there was less reduction inside the grains, and so fewer channels were created to enable further reduction of the minerals. Although soil 60500 was selected because of its relatively low FeO content, there are crystalline lunar samples that contain $\ll 1$ wt % FeO such as the Genesis rock (Meyer, 2011). Such an iron-poor material would produce negligible amounts of water and therefore oxygen. However, lunar soils comprise unconsolidated material of different lithologies, therefore the FeO content is generally at least 4 wt % (McKay et al., 1991a).

As with the NU-LHT-2M simulant, the Apollo soils contain trace sulfide bearing minerals (Meyer, 2009, 2010), and consequently H_2S could be produced from the reduction of such minerals. Hydrogen sulfide would be damaging to electrolysis plants required to separate the oxygen and hydrogen from the product water, and is therefore an undesirable product (Williams, 1985). H_2S will condense at a -80 °C cold finger at pressures > 320 mbar, therefore H_2S could have collected at the cold finger. However, no measurable H_2S was measured in the spectra of the water released from the cold finger. Therefore, if any H_2S was produced and condensed at the cold finger, it would have either sublimed and been removed when the system was placed under vacuum, or the quantity of H_2S produced was simply too small to measure. One solution could be the use of a warmer cold finger (temperature dependent on the saturation vapour limit of water in the volume under consideration) which would ensure only water is condensed because water has a higher boiling point than other unwanted products such as H_2S.

Both of the Apollo soils studied here are mature and likely contain some of the highest quantities of nanophase iron (np-Fe). However, even mature soils contain < 1 wt % np-Fe (Morris, 1980; Taylor and Liu, 2010). Thompson et al. (2016) shows that np-Fe increases in oxidation with maturity, which could therefore result in minor amounts of additional

FeO available for reduction in mature soils. The finer fractions of lunar soils contain the highest proportion of np-Fe (Taylor et al., 2010), but the fines were removed from the soils before reduction. np-Fe is known to form on grain rims, and throughout amorphous silicates (identified here as the vesiculated glass in agglutinates) (Basu, 2005), and BSE images showed that reduction occurs throughout minerals not just on the edges, and was not identified in measurable amounts in the vesiculated glasses. Therefore, the results of this study support those of Allen et al. (1996) suggesting that the contribution of oxidised np-Fe to the reduction of minerals in lunar soils is negligible.

The limited supply of Apollo lunar samples available for analysis means that destructive ISRU studies on large samples for a full scale reactor that produces tonnes of oxygen (e.g. Christiansen et al., 1988; Gibson and Knudsen, 1985)) are unlikely to be achieved. However, as the sample sizes required for a ProSPA-type oven are relatively small at $\sim$ 45 mg, certain lunar soils were deemed suitable for such experiments. In this case, the contingency sample collected during Apollo 11, and a rake sample collected during Apollo 16. Another recommended Apollo soil that could be trialled in such destructive studies would be sample 70050, an Apollo 17 $>$ 2.2 kg sample deposited onto the Buddy Secondary Life Support System (BSLSS) because of a broken fender. The sample represents a mixture of the lunar soil across an entire extravehicular activity (EVA) traverse, and so it has less scientific value (it is not necessarily a representative sample of lunar soil as one might find at any one location) but could be used in engineering studies (Taylor et al., 2016).

6.7 Discussion: comparing sample types

6.7.1 Data analysis

The pressure readings obtained during the reaction phase were corrected for system temperature and then the blank reading was subtracted (P_{cr}). The pressure data before correction shows that all samples appear to still be reacting after four hours. However, when the blank was subtracted, there appears to have been no measurable reduction in the crushed meteorite (NWA 12592) and the highlands Apollo soil (60500) in the final hour of the reaction phase. The blank reading has a non-zero pressure change, potentially the result of a small flow of gas through the capillary to the mass spectrometer. In the fourth hour of the experiment it is therefore assumed that there was no further reduction experienced by the meteorite or highlands soil. If the soils sampled by ProSPA have similar composition to the 60500 or NWA 12592 then four hours should be a sufficient time frame, however longer experiments will

be required for more ilmenite rich soils if completion is desired. If the yields are expected to be low (i.e. < 10 mbar) then blank readings will be critical to ensure accurate quantification. It is recommended that there are no capillaries open to the mass spectrometer on ProSPA during the reaction phase to minimise losses and improve accuracy of yield quantification.

In Chapter 5 it was found that when the yields were higher, there was a bigger discrepancy between the amount of hydrogen reacted, and the amount of water condensed at the cold finger (n_h-n_w). The yield was higher when the reaction conditions were optimised and so the reaction proceeded more quickly. As seen in Figure 5.8 (Chapter 5), in optimised conditions more water was produced per unit time in the ilmenite grains, therefore, more residual water was trapped within the grains when the reaction was halted before completion. However, yield is also dependent on the mineralogy of the sample. As shown with the doped simulant, with more ilmenite grains present there was a greater discrepancy in the amount of hydrogen used and the amount of water produced, as water molecules were likely to be retained within a larger number of reducing grains when the reaction was terminated (Figure 6.23). A plot of n_h-n_w against yield for all samples reacted in the ISRU-BDM is shown in Figure 6.24. It can be seen that there is a clear correlation, with higher yields recorded when n_h-n_w is higher. Some water will always adsorb onto the stainless steel manifold, hence there will always be a non-zero value for n_h-n_w, even for samples which are assumed to have reacted to completion (or near completion) including the meteorite samples and the Apollo 16 soil.

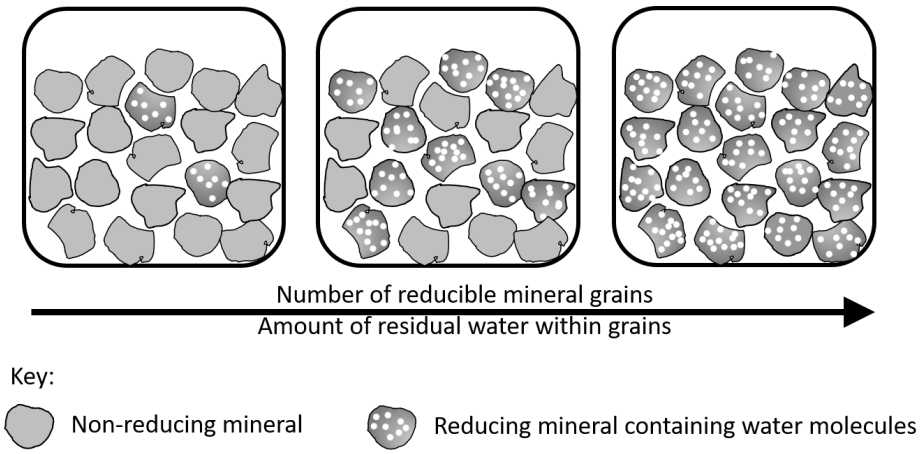

Figure 6.23: Diagram showing samples of increasing reducible mineral content. When the reaction is halted before completion, the samples with more reducible minerals contain more residual water molecules within the grains.

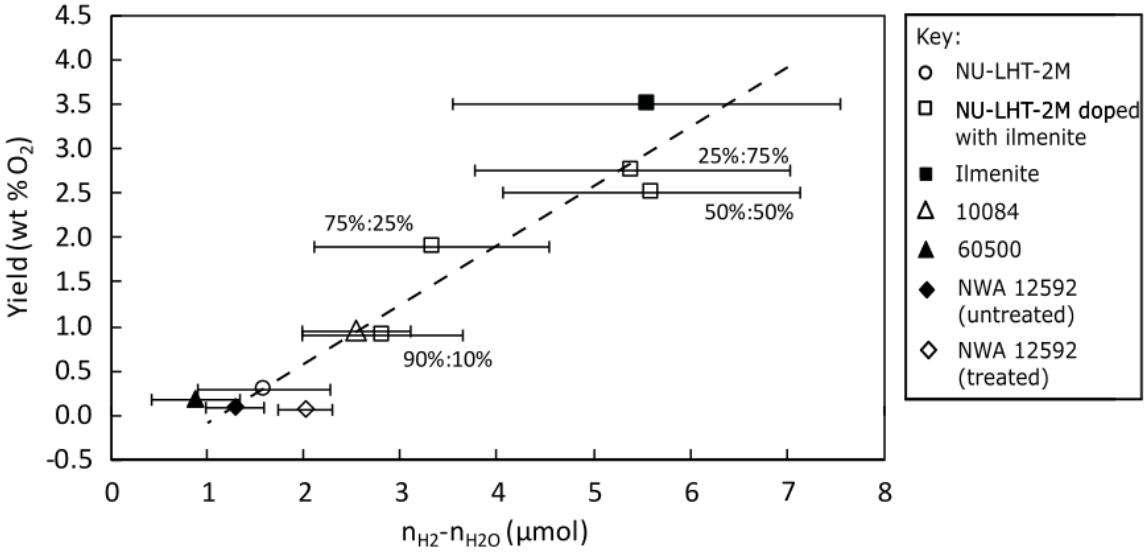

Figure 6.24: A plot showing the discrepancy between the amount of hydrogen used in the reaction and the amount of water released from the cold finger (n_h-n_w) against the calculated yields. Results are shown for all samples reacted in the ISRU-BDM under the same conditions (1000 °C for four hours with 0.3 mmol of hydrogen).

6.7.2 Sample analysis techniques

XRD spectra were useful in identifying the specific changes in mineralogy that occur following the reduction of pure ilmenite as in Chapter 5, however, when analysing the reduction of more complex samples, XRD was only suitable for identifying the production of iron as evidence of the reaction. In order to identify specifically which minerals are reducing, the SEM was the preferred tool. Using the SEM it was possible to identify reduction in grains by identifying iron blebs with BSE imaging and EDS analysis. The reacted mineral that contains the iron blebs could also be identified through EDS analysis.

6.7.3 Ilmenite content as an indicator of yields

Generally, the more FeO rich a material, the higher the oxygen yield will be from reduction with hydrogen (Allen et al., 1996). Although there are various FeO-bearing minerals in lunar soils and rocks, ilmenite is the most easily reducible, and the only mineral which can undergo complete reduction of its FeO by hydrogen. Therefore, if the FeO present in a sample is bound mostly in ilmenite, the yields will be higher than those from samples where the FeO is contained mostly in other iron oxide-bearing minerals such as pyroxene or olivine.

A more accurate predictor of ilmenite concentration in lunar soils is TiO_2 content (Lemelin et al., 2013; Papike et al., 1991). The FeO and TiO_2 content of each of the samples reduced

in the ISRU-BDM are recorded in Table 6.16. Assuming all of the TiO_2 present in each sample is found in ilmenite, a maximum possible ilmenite concentration is calculated (it should be noted that pyroxene does also have significant TiO_2 concentrations). The ilmenite estimations based on TiO_2 are more accurate in immature soils and terrestrial simulants as ilmenite is converted to impact glasses in mature soils, lowering the ilmenite content but the TiO_2 content will remain the same (Chambers et al., 1995). The two Apollo soils studied in this work are mature soils and so the ilmenite estimations are likely to be higher than the true values.

Sample	FeO (wt %)	TiO_2 (wt %)	Estimated max. ilmenite (wt %)	Average yield (wt % O_2)
Ilmenite	45.0	50	95	3.51 ± 0.05
NU-LHT-2M	3.59	0.37	0.7	0.28 ± 0.04
NU-LHT-2M:Ilmenite (90 %:10 %)	7.73	5.33	10.13	0.89 ± 0.02
NWA 12592 (untreated)	3.89	0.17	0.32	0.08 ± 0.01
NWA 12592 (treated)				0.07 ± 0.02
10084	15.81	7.54	14.33	0.94 ± 0.03
60500	5.53	0.60	1.14	0.18 ± 0.02

Table 6.16: FeO and TiO_2 content from bulk analyses and the derived maximum ilmenite content. Yields from the reduction of each sample type under optimised conditions for four hours in the ISRU-BDM are also shown in wt %O $_2$.

The ilmenite content of some of the samples studied in this chapter have been estimated in other studies. NU-LHT-2M has been estimated previously to contain 0.6 vol. % ilmenite (Rickman and Lowers, 2012), however the equivalent wt % has not been determined because the specific mineral phases are not known. It can be assumed that the wt % concentration of ilmenite in NU-LHT-2M will be higher than 0.6 wt % as ilmenite has a relatively high density compared to the other known minerals present. As NU-LHT-2M is mostly monomineralic, the grain counting technique used to estimate the ilmenite concentration by (Rickman and Lowers, 2012) is probably accurate. A similar technique was used to estimate the ilmenite content of 10084, given as 4.2 wt % (Johnson et al., 2009), which is significantly lower than the maximum possible ilmenite estimated from the TiO_2 content (Table 6.16). However, the lunar soil 10084 contains 34 % agglutinates, some of which will have ilmenite inclusions that would not be included in the grain counting estimation. The X-ray digital imaging analysis technique provides a more accurate ilmenite content in 10084 of 10.2 wt % (Chambers et al., 1995), which is much closer to the 14.33 wt % upper estimate. The ilmenite content of 60500 has not been estimated in other studies, and there is no identifiable ilmenite in NWA 12592.

The doped simulant which contains 10 % added ilmenite has less than half the FeO content of the Apollo 11 soil, however they have similar ilmenite contents and afford similar yields. A comparison of FeO content with yield, and ilmenite content with yield is shown in Figure 6.25 for the samples used in this work and other lunar or lunar-like materials reacted at 1000 °C with hydrogen in previous studies (Allen et al., 1994; Gibson et al., 1994; McKay et al., 1991b; Sueyoshi et al., 2008). It should be noted that the results from literature were obtained from fluidised systems with various hydrogen pressures. All ilmenite values are derived from TiO_2 content. It can be seen that yield is more accurately predicted by maximum estimated ilmenite content (and therefore also TiO_2 content) than from FeO content (R^2 = 0.89 and 0.58 respectively). It is expected that more accurate ilmenite estimations using X-ray digital imaging analysis (Chambers et al., 1995) would provide improved yield estimations. It should be noted that higher than expected yields can be caused by reduction of the product rutile as seen in Gibson et al. (1994). Meanwhile, lower than expected yields are likely a result of either incomplete reaction and/or overestimated ilmenite concentrations.

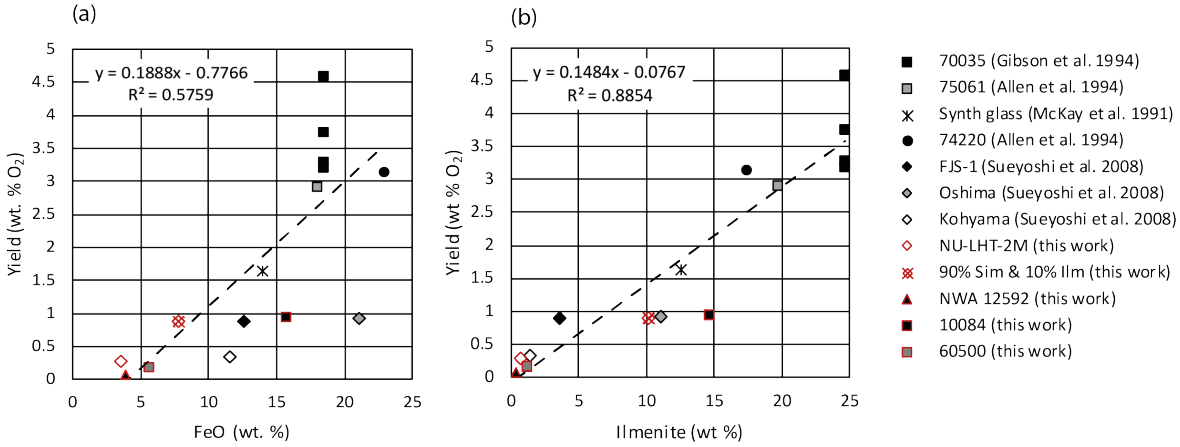

Figure 6.25: Experimental yields from lunar soils and simulants reduced by hydrogen at 1000 °C. Squares represent lunar soils, circles represent glasses, diamonds represent simulants, and triangles represent meteorites. Results are shown with respect to FeO content, and maximum possible ilmenite content.

6.7.4 Implications of the lunar environment for reduction by hydrogen experiments

There are some variables that can affect the rate of reaction for reduction by hydrogen studies that cannot currently be tested in a terrestrial laboratory environment. For example, could a low gravity environment such as that found on the Moon result in a lower density sample in the reactor oven, enabling gases to move more freely? Also, just how compositionally and geotechnically different will a high-latitude lunar soil be compared to the equatorial soils

sampled during Apollo, and how would that influence the reaction? How do Apollo samples that have been handled and exposed to Earth's atmosphere vary from the pristine lunar soils found on the lunar surface, and would any differences in these materials such as exposure to humidity influence the reaction? These questions could be answered by performing an ISRU demonstration mission at a high-latitude region of the Moon with ProSPA.

Most lunar soils are a mixture of feldspathic and mafic components. As a result, ilmenite is often likely to be present as a component in lunar soils (McKay et al., 1991a). Also, finer soils contain more ilmenite than larger-size fractions (McKay and Williams, 1979). Thus, fine soils, even those found in more highlands-like regions, are likely to produce higher yields than some lunar rocks, such as the genesis rock, that contains very little FeO and no ilmenite (Meyer, 2011). However, if a hydrogen reduction experiment were to be performed on a more titanium rich terrain, then the lunar rocks would likely contain more ilmenite than the soils, particularly compared to mature soils, a consequence of the impact melting process involved in regolith formation (Chambers et al., 1995). If an instrument has the capability to crush basaltic rock to a regolith-like consistency then it would prove to be a better target than soils for reduction by hydrogen, but for a proof of concept study all lunar soils should be able to be reduced somewhat.

The technique outlined in this work could be used anywhere on the Moon as a proof-of-concept water production demonstration. However, if considering a design to produce water in useable quantities to support a lunar base then adaptations would be required. For example, a fluidised bed would be recommended to improve the reaction rate (Hegde et al., 2011). Also, other products such as hydrogen sulfide would be produced in larger quantities from the reduction of sulfur bearing minerals present in lunar samples. Such products could prove damaging to the system, and purification of the produced water would be required before it could be used (Sanders and Larson, 2012). Other techniques are likely more suitable to produce the large scale (kg's to t's) quantities of oxygen from lunar rocks and soils that are needed to support lunar bases, such as those that can reduce all oxides through electrolysis (Lomax et al., 2020). However, these techniques are more energy intensive and require substantial infrastructure. In comparison, the technique outlined in this work is relatively simple and can be applied with small instruments on the lunar surface in the very near future.

6.8 Conclusions

Lunar soil simulants, lunar meteorites, and Apollo soils that contain iron oxide-bearing minerals such as pyroxene and olivine, along with ilmenite, can be reduced in a static system at 1000 °C in the presence of $\sim$ 0.3 mmol ($\sim$ 420 mbar) hydrogen. The highest yields were obtained for mare Apollo soil (10084), producing on average 0.94 wt % O_2, followed by a lunar highlands simulant NU-LHT-2M which produced on average 0.28 wt % O_2. Meanwhile, lower yields were obtained for the highlands Apollo soil (60500) producing an average of 0.18 wt % O_2, while the lowest yield was obtained from a crushed lunar meteorite producing on average 0.07 wt % O_2.

Apollo soils are most representative of the lunar regolith material expected to be sampled on the surface of the Moon as compared to a lunar highlands simulant and a crushed lunar meteorite. The Apollo lunar soils have the most appropriate grain size distribution, grain shape, and distribution of minerals within grains, which ultimately can influence the yields of water, and therefore oxygen, through reduction. However, as Apollo soils cannot be used for routine large-scale destructive ISRU studies, the priority for the selection of a proxy material should be on the ilmenite content. ProSPA is expected to land in a high-latitude south-polar region of the Moon which is likely to be highlands-like in terms of mineralogy. Therefore, a lunar simulant or crushed meteorite with relatively low ilmenite (< 1 %) would be recommended to represent the likely soils that will be sampled by ProSPA. As grain size also significantly influences reaction rates, the grain size distribution of any proxy material should also be representative of the expected lunar material at the proposed landing site.

The technique outlined in this work is recommended for use on small scale prospecting instruments as a proof-of-concept for early water production experiments on the Moon. It can be applied to any lunar soils and should be capable of producing a minimum of 1 μl of water from a 45 mg sample of highlands soil. If this experiment is performed on the lunar surface it would meet the "technology verification and demonstration" step of the ESA ISRU roadmap as one of the first in situ regolith reduction demonstrations. The laboratory results indicate that even with low ilmenite content in the lunar regolith, the ProSPA instrument will be capable of reducing the regolith and measuring yields within four hours. As oxygen extraction techniques are developed with specialised reactors and targeted mineral reserves the expected yields would be significantly higher. However, performing small scale reduction reactions on the lunar surface with ProSPA will help to identify any effects of the lunar environment on the reaction process, that could then feed into future reactor design.

Chapter 7

Summary and Conclusions

7.1 Summary

This thesis addresses the suitability of the ProSPA instrument for specific ISRU experiments on the lunar surface. The three aims of this work were: (1) Demonstrate that the hydrogen reduction of ilmenite reaction can proceed in a static system.; (2) Determine the optimum reaction conditions for performing hydrogen reduction of ilmenite with a ProSPA-like static system; and (3) Demonstrate successful hydrogen reduction of lunar material in a ProSPA-like static system. Through modelling, experiments, and instrument development, these aims were addressed.

7.1.1 Aim 1: Demonstrate that the hydrogen reduction of ilmenite reaction can proceed in a static system

For the reduction of regolith to be effective, a gas transport mechanism is necessary to remove the produced water from the reaction site and enable further hydrogen to be available for reaction. In a closed static system such as ProSPA (as opposed to the more common, dynamic gas flowing systems), gases are transported via diffusion as a result of partial pressure gradients. Partial pressure gradients of water can be created with a cold finger that condenses water out of the gas phase. The rate of gas diffusion in a ProSPA-like manifold was modelled in Chapter 2 to identify whether diffusion of water away from a sample was sufficient to enable the reaction to proceed in the time frame of ProSPA experiments (approximately four hours). Results from the 1D model showed that water should diffuse through a straight pipe (of ProSPA-like dimensions) on a scale of tens of minutes, which would be sufficient for the reaction to proceed and produce measurable yields within a four hour experiment. Next, a 2D model (developed by J. Martin) was used which considered 2D pipe designs more akin to

the ProSPA configuration. The 2D model also calculated the water production and hydrogen consumption rates from the reduction of the mineral ilmenite. Ilmenite is the most reactive iron oxide in lunar regolith that can be reduced by hydrogen to produce water. The 2D model was used to estimate the reaction rate and potential yields from the reduction of ilmenite in a static system. The results indicate that in a static system, the diffusion of water away from the reaction site is the rate controlling step. As the ProSPA manifold design is yet to be finalised, different pipe configurations were trialled. The reaction rate was shown to increase with shorter and/or wider pipes between the furnace and the cold finger.

Following promising results from the 2D model, ilmenite reduction was then trialled experimentally as described in Chapter 3. Experiments were performed in a ProSPA breadboard known as the BDM. An experimental procedure was outlined that started with the bake-out of an ilmenite sample to remove volatiles, followed by reduction by hydrogen for one hour at 900 °C. Finally, the cold finger was heated to release the reaction product, water, as a vapour into the closed system. Pressure measurements were used to monitor the reaction and to quantify yields. A range of ilmenite masses of up to 45 mg (the approximate sample size expected to be analysed by ProSPA) were reacted. It was shown that an 11.2 mg sample of ilmenite could reduce by up to 12 % in one hour, (i.e. 12 % of the available ilmenite was converted into iron, rutile, and water) demonstrating that reduction reactions were feasible in a static system. Larger samples reacted at a slower rate as the reactant and product gases were required to diffuse to and from deeper within the samples. Thus, it was determined that in a static system the sample geometry plays an important role in gas diffusion and therefore reaction rate.

Significant quantities of water were shown to condense onto the BDM pipework at pressures $>$ 120 mbar, a result of insufficient thermal control of the manifold. Consequently, yields could not be accurately quantified above the defined pressure limit. Therefore, a separate breadboard model was proposed which had improved thermal control and limited the amount of condensation of water onto the manifold. The ISRU-BDM, like the BDM, was designed to replicate the ISRU-relevant components of ProSPA, however, the manifold and cold finger were updated from the BDM design for improved thermal control (Chapter 4). The manifold was built with high-temperature components and placed within a heated box that operates at 120 °C to limit the condensation of water onto pipework. The cold finger was designed to be fitted inside a copper thermal mass, ensuring uniform heating and cooling of the cold finger. The ISRU-BDM was evaluated and shown to meet the required design criteria. The breadboard was used to quantify volumes of water to a higher accuracy than

with the BDM, and therefore the ISRU-BDM was deemed suitable for reduction experiments to address aims 2 and 3.

7.1.2 Aim 2: Determine the optimum reaction conditions for performing hydrogen reduction of ilmenite with a ProSPA-like static system

To maximise the potential yield from reduction experiments performed with ProSPA on the lunar surface, the reaction conditions should be optimised. Two variables that can be controlled with ProSPA that also affect the reaction rate are reaction temperature and hydrogen pressure. In Chapter 5, 45 mg samples of ilmenite were reduced with hydrogen in the ISRU-BDM for four hours under different temperature and pressure conditions.

Furnace temperatures of 850 °C to 1100 °C were trialled, and the results showed that with increasing temperature, the reaction rate increased, as is found in dynamic reactors. As the ilmenite began to melt at temperatures of > 1050 °C yields continued to increase, however, another reaction mechanism took place resulting in the formation of ferropseudobrookite. 1000 °C was deemed the optimal reaction temperature as it is within the ProSPA operational constraints.

The hydrogen pressure in a static system was shown to have a two-fold effect on the reaction rate. At the start of the reaction, lower hydrogen pressures were optimal. Initially, hydrogen quickly reacted with the outer surface of the ilmenite grains, and the produced water swiftly diffused through the small amount of hydrogen in the manifold. As the reaction proceeded, higher pressures were required to penetrate the reacted outer layer of the ilmenite grains to reach the unreacted core. The results suggest that for a four hour reaction, initial hydrogen pressures of ~ 418 mbar are optimal.

With the optimal reaction conditions, ilmenite was reduced by 33 % within four hours, producing yields of 3.51 ± 0.05 wt % O_2. The amount of hydrogen reacted was always greater than the amount of water collected at the cold finger. As the reactions were not completed within the four hour time frame, it was determined that there was residual water within the grains when the reaction was stopped, and that the amount of residual water generally increased when the reaction rate was higher.

7.1.3 Aim 3: Demonstrate successful hydrogen reduction of lunar material in a ProSPA-like static system

Applying the optimum reaction conditions identified in Chapter 5, the ISRU-BDM was used to reduce lunar-like and lunar material to determine whether a static system is suitable for

performing reduction reactions on the Moon. In Chapter 6, a lunar highland simulant, a crushed lunar meteorite, and two Apollo soils were reduced in the ISRU-BDM. The samples contained a range of ilmenite concentrations, and the two Apollo soils were representative of relatively ilmenite-rich and ilmenite-poor lunar soil. All samples reduced to some extent, with the Apollo mare soil (10084) producing the highest average yield of 0.94 ±0.03 wt % O_2 in four hours (Table 7.1). The samples with higher ilmenite concentrations produced higher yields, however, even samples with no ilmenite (lunar meteorite) reduced to some extent as other iron oxide-bearing minerals such as pyroxene and olivine were partially reduced. A static system such as ProSPA should therefore be capable of reducing lunar material and producing measurable yields regardless of the mineral composition of the regolith at the landing site.

Sample	Estimated max. ilmenite concentration (wt %)	Yield (wt % O_2)
NWA 12592	0.32	0.07 ± 0.02
60500	1.14	0.18 ± 0.02
NU-LHT-2M	0.7	0.29 ± 0.04
NU-LHT-2M:Ilmenite (90 %:10 %)	10.13	0.89 ± 0.04
10084	14.33	0.94 ± 0.03
Ilmenite	95	3.43 ±0 .14

Table 7.1: Calculated average yield of oxygen from the reduction of ilmenite, and lunar simulant and samples in the ISRU-BDM. Reactions were performed for four hours at a furnace temperature of 1000 °C, and with an average initial hydrogen pressure of between 424-436 mbar.

7.2 Recommendations for reduction experiments in a static system

This work has shown that the current ProSPA design should not require any modifications to successfully reduce lunar regolith to produce measurable quantities of water. However, the studies presented in this thesis have resulted in a series of recommendations to improve yields from reduction experiments in a static system such as ProSPA, and to improve the accuracy of yield quantification.

To improve yields:

- the pipe between the furnace and the cold finger should be as short and wide as possible so the produced water diffuses more quickly to the cold finger and condenses out of the vapour phase

- the reaction temperature should be as high as possible, providing the minerals are still solid
- For a four hour reaction time, hydrogen pressures of $\sim$ 418 mbar are optimal. For shorter reaction times, lower pressures are desirable, and for longer reactions, higher pressures are desirable
- a landing site with higher concentrations of ilmenite is preferable

To improve accuracy of yield quantification:

- ensure all components between the furnace and cold finger are uniformly heated so that the saturation vapour limit of water is not reached during experiments
- calibrate the adsorption of water onto pipework by producing adsorption isotherms for the closed system
- calibrate all volumes within the closed system
- calibrate the average temperature of the system for every possible scenario of furnace and cold finger temperature
- perform volatile extraction experiments prior to each ISRU demonstration for each sample. This will act as a bake-out, and therefore, indigenous volatiles will not contribute to the calculated yields

Other:

- if further reduction experiments are required and preserved lunar soils (e.g. Apollo samples) are not available, then lunar simulants with grain size and mineralogy (specifically ilmenite, pyroxene, and olivine content) similar to the desired lunar soil should be used as a proxy material

7.3 Future work

There are a number of potential avenues for further work as a continuation of this research. Suggested work includes further investigations and adaptations of the 2D model, further improvements of the ISRU-BDM, and further static reduction experiments.

7.3.1 2D model applications

The 2D model could be used to investigate the effects on reaction rate when considering different manifold designs, and inform where improvements could be made when considering the ProSPA manifold design. The model could also be developed to consider the reaction rate of different minerals, such as pyroxene and olivine, when in different combinations with ilmenite and non-reducing minerals. Therefore, potential yields from different materials could be predicted prior to experimental testing. A further development could be improved modelling of the diffusion of gases between grains, which was shown to have an effect on the reaction rate.

7.3.2 ISRU-BDM improvements

It is recommended that sample temperature is investigated to understand how uniformly the samples are heated within the sample holder under different furnace temperature and hydrogen pressure conditions. Different sample and sample holder dimensions could be studied to identify any limits of other potential static system designs. The ISRU-BDM system should also be optimised to minimise air leaks and perhaps reconfigure the experimental procedure to enable the use of data collection with the mass spectrometer during experiments. Consequently, the mass spectrometer could be used to quantify yields of water and to verify those calculated through pressure readings.

7.3.3 Static reduction studies

It is recommended that the ISRU-BDM is used to react all samples to completion. If the residual water within grains is lower at the end of the reaction, then the proposed hypothesis explaining why there is a discrepancy between the hydrogen lost and water produced in the reaction would be supported. A batch mode approach could be utilised to react samples to completion, where hydrogen concentrations are topped-up periodically during the experiment.

It would also be interesting to see how pyroclastic samples react in the static system, potentially showing the suitability of the simple system for other landing site locations.

7.4 Conclusions

A well-studied ISRU experiment, hydrogen reduction of regolith, has been adapted for use in a simple static system. Providing a system comprises a furnace, cold finger, and hydrogen

supply, it can be used to reduce lunar regolith to produce water. This technique could therefore be applied with the ProSPA instrument to perform one of the first ISRU demonstrations on the lunar surface as part of the Luna-27 mission.

Appendix A

2D ilmenite reduction model

The following work was produced by J. Martin as part of the SPIN scheme in 2018 (UK Space Agency, 2020), I have adapted it for inclusion here. J. Martin worked under the guidance of A. Morse and me.

The aim of the SPIN project was to develop a user-friendly application in MATLAB® to model the production and diffusivity of water from ilmenite reduction in various system set-ups. The diffusivity models outlined in Chapter 2 were utilised along with ilmenite reduction models described by Dang et al. (2015) to produce the ilmenite reduction 2D static model.

A.1 Model overview

The 2D model was developed with a focus on three key processes, the ilmenite reduction reaction, the diffusion of the product water through the manifold system, and finally the condensation of water at the cold finger. An overview of the processes for each stage of the simulation is described here.

A.1.1 Initial conditions

A cell map and matrix of volumes that corresponds to an input map and pipe dimensions are created. A matrix of temperatures is created which corresponds to inputs and the cell map, where no heat conduction is factored in between cells. The initial molar quantity of ilmenite, n_{ilm}, is determined from the input mass of ilmenite in the sample (where the molar mass of ilmenite is 152 g·mol^{-1}). The initial molar quantity of hydrogen, n_B, is set using the $H_2/FeTiO_3$ ratio input. The system has no water vapour molecules initially ($n_A = 0$) and at $t = 0$ it is assumed that all the hydrogen is evenly distributed in the system so that the pressure is equal. Pressure, P, is calculated for each cell using the ideal gas law

where $P = nRT/V$ and n is the molar amount of a gas, R is the ideal gas constant, T is the temperature of the cell, and V is the volume of the cell. The volume of each cell is related to the cell width, l_c, and pipe radius, r, as $V = l_c \pi r^2$. The pressure equalisation is solved directly to determine the initial molar quantity of hydrogen in each cell by equating the furnace, manifold, junction, and cold finger pressure (P_F, P_M, P_J, P_C respectively) as $P_F = P_M = P_J = P_C$ and Eqn. A.1, where the sum of the molar quantity of hydrogen in each cell equates to the maximum molar quantity of hydrogen (see Initialiser function in Section A.4.2 for the full solved equations).

$$\frac{n_F R T_F}{V_F} = \frac{n_M R T_M}{V_M} = \frac{n_J R T_J}{V_J} = \frac{n_C R T_C}{V_C} \tag{A.1}$$

The following processes: ilmenite reduction, diffusion of water through the system, and condensation of water at the cold finger, occur in a loop with the time elapsed increasing in each loop. The processes are described chronologically as they currently appear in the code.

A.1.2 Reaction

The ilmenite reduction reaction currently follows the model described by Dang et al. (2015). Firstly, the ratio of the molar quantity of water to hydrogen in the furnace cell is checked. If this is below the set mole fraction (10 % as standard taken from Taylor et al. (1993)) then the reaction can continue. In the case the condition is met, the reaction time, t_R, is advanced by the time interval. This measure of time is separate from the overall time elapsed of the simulation as it only advances when the reaction algorithm takes place and therefore there are no time discontinuities in the reaction fraction equation. The reaction fraction, ξ, at elapsed reaction time t_R is given in Eqn. A.2:

$$\xi = 1 - \left(1 - \frac{e^{-\frac{E_R}{RT_F}} t_R}{B_T}\right)^3 \tag{A.2}$$

where E_R is the activation energy (136.4×10^3 kJ·mol^{-1}), T_F is the furnace temperature, and $B_T = R_0/k$, where R_0 is the grain size and k is a constant (2.566×10^{-2}) derived from model results in Zhang et al. (2012). The molar quantity of water vapour in the furnace cell is then calculated at reaction time t_R as in Eqn. A.3 which represents the amount of water already present, plus the fraction of ilmenite reacted in the time interval. The same molar quantity

of hydrogen is removed during the reaction from the furnace cell.

$$n_A(t) = n_A(t - dt) + n_{ilm}(\xi(t_R) - \xi(t_R - dt)) \tag{A.3}$$

If the reaction cannot occur as a result of too much water ($>$ 10 % partial pressure H_2O to H_2) or if the reaction fraction has exceeded 1 (fully completed reaction), then nothing changes in the furnace cell. If the amount of product water calculated for the reaction within a time interval is greater than the reactant hydrogen currently available in the furnace, the amount of product water is reduced so that it equals the amount of reactant available. The reaction time, t_R, is then calculated by inversing the reaction fraction equation to make t_R the subject and determining the actual new reaction fraction from the product.

A.1.3 Diffusion

Fick's first law of diffusion is used to calculate the molar quantity of water and hydrogen that moves between each cell as a result of concentration gradients. The mean free paths of molecules, λ_{Ai} in each cell (i is used to denote a generic cell with a column and row position) are calculated using equations from Delchar (1993). The mean free path equation (Eqn. A.4) has been modified to include the number of both hydrogen (N_B) and water (N_A) molecules as they both will contribute to collisions with the water molecules. In this case, mean free path is determined by dividing the volume of each cell, V_i, by the number of molecules in each cell and the diameter of a water molecule, d_A, (see Table 2.1 in Chapter 2) and a constant, $\sqrt{2}$. The respective frequencies of collision are not considered and instead it is assumed that both water and hydrogen have equal probability of collision.

$$\lambda_{Ai} = \frac{V_i}{\sqrt{2}\,(N_B + N_A)\,i{d_A}^2} \tag{A.4}$$

The average velocity of the molecules in each cell, $\bar{C}_{iA}$, is given by Eqn. A.5.

$$\bar{C}_{iA} = \left(\frac{8k_BT_i}{\pi m_A}\right)^{\frac{1}{2}} \tag{A.5}$$

The diffusion coefficient for H_2 – H_2O transport for each cell, D_i, is calculated using Eqn. A.6 from Delchar (1993).

$$D_i = \frac{1}{3}\left(\bar{C}_A\lambda_{iA}\frac{n_{iB}}{n_{iB} + n_{iA}} + \bar{C}_B\lambda_{iB}\frac{n_{iA}}{n_{iB} + n_{iA}}\right) \tag{A.6}$$

The flux of water molecules, J_A, moving across a volume of cell length L_i as a result of the concentration between two adjacent cells (i and $i+1$) is given in Eqn. A.7.

$$J_A = D_{iA}\frac{\left(n_{iA} - n_{(i+1)A}\right)}{V_i}\frac{1}{L_i} \tag{A.7}$$

Note: the diffusion coefficients of each cell are calculated before any molecules are moved as this would cause instantaneous shifts of molecules from one side of the system to the other.

The logic behind the transport of gas molecules in the simulation is that the molar quantity that have been shifted as a result of diffusion from one cell to the next with each time interval is given by the flux multiplied by the cross sectional area and time interval, t, as in Eqn. A.8. This quantity of molecules is then also added to the $i+1$ cell. Overall the total number of particles is unchanged. If the number of molecules calculated to shift over the time interval is greater than the amount actually contained within the cell, a fail-safe is triggered where the entire amount of those molecules are shifted and no more (to avoid negative molar quantities occurring).

$$n_{iA}(t) = n_{iA}(t - dt) - J_{iA}Adt \tag{A.8}$$

It is assumed that the pressure equalisation occurs almost instantaneously in the simulation at timescales of up to 1 s. However, very small time intervals start to become less accurate due to the instantaneous shifting moving particles quicker than is true in practice.

A.1.4 Condensation

In the cold finger cell, any water molecules that are present after the shifting as a result of diffusion are removed during each simulation loop call – this describes instantaneous condensation as soon as water reaches the cold finger which is a reasonable assumption as the sharp temperature gradient in most experiments is enough to approximately have this condition. Removing these gas molecules means that the overall pressure of the system will decrease.

A.1.5 Simulation method

To equalise pressures in the system, the movement of molecules between adjacent cells is solved via simultaneous equations. An example for four adjacent cells is demonstrated in Figure A.1, although this can be extended for an arbitrary number of adjacent cells (which the code identifies and creates the necessary matrices for). Pressure in the four adjacent cells are equalised as in Eqn. A.9.

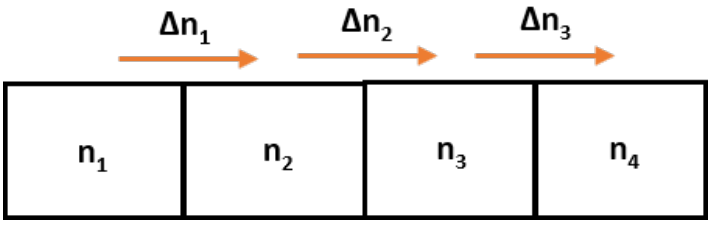

Figure A.1: Movement of gases between cells.

$$\frac{(n_1 - \Delta n_1)\, RT_1}{V_1} = \frac{(n_2 + \Delta n_1 - \Delta n_2)\, RT_2}{V_2} = \frac{(n_3 + \Delta n_2 - \Delta n_3)\, RT_3}{V_3} = \frac{(n_4 + \Delta n_3)\, RT_3}{V_3} \tag{A.9}$$

A set of three simultaneous equations for Δn_1, Δn_2 and Δn_3 are solved using inbuilt MATLAB® functions. This process is the same for longer pipe segments with utilise additional simultaneous equations. The same approach is used for equalising the pressure of junctions by considering the shifts between all adjacent cells to the central junction piece to equalise this. Because there is a separate set of equations for each pipe, this means that the whole system will not be exactly equalised and there will be small differences between each segment however the differences are negligible for the simulation and this method ensures that it behaves as desired. The simulation then repeats again following the described processes.

A.2 App GUI manual

A.2.1 Overview tab

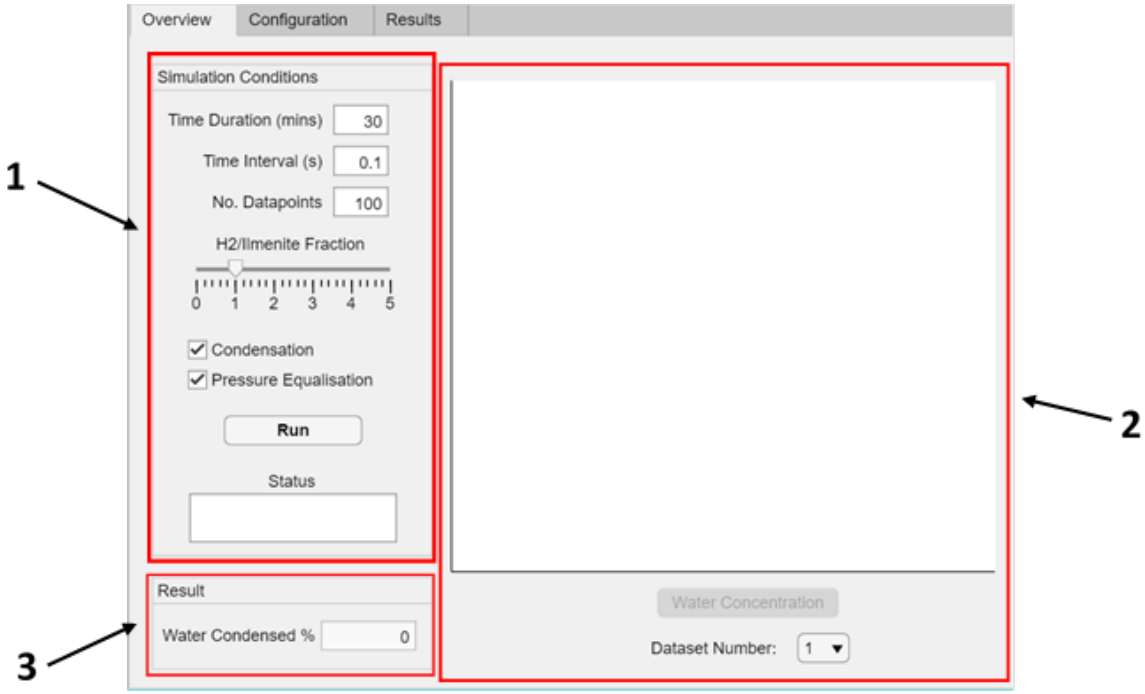

Figure A.2: GUI Overview tab.

1. Simulation conditions

- *Time Duration* – total time to simulate.
- *Time Interval* – decreasing the time interval avoids errors as it results in decreased shifts of particles at each interval, which avoids situations where the diffusion shift from one cell to another is greater than the amount of gas present in the cell.
- *No. Data points* – amount of snapshots of the simulation that will be recorded and displayed on the graphs in the Results tab.
- *$H_2/FeTiO_3$ Fraction* – slider that determines the initial amount of hydrogen in the system as a ratio of the maximum molar quantity of ilmenite sample. More precision of this is given in the Configuration tab.
- *Condensation* – allows the user to deactivate condensation of gases at the cold finger in order to perform a check that gases diffuse evenly in the model.
- *Pressure Equalisation* – see how the gas would behave without the pressure equalisation.
- *Run* – activate the simulation with all the current selections made for the inputs over all the tabs.
- *Status* – shows progress of simulation to give scale of duration to finish. If alerts are flagged during runtime they are shown here.

2. Simulation movie

- *Water Concentration* – this button activates a movie of the dataset identified by the drop down below. This movie is solely meant to act as a qualitative depiction of the simulation. The colour map represents the concentration of water vapour in each cell however it is scaled to the maximum concentration value in each case so is not suitable for comparing between movies of different runs.

3. Results

- *Water Condensed* – outputs the percentage of the molar quantity of water condensed at the cold finger, compared to the maximum molar quantity of ilmenite in the initial sample. Upon reaction completion, this should equal 100 %.

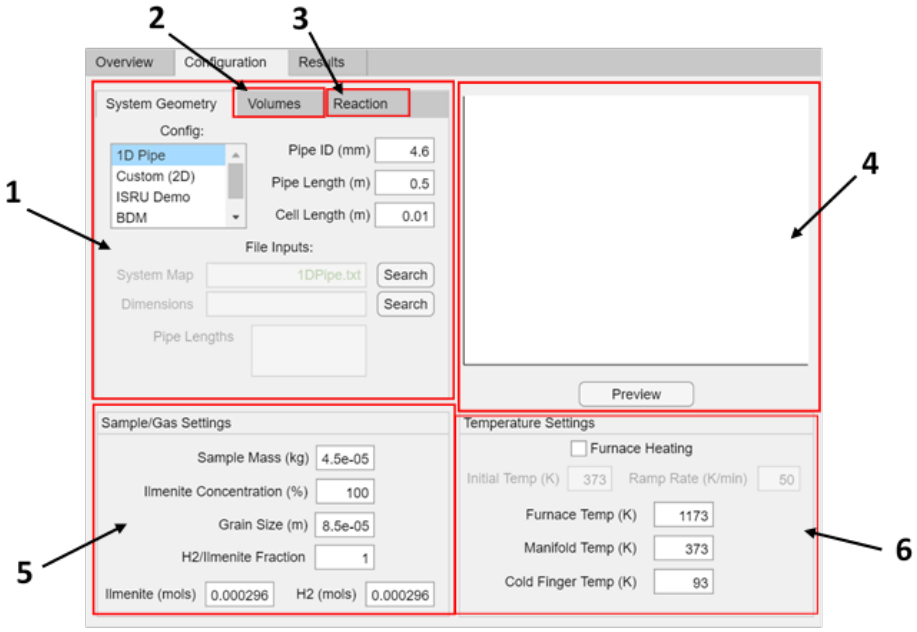

Figure A.3: GUI Configuration tab.

A.2.2 Configuration tab

1. System Geometry

- *Config* – list of preset system layouts. Each option enables/disables appropriate fields.
- *Pipe ID* – internal diameter of all pipes. Currently no functionality for different diameters for different sections. Preset for the ID of 1/4" Swagelok® fittings.
- *Pipe Length* - only enabled for the 1D case. Sets the length of the 1D pipe.
- *Cell Length* – this determines the size of each pipe cell to increase the accuracy of the system. Decreasing the cell length will increase the number of cells to process and increase the simulation runtime. Also, it increases the chance that the time interval is too large to handle the diffusion from each cell as there is less gas in each so may result in the need to decrease the time interval.
- *File Inputs* – selects the map and dimension files that construct the desired cell map. See Section A.3 for a guide on how to format these files.
- *Pipe Lengths* – the program will read the dimension files and display the pipe lengths in this box.

2. Volumes

- *Furnace/Cold Finger/Junction geometry* – in standard cell size case, each junction, cold finger and furnace will have the same dimensions as each other cell. If the exact properties of these components are known, this tab allows for these parameters to be inputted. This is the desirable case to represent the systems more accurately.

3. Reaction

- *Mole Fraction Threshold* – sets the threshold of the H_2O/H_2 mole fraction in the furnace. Any time the mole fraction is less than this, the reaction will proceed, while if it is over, no reaction will take place.

4. 2D system overview

- *Preview* – takes the current map file and dimensions and displays the system geometry on the diagram. There is no fixed scale to these diagrams, MATLAB® scales them to fit the dimensions the map takes up.

5. Sample/gas settings

- *Sample Mass* – used to calculate molar quantity of ilmenite, using a molar mass of 152 $g \cdot mol^{-1}$ for the ilmenite.
- *Concentration* – concentration of sample mass that is ilmenite and available as reactant. Amount of non-reactant currently has no effect on reaction rate.
- *Grain Size* – the average grain radius used to calculate B_T in the reaction rate.
- *H_2/$FeTiO_3$ Fraction* – same as in Overview tab. Exact precision.
- Initial molar quantity of H_2 and $FeTiO_3$ displayed.

6. Temperature settings

- *Furnace Heating* – keep fixed furnace temperature or enable heating during the simulation.
- *Initial Temp* – temperature of furnace at t=0 before heating.
- *Ramp Rate* – heating rate for furnace only.

- *Component Temps* – sets that temperature as fixed. No temperature gradients included in the simulation. This sets the final temperature of the furnace in the heating case.

A.2.3 Results tab

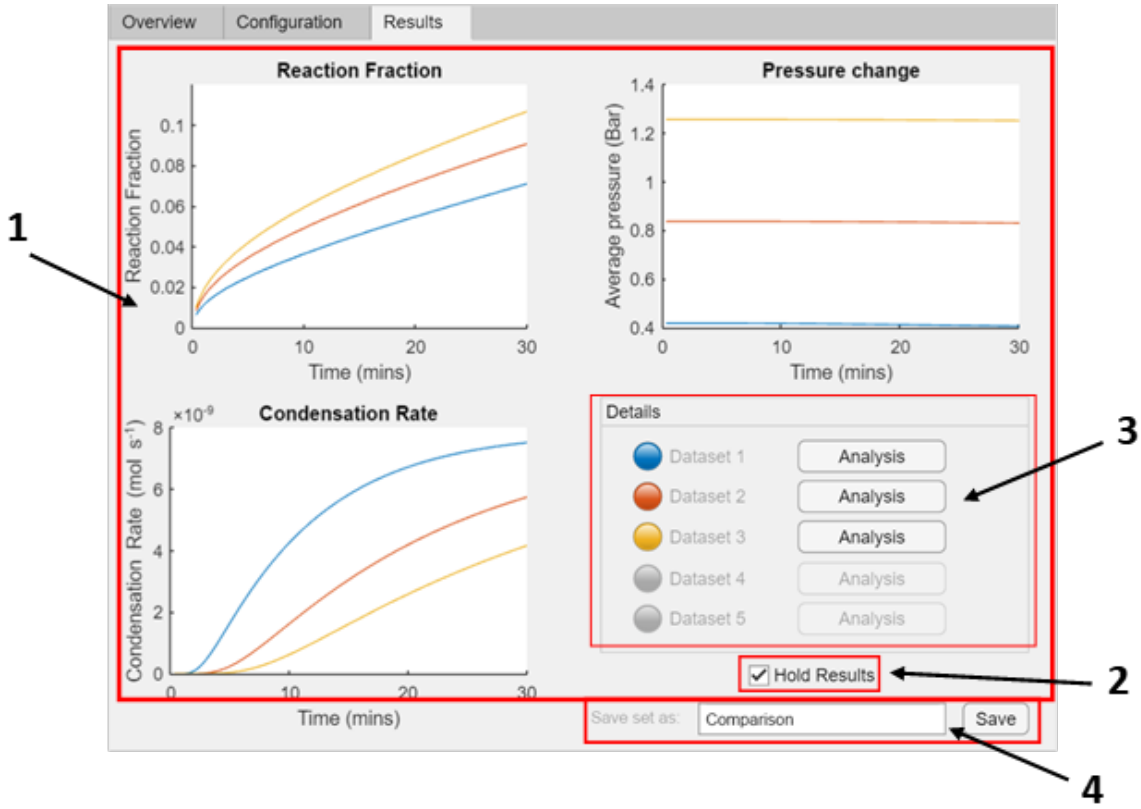

Figure A.4: GUI Results tab.

1. Graphs

- *Reaction Fraction* – measure of how complete the reduction of the sample is. Equates to a fraction of the total molar quantity of water produced in the furnace compared to initial ilmenite molar quantity.
- *Condensation Rate* – number of water molecules removed by the cold finger cell in each time interval.
- *Pressure* – takes the average of the pressure of all the cells in the system at that point in time

2. Hold results

- Ticking this will hold the current dataset and all those proceeding until the checkbox is unticked. Upon running if unticked, only the latest simulation will appear in the results.

A maximum of five results are possible after which the checkbox must be unticked to proceed.

3. Details

- This box will display all currently held datasets. The lamp light colours correspond to the curves on the graphs.
- *Analysis* – clicking on this will open up a separate dialogue box displaying details of the specific parameters used for that run.

4. Saving

- This provides the ability to save the graphs displayed currently on screen. The set will save as 'InputFieldText_ ReactionFraction', 'InputFieldText_Pressure', 'InputFieldText_CondensationRate'. The files will be saved to both .png and .fig files.
- IMPORTANT – the .fig files are saved as invisible so they do not pop up onscreen. To access these in the MATLAB® editor to further edit, enter openfig('enter filename here', 'Visible', 'on') when the figure is in the current active folder.

A.3 Input map and dimensions file

A.3.1 Input map files

To generate a custom 2D map, one must create a text file with the positions of components separated by tab spaces. A key to produce the input map files is shown in Table A.1, and examples of the files are shown in Figure A.5.

Number in text file	Component
0	No component
1	X-direction pipe
2	Y-direction pipe
3	Cross junction piece
4	Valve/dead end
5	Furnace
6	Cold finger

Table A.1: Key for creating input map files.

1D Pipe:

5	1	6

T Junction:

0	0	4
0	0	2
5	1	3
0	0	2
0	0	6

Cross Junction:

0	0	4	0	0
0	0	2	0	0
5	1	3	1	6
0	0	2	0	0
0	0	4	0	0

Figure A.5: Working examples of input map files.

Limitations

Currently there must be a sole piece that starts on the left hand side (hence the furnace is a good choice here). There is no compatibility to support further junctions that branch off the main pipe. Currently only pipe segments followed by a dead end/cold finger work. Currently only one cold finger and reactor is permitted. Examples of input map files that would not be permitted are shown in Figure A.6.

Not one piece on LHS:

4	0	0
2	0	0
3	1	6
2	0	0
5	0	0

Junction branching off another:

4	1	3	1	6
0	0	2	0	0
5	1	3	1	4

Figure A.6: Non-working examples of input map files.

A.3.2 Dimensions files

The input maps must be accompanied by a dimensions file instructing the code as to the lengths of each pipe segment. The dimensions should be entered in a single column in an order corresponding to the order of pipes encountered in the input map when indexing TOP $\rightarrow$ BOTTOM, LEFT $\rightarrow$ RIGHT.

A.4 Simulation process

A.4.1 Order of function calls:

1. All the input parameters taken from the GUI

2. Initialiser function called (calls Cell Mapper function within this)

3. Simulation function called within a loop in order to display progress of the simulation to the app (Reaction function called within the simulation)

4. Final data from last loop saved and results updated on the GUI

A.4.2 Function descriptions

- *Initialiser* – takes the input map, dimensions, temperature, sample and geometry conditions from the GUI and returns matrices mapping the initial temperatures, volumes, length and particle distributions of particles at $t = 0$

- *Cell Mapper* – uses the input map and dimensions to create a two dimensional matrix that represents each cell of the system. Returns the map and coordinates of the pipes necessary for the pressure solving algorithms.

- *Simulation* – calculates the reaction, diffusion, condensation and pressure equalisation at each time interval to simulate the system.

- *Reaction* – contains the equation used for the reduction reaction. Currently sourced from Dang et al. (2015) and Zhang et al. (2012).

Appendix B

Electronic control

B.1 Hardware

To enable automation, the ISRU-BDM was designed to include heating and cooling elements that can respond to temperatures recorded by thermocouples in the thermally independent parts of the system: at the furnace, cold finger, heated box, and outer manifold. A schematic of the ISRU-BDM electronics can be seen in Figures B.1 & B.2. Where practical, everything is powered by a 24 V DC power supply, however the heating elements require higher voltages in order to reach the required temperatures without drawing excessive current. The required temperatures and voltages of the heating elements are shown in Table B.1. Four Eurotherm® controllers with relays are used to monitor the temperatures of the thermally independent parts, and activate the relevant heaters and coolers when the temperature is below or above that which is selected. Information from each Eurotherm® is transmitted via a USB serial adaptor to the control laptop where the target temperatures are inputted by the user.

Heating element	Target temperature (°C)	Required voltage (V)
Heated box (oven heating elements)	120	230*
Outer manifold (resistance wire)	100	92**
Furnace (resistance heater)	1100	30**
Cold finger (resistance heater)	120	184**

Table B.1: Required temperature of heating elements within the ISRU-BDM and the associated voltage required. *mains electricity, **variac reduced from mains electricity.

The cold finger cooling element utilises a flow of cooled nitrogen gas. To do this the Eurotherm® signals a National Instruments™ 9472 sourcing digital output module which in turn activates a solenoid to open. The open solenoid allows room temperature nitrogen gas to flow through pipework which is placed within a dewar of liquid nitrogen before continuing to the cold finger. When the temperature of the cold finger is at or below the requested

temperature, the solenoid valve shuts. The sourcing digital output module is powered by a 24 V power supply.

All but one valve on the ISRU-BDM is pneumatically operated, the exception being the manual valve which supplies hydrogen from the external canister to the manifold within the heated box (See Figure 4.1 in Chapter 4). The pneumatic valves are controlled using another solenoid block which, when activated by a 24 V sourcing digital output module, allow 4 bar of air through to valves to open them. The sourcing digital output module is connected to a National Instruments™ CDAQ-9179 chassis which connects to the control laptop where the valves can be controlled.

The Kulite® pressure sensor is powered by a 24 V power supply and outputs pressure information in the form of voltage values, along with a zero (ground) reference value. The output voltages from the pressure sensor along with another ground wire are passed via a National Instruments™ 9923 connector block to a 9205 analogue input 32 channel module. The 9205 module is connected to the chassis and therefore the control laptop where the output voltages are processed and converted to pressures and recorded.

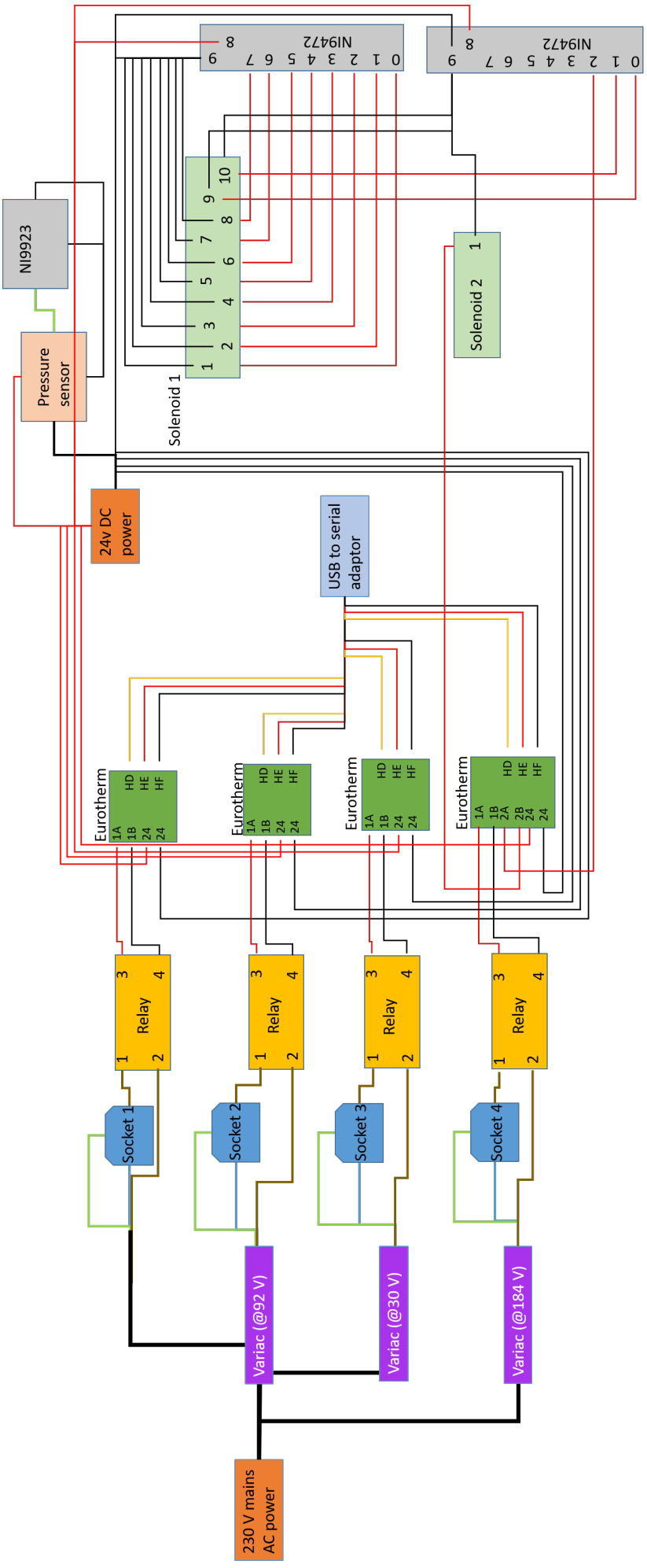

Figure B.1: Schematic for the electronics used in the ISRU-BDM.

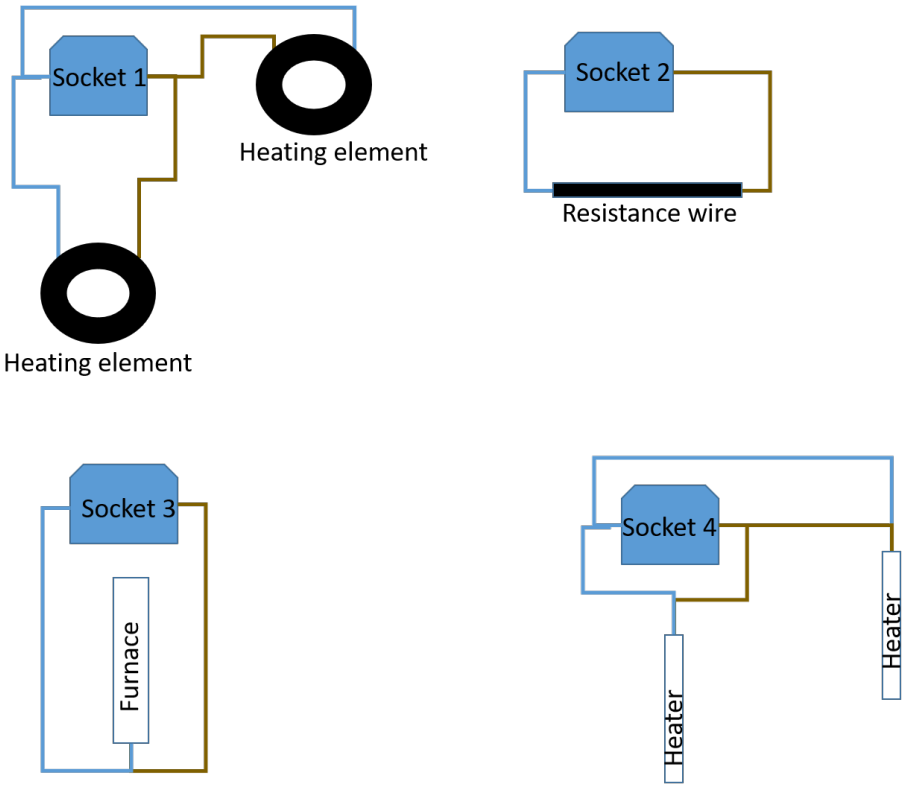

Figure B.2: Diagram showing each heating element and associated socket of the ISRU-BDM.

B.2 Software

LabVIEW™ software is used on the control laptop to activate valves and heating/cooling elements. The program was written by F. Abernethy and utilised by the author to operate the ISRU-BDM, and to write scripts to perform automated experiments. The user screen of the control laptop can be seen in Figure B.3.

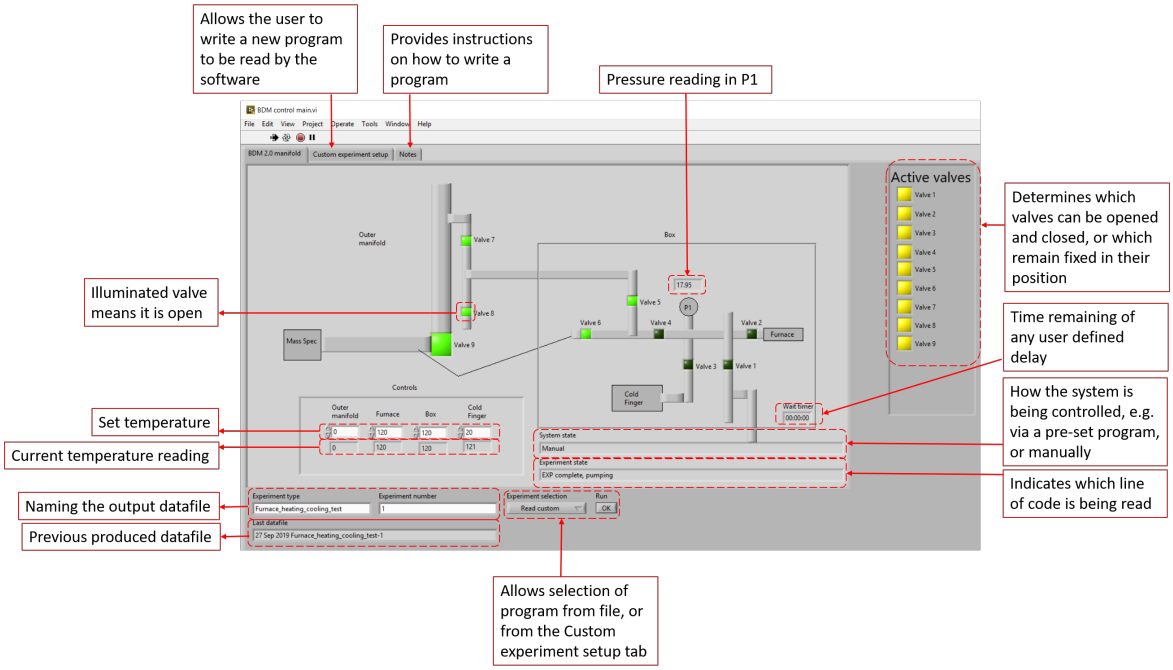

Figure B.3: The user screen of the control laptop

Automated scripts can be run from the user screen. The available commands include the opening and closing of valves, the setting of individual component temperatures, pausing until the required temperature has been reached, the recording of temperature and pressure readings independently or simultaneously, repeating readings for a defined number of times, and pausing for a defined period of time between each instruction. These instructions can be written directly into the 'Custom experiment setup' tab, or the instructions can be coded in a text file which can be read in via the user screen.

Appendix C

Sample preparation and sieving protocol

Equipment preparation:

1. All vials and caps for sample storage were sonicated in a bath of warm isopropyl alcohol (IPA) and rinsed with deionised water. They were dried with dry nitrogen gas. The glass vials were wrapped in foil and baked in a cleanroom oven at $\sim$ 100 °C for several hours. The plastic caps could not be baked and therefore 2 cm^2 sheets of Teflon, cleaned with IPA and deionised water, were placed between the cleaned vials and caps to secure samples.

2. The sieve and base plate were rinsed and wiped down with IPA, then rinsed with deionised water, and finally dried with dry nitrogen. They were then baked in a cleanroom oven at $\sim$ 100 °C for several hours.

3. Utensils such as tweezers and spatulas were wiped with IPA before each use.

Sample preparation:

1. In an ISO 7 cleanroom, the surface was wiped with IPA and the workspace was covered with aluminium foil.

2. A sheet of aluminium foil was placed on the micro-balance and tared. This base sheet was used to catch any loose grains that were lost in transfer.

3. A clean vial was placed on the balance, the mass of the vial was recorded and then removed from the micro-balance.

4. A folded sheet of aluminium foil was placed on the micro-balance and tared. This folded aluminium foil was used to measure the mass of the sample and transfer the sample into a vial.

5. The sample to be sieved was carefully opened, using an anti-static gun to minimise loss of sample.

6. A spatula was used to transfer the required amount of sample to be sieved onto the folded aluminium sheet. The mass of sample was recorded.

7. The sample was carefully transferred from the folded aluminium sheet and into the glass vial, and then sealed with a Teflon square and cap. The vial was then labelled.

8. The base foil sheet was removed from the micro-balance and disposed of. The spatula and tweezers were wiped with IPA.

9. The above steps were repeated for each sample type.

Sieving protocol:

1. In an ISO 7 cleanroom, the surface was wiped with IPA and the workspace was covered with aluminium foil.

2. A sheet of aluminium foil was placed on the micro-balance and tared. This base sheet caught any loose grains that were lost in transfer.

3. The clean sieve was placed securely onto the base plate, and a grounding cable was connected to the sieve to minimise static.

4. A folded sheet of aluminium foil was placed on the micro-balance which was then tared. This folded aluminium foil was used to measure the mass of the sample and to transfer the sample into a sieve.

5. The sample was carefully opened to be sieved, using an anti-static gun to minimise loss of sample.

6. A spatula was used to transfer the required amount of sample to be sieved onto the folded aluminium sheet. The mass of sample was recorded and the original sample vial was sealed.

7. The sample was carefully transferred from the folded aluminium sheet and onto the sieve.

8. The sieve was covered with a sheet of aluminium foil to minimise sample loss.

9. The sieve and base was shaken gently in a circular motion for $\sim$ 20 minutes.

10. A folded aluminium foil sheet was placed on the work surface to collect the sample. The sieve was removed from the base plate and the sieve was gently tapped to transfer the large grain size fraction onto the folded aluminium foil. Tweezers were used to pick up any grains that were lost in transfer.

11. The grains were carefully transferred from the aluminium foil into a glass vial. The vial was sealed with a Teflon square and cap, and was labelled. The aluminium foil was disposed of.

12. A new folded aluminium foil sheet was placed on the work surface to collect the fine grain sample. The base plate was gently tapped to transfer the fine fraction onto the folded aluminium foil. Tweezers were used to pick up any grains that were lost in transfer.

13. The fine grains were carefully transferred from the aluminium foil into a glass vial. The vial was sealed with a Teflon square and cap, and was labelled. The aluminium foil was disposed of.

14. The equipment was cleaned before it was used with another sample.

Appendix D

EATG treatment protocol

The following EATG treatment protocol was devised and implemented by J. Gibson at the Open University:

1. In a fume cupboard, powdered meteorite was placed in a 45 mm tapered screw-cap disposable polypropylene centrifuge tube (suitable for samples > 100 mg).

2. EATG solution was slowly pipetted into the tube to a quarter full using a disposable glass pipette or syringe. To start, drop by drop was added to take care in case of a vigorous reaction.

3. The sample was checked to see if it turned a strong violet colour as ferrothioglycolate was produced from the dissolution of oxidised compounds.

4. The sample and the EATG was left to react for two hours, mixing every ten minutes using a vortex mixer.

5. During this two hour period, if the purple colouration became extremely dark, the EATG reagent was replaced and continued to mix every ten minutes. Waste EATG was placed in a labelled waste container for subsequent disposal.

6. After two hours, the samples were centrifuged for five minutes at 2500 revolutions per minute (RPM) for easy removal and disposal of EATG.

7. EATG was removed and the sample was washed four times using water:IPA (50:50), using the centrifuge after each wash to remove the IPA solution. Waste IPA solution was discarded in a labelled waste container.

8. Finally, the sample was washed using IPA, and the sample was left to dry in the fume cupboard.

Bibliography

Aggarwal, H. R. and Oberbeck, V. R. (1979), Monte carlo simulation of lunar megaregolith and implications, *in* '10th Lunar and Planetary Science Conference', Vol. 10, pp. 2689–2705.

Aldridge, E. C. (2004), *Journey to Inspire, Innovate, and Discover: Report of the President's Commission on the Implementation of United States Space Exploration Policy*, Government Printing Office.

Ali, A., Jabeen, I., Gregory, D., Verish, R. and Banerjee, N. R. (2016), 'New triple oxygen isotope data of bulk and separated fractions from SNC meteorites: Evidence for mantle homogeneity of Mars', *Meteoritics & Planetary Science* **51**(5), 981–995. doi: https://doi.org/10.1111/maps.12640.

Allen, C. C., McKay, D. S. and Morris, R. V. (1992), Hydrogen reduction of lunar simulant glass, *in* '23rd Lunar and Planetary Science Conference', Vol. 23, pp. 21–22.

Allen, C. C., Morris, R. V., Lauer Jr, H. V. and McKay, D. S. (1993), 'Microscopic iron metal on glass and minerals—a tool for studying regolith maturity', *Icarus* **104**(2), 291–300. doi: https://doi.org/10.1006/icar.1993.1102.

Allen, C. C., Morris, R. V. and McKay, D. S. (1994), 'Experimental reduction of lunar mare soil and volcanic glass', *Journal of Geophysical Research: Planets* **99**(E11), 23173–23185. doi: https://doi.org/10.1029/94JE02321.

Allen, C. C., Morris, R. V. and McKay, D. S. (1996), 'Oxygen extraction from lunar soils and pyroclastic glass', *Journal of Geophysical Research: Planets* **101**(E11), 26085–26095. doi: https://doi.org/10.1029/96JE02726.

Altenberg, B. H. (1992), Oxygen production on the lunar materials processing frontier, *in* 'Lunar Materials Technology Symposium', number 93N27967.

Altenberg, B. H., Franklin, H. A. and Jones, C. H. (1993), Thermodynamics of lunar ilmenite reduction, *in* '24th Lunar and Planetary Science Conference', Vol. 24, pp. 27–28.

Anand, M., Crawford, I. A., Balat-Pichelin, M., Abanades, S., van Westrenen, W., Péraudeau, G., Jaumann, R. and Seboldt, W. (2012), 'A brief review of chemical and mineralogical resources on the Moon and likely initial in situ resource utilization (ISRU) applications', *Planetary and Space Science* **74**(1), 42–48. doi: https://doi.org/10.1016/j.pss.2012.08.012.

Bagdigian, R. M., Dake, J., Gentry, G. and Gault, M. (2015), International Space Station environmental control and life support system mass and crewtime utilization in comparison to a long duration human space exploration mission, *in* '45th Conference on Environmental Systems'.

Ballantyne, G. R., Powell, M. S. and Tiang, M. (2012), Proportion of energy attributable to comminution, *in* 'Proceedings of the 11th Australasian Institute of Mining and Metallurgy Mill Operator's Conference', pp. 25–30.

Barber, S. J., Wright, I. P., Abernethy, F., Anand, M., Dewar, K. R., Hodges, M., Landsberg, P., Leese, M. R., Morgan, G. H., Morse, A. D., Mortimer, J., Sargeant, H. M., Sheard, I., Sheridan, S., Verchovsky, A., Goesmann, F., Howe, C., Morse, T., Lillywhite, N., Quinn, A., Missaglia, N., Pedrali, M., Reiss, P., Rizzi, F., Rusconi, A., Savoia, M., Zamboni, A., Merrifield, J. A., Gibson, E. K. J., Carpenter, J., Fisackerly, R., Houdou, B., Sefton-Nash, E. and Trautner, R. (2018), ProSPA: Analysis of lunar polar volatiles and ISRU demonstration on the Moon, *in* '49th Lunar and Planetary Science Conference', number #2172.

Bardi, G., Gozzi, D. and Stranges, S. (1987), 'High temperature reduction kinetics of ilmenite by hydrogen', *Materials Chemistry and Physics* **17**(4), 325–341. doi: https://doi.org/10.1016/0254-0584(87)90085-X.

Basu, A. (1977), Steady state, exposure age, and growth of agglutinates in lunar soils, *in* '8th Lunar and Planetary Science Conference', Vol. 8, pp. 3617–3632.

Basu, A. (2005), 'Nanophase Fe^0 in lunar soils', *Journal of Earth System Science* **114**, 375–380. doi: https://doi.org/10.1007/BF02702956.

Biswas, J., Sheridan, S., Pitcher, C., Richter, L., Reganaz, M., Barber, S. J. and Reiss, P. (2020), 'Searching for potential ice-rich mining sites on the Moon with

the Lunar Volatiles Scout', *Planetary and Space Science* **181**, 104826. doi: https://doi.org/10.1016/j.pss.2019.104826.

Briggs, R. A. and Sacco, A. (1991), 'Hydrogen reduction mechanisms of ilmenite between 823 and 1353 K', *Journal of Materials Research* **6**(3), 574–584. doi: https://doi.org/10.1557/JMR.1991.0574.

Britt, D. T. (1993), The spectral effects of subsolidus reduction of olivine and pyroxene, *in* '24th Lunar and Planetary Science Conference', Vol. 24, pp. 195–196.

Burke, J. D. (2012), Perpetual sunshine, moderate temperatures and perpetual cold as lunar polar resources, *in* V. Badesu, ed., 'Moon', Springer, pp. 335–345. doi: https://doi.org/10.1007/978-3-642-27969-0.

Carpenter, J. D., Barber, S. J., Cerroni, P., Fisackerly, R., Fumagalli, A., Houdou, B., Howe, C. J., Magnani, P. G., Morse, A. D., Monchieri, E., Reiss, P., Richter, L., Rizzi, F., Sheridan, S., Waugh, L. J. and Wright, I. P. (2014), 'Accessing and Assessing Lunar Resources with PROSPECT', *Annual Meeting of the Lunar Exploration Analysis Group* .

Carpenter, J. D., Fisackerly, R. and Houdou, B. (2016), 'Establishing lunar resource viability', *Space Policy* **37**, 52–57. doi: https://doi.org/10.1016/j.spacepol.2016.07.002.

Carpenter, J. D., Hufenbach, B., Landgraf, S., de Mey, S., Borggraefe, A., Bergamasco, A., Sefton-Nash, E., Fisackerly, R., Houdou, B., de Rosa, D., Lefort, X., Trautner, R., Laurini, D., Schoonejans, P., Pastor, S., Hosseini, S. Braun, M. and Parker, D. (2018), Lunar exploration plans in ESA, *in* 'European Lunar Symposium'.

Carrier, W. D. (1973), 'Lunar soil grain size distribution', *The Moon* **6**(3-4), 250–263. doi: https://doi.org/10.1007/BF00562206.

Carrier, W. D., Olhoeft, G. R. and Mendell, W. (1991), Physical properties of the lunar surface, *in* G. H. Heiken, D. T. Vaniman and B. M. French, eds, 'Lunar Sourcebook', Cambridge University Press, pp. 475–594.

Cesaretti, G., Dini, E., De Kestelier, X., Colla, V. and Pambaguian, L. (2014), 'Building components for an outpost on the Lunar soil by means of a novel 3D printing technology', *Acta Astronautica* **93**, 430–450. doi: https://doi.org/10.1016/j.actaastro.2013.07.034.

Chambers, J. G., Taylor, L. A., Patchen, A. and McKay, D. S. (1995), 'Quantitative mineralogical characterization of lunar high-Ti mare basalts and soils for oxygen pro-

duction', *Journal of Geophysical Research: Planets* **100**(E7), 14391–14401. doi: https://doi.org/10.1029/95JE00503.

Christiansen, E. L., Simonds, C. H. and Fairchild, K. O. (1988), Conceptual design of a lunar oxygen pilot plant, Report 88-182, Eagle Engineering Inc.

Climent, B., Torroba, O., González-Cinca, R., Ramachandran, N. and Griffin, M. D. (2014), 'Heat storage and electricity generation in the Moon during the lunar night', *Acta Astronautica* **93**, 352–358. doi: https://doi.org/10.1016/j.actaastro.2013.07.024.

Colaprete, A., Schultz, P., Heldmann, J., Wooden, D., Shirley, M., Ennico, K., Hermalyn, B., Marshall, W., Ricco, A. and Elphic, R. C. (2010), 'Detection of water in the LCROSS ejecta plume', *Science* **330**(6003), 463–468. doi: https://doi.org/10.1126/science.1186986.

Cornish, L. and Doyle, A. (1984), 'Use of ethanolamine thioglycollate in the conservation of pyritized fossils', *Palaeontology* **27**(Part 2), 421–424.

Crawford, I. A. (2015), 'Lunar resources: A review', *Progress in Physical Geography* **39**, 137–167. doi: https://doi.org/10.1177/0309133314567585.

Dainty, A. M., Toksöz, M. N., Anderson, K. R., Pines, P. J., Nakamura, Y. and Latham, G. (1974), 'Seismic scattering and shallow structure of the Moon in Oceanus Procellarum', *The Moon* **9**(1-2), 11–29. doi: https://doi.org/10.1007/BF00565388.

Dang, J., Chou, K., Hu, X. and Zhang, G. (2013), 'Reduction kinetics of metal oxides by hydrogen', *Steel Research International* **84**(6), 526–533. doi: https://doi.org/10.1002/srin.201200242.

Dang, J., Zhang, G.-h. and Chou, K.-c. (2015), 'Kinetics and mechanism of hydrogen reduction of ilmenite powders', *Journal of Alloys and Compounds* **619**, 443–451. doi: https://doi.org/10.1016/j.jallcom.2014.09.057.

Dawson, V. P. and Bowles, M. D. (2004), *Taming liquid hydrogen: the Centaur upper stage rocket, 1958-2002*, National Aeronautics and Space Administration.

Dean, J. A. (1999), Thermodynamic properties, Table 6.4, *in* J. A. Dean, ed., 'Lange's handbook of chemistry', 15 edn, New york; London: McGraw-Hill, Inc.

Deer, W. A., Howie, R. A. and Zussman, J. . (1992), Ilmenite, *in* 'An introduction to the rock-forming minerals', 2 edn, Longman Scientific & Technical, pp. 390–392. doi: https://doi.org/10.1180/DHZ.

Delchar, T. A. (1993), *Vacuum physics and techniques*, Chapman and Hall.

Engelschiøn, V. S., Eriksson, S. R., Cowley, A., Fateri, M., Meurisse, A., Kueppers, U. and Sperl, M. (2020), 'EAC-1A: A novel large-volume lunar regolith simulant', *Scientific Reports* **10**(1), 5473. doi: https://doi.org/10.1038/s41598-020-62312-4.

Evans, H. T. (1970), 'Lunar troilite: crystallography', *Science* **167**(3918), 621–623. doi: https://doi.org/10.1126/science.167.3918.621.

Fegley, J. B. and Swindle, T. D. (1993), Lunar volatiles: Implications for lunar resource utilization, *in* J. S. Lewis, M. S. Matthews and M. L. Guerrieri, eds, 'Resources of Near-Earth Space', University of Arizona Press, pp. 367–426.

Fielder, G., Wilson, L. and Guest, J. E. (1966), 'The Moon from Luna 9', *Nature* **209**, 851–853. doi: https://doi.org/10.1038/209851a0.

Flahaut, J., Carpenter, J., Williams, J.-P., Anand, M., Crawford, I. A., van Westrenen, W., Füri, E., Xiao, L. and Zhao, S. (2020), 'Regions of interest (ROI) for future exploration missions to the lunar South Pole', *Planetary and Space Science* **180**, 104750. doi: https://doi.org/10.1016/j.pss.2019.104750.

Füri, E., Deloule, E., Gurenko, A. and Marty, B. (2014), 'New evidence for chondritic lunar water from combined D/H and noble gas analyses of single Apollo 17 volcanic glasses', *Icarus* **229**, 109–120. doi: https://doi.org/10.1016/j.icarus.2013.10.029.

Gaddis, L. R., Pieters, C. M. and Hawke, B. R. (1985), 'Remote sensing of lunar pyroclastic mantling deposits', *Icarus* **61**(3), 461–489. doi: https://doi.org/10.1016/0019-1035(85)90136-8.

Gaddis, L. R., Staid, M. I., Tyburczy, J. A., Hawke, B. R. and Petro, N. E. (2003), 'Compositional analyses of lunar pyroclastic deposits', *Icarus* **161**(2), 262–280. doi: https://doi.org/10.1016/S0019-1035(02)00036-2.

Garrett-Bakelman, F. E., Darshi, M., Green, S. J., Gur, R. C., Lin, L., Macias, B. R., McKenna, M. J., Meydan, C., Mishra, T., Nasrini, J. et al. (2019), 'The NASA Twins Study: A multidimensional analysis of a year-long human spaceflight', *Science* **364**(144). doi: https://doi.org/10.1126/science.aau8650.

Geankoplis, C. J. (1993), *Transport Processes and Unit Operations.*, 3 edn, PTR Prentice-Hall, Engelwood Cliffs, NJ.

Genda, H. (2018), Giant impact hypothesis, *in* W. M. White, ed., 'Encyclopedia of Geochemistry: A Comprehensive Reference Source on the Chemistry of the Earth', Springer International Publishing, Cham, pp. 617–620. doi: https://doi.org/10.1007/978-3-319-39312-4.

Gibson, M. A. and Knudsen, C. W. (1985), Lunar oxygen production from ilmenite, *in* W. W. Mendell, ed., 'Lunar bases and space activities of the 21st century', Lunar and Planetary Institute, pp. 543–550.

Gibson, M. A., Knudsen, C. W., Brueneman, D. J., Allen, C. C., Kanamori, H. and McKay, D. S. (1994), 'Reduction of lunar basalt 70035: Oxygen yield and reaction product analysis', *Journal of Geophysical Research: Planets* **99**(E5), 10887–10897. doi: https://doi.org/10.1029/94JE00787.

GmD Mineral Trade Company (2020), 'Ilmenite powder'. [Accessed 9th March 2020]. **URL:** *http://gmd-cologne.com/en/ilmenite_powder_en.html*

Goldstein, J. I., Newbury, D. E., Michael, J. R., Ritchie, N. W. M., Scott, J. H. J. and Joy, D. C. (2018), SEM image interpretation, *in* 'Scanning Electron Microscopy and X-ray Microanalysis', Springer. doi: https://doi.org/10.1007/978-1-4939-6676-9_7.

Greenwood, J. P., Itoh, S., Sakamoto, N., Warren, P., Taylor, L. and Yurimoto, H. (2011), 'Hydrogen isotope ratios in lunar rocks indicate delivery of cometary water to the Moon', *Nature Geoscience* **4**(2), 79–82. doi: https://doi.org/10.1038/ngeo1050.

Greenwood, R. C., Franchi, I. A., Gibson, J. M. and Benedix, G. K. (2012), 'Oxygen isotope variation in primitive achondrites: The influence of primordial, asteroidal and terrestrial processes', *Geochimica et Cosmochimica Acta* **94**, 146–163. doi: https://doi.org/10.1016/j.gca.2012.06.025.

Hadler, K., Martin, D. J. P., Carpenter, J., Cilliers, J. J., Morse, A., Starr, S., Rasera, J. N., Seweryn, K., Reiss, P. and Meurisse, A. (2019), 'A universal framework for space resource utilisation (SRU)', *Planetary and Space Science* p. 104811. doi: https://doi.org/10.1016/j.pss.2019.104811.

Hartmann, W. K. (1973), 'Ancient lunar mega-regolith and subsurface structure', *Icarus* **18**, 634–636. doi: https://doi.org/10.1016/0019-1035(73)90066-3.

Hartmann, W. K. (1980), Dropping stones in magma oceans: Effects of early lunar cratering, *in* 'Conference on the Lunar Highlands Crust', pp. 155–171.

Hawke, B. R., Coombs, C. R. and Clark, B. (1990), Ilmenite-rich pyroclastic deposits: An ideal lunar resource, *in* '20th Lunar and Planetary Science Conference', pp. 249–258.

Hegde, U., Balasubramaniam, R. and Gokoglu, S. (2009), Development and validation of a model for hydrogen reduction of JSC-1A, *in* '47th AIAA Aerospace Sciences Meeting including the New Horizons Forum and Aerospace Exposition', p. 1389.

Hegde, U., Balasubramaniam, R., Gokoglu, S., Rogers, K., Reddington, M. and Oryshchyn, L. (2011), Hydrogen reduction of lunar regolith simulants for oxygen production, *in* '49th AIAA Aerospace Sciences Meeting including the New Horizons Forum and Aerospace Exposition', p. 608.

Heiken, G. (1975), 'Petrology of lunar soils', *Reviews of Geophysics* **13**(4), 567–587. doi: https://doi.org/10.1029/RG013i004p00567.

Heiken, G. H., McKay, D. S. and Brown, R. W. (1974), 'Lunar deposits of possible pyroclastic origin', *Geochimica et Cosmochimica Acta* **38**(11), 1703–1718. doi: https://doi.org/10.1016/0016-7037(74)90187-2.

Hickman, J. M., Curtis, H. B. and Landis, G. A. (1990), Design considerations for lunar base photovoltaic power systems, *in* '21st Photovoltaic Specialists Conference', NASA, Kissimmee, FL.

Hiesinger, H. and Head III, J. W. (2006), New views of lunar geoscience: An introduction and overview, *in* B. L. Jolliff, M. A. Wieczorek, C. K. Shearer and C. R. Neal, eds, 'New Views of the Moon', Vol. 60, Mineralogical Society of America, pp. 1–81. doi: https://doi.org/10.2138/rmg.2006.60.1.

Honniball, C. I., Lucey, P. G., Li, S., Shenoy, S., Orlando, T. M., Hibbitts, C. A., Hurley, D. M. and Farrell, W. M. (2020), 'Molecular water detected on the sunlit Moon by SOFIA', *Nature Astronomy* . doi: https://doi.org/10.1038/s41550-020-01222-x.

Hörz, F., Grieve, R., Heiken, G., Spudis, P. and Binder, A. (1991), Lunar surface processes, *in* G. H. Heiken, D. T. Vaniman and B. M. French, eds, 'Lunar Sourcebook', Cambridge University Press, pp. 61–120.

Ichimura, A. S., Zent, A. P., Quinn, R. C., Sanchez, M. R. and Taylor, L. A. (2012), 'Hydroxyl (OH) production on airless planetary bodies: Evidence from H^+/D^+ ion-beam experiments', *Earth and Planetary Science Letters* **345-348**, 90–94. doi: https://doi.org/10.1016/j.epsl.2012.06.027.

International Space Exploration Coordination Group (2018), 'The Global Exploration Roadmap'.
URL: *https://www.nasa.gov/sites/default/files/atoms/files/ger_2018_small_mobile.pdf*

Ip, W.-H., Yan, J., Li, C.-L. and Ouyang, Z.-Y. (2014), 'Preface: The Chang'e-3 lander and rover mission to the Moon', *Research in Astronomy and Astrophysics* **14**(12), 1511–1513. doi: https://doi.org/10.1088/1674-4527/14/12/001.

Johnson, D., Jolliff, B., Zeigler, R. and Carpenter, P. (2009), Distribution of Ti in glass and mineral components of lunar soils 10084 and 71501; grain size fraction 100 to 210 μm, *in* '40th Lunar and Planetary Science Conference', number #2346.

Joly, J. P., Gaillard, F., Peillex, E. and Romand, M. (2000), 'Temperature-programmed desorption (TPD) of water from iron, chromium, nickel and 304L stainless steel', *Vacuum* **59**(4), 854–867. doi: https://doi.org/10.1016/S0042-207X(00)00393-6.

Keller, B., Clark, D. and Kirkland, J. (2009), Field test results of the PILOT hydrogen reduction reactor, *in* 'AIAA SPACE 2009 Conference & Exposition', p. 6475. doi: https://doi.org/10.2514/6.2009-6475.

Keller, J. W., Petro, N. E. and Vondrak, R. R. (2016), 'The Lunar Reconnaissance Orbiter Mission – Six years of science and exploration at the Moon', *Icarus* **273**, 2–24. doi: https://doi.org/10.1016/j.icarus.2015.11.024.

King, O., Warren, T., Bowles, N., Sefton-Nash, E., Fisackerly, R. and Trautner, R. (2020), 'The Oxford 3D thermophysical model with application to PROSPECT/Luna 27 study landing sites', *Planetary and Space Science* **182**, 104790. doi: https://doi.org/10.1016/j.pss.2019.104790.

Kleinhenz, J., Yuan, Z., Sacksteder, K. and Caruso, J. (2009), Development of a reactor for the extraction of oxygen and volatiles from lunar regolith, *in* '47th AIAA Aerospace Sciences Meeting including the New Horizons Forum and Aerospace Exposition', p. 1203.

Lai, J., Xu, Y., Zhang, X., Xiao, L., Yan, Q., Meng, X., Zhou, B., Dong, Z. and Zhao, D. (2019), 'Comparison of dielectric properties and structure of lunar regolith at chang'e-3 and chang'e-4 landing sites revealed by ground-penetrating radar', *Geophysical research letters* **46**(22), 12783–12793. doi: https://doi.org/10.1029/2019gl084458.

Landis, G. A. (1990), 'Degradation of the lunar vacuum by a moon base', *Acta Astronautica* **21**(3), 183–187. doi: https://doi.org/10.1016/0094-5765(90)90110-7.

Landis, G. A. (2007), 'Materials refining on the Moon', *Acta Astronautica* **60**(10-11), 906–915. doi: https://doi.org/10.1016/j.actaastro.2006.11.004.

Lasue, J., Wiens, R. C., Clegg, S. M., Vaniman, D. T., Joy, K. H., Humphries, S., Mezzacappa, A., Melikechi, N., McInroy, R. E. and Bender, S. (2012), 'Remote laser-induced breakdown spectroscopy (LIBS) for lunar exploration', *Journal of Geophysical Research: Planets* **117**. doi: https://doi.org/10.1029/2011JE003898.

Lawrence, D. J., Feldman, W. C., Barraclough, B. L., Binder, A. B., Elphic, R. C., Maurice, S. and Thomsen, D. R. (1998), 'Global elemental maps of the Moon: The Lunar Prospector gamma-ray spectrometer', *Science* **281**, 1484–1489. doi: https://doi.org/10.1126/science.281.5382.1484.

Lawrence, D. J., Feldman, W. C., Elphic, R. C., Little, R. C., Prettyman, T. H., Maurice, S., Lucey, P. G. and Binder, A. B. (2002), 'Iron abundances on the lunar surface as measured by the Lunar Prospector gamma-ray and neutron spectrometers', *Journal of Geophysical Research: Planets* **107**, 13–1–13–26. doi: https://doi.org/10.1029/2001JE001530.

Lee, K. A., Oryshchyn, L., Paz, A., Reddington, M. and Simon, T. M. (2013), 'The ROxygen Project: Outpost-scale lunar oxygen production system development at Johnson Space Center', *Journal of Aerospace Engineering* **26**(1), 67–73. doi: https://doi.org/10.1061/(ASCE)AS.1943-5525.0000230.

Lemelin, M., Morisset, C., Germain, M., Hipkin, V., Goïta, K. and Lucey, P. G. (2013), 'Ilmenite mapping of the lunar regolith over Mare Australe and Mare Ingenii regions: An optimized multisource approach based on Hapke radiative transfer theory', *Journal of Geophysical Research: Planets* **118**, 2582–2593. doi: https://doi.org/10.1002/2013JE004392.

Lewis, J. S., McKay, D. S. and Clark, B. C. (1993), Using resources from near-earth space, *in* J. S. Lewis, M. S. Matthews and M. L. Guerrieri, eds, 'Resources of Near-Earth Space', University of Arizona Press, pp. 3–14.

Li, S., Lucey, P. G., Milliken, R. E., Hayne, P. O., Fisher, E., Williams, J.-P., Hurley, D. M. and Elphic, R. C. (2018), 'Direct evidence of surface exposed water ice in the lunar polar regions', *Proceedings of the National Academy of Sciences* (115), 8907–8912. doi: https://doi.org/10.1073/pnas.1802345115.

Li, Y., Li, X., Wang, S., Tang, H., Gan, H., Li, S., Wei, G., Zheng, Y., Tsang, K. T.

and Ouyang, Z. (2012), In-situ water production by reducing ilmenite, *in* V. Badescu, ed., 'Moon', Springer, New York, pp. 189–200. doi: https://doi.org/10.1007/978-3-642-27969-0.

Lindsley, D. H., Kesson, S. E., Hartzman, M. J. and Cushman, M. K. (1974), The stability of armalcolite: Experimental studies in the system MgO-Fe-Ti-O, *in* '5th Lunar Science Conference', Vol. 1, pp. 521–534.

Lomax, B. A., Conti, M., Khan, N., Bennett, N. S., Ganin, A. Y. and Symes, M. D. (2020), 'Proving the viability of an electrochemical process for the simultaneous extraction of oxygen and production of metal alloys from lunar regolith', *Planetary and Space Science* **180**, 104748. doi: https://doi.org/10.1016/j.pss.2019.104748.

Lowers, H. A., Stoeser, D. B., Wilson, S. A. and Meeker, G. P. (2008), Development of lunar regolith simulant: From the macro to the micro, *in* 'Microscopy and Microanalysis', Vol. 14, Cambridge University Press, pp. 516–517. doi: https://doi.org/10.1017/S1431927608088272.

Lucey, P. G., Taylor, G. J., Hawke, B. and Spudis, P. D. (1998), 'FeO and TiO_2 concentrations in the South Pole-Aitken basin: Implications for mantle composition and basin formation', *Journal of Geophysical Research: Planets* **103**, 3701–3708. doi: https://doi.org/10.1029/97JE03146.

Manick, K., Gill, S.-J., Najorka, J. and Duvet, L. (2018), Funadamental properties characterisation of lunar regolith simulants at the European Space Agency (ESA) sample analogue curaction facility, *in* '49th Lunar and Planetary Science Conference', number #1411.

Martins, Z .and Hofmann, B. A., Gnos, E., Greenwood, R. C., Verchovsky, A., Franchi, I. A., Jull, A. J. T., Botta, O .and Glavin, D. P., Dworkin, J. P. et al. (2007), 'Amino acid composition, petrology, geochemistry, ^{14}C terrestrial age and oxygen isotopes of the shişr 033 CR chondrite', *Meteoritics & Planetary Science* **42**(9), 1581–1595.

Massieon, C. C., Cutler, A. H. and Shadman, F. (1993), 'Hydrogen reduction of iron-bearing silicates', *Industrial & engineering chemistry research* **32**(6), 1239–1244. doi: https://doi.org/10.1021/ie00018a033.

Massieon, C. C., Cutler, A. and Shadman, F. (1992), Reduction of iron-bearing lunar minerals for the production of oxygen, Master's thesis.

McKay, D. S., Heiken, G., Basu, A., Blanford, G., Simon, S., Reedy, R., French, B. M. and

Papike, J. (1991a), The lunar regolith, *in* G. H. Heiken, D. T. Vaniman and B. M. French, eds, 'Lunar Sourcebook', Cambridge University Press, pp. 285–356.

McKay, D. S., Heiken, G. H., Taylor, R. M., Clanton, U. S., Morrison, D. A. and Ladle, G. H. (1972), Apollo 14 soils: Size distribution and particle types, *in* '3rd Lunar Science Conference', Vol. 1, pp. 983–994.

McKay, D. S., Morris, R. V. and Jurewicz, A. J. (1991b), Reduction of simulated lunar glass by carbon and hydrogen and its implications for lunar base oxygen production, *in* '22nd Lunar and Planetary Science Conference', pp. 881–882.

McKay, D. S. and Williams, R. J. (1979), A geologic assessment of potential lunar ores, *in* J. Billingham, W. Gilbreath and B. O'Leary, eds, 'Space Resources and Space Settlements', U.S. Government Printing Office, chapter V-4, pp. 243–255.

Meng, Z., Chen, S., Lu, P., Wang, Z., Lian, Y. and Zhou, C. (2011), 'Research on the distribution and content of water ice in lunar pole regions using Clementine UVVIS data', *Journal of Earth Science* **22**(5), 595–600. doi: https://doi.org/10.1007/s12583-011-0210-9.

Meteoritical Bulletin Database (2019), 'Northwest africa 12592'. [Accessed 11th June 2019].
URL: *https://www.lpi.usra.edu/meteor/metbull.php?code=69534*

Meyer, C. (2009), 10084, *in* C. Meyer, ed., 'Lunar Sample Compendium'.
URL: *https://www.lpi.usra.edu/lunar/samples/atlas/compendium/10084.pdf*

Meyer, C. (2010), 60500 and 65510, *in* C. Meyer, ed., 'Lunar Sample Compendium'.
URL: *https://curator.jsc.nasa.gov/lunar/lsc/60500.pdf*

Meyer, C. (2011), 15415, *in* C. Meyer, ed., 'Lunar Sample Compendium'.
URL: *https://www.lpi.usra.edu/lunar/samples/atlas/compendium/15415.pdf*

Milliken, R. E. and Li, S. (2017), 'Remote detection of widespread indigenous water in lunar pyroclastic deposits', *Nature Geoscience* **10**, 561–565. doi: https://doi.org/10.1038/ngeo2993.

Mitrofanov, I. G., Sanin, A. B., Boynton, W. V., Chin, G., Garvin, J. B., Golovin, D., Evans, L. G., Harshman, K., Kozyrev, A. S., Litvak, M. L. et al. (2010), 'Hydrogen mapping of the lunar south pole using the LRO neutron detector experiment LEND', *Science* **330**(6003), 483–486. doi: https://doi.org/10.1126/science.1185696.

Morris, R. V. (1980), Origins and size distribution of metallic iron particles in the lunar regolith, *in* '11th Lunar and Planetary Science Conference', pp. 1697–1712.

Mortimer, J. (2016), Investigating the Distribution and Source(s) of Lunar Volatiles, PhD thesis, The Open University.

NASA (1969*a*), Apollo 11 mission report, Report MSC-00171, National Aeronatics and Space Administration.
URL: *https://www.nasa.gov/specials/apollo50th/pdf/A11_MissionReport.pdf*

NASA (1969*b*), Apollo 8 mission report, Report MSC-PA-R-69-1, National Aeronautics and Space Administration.
URL: *https://www.hq.nasa.gov/alsj/a410/A08_MissionReport.pdf*

NASA (1970), Apollo 12 mission report, Report MSC-01855, National Aeronatics and Space Administration.
URL: *https://www.hq.nasa.gov/alsj/a12/A12_MissionReport.pdf*

NASA (1971*a*), Apollo 14 mission report, Report MSC-04112, National Aeronatics and Space Administration.
URL: *https://www.hq.nasa.gov/alsj/a14/A14_MissionReport.pdf*

NASA (1971*b*), Apollo 15 mission report, Report MSC-05161, National Aeronatics and Space Administration.
URL: *https://www.hq.nasa.gov/alsj/a15/ap15mr.pdf*

NASA (1972), Apollo 16 mission report, Report MSC-07230, National Aeronatics and Space Administration.
URL: *https://www.hq.nasa.gov/alsj/a16/A16_MissionReport.pdf*

NASA (1973), Apollo 17 mission report, Report JSC-07904, National Aeronatics and Space Administration.
URL: *https://history.nasa.gov/alsj/a17/A17_MissionReport.pdf*

NASA (2017), 'Technology Readiness Level'. [Accessed 12th April 2020].
URL: *https://www.nasa.gov/directorates/heo/scan/engineering/technology/txt_accordion-1.html*

National Research Council (2007), *The scientific context for exploration of the Moon*, National Academies Press. doi: https://doi.org/10.17226/11954.

National Research Council (2011), *Vision and Voyages: For Planetary Science in the Decade 2013-2022*, National Academies Press. doi: https://doi.org/10.17226/13117.

Ness Jr, R. O., Sharp, L. L., Brekke, D. W., Knudsen, C. W. and Gibson, M. A. (1992), Hydrogen reduction of lunar soil and simulants, *in* 'Engineering, Construction, and Operations in space-III: Space'92', Vol. 1, pp. 617–628.

Norris, P. (2019), The other competitor in the space race, *in* 'Returning people to the Moon after Apollo', Springer Praxis Books, pp. 83–120. doi: https://doi.org/10.1007/978-3-030-14915-4.

Paige, D. A., Siegler, M. A., Zhang, J. A., Hayne, P. O., Foote, E. J., Bennett, K. A., Vasavada, A. R., Greenhagen, B. T., Schofield, J. T. and McCleese, D. J. (2010), 'Diviner lunar radiometer observations of cold traps in the Moon's south polar region', *Science* **330**(6003), 479–482. doi: https://doi.org/10.1126/science.1187726.

Papike, Taylor, L. and S, S. (1991), Lunar minerals, *in* G. H. Heiken, D. T. Vaniman and B. M. French, eds, 'Lunar Sourcebook', Cambridge University Press, pp. 121–181.

Pfeiffer Vacuum, G. (2013), *Vacuum technology book*, Vol. II, Pfeiffer Vacuum GmbH, Asslar, Germany.

Pieters, C. M. and Noble, S. K. (2016), 'Space weathering on airless bodies', *Journal of Geophysical Research: Planets* **121**(10), 1865–1884. doi: https://doi.org/10.1002/2016JE005128.

Prado, M. (2013), 'Major lunar minerals'. [Accessed 23rd November 2016].
URL: *http://www.permanent.com/lunar-geology-minerals.html*

Prokof'ev, V. Y. (1998), 'Types of hydrothermal ore-forming systems (from fluid inclusion studies)', *Geology of ore deposits* **40**(6), 457–470. [Translated from *Geologiya Rudnykh Mestorozhdenii*, **40**(6), 1998, 514–528].

Quattrone, P. D. (1985), Extended mission life support systems, *in* 'Seminar on Space Station Human Productivity', pp. 2–80–2–98.

Reiss, P., Grill, L. and Barber, S. J. (2019), 'Thermal extraction of volatiles from the lunar regolith simulant NU-LHT-2M: preparations for in-situ analyses on the Moon', *Planetary and Space Science* **175**, 41–51. doi: https://doi.org/10.1016/j.pss.2019.05.001.

Retsch (2004), 'The basic principles of sieve analysis'. [Accessed 10th June 2019].
URL: *https://www.retsch.com/downloads/application-reports/dl_details/1/file/53e4b553-2188-4f5f-b3ed-636500000000/*

Richardson, J. E. and Abramov, O. (2020), 'Modeling the formation of the lunar upper megaregolith layer', *The Planetary Science Journal* **1**. doi: https://doi.org/10.3847/PSJ/ab7235.

Rickman, D. L. and Lowers, H. (2012), Particle shape and composition of NU-LHT-2M, Report NASA/TM—2012–217458, National Aeronautics and Space Administration.
URL: *https://www.nasa.gov/sites/default/files/atoms/files/rickmanlowers2012particleshapecomposition.pdf*

Rickman, D. L., Young, C., Stoeser, D. and Edmunson, J. (2014), Beneficiation of Stillwater Complex Rock for the Production of Lunar Simulants, Report NASA/TM—2012–217458, National Aeronautics and Space Administration.
URL: *https://ntrs.nasa.gov/citations/20140003187*

Roush, T. L., Colaprete, A., Elphic, R., Ennico-Smith, K., Heldmann, J., Stoker, C., Marinova, M., McMurray, R., Fritzler, E. and Morse, S. (2015), 'In situ resource utilization (ISRU) field expedition 2012: Near-infrared volatile spectrometer system (NIRVSS) science measurements compared to site knowledge', *Advances in Space Research* **55**, 2451–2456. doi: https://doi.org/10.1016/j.asr.2014.08.033.

Saal, A. E., Hauri, E. H., Cascio, M. L., Van Orman, J. A., Rutherford, M. C. and Cooper, R. F. (2008), 'Volatile content of lunar volcanic glasses and the presence of water in the Moon's interior', *Nature* **454**, 192–195. doi: https://doi.org/10.1038/nature07047.

Sabat, K. C., Rajput, P., Paramguru, R. K., Bhoi, B. and Mishra, B. K. (2014), 'Reduction of oxide minerals by hydrogen plasma: An overview', *Plasma Chemistry and Plasma Processing* **34**, 1–23. doi: https://doi.org/10.1007/s11090-013-9484-2.

Sanders, G. B. and Larson, W. E. (2012), 'Progress made in lunar in situ resource utilization under NASA's exploration technology and development program', *Journal of Aerospace Engineering* **26**, 5–17. doi: https://doi.org/10.1061/(ASCE)AS.1943-5525.0000208.

Sargeant, H. M., Abernethy, F. A. J., Barber, S. J., Wright, I. P., Anand, M., Sheridan, S. and Morse, A. (2020b), 'Hydrogen reduction of ilmenite: Towards an in situ resource utilization

demonstration on the surface of the Moon', *Planetary and Space Science* **180**, 104751. doi: https://doi.org/10.1016/j.pss.2019.104751.

Sargeant, H. M., Abernethy, F., Anand, M., Barber, S. J., Landsberg, P., Sheridan, S., Wright, I. P. and Morse, A. (2020a), 'Feasibility studies for hydrogen reduction of ilmenite in a static system for use as an ISRU demonstration on the lunar surface', *Planetary and Space Science* **180**, 104759. doi: https://doi.org/10.1016/j.pss.2019.104759.

Sargeant, H. M., Bickel, V. T., Honniball, C. I., Martinez, S. N., Rogaski, A., Bell, S. K., Czaplinski, E. C., Farrant, B. E., Harrington, E. M., Tolometti, G. D. and Kring, D. A. (2020c), 'Using boulder tracks as a tool to understand the bearing capacity of permanently shadowed regions of the Moon', *Journal of Geophysical Research: Planets* **125**. doi: https://doi.org/10.1029/2019JE006157.

Schlüter, L. and Cowley, A. (2020), 'Review of techniques for in-situ oxygen extraction on the Moon', *Planetary and Space Science* **181**, 104753. doi: https://doi.org/10.1016/j.pss.2019.104753.

Schrunk, D., Sharpe, B., Cooper, B. L. and Thangavelu, M. (2007), Lunar resources, *in* 'The Moon: Resources, future development and settlement', Springer Science & Business Media, pp. 49–58.

Seboldt, W., Lingner, S., Hoernes, S., Grimmeisen, W., Lekies, R., Herkelmann, R. and Burt, D. M. (1993), Lunar oxygen extraction using flourine, *in* J. S. Lewis, M. S. Matthews and M. L. Guerrieri, eds, 'Resources of Near-Earth Space', University of Arizona Press, pp. 129–147.

Sefa, M., Setina, J. and Erjavec, B. (2014), 'A new method for determining water adsorption phenomena on metal surfaces in a vacuum', *Materials and technology* **48**(1), 119–124.

Sefton-Nash, E., Carpenter, J. D., Fisackerly, R., Trautner, R., the ESA Lunar Exploration Team, the PROSPECT user group and the PROSPECT industrial team (2018), ESA's PROSPECT package for exploration of lunar resources: Investigation domains, *in* 'European Lunar Symposium'.

Sefton-Nash, E., Fisackerly, R., Trautner, R., Barber, S. J., Reiss, P., Martin, D., Heather, D., Houdou, B. and the PROSPECT science team and industrial consortium (2020), The ESA PROSPECT payload for Luna 27: Development status, *in* '51st Lunar and Planetary Science Conference', number #2367.

Shaw, L. A. (2019), International space station as a development testbed for advanced environmental control and life support systems, *in* '49th International Conference on Environmental Systems'.

Si, X.-g., Lu, X.-g., Li, C.-w., Li, C.-h. and Ding, W.-z. (2012), 'Phase transformation and reduction kinetics during the hydrogen reduction of ilmenite concentrate', *International Journal of Minerals, Metallurgy, and Materials* **19**(5), 384–390. doi: https://doi.org/10.1007/s12613-012-0568-4.

Siegler, M. A., Keane, J. T. and Paige, D. A. (2018), Subsurface ice stability on the Moon, *in* 'Lunar Polar Volatiles', number 5038. [LPI Contribution No. 2087].

Simon, S. B., Papike, J. J. and Laul, J. C. (1982), The lunar regolith: Comparative studies of the Apollo and Luna sites. petrology of soils from Apollo 17, Luna 16, 20, and 24, *in* '12th Lunar and Planetary Science Conference', pp. 371–388.

Singh, B. and Thomas III, J. H. (1998), Fundamentals of vacuum technology and surface physics, *in* D. Hoffman, B. Singh and J. H. Thomas III, eds, 'Handbook of vacuum science and technology', Elsevier, chapter 1.8.5, pp. 45–47. doi: https://doi.org/10.1016/B978-0-12-352065-4.X5040-8.

Spudis, P. D., Bussey, B., Plescia, J., Josset, J. and Beauvivre, S. (2008), 'Geology of Shackleton Crater and the south pole of the Moon', *Geophysical Research Letters* **35**. doi: https://doi.org/10.1029/2008GL034468.

Spudis, P. D., Bussey, D. B. J., Baloga, S. M., Cahill, J. T. S., Glaze, L. S., Patterson, G. W., Raney, R. K., Thompson, T. W., Thomson, B. J. and Ustinov, E. A. (2013), 'Evidence for water ice on the Moon: Results for anomalous polar craters from the LRO Mini-RF imaging radar', *Journal of Geophysical Research: Planets* **118**, 2016–2029. doi: https://doi.org/10.1002/jgre.20156.

Stoeser, D., Wilsin, S. and Rickman, D. (2010), Design and specifications for the highland regolith prototype simulants NU-LHT-1M and -2M, Report NASA/TM—2010-216438, National Aeronautics and Space Administration.
URL: *https://www.nasa.gov/sites/default/files/atoms/files/nasa_tm_2010_216438.pdf*

Street Jr, K. W., Ray, C., Rickman, D. and Scheiman, D. A. (2010), Thermal properties of lunar regolith simulants, Report NASA/TM-2010-216348, National Aeronautics and Space Administration.

URL: *https://www.nasa.gov/sites/default/files/atoms/files/nasa_tm-2010-216348_grc_thermprop.pdf*

Sueyoshi, K., Watanabe, T., Nakano, Y., Kanamori, H., Aoki, S., Miyahara, A. and Matsui, K. (2008), Reaction mechanism of various types of lunar soil simulants by hydrogen reduction, *in* 'Earth & Space 2008: Engineering, Science, Construction, and Operations in Challenging Environments', pp. 1–8.

Talboys, D. L., Barber, S., Bridges, J. C., Kelley, S. P., Pullan, D., Verchovsky, A. B., Butcher, G., Fazel, A., Fraser, G. W., Pillinger, C. T. et al. (2009), 'In situ radiometric dating on Mars: Investigation of the feasibility of K-Ar dating using flight-type mass and X-ray spectrometers', *Planetary and Space Science* **57**, 1237–1245. doi: https://doi.org/10.1016/j.pss.2009.02.012.

Taylor, G. J., Warren, P., Ryder, G., Delano, J., Pieters, C. and Lofgren, G. (1991), Lunar rocks, *in* G. H. Heiken, D. T. Vaniman and B. M. French, eds, 'Lunar Sourcebook', Cambridge University Press, pp. 183–284.

Taylor, L. (n.d.), 'Lunar soil formation'. [Accessed 17th March 2020].
URL: *https://www.lpi.usra.edu/exploration/training/illustrations/surfaceEnviron/*

Taylor, L. A., Jerde, E. A., McKay, D. S., Gibson, M. A., Knudsen, C. W. and Kanamori, H. (1993), Production of O_2 on the Moon: A lab-top demonstration of ilmenite reduction with hydrogen, *in* '24th Lunar and Planetary Science Conference', pp. 1411–1412.

Taylor, L. A. and Liu, Y. (2010), Important considerations for lunar soil simulants, *in* 'Earth and Space 2010: Engineering, Science, Construction, and Operations in Challenging Environments', pp. 106–118. doi: https://doi.org/10.1061/41096(366)14.

Taylor, L. A., Pieters, C. M. and Britt, D. (2016), 'Evaluations of lunar regolith simulants', *Planetary and Space Science* **126**, 1–7. doi: https://doi.org/10.1016/j.pss.2016.04.005.

Taylor, L. A., Pieters, C., Patchen, A., Taylor, D. S., Morris, R. V., Keller, L. P. and McKay, D. S. (2010), 'Mineralogical and chemical characterization of lunar highland soils: Insights into the space weathering of soils on airless bodies', *Journal of Geophysical Research: Planets* **115**. doi: https://doi.org/10.1029/2009JE003427.

Taylor, L. and Carrier, W. (1993), Oxygen production on the Moon: An overview and evaluation, *in* J. S. Lewis, M. S. Matthews and M. L. Guerrieri, eds, 'Resources of Near-Earth Space', University of Arizona Press, pp. 69–108.

The Lunar Sample Preliminary Science Team (1972), Part A. A petrographic and chemical description of samples from the lunar highlands, *in* 'Apollo 16 Preliminary Science Report', National Aeronautics and Space Administration, chapter 7. Preliminary Examination of Lunar Samples, pp. 1–24.

Thompson, M. S., Zega, T. J., Becerra, P., Keane, J. T. and Byrne, S. (2016), 'The oxidation state of nanophase Fe particles in lunar soil: Implications for space weathering', *Meteoritics & Planetary Science* **51**(6), 1082–1095. doi: https://doi.org/10.1111/maps.12646.

Thornton, W. and Bonato, F. (2017), Countermeasures to loss of muscle and bone during spaceflight, *in* 'The Human Body and Weightlessness', Springer, pp. 177–219. doi: https://doi.org/10.1007/978-3-319-32829-4_7.

Turan, E. M., Stein, S. A., Maharaj, R. and Möller, K. P. (2020), 'A flow sheet for the conversion of lunar regolith using fluorine gas', *Advances in Space Research* **65**, 1852–1862. doi: https://doi.org/10.1016/j.asr.2020.01.014.

Tyrrell, H. J. V. (1964), 'The origin and present status of Fick's diffusion law', *Journal of Chemical Education* **41**(7), 397. doi: https://doi.org/10.1021/ed041p397.

UK Space Agency (2020), 'Space Placement in Industry (SPIN)'. [Accessed 10th February 2020].

URL: *https://www.gov.uk/government/publications/space-placement-in-industry-spin-award-scheme-2019*

van Milligen, B. P., Bons, P. D., Carreras, B. A. and Sánchez, R. (2005), 'On the applicability of Fick's law to diffusion in inhomogeneous systems', *European Journal of Physics* **26**(5), 913–925. doi: https://doi.org/10.1088/0143-0807/26/5/023.

Vaniman, D., Dietrich, J., Taylor, G. J. and Heiken, G. (1991), Exploration, samples, and recent concepts of the Moon, *in* G. H. Heiken, D. T. Vaniman and B. M. French, eds, 'Lunar Sourcebook', Cambridge University Press, p. 5.

Vaniman, D., Pettit, D. and Heiken, G. (1992), Uses of lunar sulfur, *in* 'The Second Conference on Lunar Bases and Space Activities of the 21st Century', Vol. 2, pp. 429–435.

Vuolo, M., Baiocco, G., Barbieri, S., Bocchini, L., Giraudo, M., Gheysens, T., Lobascio, C. and Ottolenghi, A. (2017), 'Exploring innovative radiation shielding approaches in space: A material and design study for a wearable radiation protection spacesuit', *Life Sciences in Space Research* **15**, 69–78. doi: https://doi.org/10.1016/j.lssr.2017.08.003.

Wang, Y., Yuan, Z., Matsuura, H. and Tsukihashi, F. (2009), 'Reduction extraction kinetics of titania and iron from an ilmenite by H_2–Ar gas mixtures', *ISIJ international* **49**(2), 164–170. doi: https://doi.org/10.2355/isijinternational.49.164.

Warren, P. H. and Wasson, J. T. (1979), 'The origin of KREEP', *Reviews of Geophysics* **17**, 73–88. doi: https://doi.org/10.1029/RG017i001p00073.

Watson, E. B. and Baxter, E. F. (2007), 'Diffusion in solid-Earth systems', *Earth and Planetary Science Letters* **253**(3-4), 307–327. doi: https://doi.org/10.1016/j.epsl.2006.11.015.

Watson, K., Murray, B. and Brown, H. (1961), 'On the possible presence of ice on the Moon', *Journal of Geophysical Research* **66**, 1598–1600. doi: https://doi.org/10.1029/JZ066i005p01598.

Weston, G. F. (1985), Fundamentals of vacuum science and technology, *in* G. Weston, ed., 'Ultrahigh vacuum practice', Butterworth & Co. Ltd, London, UK, pp. 1–21. doi: https://doi.org/10.1016/B978-0-408-01485-4.50004-0.

Wieczorek, M. A., Weiss, B. P. and Stewart, S. T. (2012), 'An impactor origin for lunar magnetic anomalies', *Science* **335**, 1212–1215. doi: https://doi.org/10.1126/science.1214773.

Wiggins, S. E., Johnson, B. C., Bowling, T. J., Melosh, H. J. and Silber, E. A. (2019), 'Impact fragmentation and the development of the deep lunar megaregolith', *Journal of Geophysical Research: Planets* **124**, 941–957. doi: https://doi.org/10.1029/2018JE005757.

Williams, R. J. (1985), Oxygen extraction from lunar materials: An experimental test of an ilmenite reduction process, *in* 'Lunar bases and space activities of the 21st century', p. 551.

Williams, R. J., McKay, D. S., Giles, D. and Bunch, T. E. (1979), Mining and beneficiation of lunar ores, *in* J. Billingham, W. Gilbreth and B. O'Leary, eds, 'Space Resources and Space Settlements', National Aeronautics and Space Administration, pp. 275–188.

Wright, I. P., Barber, S. J., Morgan, G. H., Morse, A. D., Sheridan, S., Andrews, D. J., Maynard, J., Yau, D., Evans, S. T. and Leese, M. R. (2007), 'Ptolemy – an instrument to measure stable isotopic ratios of key volatiles on a cometary nucleus', *Space Science Reviews* **128**, 363–381. doi: https://doi.org/10.1007/s11214-006-9001-5.

Yazawa, Y., Yamaguchi, A. and Takeda, H. (2012), Lunar minerals and their resource utilization with particular reference to solar power satellites and potential roles for humic substances for lunar agriculture, *in* V. Badescu, ed., 'Moon', Springer, pp. 105–138. doi: https://doi.org/10.1007/978-3-642-27969-0_5.

Yoshida, H., Watanabe, T., Kanamori, H., Yoshida, T., Ogiwara, S. and Eguchi, K. (2000), Experimental study on water production by hydrogen reduction of lunar soil simulant in a fixed bed reactor, pp. 0704–0188.

Zellner, N. E. B. (2019), 'Lunar impact glasses: Probing the Moon's surface and constraining its impact history', *Journal of Geophysical Research: Planets* **124**, 2686–2702. doi: https://doi.org/10.1029/2019JE006050.

Zeng, X., He, C. and Wilkinson, A. (2010), 'Geotechnical properties of NU-LHT-2M lunar highland simulant', *Journal of Aerospace Engineering* **23**(4), 213–218. doi: https://doi.org/10.1061/(ASCE)AS.1943-5525.0000026.

Zhang, G. (2000), Reduction of Rutile and Ilmenite by Methane-hydrogen Gas Mixture, PhD thesis, University of New South Wales.

Zhang, G.-H., Chou, K.-C. and Zhao, H.-L. (2012), 'Reduction kinetics of $FeTiO_3$ powder by hydrogen', *ISIJ international* **52**, 1986–1989. doi: https://doi.org/10.2355/isijinternational.52.1986.

Zhao, Y. and Shadman, F. (1993), Production of oxygen from lunar ilmenite, *in* J. S. Lewis, M. S. Matthews and M. L. Guerrieri, eds, 'Resources of Near-Earth Space', University of Arizona Press, pp. 149–178.